



POLITECNICO DI TORINO  
Repository ISTITUZIONALE

Innovative materials for high temperature structural applications: 3rd Generation -TiAl fabricated by Electron Beam Melting

*Original*

Innovative materials for high temperature structural applications: 3rd Generation -TiAl fabricated by Electron Beam Melting / Ternier, Mathieu. - (2014).

*Availability:*

This version is available at: 11583/2527509 since:

*Publisher:*

Politecnico di Torino

*Published*

DOI:10.6092/polito/porto/2527509

*Terms of use:*

Altro tipo di accesso

This article is made available under terms and conditions as specified in the corresponding bibliographic description in the repository

*Publisher copyright*

(Article begins on next page)

**POLITECNICO DI TORINO**



**Innovative materials for high temperature structural applications: 3<sup>rd</sup> Generation  $\gamma$ -TiAl fabricated by Electron Beam Melting**

**Mathieu TERNER**

*PhD Thesis in Materials Science and Technology*

*Cycle XXVI*

*January 2014*

Tutor: Prof. Claudio BADINI  
Co-Tutor: Dr. Sara BIAMINO

*Department of Applied Science  
and Technology*

Examiner:

Prof. Marco VANNI  
Prof. Marcello BARICCO  
Prof. Philippe LOURS  
Prof. Edoardo GARRONE

## Summary

In the aeronautics industry, the propulsion systems stand among the most advanced and critical components. Over the last 50 years, gas turbine aeroengines were subjected to intensive research to increase efficiency and reduce weight, noise and harmful emissions. Together with design optimization, breakthrough in materials science for structural applications triggered the development of the most advanced gas turbine engines. For low temperatures, basically ahead of the combustion section, lightweight Ti alloys are preferred for their good mechanical properties. For high temperatures instead, Ni-based superalloys exhibit outstanding properties up to very high temperatures despite a rather high material's density.

Research have focused on enhancing to the maximum the potential of materials in gas turbine engines. According to the application, the components experience various mechanical and environmental constraints. Special designs, manufacturing process, material compositions and protective coatings have been developed to push the limits of advanced materials. Nowadays, the attention is focused on innovative materials to replace the existing Ti and Ni based alloys leading to substantial benefits. Light weight composite materials in particular were found very attractive to replace some components' Ti alloys. At higher temperatures, it is of great interest to replace Ni-based superalloys by materials with lower density and/or higher temperatures applications, which in turn would lead to substantial weight reduction and increase efficiency.

At the highest temperatures range, in particular in the combustion chamber and high pressure turbine sections, ceramic based materials offer promising balance of properties. Research are dedicated to overcome the drawbacks of ceramics for such structural applications, and in particular their brittle fracture behavior, by addition of reinforcing fibers. At lower temperatures range, TiAl based intermetallics emerged as very promising materials at half the density of Ni-based superalloys. Significant weight reduction could be achieved by the introduction of TiAl based alloys for rotating components of the compressor and low pressure turbine. 2<sup>nd</sup> generation  $\gamma$ -TiAl alloys were lately introduced in GE's GENx and CFM's LEAP engines.

The present work concerns the fabrication by the additive manufacturing technique Electron Beam Melting of 3<sup>rd</sup> generation  $\gamma$ -TiAl alloys for high temperatures application in gas turbine aeroengines. EBM, building parts layer by layer according to CAD, offers many advantages compared to other manufacturing processes like casting and forging. Reported by Avio, 2<sup>nd</sup> generation  $\gamma$ -TiAl alloys have been successfully fabricated by EBM. To increase the material's potential, the production of 3<sup>rd</sup> generation  $\gamma$ -TiAl alloys Ti-(45-46)Al-2Cr-8Nb was therefore studied. The optimization of the EBM parameters led to high homogeneity and very low post-processing residual porosity  $\leq 1\%$ . The fine equiaxed microstructure after EBM could be tailored towards the desired mechanical properties by simple heat treatment, from equiaxed to duplex to fully lamellar. In particular, a duplex microstructure composed by about 80 % lamellar grains pinned at grain boundaries by fine equiaxed grains was obtained after heat treatment slightly over the  $\alpha$  transus temperature.

The study showed that addition of a higher amount of Nb significantly increased the oxidation resistance of the material, thus increasing the application temperature range of these  $\gamma$ -TiAl alloys.

## Acknowledgments

In this section, I can express my gratitude to a number of people that made this work possible and more importantly enjoyable. Since November 2010 when I first arrived in Torino, I have crossed the path of many people I will never forget.

In a first instance, I'd like to thank all of my colleagues at the Dipartimento di Scienza dei Materiali of Politecnico di Torino. I wish I could name everyone, but instead I'll name just one: Paolo Epicoco. Many thanks to you for teaching me everything you knew about TiAl, EBM and the different machines from our laboratories. Nevertheless, each and everyone have been an important part of the success of my experience. A special thank goes to Dr. Sara Biamino for her supervision: you were a great tutor. Finally, I must express my gratitude to professors Claudio Badini and Paolo Fino, heads of the research group. Nothing would have been possible without your support.

People in Avio were as much responsible for the smooth progress of my thesis. Thanks to Silvia Sabbadini and Federica Pelissero in charge of TiAl for providing work all these years. Thank you to Andrea Penna for enlightening the production of TiAl by EBM.

Since work is not all, this wonderful country I'm living in for more than 3 years is a big part of the great time I had. Italia is exceptional: its beauty, its food, its history and art, its people. Italy exhibits the best and the worst of this world. Torn between magnificent nature and chaotic driving, great people and political scandals, greatest art and fraud, finest cuisine and poisoned agriculture. I like to think that while France is convinced of its "greatness" and spread it all over, Italy knows it but doesn't need to show off.

My deepest acknowledgments go to Tarik Annaoui, the very first person I met in Torino. Thank you my friend to have shared with me your home and your friends. Many thanks as well to the Magariello brothers, Filippo, Guillaume, Adriana and all the others for the wonderful moments. Last but not least, I am very thankful to Giulia Briselli, my little piece of Toscana that I'll keep close to me. Thank you for your support, trust and patience.

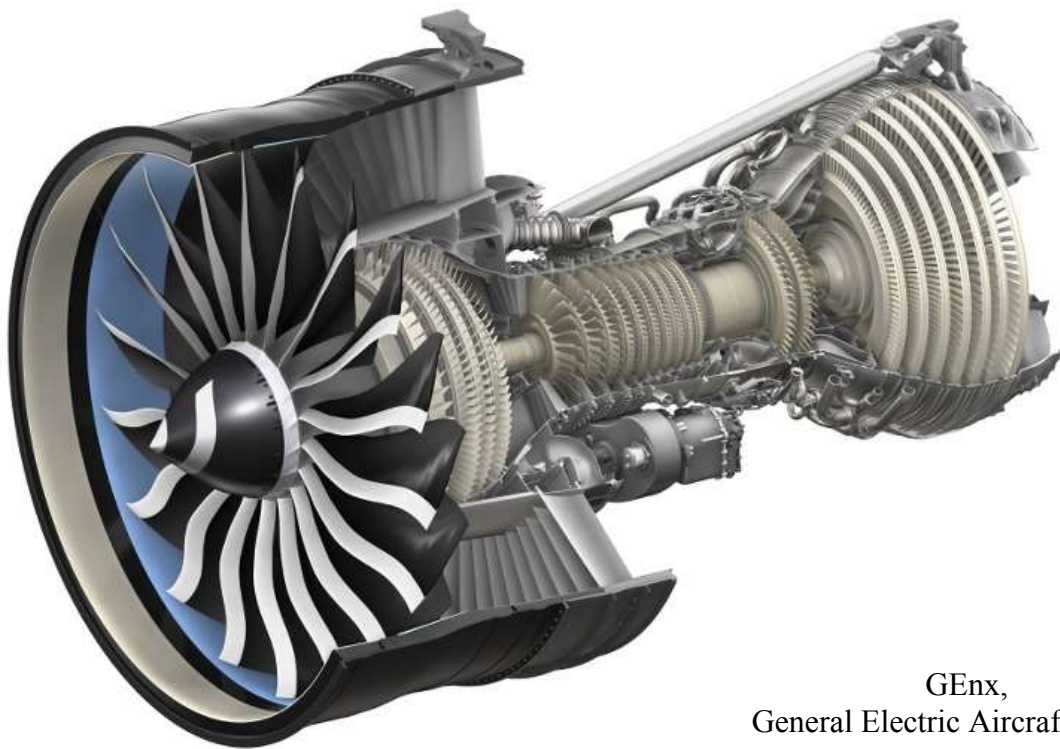
I wish to conclude this acknowledgments section by greeting everyone I couldn't cite: colleagues from Politecnico and Avio, friends from Italy and beyond, mates from the New BM basketball team, family and friends back home. I am a happy man and I owe it to you all.

## Index

<b>SUMMARY .....</b>	<b>1</b>
<b>ACKNOWLEDGMENTS.....</b>	<b>2</b>
<b>INDEX.....</b>	<b>3</b>
<b>PART I MATERIALS SCIENCE INNOVATIONS FOR GAS TURBINE APPLICATION IN THE AERONAUTICS FIELD.....</b>	<b>5</b>
<b>I. MATERIALS DEVELOPMENT .....</b>	<b>6</b>
1. <i>Materials science for evolution .....</i>	<i>6</i>
2. <i>Materials science today .....</i>	<i>7</i>
3. <i>Prospective for HT structural materials in the aeronautics .....</i>	<i>8</i>
<b>II. PRINCIPLE, PERFORMANCE AND MATERIALS OF AEROENGINE GAS TURBINES .....</b>	<b>9</b>
1. <i>Gas turbines in the aeronautic industry.....</i>	<i>9</i>
2. <i>Turbofan engines .....</i>	<i>15</i>
A. <i>Fan module.....</i>	<i>17</i>
B. <i>Core module.....</i>	<i>17</i>
C. <i>Low pressure turbine module .....</i>	<i>18</i>
3. <i>Advanced materials for the main components.....</i>	<i>18</i>
A. <i>Titanium alloys .....</i>	<i>19</i>
B. <i>Superalloys .....</i>	<i>20</i>
<b>III. INNOVATIVE HIGH TEMPERATURE MATERIALS FOR THE AERONAUTICS .....</b>	<b>22</b>
1. <i>Ceramics for very high temperature structural applications.....</i>	<i>23</i>
A. <i>Ceramic Matrix Composites .....</i>	<i>24</i>
B. <i>Eutectic ceramics.....</i>	<i>27</i>
C. <i>SiAlON ceramics and composites .....</i>	<i>30</i>
D. <i>Hybrid MoSi<sub>2</sub> base ceramic composites .....</i>	<i>34</i>
2. <i>TiAl alloys for high temperature structural applications .....</i>	<i>38</i>
A. <i>Chemistry of <math>\gamma</math>-TiAl alloys:.....</i>	<i>41</i>
B. <i>Mechanical properties .....</i>	<i>45</i>
a. <i>Tensile properties .....</i>	<i>45</i>
b. <i>Creep properties .....</i>	<i>51</i>
c. <i>Toughness and crack growth resistance.....</i>	<i>54</i>
d. <i>Hardness .....</i>	<i>58</i>
e. <i>Oxidation.....</i>	<i>62</i>
<b>PART II THE PRODUCTION OF 3RD GENERATION <math>\Gamma</math>-TiAl ALLOYS BY ELECTRON BEAM MELTING: FABRICATION, CHARACTERIZATION AND MICROSTRUCTURE SET-UP.....</b>	<b>64</b>
<b>I. THE ADDITIVE MANUFACTURING PROCESS ELECTRON BEAM MELTING (EBM) .....</b>	<b>65</b>
<b>II. CHARACTERIZATION OF THE BASE MATERIAL: HIGH Nb CONTAINING PRE-ALLOYED POWDERS.....</b>	<b>69</b>
1. <i>Chemical composition .....</i>	<i>69</i>
2. <i>Particle size distribution.....</i>	<i>70</i>
3. <i>Morphology.....</i>	<i>71</i>
4. <i>Flowability.....</i>	<i>72</i>
5. <i>Apparent density.....</i>	<i>72</i>

<b>III. FABRICATION OF Ti-(45-46)Al-2Cr-8Nb SAMPLES BY EBM .....</b>	<b>73</b>
1. <i>The measure of residual porosity to optimize the EBM process.....</i>	<i>75</i>
A. First trial .....	76
B. Second trial.....	77
C. Third trial.....	78
D. Fourth trial .....	80
E. Fifth trial.....	81
2. <i>Characterization of the massive samples .....</i>	<i>82</i>
A. Chemical composition .....	84
a. Core of the samples .....	84
b. Core-edge composition difference .....	85
B. Phase analysis by X-ray diffraction.....	86
C. Microstructure analysis of the materials as-EBM .....	88
D. Phase transitions analysis by TMA .....	92
a. Comparison between TMA and DSC.....	93
b. Effect of alloying elements to validate the model.....	95
c. Dynamic to static results.....	96
d. TMA of the EBM optimization trials .....	97
<b>IV. MICROSTRUCTURE SET-UP BY POST PROCESSING HEAT TREATMENT .....</b>	<b>100</b>
1. <i>Hot Isostatic Pressing (HIP).....</i>	<i>100</i>
A. Reduction of residual porosity by Hot Isostatic Pressing.....	100
B. Recrystallization by Hot Isostatic Pressing .....	102
2. <i>Heat treatments around <math>T_\alpha</math> to set the microstructure .....</i>	<i>106</i>
A. Set-up of Ti-45Al-2Cr-8Nb's microstructure .....	106
B. Set-up of Ti-46Al-2Cr-8Nb's microstructure .....	110
C. Details of the 80 % lamellar microstructure .....	111
<b>V. OXIDATION BEHAVIOR OF 2<sup>ND</sup> AND 3<sup>RD</sup> GENERATION <math>\gamma</math>-TiAl ALLOYS .....</b>	<b>115</b>
1. <i>Thermogravimetric analysis in air up to 1000 °C.....</i>	<i>116</i>
2. <i>Thermogravimetric analysis in air during isothermal oxidation at 750, 850 and 950 °C for 10 hours.....</i>	<i>118</i>
3. <i>Isothermal oxidation in air at 850 °C up to 100 hours. ....</i>	<i>120</i>
4. <i>Isothermal oxidation in air at 950 °C up to 50 hours .....</i>	<i>125</i>
<b>VI. MECHANICAL PROPERTIES.....</b>	<b>127</b>
1. <i>Tensile properties.....</i>	<i>127</i>
2. <i>Creep resistance.....</i>	<i>129</i>
<b>CONCLUSION.....</b>	<b>130</b>
<b>TABLE OF FIGURES.....</b>	<b>132</b>
<b>BIBLIOGRAPHY .....</b>	<b>137</b>

**PART I**  
**Materials science innovations for gas turbine  
application in the aeronautics field**



Genx,  
General Electric Aircraft Engines

# I. Materials development

## 1. Materials science for evolution



For the occasion of the TMS 2007 Annual Meeting & Exhibition in Orlando, the journal JOM announced in September 2006 the world's greatest moments in materials science and engineering history. Professionals in the materials field as well as the general public voted for their top ten moments from a list of 100 nominees. The results are displayed on the timeline below in figure 1 [1, 2].

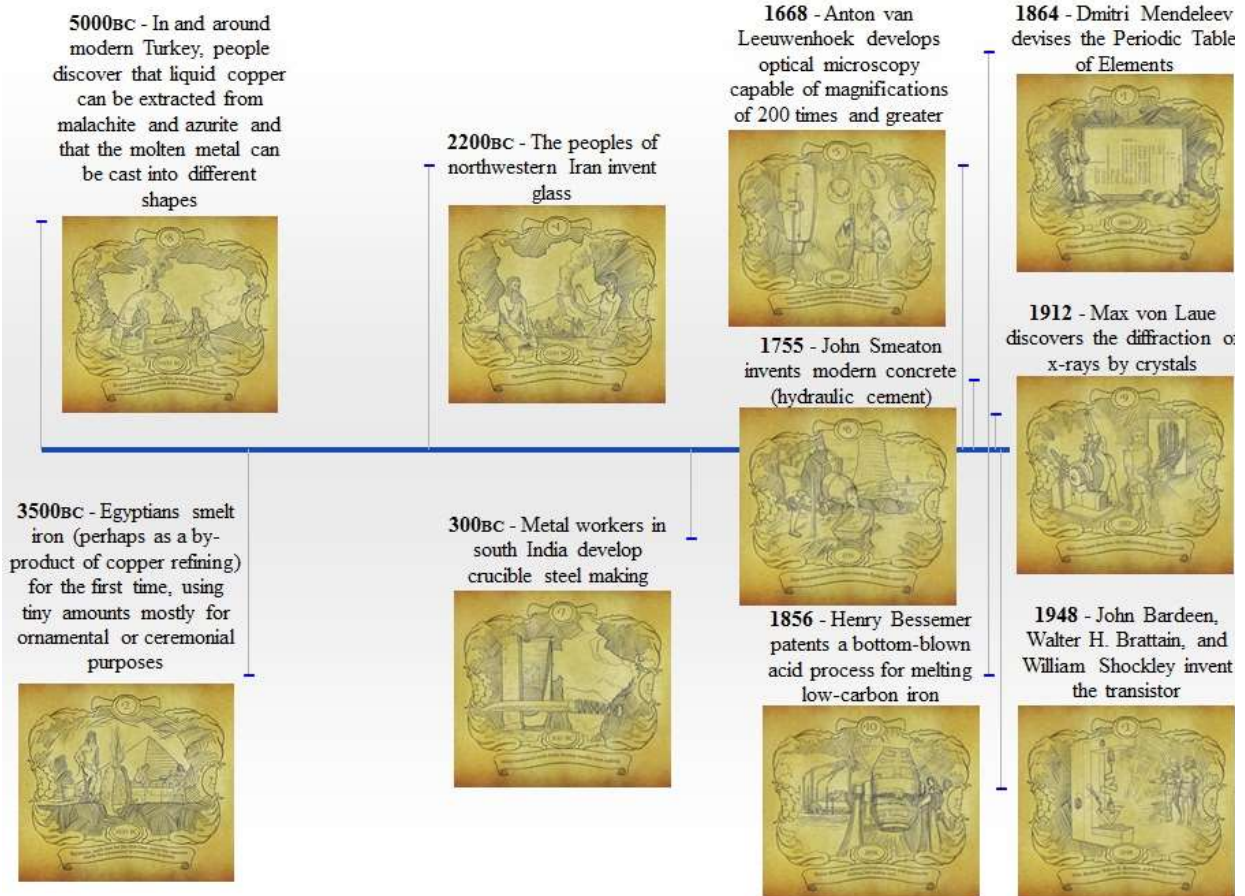


Figure 1: Timeline of the JOM top 10 greatest moments in materials science and engineering history



These are only the top events chosen by the voters, among a very long list of key moments. It can also be cited the discovery of radioactivity in 1896 by Pierre and Marie Curie, which marks the beginning of modern-era studies on spontaneous radiation and applications of radioactivity for civilian and military applications. Or the publication by Niels Bohr in 1913 of his model of atomic structure, which introduces the theory that electrons travel in discrete orbits around the atom's nucleus, with the chemical properties of the element being largely determined by the number of electrons in each of the outer orbits.

Materials are everywhere, so is materials science. Everything or most is selected, designed, produced, optimized to answer our needs. The progress and development of our kind over the time is related to breakthrough in science and technology. Advances in materials science nowadays push our limits to what seemed impossible in the past. And to what will be possible in the future !

## 2. Materials science today

Today, tons of people or goods can be flown or shipped from one side of the planet to another. Millions of data can be carried on a device smaller than a nut. Hundreds of people can live in buildings over 200 meters high. We can drive over 300 km.h<sup>-1</sup>. Space is filled with orbital telescopes and transmission satellites.



**Figure 2: Examples of applications where materials science advances are a key factor: Aeronautics, Automobile, Marine, Civil, Space, Informatics, Energy**

Materials must be developed to perform their duty in the best way possible. The manufacturing processes are optimized, the reduction of weight and dimensions is sought, the overall costs tend to be lowered, the harmful emissions reduced. Depending on the application, the materials properties required vary drastically. Any function comes with a set of properties required for the part (mechanical properties, cost, resistance to environment, ...).

Basically, materials can be divided into 5 categories:

- Metals and Alloys
- Ceramics
- Plastics
- Semiconductors
- Composites

In the aeronautic industry, since the machines are intended to fly, the lighter the better. A lot of research thus aimed to reduce the overall weight of the flying objects, without impacting the security and comfort. In civil aviation for example, metallic cutlery was replaced by plastic. The weight of the seats were reduced by half. Large parts of the structure were replaced by light weight composite materials. Of course, it must be assured the integrity of the mechanical properties and environmental resistance to overcome the stress in operation. It must also be economically viable regarding materials, production and maintenance costs. Therefore, materials development intend to find the best compromise between performance and cost.

This thesis focuses on materials for aeroengines high temperature structural applications. Therefore, candidate materials are: metals and alloys for their wide set of properties and manufacturing convenience, ceramics and ceramic based composites for their outstanding high temperature properties and potential lightness.

### **3. Prospective for HT structural materials in the aeronautics**

In aeronautics, the high temperature field basically means the engines. In 1993, J.P. Angus for Rolls Royce<sup>[3]</sup> identified the important criteria to judge the suitability of the engines:

- Safety
- Thrust
- Weight
- Fuel burn
- Life cycle cost (LCC)
- Environmental

Among these criteria, which relative importance depends on application, the key performance is surely the *thrust to weight ratio*. In other words, the forward force applied to the aircraft (net thrust) by an engine divided by its weight. Regarding materials' science, increasing the thrust to weight ratio can be done in two ways<sup>[4]</sup>:

- Increase thrust : it suggests higher material operating temperatures. Increasing the operating temperature leads to better cycle efficiency. Consequently, it allows to whether reduce fuel consumption or increase thrust.
- Reduce weight : it corresponds to materials with higher specific strength and stiffness.

So far, research focused on metallic materials such as Ni based superalloys. Today, the best Ni based superalloys exhibit acceptable temperature resistances up to 1150 °C (even 1200 °C for short time) which is about 90 % of melting temperatures. Cast alloys have been optimized from equiaxed multi-grained to directionally solidified microstructures and even single crystals. Complex designs have been set up to allow air cooling of the blades through inner channels. Thermal and environmental coatings have been developed.

Nowadays though, progress seems to have reached the limit of Ni-based superalloys and alternative materials are studied. As just mentioned, there are two approaches: the current materials in use could be replaced by either materials with lower density and/or higher temperature capability, and of course exhibiting the same properties. Some of the most promising candidates are reviewed later in section III.

## II. Principle, performance and materials of aeroengine gas turbines

### 1. Gas turbines in the aeronautic industry

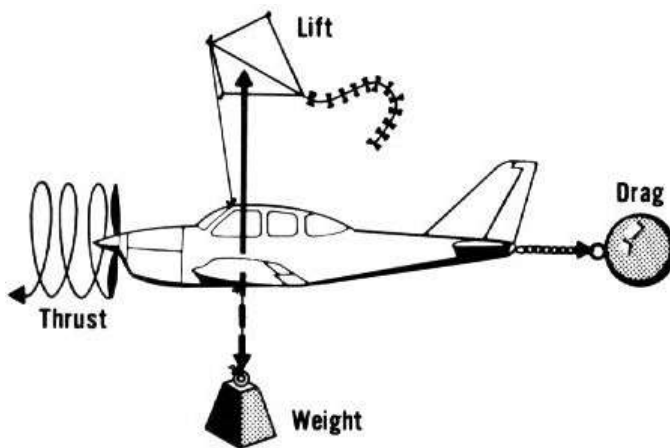


**Figure 3: Forces applied to an aircraft in flight**

An aircraft is subjected to 4 forces during flight represented the opposite figure 3. These forces are actually 2 pairs of opposite forces (figure 3).

Weight is the downward force resulting from earth's gravity. Lift is the opposite upward force that keeps the vehicle in the air. The weight must be overcome by the lift in order to fly. Drag is the force resulting from air resistance. Finally, the thrust is the driving force opposed to drag.

Thrust is thus a propulsion force created by a power source: the engine. There are two ways to create a propulsion force.

The first way is rocket propulsion<sup>[5-7]</sup>. This is based on Newton's third law of motion commonly translated: *"To every action there is always an equal and opposite reaction: or the forces of two bodies on each other are always equal and are directed in opposite directions."*

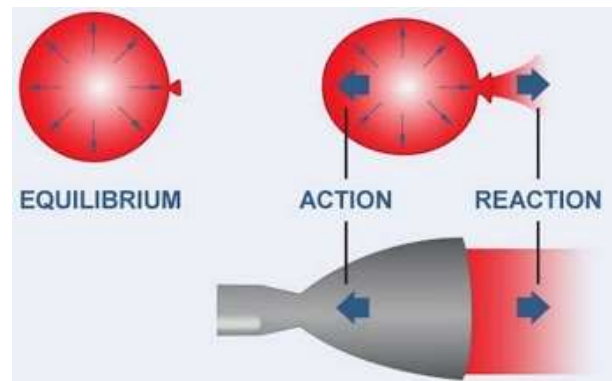


Figure 4: Schematic representation of rocket propulsion

Propellants are combined in a combustion chamber where they chemically react to form hot gases which are then accelerated and ejected at high velocity through a nozzle, thereby imparting momentum to the engine (figure 4). The thrust force of a rocket motor is the reaction experienced by the motor structure due to ejection of the high velocity matter.



Figure 5: Example of rocket propulsion. Ariane launch on 26<sup>th</sup> November 2010 (left) and a missile (right).

The second way is air-breathing propulsion<sup>[7-14]</sup>. The principle is to seize mass from the surroundings and set the mass in motion backwards, using the reaction force to propel the vehicle. The basic 4-steps principle is:

- Intake of air
- Compression of the air
- Combustion, where the fuel is injected and burnt to convert the stored energy
- Expansion and exhaust, where the converted energy is put to use

Many different types of aero engine could be listed or grouped, and only a few general examples will be presented. Two categories can be distinguished. Often referred as "jet engine", a turbojet and a ramjet create thrust from the action of a fluid jet leaving the engine. On the other hand, a turbofan and a turboprop create most of the thrust through the use of a fan and a propeller respectively. These engines are basically divided into 2 sections:

- The core of the engine produces power to drive the propulsion section
- The propulsion section generates the thrust

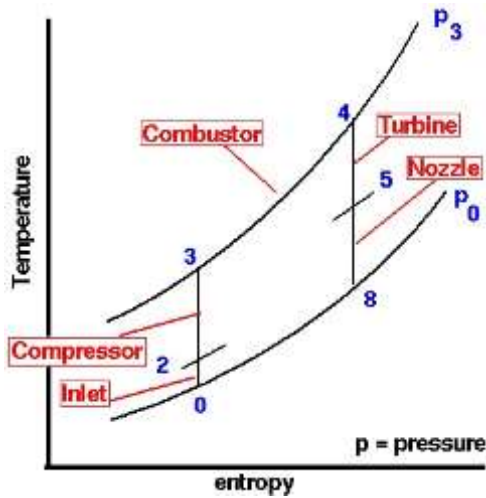


Figure 6: T-s diagram of the Brayton cycle [15]

Except for the ramjet engine, the core of the engine is the gas generator to supply high temperature and pressure gas. It is composed by a compressor, a combustor and a turbine. The principle is based on the Brayton thermodynamic cycle which is used in all gas turbine engines (figure 6) [7, 11, 14-16]. Air is sucked into the engine (0-2) and compressed (2-3). This increases the pressure and reduces the volume which leads to an increase in temperature. High pressured air is mixed with fuel and burn to convert chemical to thermal energy (3-4). The temperature and volume increase while the pressure remains stable. It then expands through the turbine to drive the compressor (4-5). Temperature and pressure decrease which leads the volume to increase.

A schematic model of the gas generator is displayed figure 7 [8, 16]. The purpose of any gas generator is to supply high pressure and temperature gas. The different section identified in figure 6 were represented in figure 7 by red numbers.

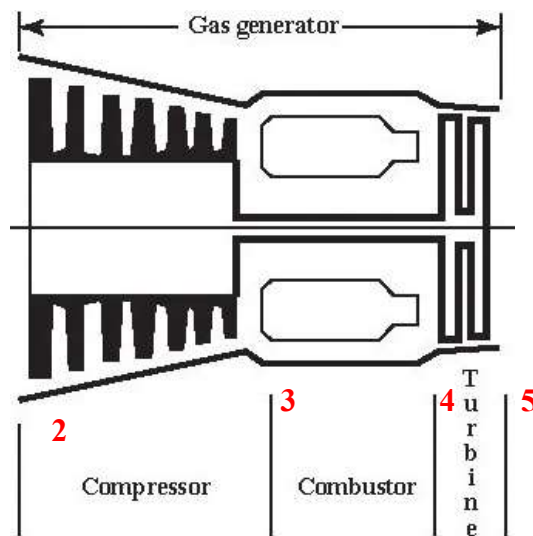
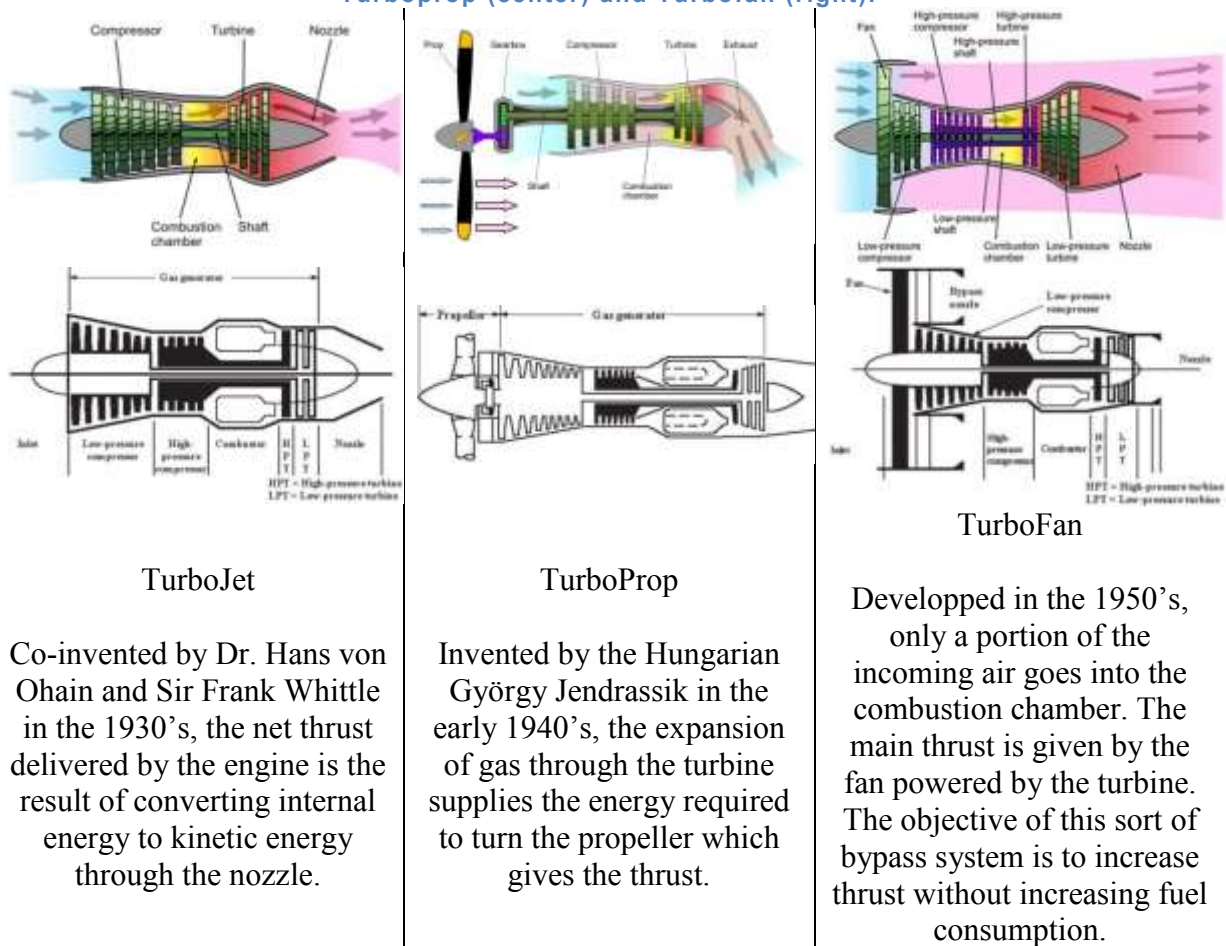


Figure 7: Schematic drawing of the gas generator, core of any gas turbine engine [7]

As air passes through a gas turbine engine, aerodynamic and energy requirements demand changes in the air's velocity and pressure. During compression, a rise in the air pressure is required, but not an increase in its velocity. After compression and combustion have heated the air, an increase in the velocity of gases is necessary in order for the turbine rotors to develop power. The size and shape of the ducts through which the air flows affect these various changes. Where a conversion from velocity to pressure is required, the passages are divergent. Conversely, if a conversion from pressure to velocity is needed, a convergent duct is used.

The propulsion section that generates the thrust can be of two types [7, 8, 13, 14, 17-19]. In a jet engine (left in figure 8), a last stage nozzle converts the thermal energy from the hot pressured gas into kinetic energy and momentum. Else, the hot and pressured gas expand in a second turbine which extracts work and drives a shaft connected to a fan or a propeller (center and right in figure 8).

**Figure 8: Schematic drawings of the different gas turbine engines. Turbojet (left), TurboProp (center) and Turbofan (right).**



The suitable type of engine is determined according to its application and engines are classified by performance parameters [4, 7, 14, 16, 19]. For example, the thermal efficiency of an engine. Thermal efficiency is defined as the net rate of organized energy (shaft power for turbofans or turboprops, kinetic energy for turbojets) out of the engine divided by the rate of thermal energy available from the fuel in the engine:

$$\eta_T = \frac{\dot{W}_{out}}{\dot{Q}_{in}} \quad [7]$$

Where  $\dot{W}_{out}$  is the net power out of the engine and  $\dot{Q}_{in}$  the rate of thermal energy released.

Another parameter is the propulsive efficiency, which is the measure of how effectively the engine power is used to power the aircraft. In other words, the ratio of the aircraft power (thrust times velocity) to the power out of the engine. For a jet engine with a single inlet and single exhaust, an exit pressure equal to the ambient pressure, a mass flow of fuel way lower than that of air and very small installation losses, the propulsive efficiency is:

$$\eta_P = \frac{TV_0}{\dot{W}_{out}} = \frac{2}{V_e/V_0 + 1} \quad [7]$$

Where  $T$  is the thrust of the propulsive system,  $V_0$  and  $V_e$  are the velocities at inlet (velocity of the aircraft) and exit respectively.

Turbojet engines have high values of the velocity ratio  $V_e/V_0$  with corresponding low propulsive efficiency, whereas for turbofan engines it is the opposite. The thermal and propulsive efficiency can be combined to give the overall efficiency of a propulsion system. Multiplying the parameters, we get the ratio of the aircraft power to the rate of thermal energy released in the engine:

$$\eta_0 = \eta_P \eta_T = \frac{TV_0}{\dot{Q}_{in}} \quad [7]$$

The general trends of efficiency are plot figure 9 for typical aircraft engines. The poor efficiency of turbojet engines makes it the less attractive economically. To this day, progress have been made to increase the engines' overall efficiency

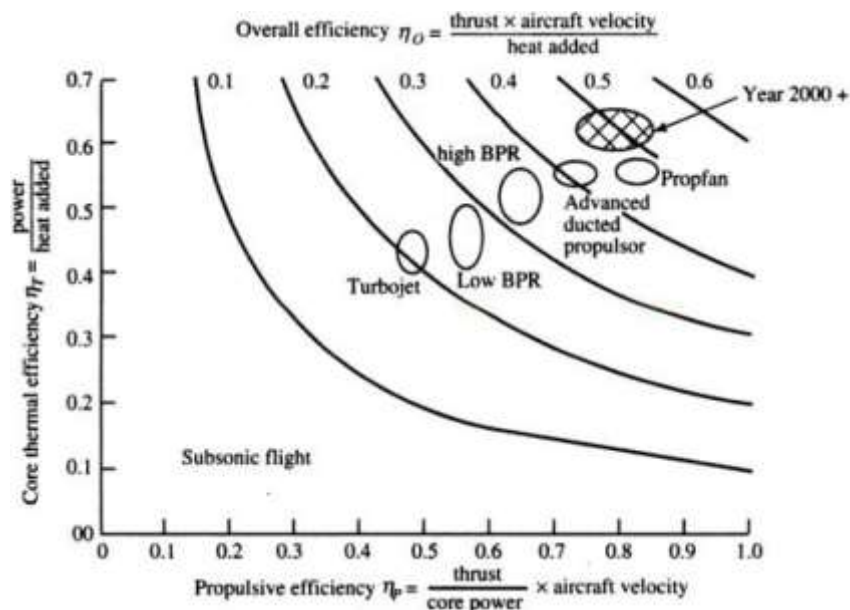


Figure 9: Efficiency characteristics of typical aircraft engines [7]

One of the most important performance parameter is the thrust of the engine. The general trend of specific thrust versus aircraft speed is displayed figure 10 for the typical engines. It is the amount of output power or thrust per unit of mass flow entering the engine. For example, a modern civil turbofan with a high by-pass ratio has a low specific thrust to keep the jet noise at an acceptable level and to achieve low fuel consumption. In this case, the engine must be relatively large in diameter for the net thrust it produces.

On the other hand, a modern military aircraft has a high specific thrust which usually reduces the dimension of the engine for aerodynamic issues.

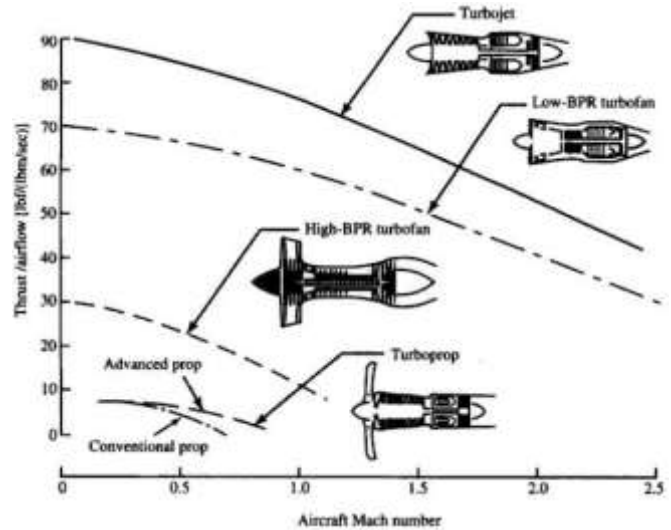


Figure 10: Specific thrust characteristics of typical aircraft engines <sup>[7]</sup>

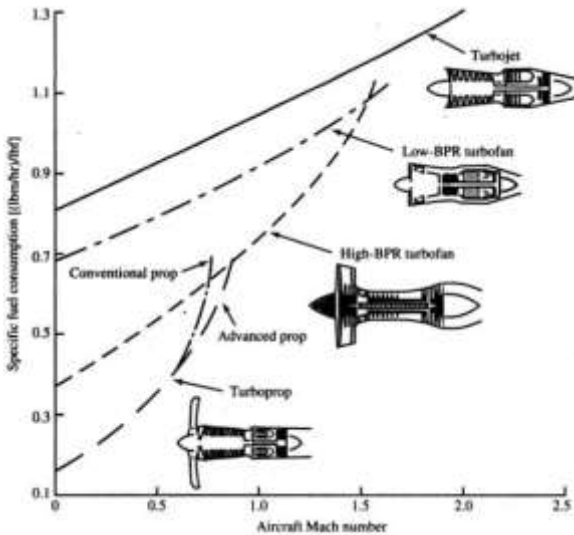


Figure 11: Thrust specific fuel consumption characteristics of typical aircraft engines <sup>[7]</sup>

Finally, another important performance parameter is the specific fuel consumption. This is the rate of fuel used by the propulsion system per unit of thrust produced. It is important to minimize the specific fuel consumption for applications where the weight and cost of the fuel is an issue. In other words, civil aviation. The general trends for the typical aircraft engines are displayed figure 11.



## 2. Turbofan engines

Turbofan engines are commonly used nowadays in the aeronautic industry [4, 7, 8, 13, 14, 17, 20]. For a certain realm of flight, a turbofan is more economical and efficient than a turbojet and has a better aerodynamic performance than turboprops at high subsonic speed. The turbofan engines market is dominated by 3 giants: General Electric, Rolls Royce and Pratt & Whitney. Many other companies also contribute: Honeywell, MTU, SNECMA, Avio, etc. Different joint-venture between the leading companies were created. To name a few: CFM International between General Electric and SNECMA formed to build and support the CFM56 series, Engine Alliance between General Electric and Pratt & Whitney to create engines for high-capacity and long range aircraft.

Every model of engine is different. Depending on the family of aircraft and the flight conditions, requirements vary widely. The configuration, fuel consumption, technology, certification are proper to the engine type. However, from a materials point of view, all kind of turbofan are similar. The temperature and pressure range for the different sections are similar. The design is similar in that the manufacturing process of the components are similar. The materials science approach to increase efficiency (or reduce weight) is the same. The general purpose for any engine manufacturer is to increase the temperature in the hot sections in order to increase efficiency. Also, increasing the specific properties (divided by materials density) is sought in order to reduce the overall weight of the engine. Of course, doing both is the ultimate goal.

As an example in figures 12 and 13, the CFM56-7 engine was chosen to detail the different sections of a turbofan engine [8, 17, 21-24]. This engine is produced by CFM International (GE and SNECMA) for the Boeing 737 family. In service since 1994 (engine certification in October 1996), this popular engine fleet evolved over the years. The Tech Insertion configuration emerged in 2007, and since mid-2011 all delivery are in CFM56-7BE configuration with even better performance and cost efficiency.



**Figure 12: Schematic cutaway representation of CFM56-7B developed by CFM International**

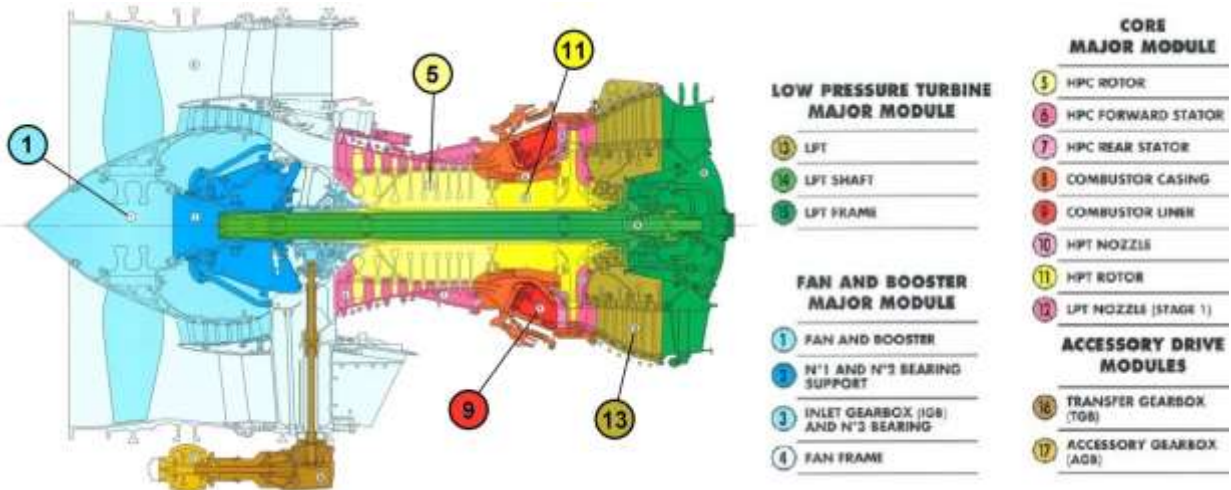


**Figure 13:** Schematic technological drawing of the CFM56-7B engine displaying the different components [23]

The CFM56-7 is a dual rotor, variable stator, high bypass ratio turbofan power plant designed for subsonic service. The engine incorporates a single-stage High Pressure Turbine (HPT: 11 in figure 13) which drives a 9-stage High Pressure Compressor (HPC: 5 in figure 13). The integrated fan and Low Pressure Compressor (LPC: 1 in figure 13) are driven by a 4-stage Low Pressure Turbine (LPT: 13 in figure 13). The annular designed combustion chamber (9 in figure 13) increases the HPC discharge air velocity to drive the high and low pressure turbines. The design and configuration of the engine is based on obtaining long life, high reliability, and easy access for line maintenance. The engine is composed of major sub-assemblies or modules, which permits the changing of a major assembly without completely disassembling the engine. The different sections of the engine will be further describe in the following.

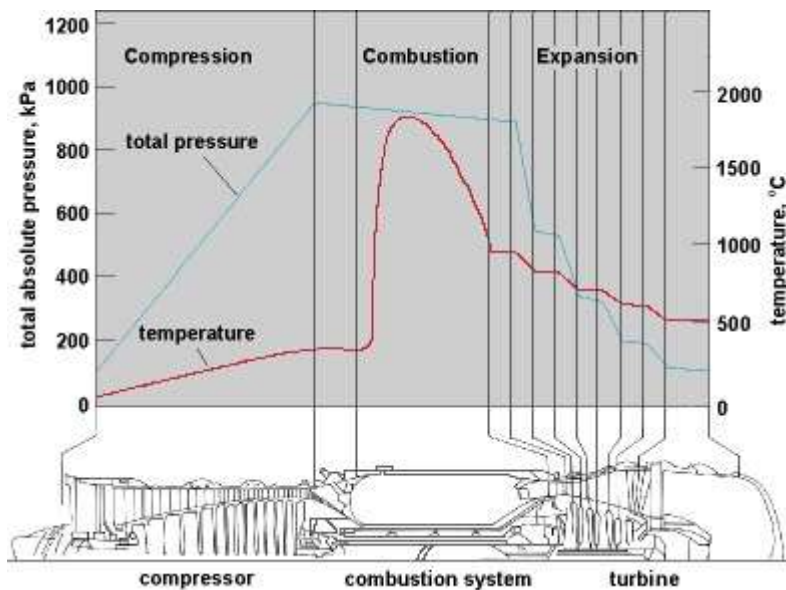


**Figure 14:** Temperature and pressure profiles of air in a gas turbine [25]

In figure 14, the profile of temperature and pressure of gas flow in the core of the engine is displayed. From figure 14, an increase in total pressure and temperature takes place through the compressor. The hot air is then mixed with fuel and burnt in the combustion chamber. Finally, the gaseous energy of the hot gas is discharged and transformed through the HPT and LPT to drive the compressor and the fan respectively. The different sections of such a gas turbine engine are presented in further details.

### A. Fan module



**Figure 15:** Exploded view of the fan major module of the CFM56-7 engines <sup>[26]</sup>

The head of the engine is composed by the fan and the booster or low pressure compressor. The primary function of the fan is to produce most of the thrust. In the case of the high bypass ratio turbofan CFM56-7 family, 80% of the air flow by-pass the core of the engine (secondary air flow).

On the other hand, 20% of the air flow is directed towards the core of the engine. The aim is to provide a clean and unrestricted airflow to the engine. Clean and undisturbed inlet airflow extends engine life by preventing erosion, corrosion and foreign object damage.

### B. Core module

The core of the engine is the gas generator mentioned earlier in section II.1. It is basically composed by the high pressure compressor (HPC), the combustor and the high pressure turbine (HPT).



**Figure 16:** Exploded view of the core major module of the CFM56-7 engines <sup>[26]</sup>

The role of the compressor is to supply all the air the turbine needs, at high static pressure. Each stage incrementally boosts the pressure from the previous stage. A single stage of compression consists in a set of rotor blades attached to a rotating disk, followed by a stator vanes attached to a stationary ring. At the compressor inlet, the air is approximately at 15 °C and 100 kPa. The overall pressure ratio is 32.8:1 for the 9-stage compressor of CFM56-7 engines. The temperature of the air at the compressor outlet can reach 700 °C for the most advanced engines. In general terms, the compressor rotor blades convert mechanical energy into gaseous energy.

The air in such state enters the combustion section or combustor, where it is mixed with fuel and burnt. This task is accomplished with a minimum pressure loss and a maximum heat release. The temperature of the flame in the combustion section can be as high as 1930 °C, which is higher than the metals in the engine can endure. Therefore, air from the secondary airflow is admitted in a controlled manner to direct the flame pattern, cool the liner walls and reduce the temperature. The maximum outlet temperature of the combustor depends on the HPT materials and can be as high as 1200 °C.

The CFM56-7 engines have a single-stage high pressure turbine (HPT). The turbine converts the gaseous energy of the mixture (air + burnt fuel) out of the combustor into mechanical energy in order to drive the compressor. This is done by expanding the hot and high-pressure gases to a lower temperature and pressure.

### **C. Low pressure turbine module**

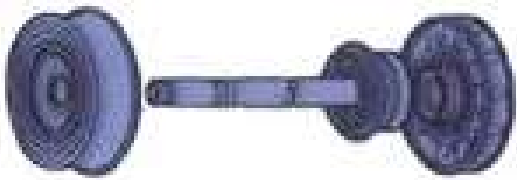


**Figure 17: Exploded view of the LPT major module of the CFM56-7 engines**  
[26]

The low pressure turbine is the element that drives the fan, which produces most of the thrust. The turbine converts the gaseous energy into mechanical energy by expanding the hot and high-pressure gases. Each stage of the turbine consists of a row of stationary vanes followed by a row of rotating blades, in the reverse order of the compressor.

In the compressor, energy is added to the gas by the rotor blades, then converted to static pressure by the stator vanes. On the contrary in the turbine, the stator vanes increase gas velocity and the rotor blades extract energy. The temperature and pressure of the gases decrease gradually through the turbine, but temperature at the turbine outlet could be as high as 700 °C.

After the gas has passed through the turbine, it is discharged through the exhaust. A significant amount of energy remains in the exhaust gas that has not been converted by the turbine into mechanical energy to drive the compressor and the fan. Through the convergent duct or exhaust nozzle, the gas is accelerated and used to produce jet thrust.

## **3. Advanced materials for the main components**

Progresses in gas turbine engines technology, with higher power ratings and efficiency levels, were largely due to advancements made in the field of materials. The development of materials with higher performance levels, together with design optimization, have been a critical breakthrough over the years. As suggested previously, this have been realized by increasing the temperature capability of materials and/or specific properties (to reduce weight).

An aircraft gas turbine is composed by thousands of structural components having different functions, experiencing different constraints, evolving in different environments. These components must have the proper tensile strength, stress rupture life, creep properties, fatigue etc. For materials operating at high temperatures, oxidation and hot corrosion resistance are crucial and coating technologies are often required. The main components previously described in section II.2 are critical to the performance of the engine. Advanced materials with high performance are used. Manufacture of these materials usually involves advanced processing methods.

The opposite pie chart shows the ratio of materials with respect to the total weight of the engine (figure 18) [5, 11, 27]. Steels, Nickel and Titanium alloys represent the major part of modern Turbofan engines. However, the attention is focused on lighter composite materials, advanced high temperature Ni-based superalloys and thermal barrier coatings, upcoming intermetallics and ceramics. The scope is always to reduce the overall weight of the engine and increase the temperatures in order to raise fuel efficiency and reduce noise, carbon and nitrogen oxides emissions.

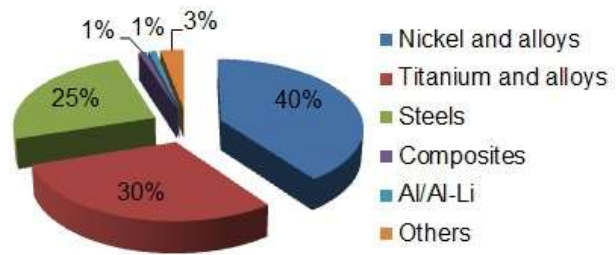


Figure 18: Material composition in Turbofan engines by total weight

### A. Titanium alloys

Titanium [14, 28-30] is a material with high strength to weight ratio. When high mechanical properties are necessary at medium range temperature and oxidation is not much an issue, titanium alloys fit perfectly.

Titanium content has increased from 3 % in the 1950s to about 33 % today of the aeroengine weight. Most structural parts of the high pressure compressor are made of titanium. Material selection is focused around light weight, high integrity and balanced solution for the designs. The now famous Ti-6Al-4V is used for static and rotating components. Castings are used to manufacture the more complex static parts while forging is typically preferred for the rotating components. This alloy is used in particular for fan disc, low pressure compressor discs and blades and for the first compressor stages up to 315 °C of the PW4084 engine.

Many Ti-based alloys have been further developed, along with optimized processing routes to set the desirable microstructure, in order to increase creep, fatigue strength and enhance temperature capabilities. For example, Ti6242 (see table 1) is an attractive high temperature alloy commercially available used for rotating components at temperatures up to 540 °C. It is used in high pressure compressors at temperature too high for Ti64 for structural applications.

Grade designation	Chemical composition	Maximum service temperature (°C)
Ti64	Ti-6Al-4V	315
Ti811	Ti-8Al-1Mo-1V	400
Alloy 685	Ti-6Al-5Zr-0.5Mo-0.25Si	520
Alloy 829	Ti-5.5Al-3.5Sn-3Zr-1Nb-0.25Mo-0.3Si	550
Alloy 834	Ti-5.8Al-4Sn-3.5Zr-0.7Nb-0.5Mo-0.35Si-0.06C	600
Ti1100	Ti-6Al-2.8Sn-4Zr-0.4Mo-0.4Si	600
Ti6242	Ti-6Al-2Sn-4Zr-2Mo	
Ti6242S	Ti-6Al-2Sn-4Zr-2Mo-0.2Si	540

Table 1: Titanium alloys used for compressor parts in aircraft engines [28]

However, the maximum temperature limit of advanced titanium alloys is about 600 °C. The hottest parts of the last stages of the high pressure compressor may exceed this temperature. They are typically made of Ni-based alloys, at nearly twice the weight. Furthermore, different thermal expansion and bonding techniques create problems. Efforts focus on producing a compressor entirely made of titanium alloys, which means the development of titanium alloys that can be used at temperatures over 600 °C.

## **B. Superalloys**

Superalloys [11, 14, 28, 31, 32] are typically Ni-based or Co-based alloys, probably the most advanced and investigated materials for high temperature applications in gas turbine engine.

The parts of the combustor in a gas turbine experience very high temperatures. The increasing firing temperatures and the need to better emission control require the use of advanced structural materials. Ni-based superalloys are presently the best option for their high creep and oxidation/corrosion resistance. For the combustor parts, they are usually processed from sheets. The composition of the alloys 617, 230 and Nimonic 263 are detailed in table 2. A Co-based superalloy with higher creep strength has been used lately to meet even higher firing temperatures.

<b>Grade</b>	<b>Chemical composition</b>
<b>Nimonic 263</b>	Ni-20Cr-20Co-0.4Fe-6Mo-2.1Ti-0.4Al-0.06C
<b>HA188</b>	Co22Cr22Ni1.5Fe14W0.05C0.01B
<b>617</b>	54Ni22Cr12.5Co8.5Mo1.2Al
<b>230</b>	55Ni22Cr5Co3Fe14W2Mo0.35Al0.10C0.015B

**Table 2:** Sheets superalloys for combustor parts in aeroengine gas turbine engines [28]

Powder metallurgy (PM) routes for producing superalloys found a great success, although forging and casting are accepted techniques to produce disks and blades respectively. Originally, conventional ingot metallurgy routes were adopted to manufacture turbine disks. For example the alloys A286 and 718. For high strength superalloys though, for example IN100 and Rene95, they are sometimes difficult to forge by conventional methods. PM processing offered many advantages. First of all, it allowed the production of alternative alloys that ingot metallurgy route struggled to produce. The properties of PM parts are enhanced thanks to a better control of the microstructure: finer grain size can be obtained, better homogeneity and alloys development flexibility. In addition, PM routes are near-net-shape process which advantageously reduce material wastes and post processing operations. It also allows more freedom in design. The following table 3 lists some superalloys, mostly Ni-based, used for the manufacture of turbine discs in aircraft gas turbine engine.

Grade	Chemical composition
<b>A286</b>	Fe-15Cr-25Ni-1.2Mo-2Ti-0.3Al-0.25V-0.08C-0.006B
<b>718</b>	Ni-19Cr-18.5Fe-3Mo-0.9Ti-0.5Al-5.1Cb-0.03C
<b>IN 100</b>	60Ni-10Cr-15Co-3Mo-4.7Ti-5.5Al-0.15C-0.015B-0.06Zr1.0V
<b>Rene 95</b>	61Ni-14Cr-8Co-3.5Mo-3.5W-3.5Nb-2.5Ti-3.5Al-0.16C-0.01B-0.05Zr
<b>LC Astroloy</b>	56.5Ni-15Cr-15Co-5.25Mo-3.5Ti-4.4Al-0.06C-0.03B-0.06Zr
<b>MERL-76</b>	54.4Ni-12.4Cr-18.6Co-3.3Mo-1.4Nb-4.3Ti-5.1Al-0.02C-0.03B-0.35Hf-0.06Zr
<b>Rene88 DT</b>	56.4Ni-16Cr-13Co-4Mo-4W-0.7Nb-3.7Ti-2.1Al-0.03C-0.015B-0.03Zr
<b>Udimet 720</b>	55Ni-18Cr-14.8Co-3Mo-1.25W-5Ti-2.5Al-0.035C-0.033B-0.03Zr

**Table 3: Ingot metallurgy (A286 and 718) and PM superalloys for turbine discs in aeroengine gas turbine engines <sup>[28]</sup>**

The turbine vanes and blades are critical components requiring the most advanced high temperature materials. The temperature is very high due to the hot gases after burning. Pressures are high as well and the high speed rotating elements are subjected to centrifugal forces. Creep strength is thus a primary requirement for turbine vanes and blades materials. The forgeability problems of superalloys which require hot workability constrained the composition range possibilities. Cast superalloys were therefore developed. The composition of alloys could thus be tailored for high temperature strength.

In gas turbine engines, the most severe conditions belong to the first stage turbine blades or buckets (rotating airfoils). They must withstand severe combination of temperature (hot gas), stress (centrifugal force) and environment (air and combustion products). On the other hand, vanes or nozzles (stationary airfoils) are subjected to lower mechanical stresses since they are fixed. However, they must be able to withstand high temperatures and thus require excellent high temperature oxidation and corrosion resistance.

Conventional equiaxed investment casting was originally used to produce turbine parts in the most demanding gas turbine engines. The rather coarse equiaxed microstructure of casting assured good mechanical properties in all directions at high temperature. For example, rotating turbine blades made of alloy IN713 were early produced. In order to enhance materials capabilities, the chemical composition and post process treatment were optimized. To increase the creep strength,  $\gamma'$  volume fraction increased (IN100, Rene100). Higher amount of refractory solid solution strengtheners, like W and Mo, were added to increase temperature capabilities (MAR-M200, MAR-M246, IN792, M22). Small amount of Hf, up to 2 wt.%, improved ductility. Higher Cr content increased corrosion resistance at the cost of some high temperature strength (Rene41, Rene77, Rene80, IN738C, Udimet700, Udimet710).

The major failure mechanism for gas turbine airfoils involved nucleation and growth of cavities along transverse grain boundaries. Therefore, effort was made to eliminate such defects and directional solidification (DS) was developed. The creep resistance and rupture strength could be increased through DS by eliminating transverse grain boundaries and the turbine blade metal temperature capability could be increased by about 14 °C with respect to conventionally cast superalloys. Single crystal (SC) blade technologies were subsequently developed increasing of about 30 °C the metal temperature capability of turbine blades. In SC castings, all grain boundaries are eliminated from the microstructure and a single crystal with a controlled orientation is produced in an airfoil shape. Since there is no grain boundary in such material, grain boundary strengtheners such as C, B, Zr and Hf are no longer necessary which helped increasing the melting temperature of the metals and consequently the high temperature strength. The following figure 19 shows turbine blades fabricated by conventional, directional solidification and single crystal castings.

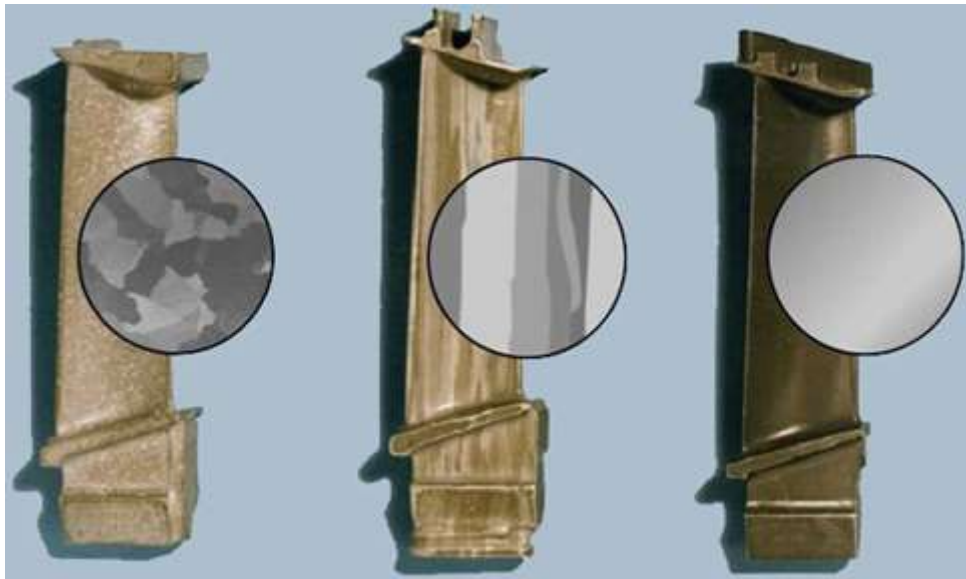


**Figure 19:** Conventionally cast, directionally solidified (DS) and single crystal (SC) blade technologies

### **III. Innovative high temperature materials for the aeronautics**

For the past 50 years, research have focus on materials that are stronger, lighter and at higher temperature. So far, research focused on metallic materials such as Ni based superalloys. Today, the best Ni based superalloys exhibit acceptable temperature resistances up to 1150 °C (even 1200 °C for short time) which is about 90 % of melting temperatures. Cast alloys have been optimized from equiaxed multi-grained to directionally solidified microstructures and even single crystals. Complex designs have been set up to allow air cooling of the blades through inner channels. Thermal and environmental coatings were developed. However, it seems that today's materials have been pushed up to their limits. This is why attention is now focused on new light and resistant materials for high temperature.



## 1. Ceramics for very high temperature structural applications

Ceramic materials have the highest potential to provide the above characteristics [3]. Ceramics come in many forms, in respect to their chemical composition and their structure. Mainly, ceramics can be divided into two categories : monolithic ceramic and ceramic matrix composites. As shown figure 20, ceramics have the potential to provide better specific strength that any other type of material.

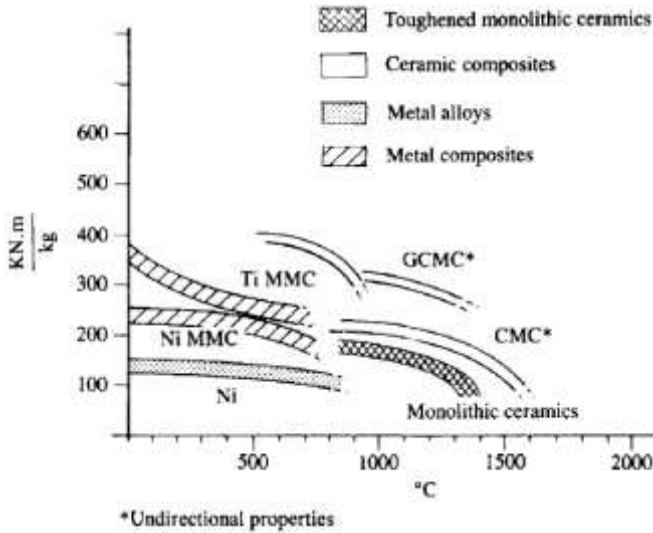


Figure 20: Specific strength comparison of ceramics and metals [3]

Monolithic ceramics are essentially homogeneous but brittle. They can be toughened into ceramic composites which offer a wide range of possibilities. There are three key elements of these materials :

- Fibers
- Matrix
- Fiber/matrix interface layer

In addition, there is a wide range of possible fiber architectures.

Thus, a promising scope of material can be obtained based on different combination of fibers (type and architecture), matrix and interface.

The important difference between monolithic ceramics and ceramic composites is their failure mode, presented in figure 21. In the case of monolithic ceramics, the stress/strain behavior is linearly elastic up to the point of failure. The failure is thus sudden and complete even though good ultimate tensile strengths can be achieved. The number and size of defects, which are proportional to the volume of the components, influence the occurrence of failure. Consequently, monolithic ceramics are more suitable for small components.

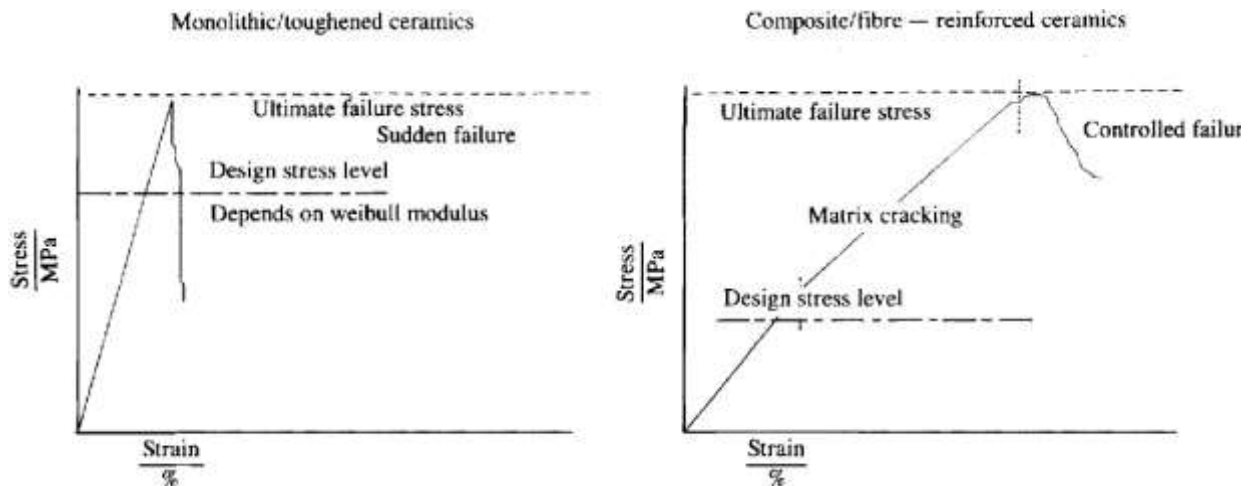


Figure 21: Comparison of monolithic ceramics and ceramic composites stress vs. strain behavior [3]

In comparison, ceramic composites behave differently. First, they have a linear elastic behavior up to a point where microcracks start developing in the matrix. From this point on, the behavior is non-linear and irreversible. The failure is thus much more controlled which makes life prediction more realistic and these materials more attractive for aero engine use. In addition in the case of ceramic composites, the failure process is different than that of classical composite behavior. For example, in carbon fiber reinforced plastics the main load is carried by the fibers when the less stiff matrix allows load transfer between fibers. However in ceramic composites, the fibers act as crack deflectors, increasing the energy needed to grow a crack.

There is also another family of ceramic materials called hybrid composites. It consists in a matrix of ceramic/intermetallic composite, that can be or not reinforced by fibers. Basically, it exhibits better mechanical properties but at lower temperature compared to ceramics and CMC's. Finally, eutectic ceramics which consists in a two phase ceramic densified from melted compounds at eutectic point are also under research.

### *A. Ceramic Matrix Composites*

An alternate approach to monolithic ceramics was pursued starting in the 1970s when high-strength SiC-based fibers became available <sup>[33]</sup>. SEP in France developed a composite consisting of SiC-based fibers (Nicalon fibers from Japan) in a chemical vapor infiltration matrix. The composite had a higher strain to failure than monolithic ceramics and thus did not fracture in a catastrophic brittle mode. This general category of composite became known as CVI SiC/SiC. Later General Electric Company developed a melt-infiltrated reaction-sintered composite material (MI-SiC/SiC) and Dow Corning developed a polymer infiltrated and pyrolyzed (PIP-SiC/SiC) composite. It is determined that the SiC/SiC ceramic matrix composites were susceptible to degradation due to interaction with the application environment (especially oxygen and water vapor) at high temperature.

J-Y. Guedou <sup>[34]</sup> mentions the development of composites with long SiC fibers and ceramic matrix (C or SiC) for aerospace structures. For example, such materials have been used for nozzle flaps in aero-engines (SiC-SiC nozzle flap). As suggested before, CMC are not brittle unlike bulk ceramics thank to the carbon interphase between fibers and matrix. However, this interphase is suggest to oxidation. Other structural parts such as combustors, airfoils, turbine blades and vanes are suggested. In 1999, Ohnabe et al. <sup>[35]</sup> presented potential applications of CMCs to aero-engine components. Extensive developments on interface layers, fiber improvements, matrix modification and surface coatings were conducted during the 1990s and are continuing. Parallel effort have focused on oxide/oxide ceramic matrix composites that are inherently more stable in an oxidizing environment.

Materials usually used for both fibers and matrix are carbon (C), Silicon carbide (SiC), Alumina ( $\text{Al}_2\text{O}_3$ ) and mullite ( $\text{Al}_2\text{O}_3\text{-SiO}_2$ ). In 2006, J.A. DiCarlo and M. van Roode <sup>[36]</sup> reviewed the development of ceramic materials for hot section applications in gas turbine. The key performance requirement for hot-section ceramic material is the ability to display 3-dimensional strength properties that sufficiently exceed the stresses than can arise in a given component under its anticipated service conditions over a period of time generally equivalent to the component inspection cycle.

- The first structural requirement for the ceramic material is that in its as-produced condition it should display sufficient strength properties to exceed maximum 3D stresses that will be experienced by the part.
- The second requirement is that the ceramic material should maintain this strength advantage under the maximum temperatures and hot-time conditions within the component inspection cycle.
- The third structural requirement for ceramic material is that it should display a sufficient capability to withstand the less predictable degrading effects that can arise from external factors during component service : foreign object impact (high fracture toughness), erosion/corrosion at high temperature.

Basically, CMCs are preferred to monolithic ceramics because of their inherent high fracture toughness. When the crack propagation in a monolithic ceramic typically results in catastrophic failure at very low strain, for a CMC component the reinforcing fibers will bridge the cracks providing the material with significantly more strain capability.

Table 4 lists vendors, constituents, average room temperature thermostructural properties for some advanced Ox/Ox and SiC/SiC systems of current interest within the US for hot section turbine components.

CMC System	1	2	3	4	5	6	7
Composition	Ox/Ox	SiC/SiNC	SiC/SiC	SiC/SiC	SiC/SiC	SiC/SiC	SiC/SiC
Name	AS-720N	S300	HyPer-Comp Pre-Preg	MI-HNS	NASA N24-A	NASA N26-B	NASA N26-C
Vendor	COI Ceramics	COI Ceramics	GE Energy	Goodrich	GE Energy	GE Energy / StarFire	GE Energy / StarFire
Fiber Type	Nextel 720	Sylramic	Hi-Nicalon	Hi-Nicalon Type S	Sylramic-iBN	Sylramic-iBN	Sylramic-iBN
Architecture of Test Panel	2D-woven 0/90 fabric	2D-woven 0/90 fabric	2D cross-ply 0° tape	2D-woven 0/90 fabric	2D-woven 0/90 fabric	2D-woven 0/90 fabric	2.5D-woven 0/90
Fiber Vol. % (X, Y, Z)	22/22/0	24/24/0	12/12/0	18/18/0	18/18/0	18/18/0	17/19/3
Matrix Process	Sol Gel	PIP SNC	Pre-Preg SiC + C + Si	CVI + slurry SiC + Si	CVI + slurry SiC + Si	CVI + PIP SiC	CVI + PIP SiC
Matrix Porosity, %	~48		~2	~5	~5	~15	~15
X- Modulus, GPa	76	165	285	250	250	190	190
X- PLS, MPa	N.A.	140	167	180	180	150	150
X- UTS, MPa	195	340	321	380	450	380	360
XY- UTS, MPa	~40	~60	210	240	240		
Z- UTS MPa	2.7		40	15	15	15	25
X- Cond., W/m K	2	8	34		50		
Z- Cond., W/m K	2	4	25	28	25	28	50

Table 4: Nominal constituent and room temperature thermostructural properties for some advanced CMC systems of current interest for hot section engine components <sup>[36]</sup>

The as-produced systems in table 4 (but 1 and 2) should provide sufficient strength capability for combustor liners, turbine shrouds and turbine vanes that might experience in-plane direction stresses up to 100 MPa. However, they currently do not have enough strength capability for turbine blades that might experience in-plane stresses as high as 300 MPa. In addition, for turbine vanes and blades, most of the systems would not provide the additional strength requirements of about 30 MPa for the Z-direction or thru-thickness tensile strength.

To be considered as potential hot section component material, the CMC systems have to display the capability to retain a sufficient portion of their as-produced strengths under the projected service conditions for the component. Table 5 below shows some limited 500 hours rupture strength data of the CMC systems in table 4.

CMC System	AS-720N	S300	HyPer-Comp Pre-Preg	MI-HNS	NASA N24-A	NASA N26-B	NASA N26-C
<b>500-hour Rupture Strength in X-direction, MPa</b>							
1100°C	150		145				
1200°C	<30		135		130		
1315°C			110	~100	100	>150	>150
1450°C					<10	>70	>70
Refs	[17]	[18]	[19,25]	[20]	[21]	[22]	[23]
<b>Approximate Upper Use Temperature (UUT) for 500 Hot Hours and X-UTS &gt; 100 MPa</b>							
	1150°C		1320°C	1300°C	1300°C	1400°C	1400°C

**Table 5: 500-hour rupture strength in X-direction and upper use temperatures for the CMC in Table 4** <sup>[36]</sup>

The upper use temperatures (UUT) range from ~ 1150 °C for the Ox/Ox CMC to ~ 1400 °C for the Si-free NASA SiC/SiC MC systems. Thus all of these CMC systems are very competitive with the best metallic superalloys that have densities about 3 times greater than the CMC and can only provide 100 MPa for 500 hours at ~ 1100 °C. Because CMC rupture behavior is typically controlled by thermally-activated creep mechanisms, UUT for longer or shorter service lives can be crudely estimated by assuming an increase or decrease in table 5 UUT values of ~ 60 °C for every order of magnitude change in time from 500 hours. Thus, UUT for the NASA N24A system could be expected to decrease to ~ 1240 °C for 5000-hour hot-time component and to increase to ~ 1360 °C for 50-hour hot-time component.

Attempts to implement CMC systems in gas turbine engine applications have been on-going for more than 20 years. Initial CMC systems were limited in performance due to thermally unstable fibers (Nicalon and Nextel 610), interfacial coatings with poor environmental resistance (carbon), and high porosity SiC matrices produced by CVI. However much progress technologies included the availability of the Nextel 720 fiber, the Hi-Nicalon and Hi-Nical Type S fibers, the Sylramic and Sylramic-iBN fibers, BN-based interfacial coatings, low porosity Si-based matrices by melt infiltration, and silicon-free stoichiometric SiC matrices. Nevertheless, other issues related to component producibility, design and affordability still continue to limit the implementation of CMC in turbine engine applications.

## **B. Eutectic ceramics**

The major problems of structural ceramics is their intrinsic brittleness. However, new systems associating different ceramics have been studied and show some “plasticity” [34]. Eutectic ceramics consist in a combination of 2 or 3 oxides : alumina or zirconia and complex oxides such as perovskite  $\text{ReAlO}_3$  and garnet  $\text{Re}_3\text{Al}_5\text{O}_{12}$ , where Re is a rare earth element (Re: Gd, Eu and Re: Y, Yb, Er, Dy respectively) [37]. In the case of ternary systems, cubic zirconia is added to improve fracture toughness. They exhibit a low density and have a microstructure which consists in tortuous shape phases overlapping each other. The mechanical properties of two phase eutectic ceramics are better than that of either constituent alone, because of the strong constraining effects provided by the interlocking microstructure [38]. In the domain of structural materials for very high temperature applications, the use of directionally solidified eutectic oxides is envisaged for vanes, hollow non-cooled nozzles, turbine blades and liner panels in the combustion chamber.

In 1998, Y. Waku [39] mentions MGC (melt growth composite) material. It is a innovative ceramic composite made by melting and unidirectional solidification of raw material oxides using an eutectic reaction to precisely control the crystal growth. Unlike conventional powder sintering method, which leads to impurity and amorphous phases forming at grain boundaries, these microstructural factors are eliminated by precise control of the stable high temperature microstructure.

$\text{Al}_2\text{O}_3/\text{GdAlO}_3$  system MGC (figure 22) is composed by a  $\langle 214 \rangle$  single-crystal  $\text{Al}_2\text{O}_3$  with a hexagonal structure and a  $\langle 111 \rangle$  single-crystal  $\text{GdAlO}_3$  phase with a perovskite structure, thus referred to as GAP (gadolinium aluminium perovskite). In figure 22B, it can be seen the configuration of the GAP phase alone (the  $\text{Al}_2\text{O}_3$  phase has been removed by maintaining the sample at 1650 °C in graphite powder for 2 h). The single crystal GAP has a continuously connected porous structure of irregular shape [39]. M. Parlier and al. [37] specified that the phases are perfectly similar in shape and size in sections parallel or perpendicular to the growth direction, thus revealing the three-dimensional configuration of the microstructure. The two phases interpenetrate without grain boundaries, pores or colonies. Similarly,  $\text{Al}_2\text{O}_3/\text{Er}_3\text{Al}_5\text{O}_{12}$  and  $\text{Al}_2\text{O}_3/\text{Y}_3\text{Al}_5\text{O}_{12}$  are composed by a single-crystal  $\text{Al}_2\text{O}_3$  with a hexagonal structure and a single-crystal  $\text{Er}_3\text{Al}_5\text{O}_{12}$  and  $\text{Y}_3\text{Al}_5\text{O}_{12}$  respectively with a garnet structure, thus referred to as EAG and YAG respectively. Ternary composites can be realized by addition of zirconia  $\text{ZrO}_2$  to increase fracture toughness. The cubic zirconia phase grows essentially at the interface between the oxides and in the alumina phase.

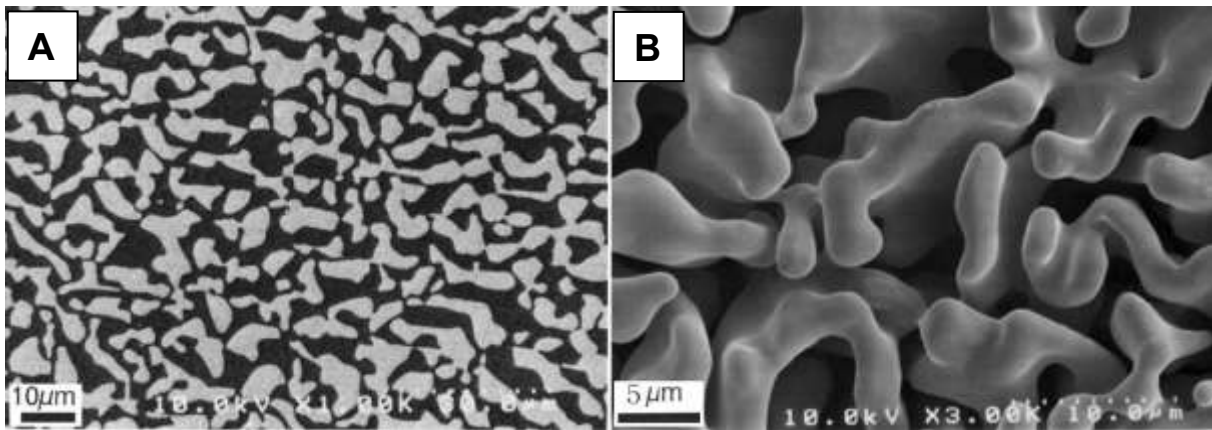


**Figure 22:** SEM images showing the microstructure of a cross section perpendicular to the solidification direction of the Al<sub>2</sub>O<sub>3</sub>/GAP system MGC material (a), and the configuration of single crystal GAP (b) [39]

Figure 23 shows typical stress displacement curves of Al<sub>2</sub>O<sub>3</sub>/GAP system MGC material and sintered composite obtained from a 3-point flexural test at 1600 °C. For comparison, a stress displacement curve of Al<sub>2</sub>O<sub>3</sub>/YAG system MGC material is also shown [39]. It is observed a yielding behavior under high stress for the Al<sub>2</sub>O<sub>3</sub>/GAP system MGC material, with a yield strength of about 700 MPa. Moreover, the fracture energy (inferred from the area under the stress displacement curve) is a dozens of times that of the Al<sub>2</sub>O<sub>3</sub>/YAG system MGC material, which undergoes brittle fracture at this temperature. It is observed by transmission electron microscopy that the plastic deformation occurred by dislocation motion in both single crystal Al<sub>2</sub>O<sub>3</sub> and GAP.

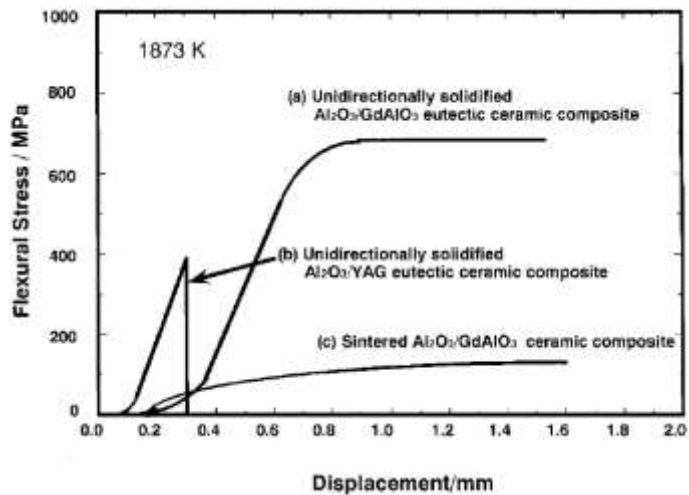


**Figure 23:** Typical stress-displacement curves in three-point flexural test at 1873K of MGC materials. (a) Al<sub>2</sub>O<sub>3</sub>/GAP system MGC materials, (b) Al<sub>2</sub>O<sub>3</sub>/YAG system MGC materials, (c) Al<sub>2</sub>O<sub>3</sub>/GAP sintered composite [39]

The thermal stability of microstructure and residual strength characteristics have been evaluated for binary eutectic composites [40]. After exposure for 500 h at 1700 °C, Al<sub>2</sub>O<sub>3</sub>/YAG and Al<sub>2</sub>O<sub>3</sub>/GAP eutectic composites didn't exhibit any microstructural change or reduction in the residual flexural strength. Also, these MGC components show excellent mid-term oxidation resistance and there's no change in weight, shape and dimensions of components after exposure in air at 1700 °C. Hot corrosion resistance has also been studied at 1700 °C in a 30 % moisture environment. No weight loss and no strength reduction were observed, even after being exposed 10 h.

Fracture toughness is a critical technical issue for a practical application of eutectic composites [40]. First, there is a remarkable orientation dependency and a large scatter in fracture toughness of  $\text{Al}_2\text{O}_3/\text{YAG}$  eutectic composites for every plane consider. Fundamentally, the fracture toughness is lower for the YAG phase than for the  $\text{Al}_2\text{O}_3$  phase. Fine interfaces have little influence on fracture toughness. The low fracture toughness is predominantly controlled by the YAG phase in the microstructures. However, the mean value of fracture toughness was approximately 1.3 times higher for the ternary eutectic when compared to the binary eutectic. The room temperature fracture toughness of  $\text{Al}_2\text{O}_3/\text{YAG}$  binary eutectic composite was found to range from 2.5 to 4  $\text{MPa}\cdot\text{m}^{1/2}$  and is quasi constant up to 1700 °C. The temperature dependency of the fracture toughness of both single phases offset each other which leads to a quasi-constant fracture toughness for the binary  $\text{Al}_2\text{O}_3/\text{YAG}$  eutectic composite up to 1700 °C.

The relationship between fatigue crack growth rate  $da/dN$  (a is the crack length and N the fatigue cycle) and maximum stress intensity factor  $K_{\max}$  is shown figure 24 for  $\text{Al}_2\text{O}_3/\text{YAG}$  eutectic composite [40].

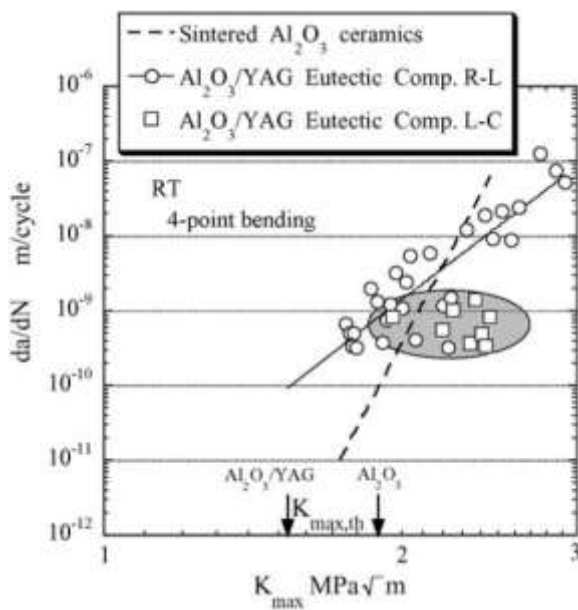


**Figure 24: Relationship between fatigue crack growth rate  $da/dN$  and maximum stress intensity factor  $K_{\max}$  [40]**

Test were conducted by four-point bending tests at room temperature in the R-L and L-C directions (respectively parallel and perpendicular to solidification direction). For comparison, the dotted line shows sintered  $\text{Al}_2\text{O}_3$  ceramics data.

In the R-L direction, the  $da/dN - K_{\max}$  relationship follow Paris law :

$$\frac{da}{dN} = C(\Delta K)^m \quad [40]$$

Where C and m are materials constant. The m value is slightly smaller for  $\text{Al}_2\text{O}_3/\text{YAG}$  eutectic composite than for sintered  $\text{Al}_2\text{O}_3$  ceramic. Fundamentally, there is no transition in fatigue failure mechanism of  $\text{Al}_2\text{O}_3/\text{YAG}$  eutectic composite and it is predominantly controlled by cleavage fracture.

On the other hand, the relationship can't be followed by Paris law in the L-C direction, and  $da/dN$  is almost constant regardless of  $K_{\max}$ . In this case, fatigue crack growth is stopped at the interface and then restarted after numerous fatigue cycle: fatigue crack growth is discontinuous.

### C. SiAlON ceramics and composites

SiAlONs are ceramic alloys based on the elements silicon (Si), aluminum (Al), oxygen (O) and nitrogen (N) [41]. They were developed in the 70s to solve the problem of silicon nitride ( $\text{Si}_3\text{N}_4$ ) being difficult to fabricate. In SiAlON, there is substitution of Si by Al with corresponding atomic replacement of N by O, to satisfy the valence requirements. The resulting “solution” exhibit superior properties than the original pure solvent. The fundamental structural unit of  $\text{Si}_3\text{N}_4$  is  $\text{SiN}_4$  tetrahedron, which is analogous to the  $\text{SiO}_4$  structural units in silicates. The Si-N bonds are short and very strong. This strong, rigid, compact structure is responsible for many of the important properties of  $\text{Si}_3\text{N}_4$ .

$\beta$ -SiAlON is based upon atomic arrangement existing in  $\beta$ - $\text{Si}_3\text{N}_4$ . Up to 2/3 of the silicon in  $\beta$ - $\text{Si}_3\text{N}_4$  can be replaced by Al without causing a change in structure. The chemical replacement is one of changing Si-N bonds for Al-O bonds. The bond lengths are about the same but Al-O bond strength is significantly higher than that of Si-N. In SiAlON, the Al is coordinated as  $\text{AlO}_4$  and not as  $\text{AlO}_6$  as in alumina ( $\text{Al}_2\text{O}_3$ ). Therefore, in  $\beta$ -SiAlON the bond strength is 50 % higher than in  $\text{Al}_2\text{O}_3$ . Thus SiAlONs intrinsically have better properties than both  $\text{Si}_3\text{N}_4$  and  $\text{Al}_2\text{O}_3$ .

$\beta$ -SiAlON has the general formula  $\text{Si}_{6-z}\text{Al}_z\text{O}_z\text{N}_{8-z}$  where  $z \leq 4.2$  and requires a sintering additive such as Yttria ( $\text{Y}_2\text{O}_3$ ), Magnesia ( $\text{MgO}$ ) or a rare earth oxide to densify. As a solid solution, the vapour pressure of  $\beta$ -SiAlON is lower than that of  $\text{Si}_3\text{N}_4$ , which leads to a better densification using normal sintering techniques and reduces decomposition at high temperatures. Pressureless, gas pressuring (GPS), hot pressing (HP), hot isostatic pressing (HIP) and spark plasma sintering (SPS) are the common sintering techniques used in the production of SiAlON ceramics.

For example, when sintered above 1700 °C with Yttria as sintering aid, elongated hexagonal shaped  $\beta$ -SiAlON grains are precipitated and grow in the oxynitride liquid phase formed from the sintering additive. Subsequently, the liquid phase forms a refractory intergranular glass during cooling. This material, with elongated  $\beta$  grains, is characterized by high strength and toughness. Interestingly, it is possible through controlled processing to convert this intergranular glass to Yttrium aluminum garnet (YAG) which is a refractory crystalline phase. This gives to the material better high temperature properties and the material can retain its strength at temperatures up to 1350 °C.

The  $\beta$ -SiAlON composition  $\text{Si}_4\text{-Al}_2\text{-O}_2\text{-N}_6$  ( $z = 2$ ) was prepared from a mixture of  $\text{Si}_3\text{N}_4$ , AlN,  $\text{Al}_2\text{O}_3$  and  $\text{Y}_2\text{O}_3$  doped with different amounts of  $\text{Y}_2\text{O}_3$  (respectively 5 and 3.5 wt.%). Table 6 gives the mechanical properties (hardness and fracture toughness) of densified samples sintered by various techniques.

Sintering technique	Sample	Sintering temperature (°C)	Density (%)	Fracture toughness ( $\text{MPa m}^{1/2}$ )	Hardness (HV0.05)
GPS	Y5	1825	99.4	$6.4 \pm 0.4$	$14.2 \pm 0.1$
	Y3.5	1725	100	$4.4 \pm 0.3$	$16.5 \pm 0.3$
Pressureless	Y5	1850	96.6	$5.7 \pm 0.21$	$12.6 \pm 0.16$
	Y3.5	1775	99.4	$5.8 \pm 0.07$	$15.6 \pm 0.1$
SPS	Y5	1550	100	$5.7 \pm 0.05$	$15.8 \pm 0.7$
	Y3.5	1550	100	$4.8 \pm 0.05$	$16.7 \pm 0.5$

**Table 6: Density and mechanical properties of samples sintered by various sintering techniques at different temperatures [41]**



In order to enhance the reliability of the material, the fracture resistance was increased by fiber reinforcement. In 1996, Inoue et al. [42] incorporated unidirectionally oriented highly heat resistive SiTiCO fibers (Lox-M type Tyranno fibre<sup>®</sup>) into  $\beta$ -SiAlON ceramics.  $\beta$ -SiAlON properties strongly depends on the composition, that is the substitution ratio  $z$  introduced earlier. Basically, the strength decreases and the oxidation resistance and sinterability increase with increasing  $z$  value. A value of  $z = 4$  was selected here ( $\text{Si}_2\text{Al}_4\text{O}_4\text{N}_4$ ) as the sinterability is relatively high. However, a sintering temperature of 1700-1800 °C is required, which is too high for the fibers that allow a maximum processing temperature of 1600 °C. Therefore, a sintering additive (3 wt.%  $\text{Y}_2\text{O}_3$ ) is used. The composite was fabricated by the filament winding method, followed by hot-pressing.

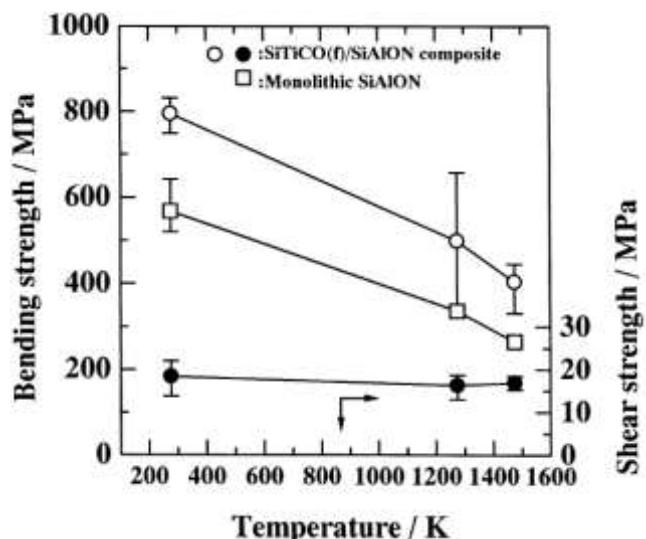
The bulk density and open porosity measured by water immersion method are shown table 7. In addition, the relative density of the composite, defined as the ratio of its bulk density to the pore free density is calculated.

	Bulk density (Mg/m <sup>3</sup> )	Open porosity (%)	Relative density (%)
Monolithic SiAlON	3.28	0.15	—
SiTiCO fibre/SiAlON	2.64	9.34	91.0

**Table 7: Bulk density, open porosity and relative density of monolithic SiAlON and SiTiCO fibre/SiAlON composite** [42]

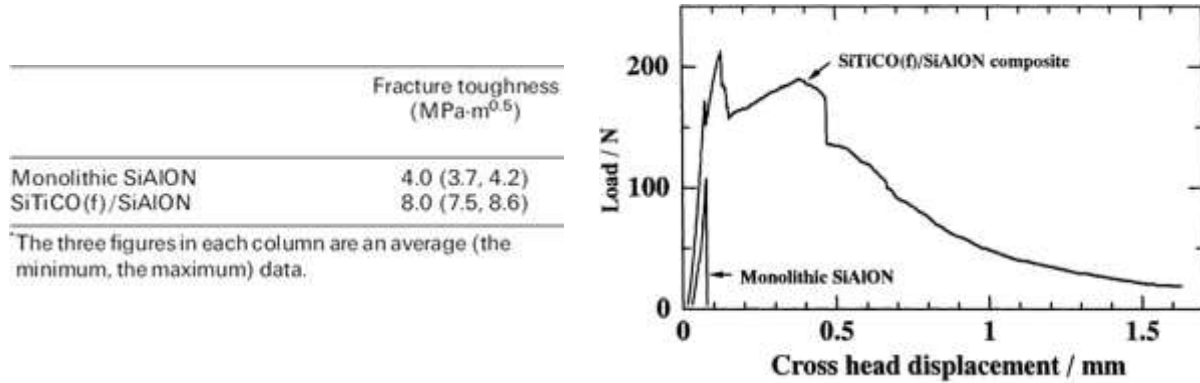
The very small amount of open porosity in the monolithic ceramic suggests a quasi-full sintering. On the other hand, the open porosity of the composite is 9.34 %. It seems that the fibers incorporation hindered the matrix sintering. Microstructural observation allowed to described porosity. Pores exist in the places where the fibers gather closely, but the matrix seems to be well densified and a single filament is sufficiently surrounded by the matrix.

Figure 25 shows the temperature dependence of the bending strength of monolithic SiAlON and the composite. The shear strength is also shown in figure 25. The fracture behavior of the composite at room temperature is a typical non-brittle type. The strength of both monolithic and composite decreases when increasing the temperature. However, the composite exhibits a higher strength by about 200 MPa at high temperature. On the contrary, the shear stress of the composite shows no such thermal degradation. The surface of monolithic SiAlON before and after the bending test at 1473 K was examined and an oxide layer consisting of amorphous silica containing yttrium is believed to cause the thermal degradation of strength.



**Figure 25: Temperature dependence of the bending of monolithic SiAlON (squares) and SiTiCO<sub>(f)</sub>/SiAlON composite (empty circles) and the interlamellar shear strength of the composite (full circles)** [42]

The fracture toughness and typical load-deflection curves of monolithic SiAlON and the SiTiCO<sub>(f)</sub> composite are shown in figure 26.



**Figure 26:** Fracture toughness and Load-deflection curves of monolithic SiAlON and SiTiCO(f)/SiAlON composite measured by SENB method <sup>[42]</sup>

Before the load reaches the maximum load point, the curve for the composite indicates a deviation from the linear relationship. This departure from the elastic response means that the crack has already propagated from the notch tip. Direct observation of the tests specimen reveals that the delamination fracture starts from the notch tip, running parallel to the fiber orientation direction. This delamination at the notch tip greatly reduces stress intensification. At the maximum load point, the tensile fracture takes place but is arrested immediately by the next fiber layer. In the later stage after this point, quite a lot of delamination and partial tensile fracture occur simultaneously up to the final fracture.

Remarkable strength improvement from ambient temperature up to 1473 K is achieved by the fiber reinforcement. The fracture behavior of the composite is non-brittle with quite a large amount of energy consumption. Fracture toughness and fracture resistance are both improved by the fiber incorporation. The composite is a tough and very damage tolerable material. It also shows toughness against impact fracture <sup>[42]</sup>.

Demir et. al <sup>[43, 44]</sup> studied the effect of heat treatment of Nicalon SiC short fibers to reinforce  $\beta$ -SiAlON ( $z = 1$ ) ceramics. SiC-based fibers have a better resistance to oxidation than other ceramic fibers. However, the tensile strength of Nicalon SiC fibers decreases dramatically with significant weight loss as the temperature is raised beyond 1200 °C. Heat treatment in a CO atmosphere offers an attractive route for obtaining carbon coatings on the fibers. Demir et al. revealed that heat treated fibers within the  $\beta$ -SiAlON ( $z = 1$ ) matrix eased the densification by hot pressing and increased composite strength compared with as received continuous fiber reinforcement. Combined with the oxide additive 2 % MgO, 7 % Y<sub>2</sub>O<sub>3</sub> and 8 % Sm<sub>2</sub>O<sub>3</sub>, the densification was the highest at low temperature (1550 °C) and strength and fracture toughness values were the best (620 MPa, 13 MPa·m<sup>1/2</sup> respectively) when compared to other tested continuous fiber reinforced specimens.

Continuous fiber reinforcement provides higher strength along the fiber direction but across the fiber direction gives poor mechanical properties. In order to avoid this and reduce costs, short fiber reinforcement was needed to provide isotropic mechanical properties. 5, 10 and 15 vol.% of heat treated short fibers were added to the  $\beta$ -SiAlON starting powders. The heat treated fibers were chopped and mixed with  $\beta$ -SiAlON ( $z = 1$ ) starting powders and alcohol and subsequently pressed to form green bodies. The short fiber containing green bodies were uniaxially hot pressed within a graphite die at temperatures between 1550 and 1700 °C.



**Figure 27:** 10 % short fiber reinforced  $\beta$ -SiAlON composites hot pressed at 1650 °C [43]

10 % CO heat-treated short fiber reinforced  $\beta$ -SiAlON composite hot pressed at 1650 °C exhibit a uniform fiber distribution and dense matrix (figure 27). It is the most desirable structure for CMCs as weak interface layer is present to prevent catastrophic fracture like monolithic ceramics. All desired properties (maximum densification, uniform distribution, weak interface and non-degraded fibers) have been obtained at this temperature. When a load is applied, a crack initiates and propagates up to fiber/matrix interface. The crack is deflected at the weak interface and the load transfer to the strong fiber : toughening effect is achieved.

Micro Vickers indentation hardness test and associated fracture toughness test were carried out for both monolithic  $\beta$ -SiAlON and short fiber reinforced composites (figure 28).

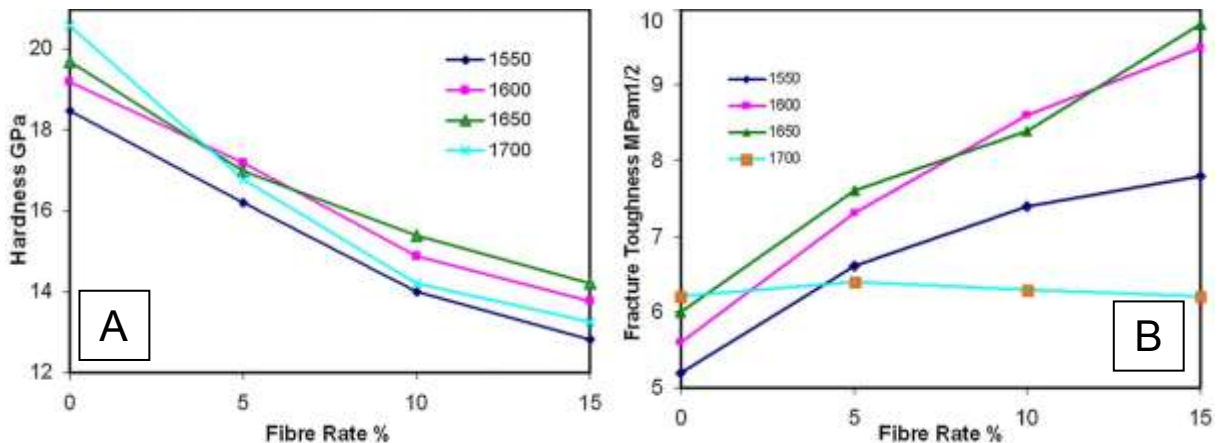


**Figure 28:** Micro-Hardness (A) and fracture toughness (B) of  $\beta$ -SiAlON composites as a consequence of short fibers rate [43]

In general, fiber addition causes slight decrease in density but dramatic decrease in hardness and moderate increase in fracture toughness. As a result of high pressure CO heat-treatment, isotropic mechanical property improvements were provided for  $\beta$ -SiAlON matrix composites with the short fiber reinforcement. These isotropic CMC materials can be used as structural parts for high temperature applications [43, 44].

#### D. Hybrid $\text{MoSi}_2$ base ceramic composites

In 1999, M.G. Hebsur [45] pointed out the potential of  $\text{MoSi}_2$  for high temperature applications. Based on high temperature oxidation behavior,  $\text{MoSi}_2$  is one of the few intermetallics to have potential for further development for high temperature applications. Since  $\text{MoSi}_2$  is a silica former, it can withstand at least 200 °C higher temperatures (up to 1500 °C) than alumina formers (like NiAl).

However,  $\text{MoSi}_2$  present critical drawbacks : brittle at low temperatures (figure 31), inadequate creep resistance at high temperature (figure 30), subject to accelerated oxidation at temperature between 450 and 550 °C (figure 35) and relatively high coefficient of thermal expansion (CTE) when compared to that of potential reinforcing fibers such as  $\text{SiC}_{(f)}$  (figure 29) which would lead to serious cracking in the matrix during thermal cycling of such a composite. Many research work have been conducted but an acceptable compromise between material properties was hard to find.

Nevertheless, addition of about 30-50 vol.% of  $\text{Si}_3\text{N}_4$  particulate improved low temperature accelerated oxidation resistance by forming  $\text{Si}_2\text{ON}_2$  protective scale. Also, it showed to improve high temperature oxidation resistance and compressive strength. For example, the brittle-to-ductile transition temperature (BDTT) of  $\text{MoSi}_2$ -30vol.% $\text{Si}_3\text{N}_4$  measure in four-point bending was found between 900 and 1000 °C. More importantly, addition of  $\text{Si}_3\text{N}_4$  significantly lower the CTE thus allowing the reinforcement by fibers such as  $\text{SiC}_{(f)}$ . The opposite figure 29 exhibit the CTE measurements made on  $\text{MoSi}_2$  and  $\text{MoSi}_2$ - $\text{Si}_3\text{N}_4$  base materials and composites plotted as a function of temperature.

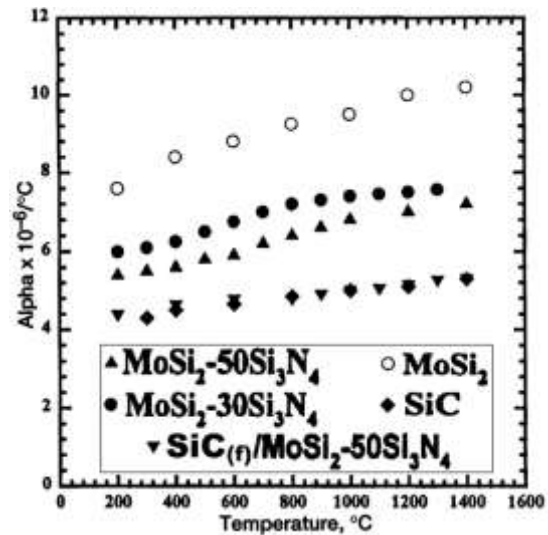


Figure 29: Thermal expansion data for  $\text{MoSi}_2$  base materials and  $\text{SiC}$  reinforcing phase [45]

$\text{Si}_3\text{N}_4$  ceramics on their side show good thermo-mechanical properties at high temperature, an acceptable oxidation resistance, low density of about 3.2 and a low expansion coefficient of  $2.5 \cdot 10^{-6} \text{ } ^\circ\text{C}^{-1}$ . However, their toughness is insufficient and environmental barrier coatings are needed.  $\text{MoSi}_2$  additions enable to improve those two points, as seen in the following tables 8 and 9 [34].

Flexural strength (MPa)	$\text{Si}_3\text{N}_4$	$\text{Si}_3\text{N}_4/\text{MoSi}_2$ 90/10
at 20°C	820	780
at 1400°C	730	720
at 20°C after 10000 h at 1500°C	260	509

Table 8: Mechanical properties improvement on  $\text{Si}_3\text{N}_4$  by  $\text{MoSi}_2$  addition [34]

Fracture toughness ( $\text{MPa}\cdot\text{m}^{0.5}$ )	$\text{Si}_3\text{N}_4$	$\text{Si}_3\text{N}_4/\text{MoSi}_2$ 50/50	$\text{Si}_3\text{N}_4/\text{MoSi}_2$ 30/70
at 20°C	6	5	5
at 1000 °C	6	7	10
at 1200°C	6	9	12

Table 9: Toughness improvement on  $\text{Si}_3\text{N}_4$  by  $\text{MoSi}_2$  addition [34]

M.G. Hebsur<sup>[45]</sup> showed in previous work that nitride additions substantially increased compressive strength behavior at all temperature. In figure 30, the results of constant load compression creep tests at 1200 °C for  $\text{MoSi}_2\text{-}50\text{Si}_3\text{N}_4$  were compared to that of monolithic  $\text{MoSi}_2$ ,  $\text{MoSi}_2\text{-}40\text{SiC}$  and a single crystal Ni base superalloy.

$\text{MoSi}_2\text{-}50\text{Si}_3\text{N}_4$  is almost 5 order of magnitude stronger than binary  $\text{MoSi}_2$  and comparable to  $\text{MoSi}_2\text{-}40\text{SiC}$  (figure 30). The derived stress exponent ( $n = 5.3$ ) and the activation energy ( $Q = 520 \text{ kJ}\cdot\text{mol}^{-1}$ ) imply a diffusion controlled dislocation mechanism.

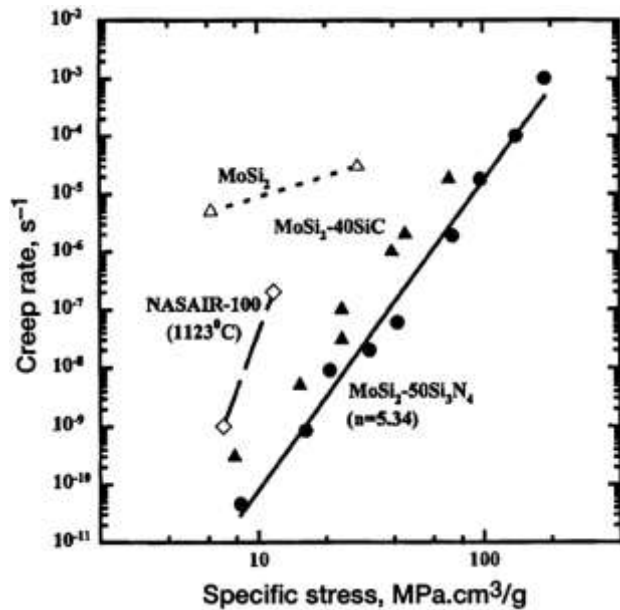


Figure 30: Second stage creep rate versus specific stress at 1200 °C for  $\text{MoSi}_2\text{-}50\text{Si}_3\text{N}_4$  compared with other materials<sup>[45]</sup>

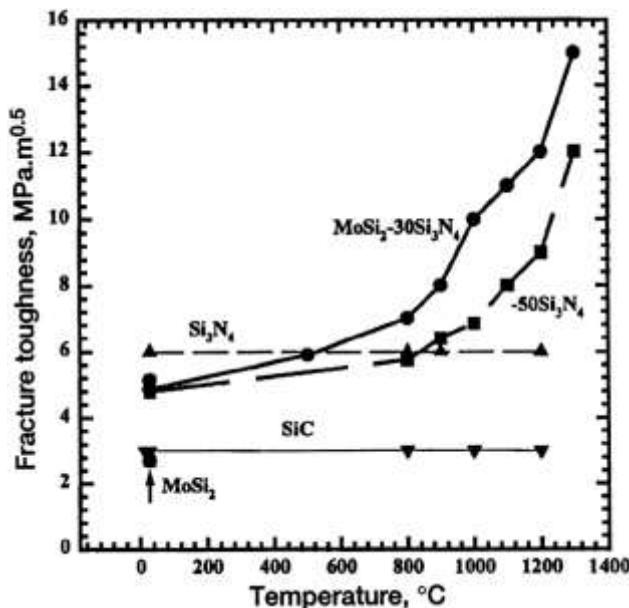


Figure 31: Temperature dependence of fracture toughness of  $\text{MoSi}_2\text{-Si}_3\text{N}_4$  base materials<sup>[45]</sup>

The fracture toughness of  $\text{MoSi}_2$  and  $\text{MoSi}_2\text{-Si}_3\text{N}_4$  base materials were measured on chevron notched four point bend specimen. Figure 31 shows the results for  $\text{MoSi}_2\text{-Si}_3\text{N}_4$  base materials depending on temperature and for SiC and  $\text{Si}_3\text{N}_4$  for comparison. At room temperature, fracture toughness was  $5.2 \text{ MPa}\cdot\sqrt{\text{m}}$  for both  $\text{MoSi}_2\text{-}30\text{Si}_3\text{N}_4$  and  $\text{MoSi}_2\text{-}50\text{Si}_3\text{N}_4$  which is about twice the value for monolithic  $\text{MoSi}_2$ . Further improvement of room temperature fracture toughness can be achieved by either microalloying  $\text{MoSi}_2$  with elements like Nb, Al and Mg or by growing randomly oriented long whisker type  $\beta\text{-Si}_3\text{N}_4$  grains (by proper choice of consolidation and heat treatments). The latter proved to increase room temperature fracture toughness by a factor 3.

To further increase the materials properties of  $\text{MoSi}_2\text{-Si}_3\text{N}_4$  base materials, SiC fibers were used for reinforcement [45]. A mixture of commercially available  $\text{MoSi}_2$  and 30-50 vol.% of  $\text{Si}_3\text{N}_4$  powders were mechanically alloyed by attrition milling. Composite plates of various thickness consisting of 6, 12 or 56 plies of 30 vol.% SCS-6 fibers having 0, 0/90 and 90 orientations in a  $\text{MoSi}_2\text{-Si}_3\text{N}_4$  matrix were prepared by powder cloth technique and consolidated by vacuum hot pressing followed by hot isostatic pressing (HIP) to achieve full density.

Figure 32 shows the load versus time plot for SCS-6/ $\text{MoSi}_2\text{-Si}_3\text{N}_4$  composite from chevron notched four point bend specimens. It is also shown the behavior of the single matrix  $\text{MoSi}_2\text{-Si}_3\text{N}_4$  for information. The room temperature tensile nominal stress-strain curve for SCS-6/ $\text{MoSi}_2\text{-Si}_3\text{N}_4$  is shown figure 33. In figure 32, the composite specimen did not break even after 2 hours. The apparent critical stress intensity factor  $K_{Ic}$  calculated from the maximum load data was greater than  $35 \text{ MPa}\cdot\sqrt{\text{m}}$ , which is 7 times tougher than the monolithic material. The toughness of the hybrid composite also increased with temperature reaching as high as  $65 \text{ MPa}\cdot\sqrt{\text{m}}$  at  $1400^\circ\text{C}$  in argon atmosphere. The stress-strain curve in figure 33 indicates a composite-like behavior with three distinct regions. First, an initial linear region is observed. Then, a non-linear region due to cracking in the matrix normal to the loading direction. Finally, a second linear region controlled by fiber bundle strength.

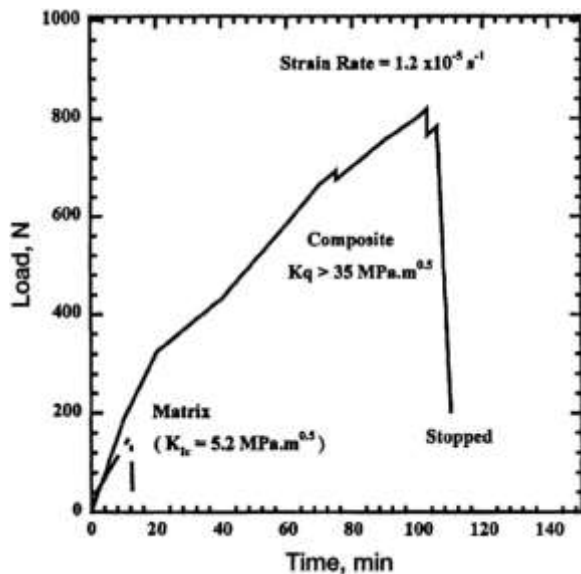


Figure 32: Load-time curves from chevron notched 4 point bend specimens of SCS-6/ $\text{MoSi}_2\text{-Si}_3\text{N}_4$  and  $\text{MoSi}_2\text{-Si}_3\text{N}_4$  tested at room temperature [45]

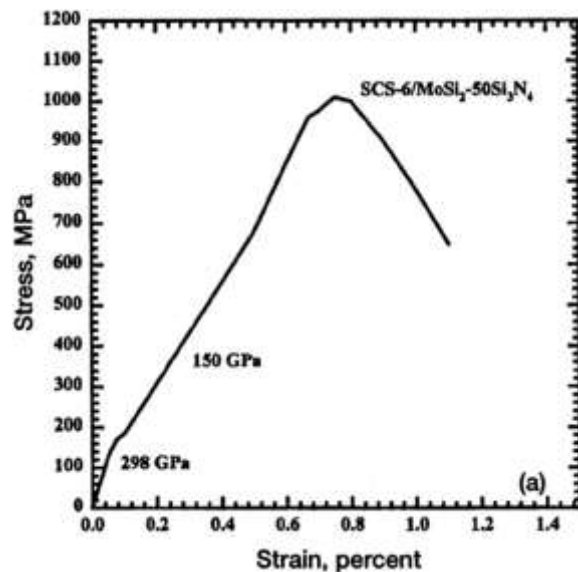


Figure 33: Room temperature tensile stress-strain curves for 6-ply SCS-6/ $\text{MoSi}_2\text{-Si}_3\text{N}_4$  hybrid composites [45]

High temperature tensile tests were performed in air at temperature up to 1400 °C. This is believed to be an advantage over CMC's which exhibit matrix cracking at all temperatures. Figure 34 shows the temperature dependence of ultimate tensile strength of SCS-6/ $\text{MoSi}_2$ - $50\text{Si}_3\text{N}_4$  compared to competitive materials (single crystal PWA1480 and reaction bonded silicon nitride SCS-6/RBSN). PWA 1480 exhibits higher tensile strength than both  $\text{MoSi}_2$  base and RBSN base composites between room temperature and 1000 °C. However, the density of PWA 1480 is almost three times higher than that of both composites, and hence is at a disadvantage on a specific strength basis. Not shown in figure 34, typical two-dimensional woven SiC/SiC composites exhibit much lower strengths ( $\approx 200$  MPa) between room temperature and 1200°C. However, SiC/SiC composites retain their strengths beyond 1200°C.

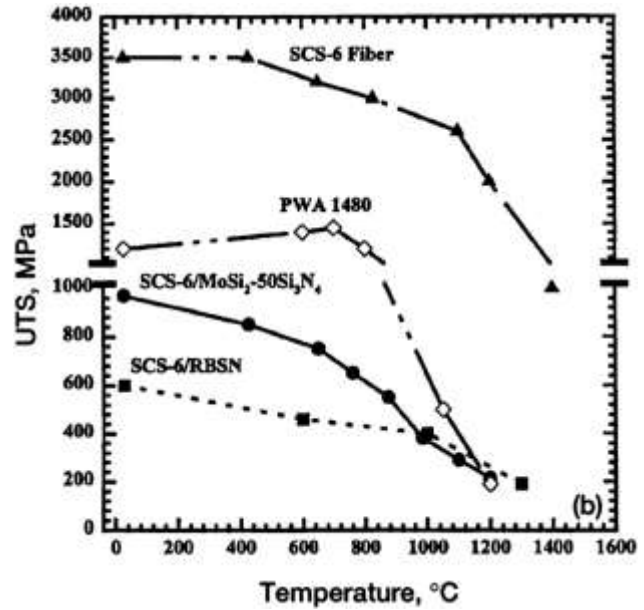


Figure 34: Temperature dependence of ultimate tensile strength of 6ply SCS-6/ $\text{MoSi}_2$ - $50\text{Si}_3\text{N}_4$  hybrid composites compared with other materials [45]

Cyclic oxidation tests of 55 min heating + 5 min cooling were conducted in air at 500 °C, the critical temperature for maximum accelerated oxidation of  $\text{MoSi}_2$ . Figure 35 shows the specific weight gain versus the number of cycles at 500 °C. Cyclic oxidation tests at a higher temperature of 1250 °C were also conducted and the results are presented figure 36.

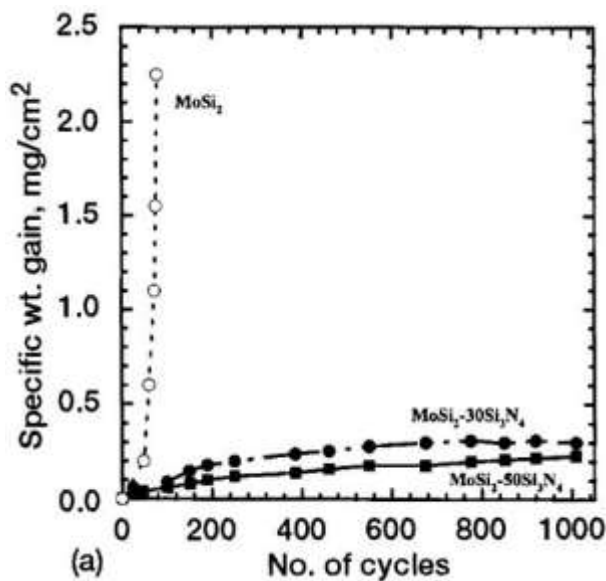


Figure 35: Oxidation behavior of  $\text{MoSi}_2$ -base materials cyclically oxidized at 500 °C in air [45]

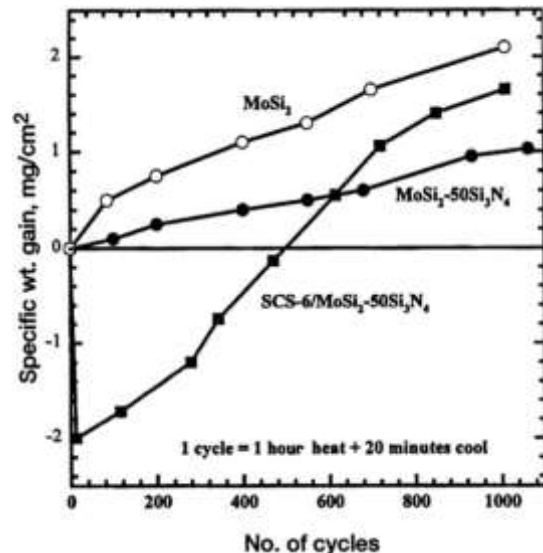


Figure 36: Specific weight gain versus number of cycles plot for  $\text{MoSi}_2$ - $50\text{Si}_3\text{N}_4$  monolithic and SCS-6/  $\text{MoSi}_2$ - $50\text{Si}_3\text{N}_4$  hybrid composite cyclically oxidized at 1250 °C in air [45]

At 500 °C, the beneficial effect of  $\text{Si}_3\text{N}_4$  addition is obvious and both  $\text{MoSi}_2\text{-}30\text{Si}_3\text{N}_4$  and  $\text{MoSi}_2\text{-}50\text{Si}_3\text{N}_4$  exhibit a very little weight gain indicating the absence of accelerated oxidation (figure 35). Similar conditions were used to study the behavior of hybrid composites. Results on SCS-6/ $\text{MoSi}_2$  and SCS-6/ $\text{MoSi}_2\text{-Si}_3\text{N}_4$  composites were outstanding. SCS-6/ $\text{MoSi}_2$  specimen, which had matrix cracks, was completely disintegrated into powder within 24 cycles, while SCS-6/ $\text{MoSi}_2\text{-Si}_3\text{N}_4$  specimen was intact even after 200 cycles.

At 1250 °C,  $\text{MoSi}_2\text{-}50\text{Si}_3\text{N}_4$  exhibited superior oxidation resistance than  $\text{MoSi}_2$  alone (figure 36). The specific weight gain of  $\text{MoSi}_2\text{-}50\text{Si}_3\text{N}_4$  was less than  $1 \text{ mg}\cdot\text{cm}^{-2}$  in 1000 h, almost comparable to CVD SiC (considered the best  $\text{SiO}_2$  former). The composite initially lost weight due to oxidation of carbon on SCS-6 fibers (figure 36). This was followed by steady weight gain, less than  $2 \text{ mg}\cdot\text{cm}^{-2}$  in 1000 h. X-ray diffraction on the surface of  $\text{MoSi}_2\text{-}50\text{Si}_3\text{N}_4$  and SCS-6/ $\text{MoSi}_2\text{-}50\text{Si}_3\text{N}_4$  indicated strong peaks of  $\alpha$ -cristobalite, which is a crystalline form of  $\text{SiO}_2$  and a protective oxide [45].

## 2. TiAl alloys for high temperature structural applications

TiAl-based alloys have been studied for about half a century as an alternative material to brittle ceramics and heavy Ni-based superalloys for high temperature applications. In particular, it would be of a great benefit to reduce the weight of rotating parts that work at rather high temperatures [46-68].

T. Tetsui in 1999 wrote [53]: *“The high-temperature properties of TiAl are not as good as for ceramics or Ni-based superalloys, while toughness, cost and manufacturing capability (e.g. for large castings) are substantially inferior to those of heat-resistant steels and Ni-based superalloys. Thus, lightness is the only merit of TiAl compared with ordinary metallic materials. This suggests that the most suitable applications for TiAl are small components where weight reduction is accompanied by obvious advantages in terms of the equipment being considered, and/or TiAl is preferable to ceramics for some particular reason. In addition, the applicable temperature range is the same or lower than for Ni-based conventional cast superalloys, but at temperatures below 500 °C, where light weight Ti alloys could be used, there is no particular merit associated with the use of TiAl.”*

It is therefore suggested that TiAl-based alloys most suitable applications are reciprocating or rotating high-temperature structural components [48-52, 54-57, 59, 65-68]. The primary property required for materials for rotating structural parts is endurance against centrifugal stress generated during rotation. Since the centrifugal stress is proportional to specific gravity, specific strength is an appropriate measure. And TiAl alloys with an appropriate composition and microstructure have shown outstanding specific strength when compared to current superalloys in the temperature range considered (figure 37). Therefore, a significant weight reduction could be achieved by replacing rotating parts traditionally in superalloys by TiAl-based intermetallics. Furthermore, also the supporting disks could be lightened since the applied stress would be lower.



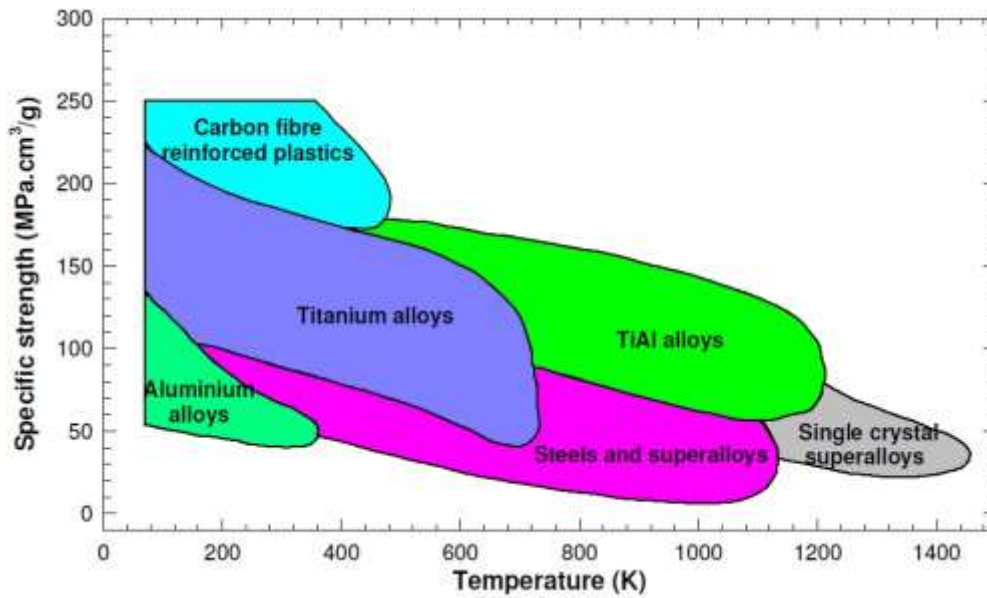


Figure 37: Temperature dependence of specific strength of various groups of alloys [69]

Wu [57] summarized the properties that make TiAl alloys of interest, displayed in figure 38:

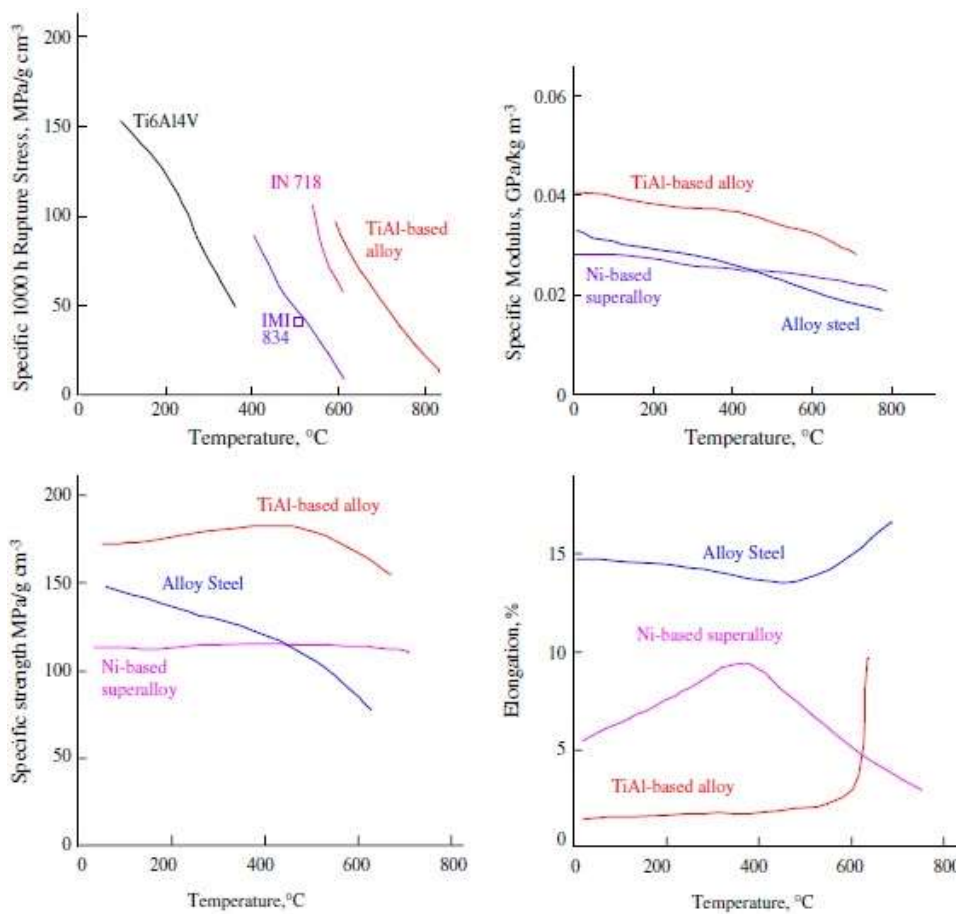
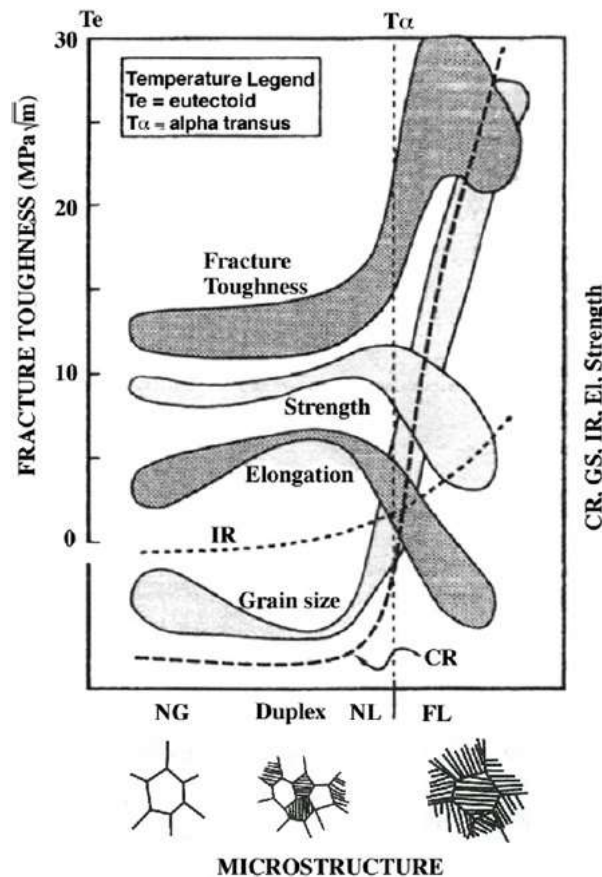


Figure 38: Specific properties that make TiAl-based alloys of interest when compared to alloy steel, Ti alloys and Ni-based superalloys [57]

From figure 38, the specific 1000h rupture strength, the specific modulus and the specific strength are higher for TiAl-based alloys than Ni-based superalloys. However, the room temperature ductility is poor and is typically about 1 % for TiAl-based alloys. This low ductility is critical for application of TiAl-based alloys as structural components. The minimum value of 1 % ductility is often required [48, 50, 52, 57]. Thereby, a good compromise between room temperature ductility and other mechanical properties is, as usual, to find. Finally, a good oxidation resistance is fundamental. TiAl-based alloys suffer from severe oxidation above 800 °C [48, 53, 55, 56, 67, 70-77].

The mechanical properties of TiAl alloys are very sensitive to microstructural morphology. The microstructure of TiAl-based alloys is determined by the process (castings, hot-worked, PM), the temperature (heat treatment, HIP) and the chemical composition. Basically, the microstructure of the dual-phase titanium aluminides can be broadly classified into four types : near-gamma (NG), duplex, nearly-lamellar (NL) and fully-lamellar (FL). Figure 39 displays the effect of microstructural morphology on mechanical properties of  $\gamma$ -TiAl alloys. A schematic drawing of the different microstructure types was inserted in figure 39. The duplex microstructure exhibits good room temperature ductility and strength, but for high temperature properties such as creep and fatigue resistance, a fully lamellar microstructure is desirable [48, 50, 55-57, 75, 78-82]. The low room temperature ductility and strength of fully lamellar microstructure is mainly due to its coarse grains. By decreasing the grain size in lamellar structures, the ductility and strength are expected to increase.



**Figure 39:** Dependence of mechanical properties such as fracture toughness, strength, elongation, impact resistance (IR), creep resistance (CR), and grain size on the microstructure type (Near Gamma, Duplex, Fully Lamellar) [50]

Many different processing routes were developed over the years to produce TiAl parts. Investment casting, ingot metallurgy and powder metallurgy are popular techniques used to produce TiAl parts. One of the major drawbacks of TiAl compared to Ni-based superalloys is its production costs, largely due to the difficulty of processing materials with fairly low ductility [48, 50, 55, 57, 77, 83].

Ingot metallurgy and casting involve the production of TiAl ingots and castings by skull melting. The resulting materials often suffers of chemical inhomogeneity and segregation and exhibit large columnar grains. However, improvements in chemical homogeneity and microstructure refinement can be achieved. Furthermore, such TiAl parts often need costly post-processing to satisfy the required properties [48, 50, 53, 55, 56]. For example, extrusion, forge, Hot Isostatic Pressing (HIP), ageing treatments etc. Finally, such processing routes often requires the formation of the  $\beta$ -phase which allows a certain workability although preferably avoided for the benefit of creep strength [48, 55, 57, 77].

Powder metallurgy offers the potential of minimizing many of the problems associated to the production of TiAl parts [47, 48]. A gas-atomized pre-alloyed powder is usually used. However, during atomization the liquid metal interacts with the inert gas environment (argon Ar or helium He) leading to entrapment of gas within the particles creating spherical pores [48, 50, 65, 75, 84-86]. Anyway, powder metallurgy routes offer interesting insights. In particular, the production of near-net-shape parts with good properties at good productivity and waste reduction.

### *A. Chemistry of $\gamma$ -TiAl alloys:*

Over the years, many research have tend to optimize the chemistry of TiAl-based alloys [48]. The chemical composition has a strong influence on material properties. First generations of alloys containing (45-50) at.% of Al were developed to give birth to the so-called  $\gamma$ -TiAl. The aluminum content have a significant effect on ductility. The graphs in figure 40 show the influence of aluminum content on room temperature ductility and yield strength in the case of Ti-xAl-2Cr-2Nb alloys [87]. The highest levels of ductility are reached for an aluminum content around 47-48 at.%. Figure 40 should be seen as a trend since the addition of alloying elements (in particular Cr) and the microstructure play an important role on strength and ductility values. First generation alloys for engineering purpose with a composition Ti-48Al-1V-(0.1-0.3)C were developed on the base of ductility and creep resistance. However, they exhibited poor properties with regards to the requirements of gas turbines structural parts.

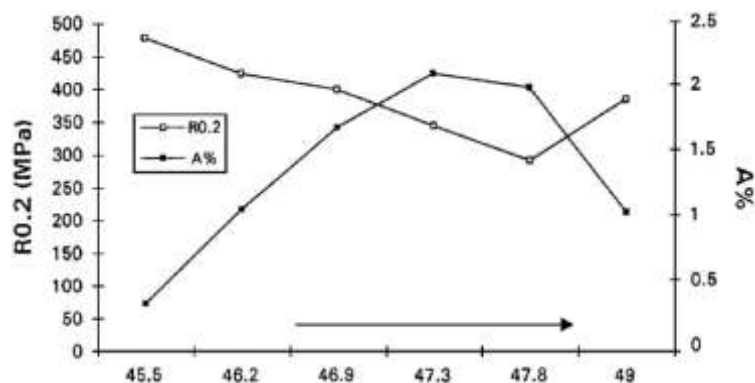


**Figure 40:** Influence of the Al content on strength and ductility in the case of Ti-xAl-2Cr-2Nb alloys [87]

A second generation of  $\gamma$ -TiAl alloys contained a substantial amount of alloying elements. Alloying with chromium up to 2 at% was found to increase significantly the ductility of the material, while refractory elements addition like niobium or molybdenum was beneficial for high temperature properties such as creep and oxidation resistance. In particular, a Ti-48Al-2Cr-2Nb alloy was developed by General Electric Company and demonstrated a relatively good balance of properties up to 750 °C [28, 48, 61, 75, 86].

Finally, alloying with higher amounts of refractory elements such as Nb, Ta or Mo up to 10 at.% led to the development of high temperature 3<sup>rd</sup> generation  $\gamma$ -TiAl [28, 48, 50, 57, 65, 88]. In general, the total amount of alloying elements should be  $\leq 10$  at.% otherwise the material's density becomes substantially higher. Wu [57] suggested that all alloys are limited by low ductility and that a base composition of Ti-(45-46)Al-(4-8)Nb with minor additions offers the best properties.

Wereley et al. [50] in 2012 described the state of the art of  $\gamma$ -TiAl with outstanding high temperature mechanical properties. The four alloys identified are listed in table 10 with their composition and major strengths, as described in the article.

Alloy name	Composition (at.%)	Alloy strengths
<b>General Electric, USA. 48-2-2</b>	Ti-48Al-2Cr-2Nb	Ductility, fracture toughness and oxidation resistance
<b>Plasee, Austria. <math>\gamma</math>-MET</b>	Ti-45Al-(5-10)Nb	High temperature strength, creep, fatigue and oxidation resistance
<b>GKSS Research Center, Germany. TNB Alloy</b>	Ti-(45-47)Al-10Nb	High temperature strength, creep and oxidation resistance
<b>Martin Marietta Laboratories, USA. XD<sup>TM</sup> TiAl</b>	Ti-45Al-2Mn-2Nb-0.8B	Ductility, high temperature strength, stiffness, creep and oxidation resistance

**Table 10: TiAl state-of-the-art alloys [50]**

In 2007, the General Electric's cast Ti-48Al-2Cr-2Nb alloy passed the FAR33 certification for GENx engines for medium-capacity, long-range aircrafts (Boeing 787 and 747-8). TiAl turbine blades were introduced in the last two stages of the low pressure turbine of the GENx engine. This is the greatest breakthrough in the TiAl industry regarding aerospace so far. As of June 2013, there are 274 GENx engines in service [14, 48, 59, 89-91].

As successor to the CFM56 family, the LEAP engine is being developed by GE and SNECMA. It was also introduced TiAl alloys for the last stage of the low pressure turbine blades as a breakthrough in materials technology [21, 22, 89, 92]. The engine will begin flight tests in 2014, leading to engine certification in 2015 and entry into commercial service in 2016. The LEAP family was chosen to power the A320neo, B737MAX and the Chinese COMAC919.

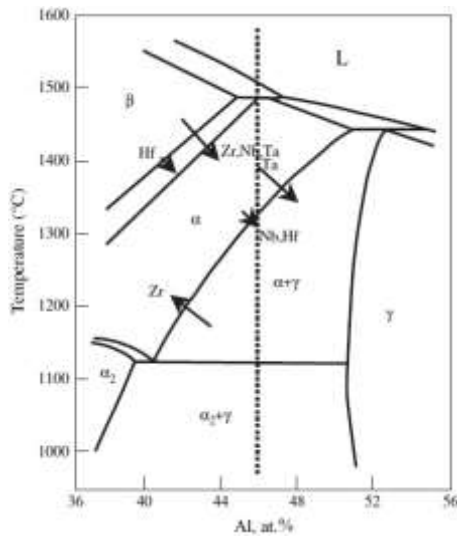


**Figure 41:** Section of the TiAl phase diagram showing the effect of alloying elements on phase boundaries [57]

Basically, alloying elements have two general effects. The first is to shift the phase boundaries in the phase diagram [57]. Figure 41 shows the effect of some alloying elements on phase transition boundaries. The arrows indicate the sense of movement of the phase boundaries for ternary alloying additions with the length of the arrow indicating the potency of each element. The revisited phase diagram of TiAl-8Nb is displayed later in figure 90 in the section III.2.B of Part II.

On the other hand, alloying elements modify the microstructure and properties of TiAl-based alloys.

The effects of alloying elements on TiAl-based alloys properties have been widely reported and are presented in table 11 below [48, 50-52, 54-57, 65-67, 74, 75, 77, 83, 86, 88, 93-95]. The list is not exhaustive, but represent a valuable screening for chemical composition statements.

Element	Optimal content (at.%)	Effects
Aluminum (Al)	46 - 48	Insures the highest room temperature ductility
Chromium (Cr)	1.2 - 2	Improves room temperature ductility and corrosion resistance ( $\beta$ -stabilizer)
Niobium (Nb)	6 - 8	Improves oxidation resistance, creep resistance, high-temperature strength and erosion resistance ( $\beta$ -stabilizer)
Silicon (Si)	0.3 - 0.4	Improves creep strength and oxidation resistance
Nickel (Ni)	0.5 - 1.2	Increases internal friction and improves resonance resistance Improves oxidation resistance ( $\beta$ -stabilizer)
Yttrium (Y)	0.1 - 0.3	Increase oxidation resistance Grain size reduction Reduces ductility
Tungsten (W)	0.5	Increase oxidation and creep resistance Grain size reduction
Vanadium (V)	0.5 - 1.1	Improves high temperatures tensile strength and ductility Improves castability Grain size reduction ( $\beta$ -stabilizer)
Boron (B)	0.5 - 1	Grain size reduction Increases room temperature ductility

<b>Zirconium (Zr)</b>	0.2	Increase oxidation resistance ( $\beta$ -stabilizer)
<b>Hafnium (Hf)</b>	0.2	Increase oxidation resistance ( $\beta$ -stabilizer)
<b>Tantalum (Ta)</b>		Improves creep and oxidation resistance Tendency for hot cracking ( $\beta$ -stabilizer)
<b>Molybdenum (Mo)</b>	0.4 – 0.8	Improves creep and oxidation resistance Improves high temperature strength Grain size reduction ( $\beta$ -stabilizer)
<b>Iron (Fe)</b>	0.4 – 0.8	Improves creep resistance Grain size reduction ( $\beta$ -stabilizer)
<b>Carbon (C)</b>	0.05 – 0.12 (wt.%)	Increase creep and oxidation resistance
<b>Manganese (Mn)</b>	0.2 - 4	Grain size reduction Improves ductility ( $\beta$ -stabilizer)
<b>Cobalt (Co)</b>	1 - 3	Increase Creep resistance ( $\beta$ -stabilizer)

**Table 11: Effect of alloying element addition to  $\gamma$ -TiAl alloys**

The chemical composition must be set according to the requisites of the parts. In the case of gas turbine components, efforts focus on integrity, ductility, optimized oxidation resistance, high temperature strength and creep. In addition, the EBM process does not particularly require specific additions. For example, addition of boron is often preferred to reduce the grain size of cast materials.  $\beta$ -stabilizer elements addition is usually necessary for wrought alloys to improve hot workability. The EBM process allowed to optimize the chemical composition towards the best set of material's properties with no regards to the processability.

In this study, the chemical composition was set in the scope of producing high temperature 3<sup>rd</sup> generation  $\gamma$ -TiAl by EBM for low pressure turbine blades in gas turbine engines. The alloys should thus possess a minimum ductility of 1%, a minimum fracture toughness of about 15 MPa. $\sqrt{m}$ , comparable specific strength and creep resistance than typical Ni-based superalloys for such applications, enhanced properties with respect to 2<sup>nd</sup> generation  $\gamma$ -TiAl alloys, and good reliability. The following composition was therefore suggested:

- **Aluminum (Al):** 46 to 48 at.% to insure good oxidation resistance and room temperature ductility.
- **Chromium (Cr):** 1.5 to 2 at.% to insure good room temperature ductility and corrosion resistance at medium temperature.
- **Niobium (Nb):** 7 to 8 at.% to insure good creep, high temperature strength, oxidation resistance and erosion resistance.
- Balance of **titanium (Ti)** and inevitable impurities.

## B. Mechanical properties

Generally, the common properties of 1<sup>st</sup> and 2<sup>nd</sup> generation  $\gamma$ -TiAl alloys are summarized in table 12 [48, 75, 96, 97]. The variations depend on alloy composition, alloying elements nature and content, microstructure and manufacturing process.

Structure	L1 <sub>0</sub> /D0 <sub>19</sub>
Density	3.7-4.0 g/cm <sup>3</sup>
Young's modulus at Room Temperature	160-180 GPa
Yield strength at Room Temperature	400-650 MPa
Tensile strength at Room Temperature	450-800 MPa
Temperature limit due to creep	900-1000 °C
Temperature limit due to oxidation	900 °C
Tensile strain to fracture at room temperature	1-4 %
Tensile strain to fracture at high temperature	10-60 %
Fracture toughness K <sub>Ic</sub> at room temperature	10-20 MPa√m
Thermal conductivity	22 W.m <sup>-1</sup> .K <sup>-1</sup>

**Table 12:** General properties of 1st and 2nd generation  $\gamma$ -TiAl alloys

The mechanical properties of  $\gamma$ -TiAl alloys are strongly sensitive to both alloy composition and microstructure. It is therefore difficult to accurately review the mechanical properties of such material from the literature. The core of the present thesis is the production by EBM, the characterization of the massive materials and the microstructural set-up through heat treatment of 3<sup>rd</sup> generation  $\gamma$ -TiAl alloys. The effect of the microstructure was thus highlighted.

### a. Tensile properties

The tensile properties of different TiAl-based alloys at room temperature have been studied. The tensile strength of a cast 8.5Nb-TiAl-based alloy (Ti-45Al-8.5Nb-0.3W-0.3B-0.05Y, named as TAWBY) are displayed in table 13 [82]. On the one hand, a fully lamellar microstructure was set by annealing treatment in the  $\alpha$  single-phase field at 1310°C for 30 min. On the other hand, a duplex microstructure was set by annealing in the ( $\alpha$ + $\gamma$ ) phase field at 1250°C for 1h. The UTS of the alloy with a duplex microstructure was about 250 MPa higher compared to the FL alloy, which emphasized the important role of microstructure (table 13).

Alloy and microstructure		Temperature and properties		
		RT		
		UTS, MPa	YTS, MPa	$\delta$ , %
Ti-46Al-5Nb-1W	FL	518	476	0.35
Ti-48Al-8Nb-1B	FL	699	569	0.61
Ti-44Al-4Nb-4Zr-1B	FL	665	650	0.2
TAWBY	FL	532	–	0.5
	DP	789	–	0.8

**Table 13:** Tensile strength of TAWBY (Ti-45Al-8.5Nb-0.3W-0.3B-0.05Y) alloys at room temperature compared to other fully lamellar high Nb containing TiAl alloys <sup>[82]</sup>

The tensile properties of other high Nb containing alloys at room temperature are also displayed in table 13 for comparison. One can note the low ductility at room temperature of all of the alloys. Alloys containing high amount boron, used for grain size refinement (table 11), exhibited rather high tensile strength but ductility was still very low.

TiAl alloys usually exhibit a low ductility at room temperature. Alloying elements addition and in particular chromium improves ductility <sup>[48, 59, 60, 75, 98, 99]</sup>. Figure 42 shows the evolution of tensile ductility as a function of Cr content for Ti-48Al based alloys, where the maximum was found for addition of 2 at.%.

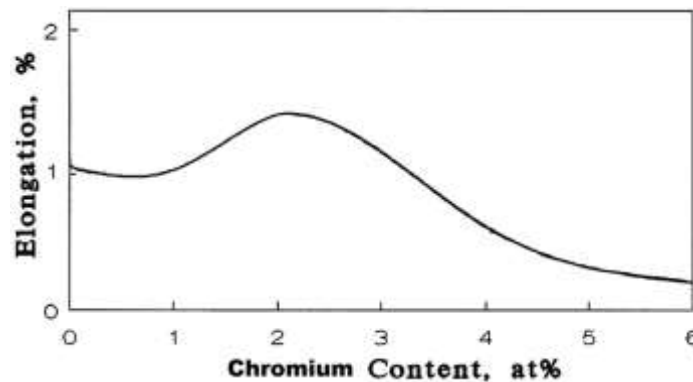


**Figure 42:** Tensile ductility at room temperature as a function of Cr content in Ti-48Al-xCr alloys



The microstructure and in particular the grain size of  $\gamma$ -TiAl alloys has a great influence on their ductility. The finer grain size of duplex microstructures is preferred for ductility. Basically, the ductility of gamma alloys decreases when the grain size increases. The ductility at room temperature of two-phase TiAl alloys (Ti-(46-48)Al-3(Cr,Mn,V)-(2-3)Nb-(0-1)(W,Hf,Mo)) with different microstructures is plot figure 43 as a function of grain size <sup>[80]</sup>.

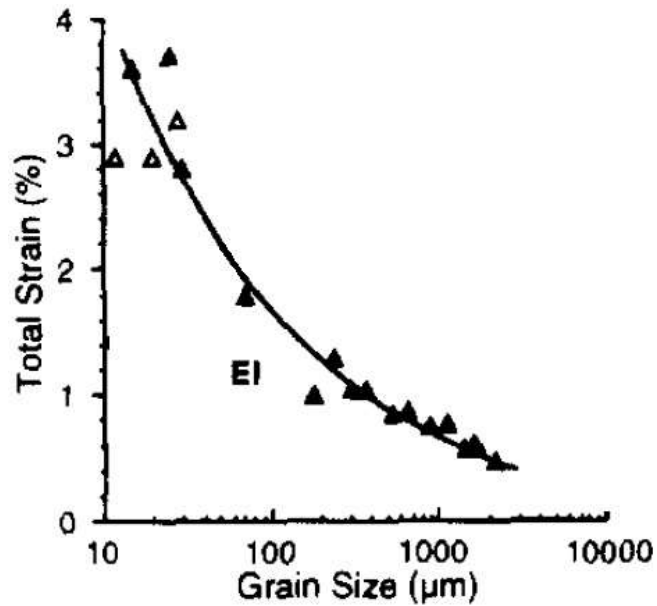


**Figure 43:** The total strain to fracture values are plotted against grain size for both duplex and lamellar TiAl alloys (Ti-(46-48)Al-3(Cr,Mn,V)-(2-3)Nb-(0-1)(W,Hf,Mo)) <sup>[80]</sup>

The strength levels at room temperature in the rolling direction of an annealed sheet material Ti-46Al-9Nb showing an equiaxed near-gamma microstructure (NG) was found even higher <sup>[85]</sup>. The tested material showed a yield strength of 754 MPa and an ultimate tensile strength of 881 MPa. The stress-strain curve is displayed in the opposite figure 44.

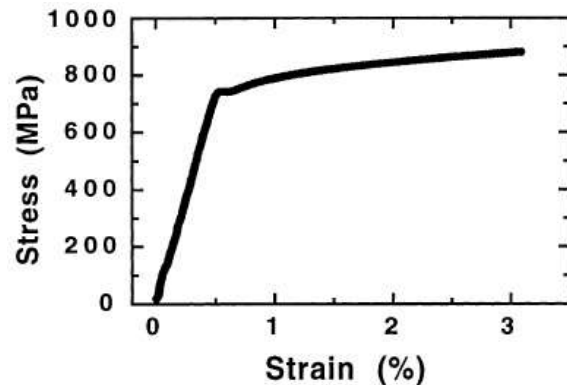


**Figure 44:** Stress-strain curve of a tensile test conducted at RT on annealed (1000°C/3h) sheet material <sup>[85]</sup>

The effect of microstructure on tensile properties at ambient temperature of six alloys with a lower content of Nb was investigated<sup>[100]</sup>. The processing routes and chemical compositions were significantly different. The results of the tensile tests are displayed in table 14. The lowest strength levels were found for the forged MD Ti-47Al-2Nb-2Cr-0.2B with a highly equiaxed microstructure. On the other hand, the fine fully lamellar microstructure of Ti-47Al-2Cr-2Nb prepared by PM techniques led to outstanding strength levels and 1 % ductility.

Microstructure/Composition (At. Pct)	Equiaxed $\gamma$ Phase	Lamellar Colony Size, $D$	$\gamma$ Grain Size	Yield Strength (MPa)	Fracture Strength (MPa)	Elongation (Pct)
XD nearly lamellar / Ti-47.7Al-2.0Nb-0.8Mn + 1 vol pct TiB <sub>2</sub>	~30 pct	120 $\mu$ m	~23 $\mu$ m	546	588	0.7
MD fully lamellar/ Ti-47Al-2Nb-2Cr-0.2B	~4 pct	145 $\mu$ m	5 to 20 $\mu$ m	426	541	0.8
MD duplex/ Ti-47Al-2Nb-2Cr-0.2B	90 pct	—	17 $\mu$ m	384	489	0.9
P/M lamellar/ Ti-47Al-2Nb-2Cr	<5 pct	65 $\mu$ m	~1 $\mu$ m	975	1010	1.0
G7 coarse lamellar/ Ti-47.3Al-2.3Nb-1.5Cr-0.4V	<5 pct	1 to 2 mm	10 to 40 $\mu$ m	450	525	1.0
G7 duplex/ Ti-47.3Al-2.3Nb-1.5Cr-0.4V	90 to 95 pct	—	15 to 40 $\mu$ m	450	590	4.0

**Table 14: Microstructural features and tensile properties at room temperature of some  $\gamma$ -TiAl alloys<sup>[100]</sup>**

The effect of the microstructural features in table 14 is more confused. Despite very different microstructures, the cast G7 Ti-47.3Al-2.3Nb-1.5Cr-0.4V alloys exhibited similar strength, although the quasi-equiaxed microstructure showed higher UTS and ductility as expected. However, the forged MD Ti-47Al-2Nb-2Cr-0.2B alloys exhibited the opposite behavior. It emphasized the important role of the processing route and the chemical composition on the tensile properties of  $\gamma$ -TiAl alloys. The lowest ductility was found for the Cr-free XD Ti-47.7Al-2Nb-0.8Mn alloy.

The tensile properties of the alloys in table 13 were investigated at higher temperatures<sup>[82]</sup>. Table 15 shows the properties at 700, 760, 800 and 870 °C of the TAWBY alloys and other high Nb containing TiAl alloys. From table 15, it appears that lamellar microstructures retained strength levels up to higher temperatures when compared to duplex microstructures.

Alloy and microstructure	Temperature and properties												
	700 °C			760 °C			800 °C			870 °C			
	UTS, MPa	YTS, MPa	$\delta$ , %	UTS, MPa	YTS, MPa	$\delta$ , %	UTS, MPa	YTS, MPa	$\delta$ , %	UTS, MPa	YTS, MPa	$\delta$ , %	
Ti-46Al-5Nb-1W	FL	471	416	0.49									
Ti-48Al-8Nb-1B	FL	641	506	10.80									
Ti-44Al-4Nb-4Zr-1B	FL	627	563	0.44									
K5	FL						502	375	3.2	485	362	12	
	DP						468	345	40.0				
Ti-47Al-2Nb-2Cr-4Ta	DP						495	363	23.3	403	334	14.6	
TAWBY	FL				535	435	3.0	590	460	3.1	480	335	22
	DP				520	410	3.8	540	410	8.6	405	285	46

**Table 15: Tensile strength of TAWBY (Ti-45Al-8.5Nb-0.3W-0.3B-0.05Y) alloys at high temperatures compared to other  $\gamma$ -TiAl alloys<sup>[82]</sup>**

The tensile stress vs. strain curves at different temperatures of the equiaxed NG Ti-46Al-9Nb sheet material are plotted in figure 45. The numerical values of yield and ultimate tensile strengths are displayed table 16<sup>[101]</sup>.

Temperature [°C]	Strain rate [s <sup>-1</sup> ]	$\sigma_{0.2}$ [MPa]	$\sigma_m$ [MPa]
800	$1 \times 10^{-4}$	440	546
850	$1 \times 10^{-4}$	362	414
900	$1 \times 10^{-4}$	278	304
950	$1 \times 10^{-4}$	193	217
1000	$1 \times 10^{-4}$	123	146

$\sigma_{0.2}$ : yield strength;  $\sigma_m$ : ultimate tensile strength;

**Table 16:** Mechanical properties of Ti-46Al-9Nb sheet material as obtained from tensile tests<sup>[101]</sup>

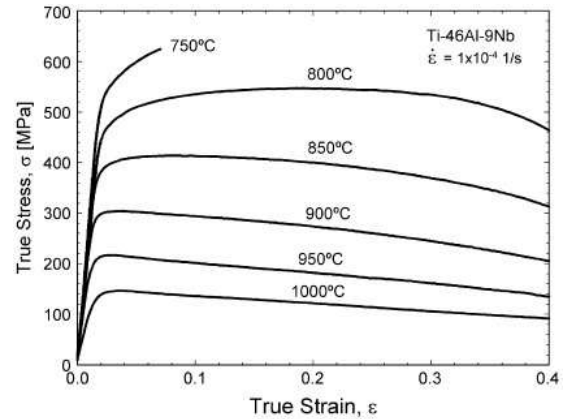


**Figure 45 :** Tensile flow behavior of Ti-46Al-9Nb sheet material which shows a NG structure : true stress vs. strain curves for a constant strain rate<sup>[101]</sup>

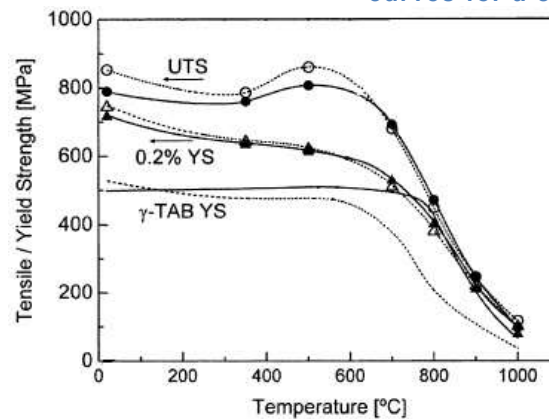


**Figure 46:** Tensile strength (circles) and yield strength (triangles) as a function of temperature, obtained from primary annealed Ti-46Al-9Nb sheets with NG microstructure in the rolling direction (open symbols) and transverse to the rolling direction (closed symbols)<sup>[85]</sup>

The equiaxed microstructure of the Ti-46Al-9Nb alloys showed high levels of strength up to about 750 °C. At higher temperatures though, the strength decreased drastically. In figure 46, the dependence of strength over temperature was highlighted<sup>[85]</sup>. Without symbols, the yield strength for a conventional  $\gamma$ -TiAl alloy sheet is shown.

Finally, the tensile properties of an isothermally forged Ti-50Al-7.5Nb sample with a near-gamma (NG) structure is shown figure 47 [102]. The strength levels were significantly lower than that of the previous materials.

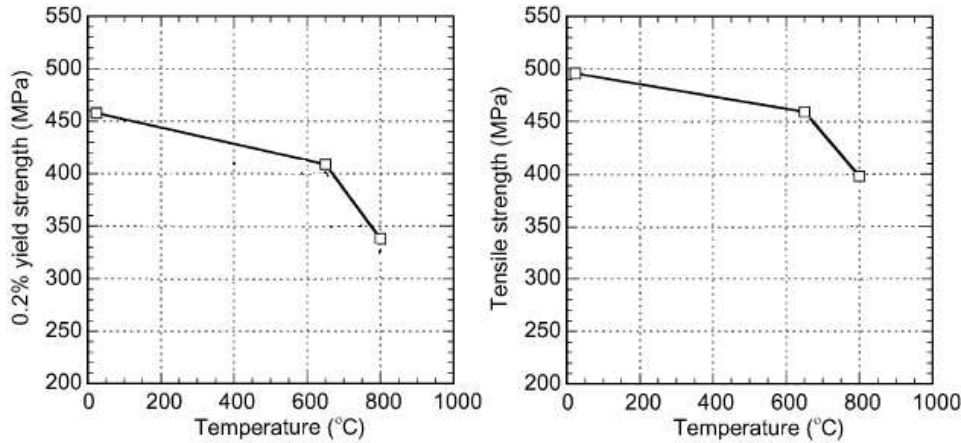


**Figure 47:** Tensile strengths of isothermally forged Ti-50Al-7.5Nb showing a near-gamma (NG) microstructure at various temperature [102]

The microstructure morphology (DP or FL) has a great influence on tensile properties but substantial variations are also attributed to actual grains morphology such as grains size and lamellar spacing. The effect of the microstructural features was studied for a wrought TiAl alloy (Ti-(46-48)Al-3(Cr,Mn,V)-(2-3)Nb-(0-1)(W,Hf,Mo)) [80]. Different duplex and lamellar structures were produced through specific annealing treatments and processing routes. The results of tensile tests for duplex and lamellar microstructures with different grain size are shown figure 48. Figure 49 shows the effects of grain size and lamellar spacing on yield strength.

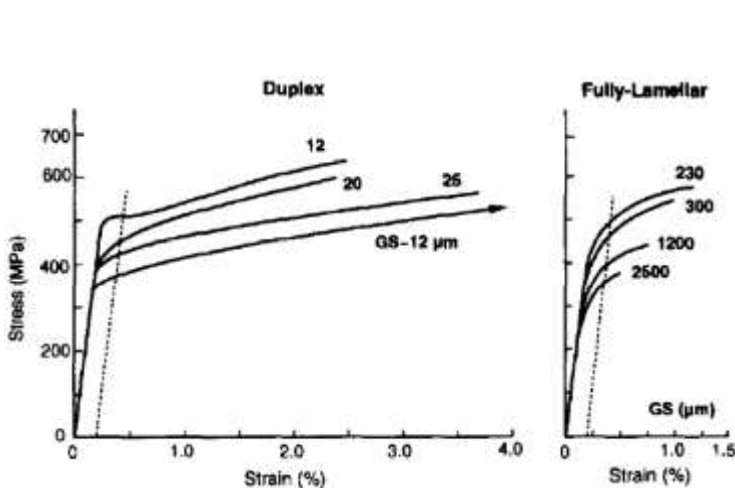


**Figure 48:** Tensile flow curves for TiAl alloys in two typical microstructural forms with various grain size [80]

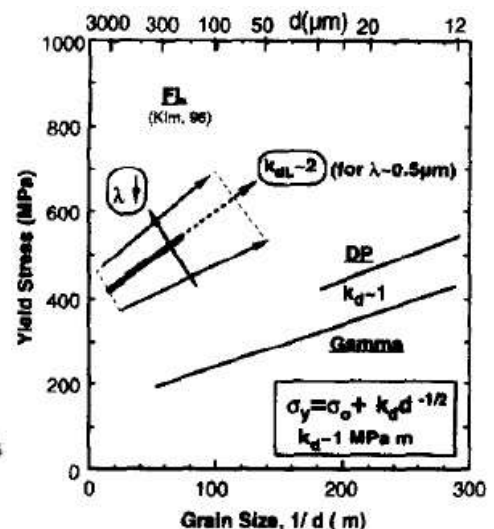


**Figure 49:** Relationships between yield stress, grain size ( $d$ ) and lamellar spacing ( $\lambda$ ) in FL materials [80]

Logically, the strength increases when the mean grain size decreases for both microstructural forms. The relationship between the yield strength and the grains size was found to satisfy the Hall-Petch relationship:

$$\sigma_y = \sigma_0 + k_y d^{-1/2} \quad [80]$$

Where  $\sigma_0$  and  $k_y$  are material's constants and  $d$  is the mean grain size.

The effect of lamellar spacing on yield strength was also substantial (figure 49). Both the Hall-Petch constant and the intrinsic strength ( $\sigma_0$ ) increase when the lamellar spacing decreases.

### b. Creep properties

A good creep resistance is very important for high temperature structural applications. The specific creep resistance of  $\gamma$ -TiAl alloys should be at least similar to that of Ni-based superalloys in current use. Most of TiAl alloys do not satisfy these conditions at temperatures over 700 °C. Niobium addition enhances significantly the creep properties of  $\gamma$ -TiAl alloys [48, 59, 60, 75, 79, 81, 96-98, 103]. It is found to increase the activation energy and, thus, slows down diffusion. Thus, the stress required to initiate dislocation glide and twinning is higher.

As for the tensile properties, creep properties are also very sensitive to microstructure. In general, the small grain size of NG and DP alloys is detrimental to creep resistance because of grain boundary sliding [96].

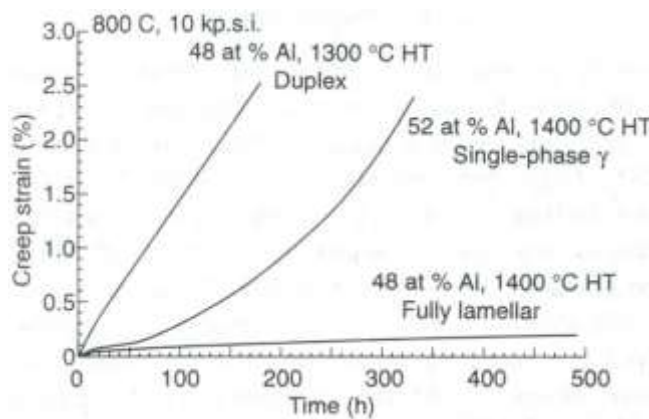


**Figure 50** : A comparison of the creep curves of the three typical microstructures in  $\gamma$ -based alloys [97]

Without special control, the grain size of lamellar structure is at least 10 times larger than that of  $\gamma$  and duplex structure. Despite  $\alpha_2$  lamellas show better resistance to deformation and fracture at low temperature, they should become weaker at creep temperature. Thus, the usual better creep resistance of lamellar structure is primarily a result of its large grain size. The opposite figure 50 compares the creep curves of the three typical microstructures in  $\gamma$ -based alloys [97].

The effect of the microstructural form on the creep response of a TNB sheet material (Ti-46Al-9Nb alloys) at 700°C under 225 MPa is shown in figures 51 and 52 [79].

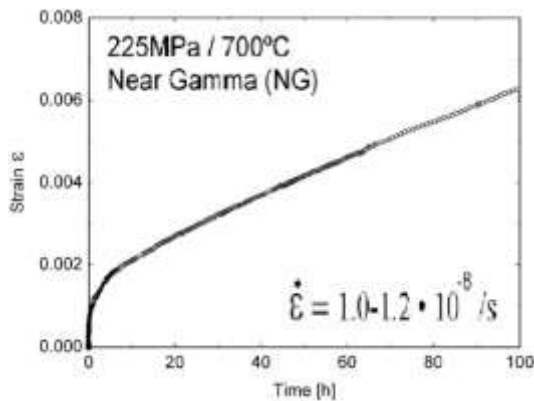


Figure 51 : Creep property of TNB (Ti-46Al-9Nb) sheets with NG microstructure in rolling direction [79]

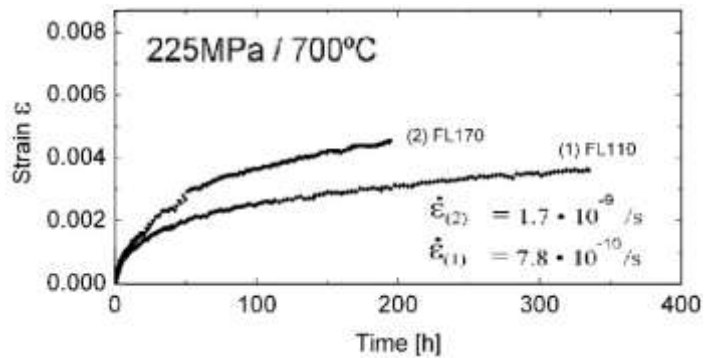


Figure 52 : Creep behavior of TNB (Ti-46Al-9Nb) sheet materials with a fine-FL microstructure. The mean lamellar spacing is 110 nm  $\pm$  27 for (1) and 170 nm  $\pm$  43 for (2) [79]

The lamellar material shows a better creep behavior than the fine-grained near-gamma (NG) material. The creep rate of the fine-FL (the mean lamellar spacing was  $\sim$  110nm for (1) and  $\sim$  170nm for (2)) was about 10 times smaller than that of the NG microstructure. The effect of the lamellar grain feature such as lamellar spacing is highlighted in figure 52. The smaller the lamellar spacing, the smaller the creep rate.

Fully lamellar TNB (Ti-46Al-9Nb) sheets with different lamellar spacing were prepared by heat treatment with different cooling rate [79]. The higher the cooling rate, the smaller the lamellar spacing. In figure 53, the short-time creep curves for FL specimens with a mean lamellar spacing of 470nm, 170nm and 110nm are shown. Tests have been realized at 150MPa / 800°C (open symbols) or 225MPa / 700°C (full symbols). Figure 54 shows the creep tests results for long-time exposure at 150MPa / 800°C of the three fully lamellar materials.

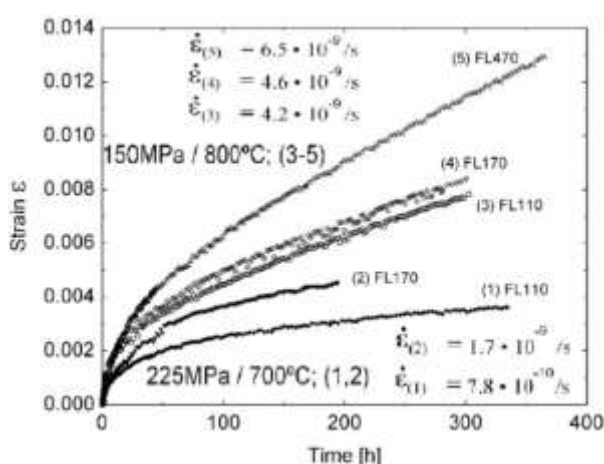


Figure 53 : Creep behavior of fully lamellar Ti-46Al-9Nb sheet material with different lamellar spacing: FL110 (1,3); FL170 (2,4); FL470 (5) in nanometer [79]

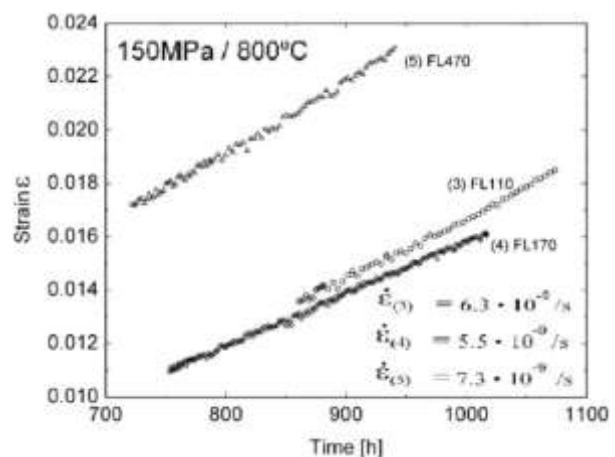
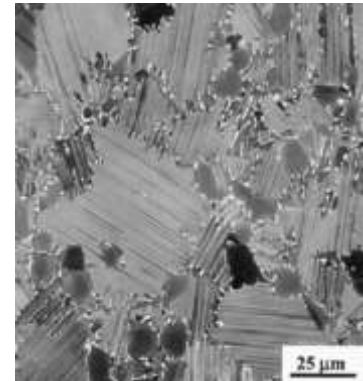


Figure 54 : Section of the long-term creep experiment behavior of Ti-46Al-9Nb sheet material with different lamellar spacing at 800°C after second stress change (125-150 MPa) [79]

The creep behavior was found quite sensitive to the lamellar spacing of the lamellar grains: a reduction of the average lamellar spacing decreases both the primary and secondary creep rates.

The creep resistance of a high Nb containing nearly lamellar material (Ti-45Al-10Nb) was studied [103]. Ti-45Al-10Nb had been annealed at 1300 °C for 15 minutes followed by controlled furnace cooling after thermo-mechanical processing. This led to a lamellar volume fraction of about 80% and a fine lamellar colony mean size of about 40 $\mu$ m. The presence of equiaxed  $\gamma$  grains along lamellar colony boundaries generally decreases the creep resistance of TiAl-base alloys. Nevertheless, the minimum creep rates of Ti-45Al-10Nb and other  $\gamma$ -TiAl alloys were compared (table 17). The alloy B (with a very fine lamellar spacing) and C are highly creep-resistant TiAl-base alloys, wrought and cast respectively.



**Figure 55:** Back-scattered electron micrograph of the microstructure of Ti-45Al-10Nb prior to creep test [103]

Alloy	Stress (MPa)	Microstructure	Minimum creep rate ( $1 \text{ s}^{-1}$ )
A	Ti-45Al-10Nb	L + 20% ( $\gamma + \omega$ )	$6 \times 10^{-9}$
B	Ti-47Al-2Nb-2Cr	Fully-lamellar	$4 \times 10^{-9}$
C	Ti-48Al-2W-0.5Si	Nearly-lamellar	$4.6 \times 10^{-9}$
D	Ti-47Al-2Nb-2Cr	L + 20% $\gamma$	$3.4 \times 10^{-8}$

**Table 17:** Comparison of the minimum creep rates of TiAl-base alloys at 760°C [103]

The minimum creep rate of the 10Nb alloy (A) was comparable to that of alloys B and C even though it showed a relatively large amount of equiaxed  $\gamma$  grains. It was attributed to the addition of Nb that greatly improved creep resistance. Compared to the alloy D with a similar nearly-lamellar microstructure, the minimum creep rate of Ti-45Al-10Nb was much lower. Studies suggested that the rate-limiting process for creep deformation of TiAl-base alloys varied from climb/recovery controlled process at low stresses to viscous glide controlled process at high stress regime. The transition stress between recovery-controlled regime to glide-controlled regime depends on the internal stress required to initiate dislocation glide. High Nb alloying in  $\gamma$  phase was found to increase the critical resolved shear stress (CRSS) for dislocation glide. Furthermore, the dislocation climb rate may also be reduced due to the low diffusivity of Nb solute and the lower stacking fault energy in high Nb containing alloys. It explains the good creep properties of the nearly lamellar Ti-45Al-10Nb despite the fine grain size and substantial amount of equiaxed grains.

c. Toughness and crack growth resistance

The fatigue crack growth behavior of  $\gamma$ -TiAl alloys is critical for structural applications in gas turbine engines. The fatigue crack growth  $\gamma$ -TiAl alloys having different microstructures were studied early in 1996 [104]. The fatigue crack growth rate decreased when the amount of lamellar phase increased. Equiaxed microstructures exhibited the highest crack growth while fully lamellar materials the lowest. In fact, the presence of hard  $\alpha_2$  together with soft  $\gamma$  phases in the lamellar grains result in a high resistance to crack propagation. It was observed that the crack growth occurred by microcrack nucleation, growth and coalescence, similar to ceramic materials. Figure 56 shows the schematic model of the fatigue crack growth process as concluded from the study.

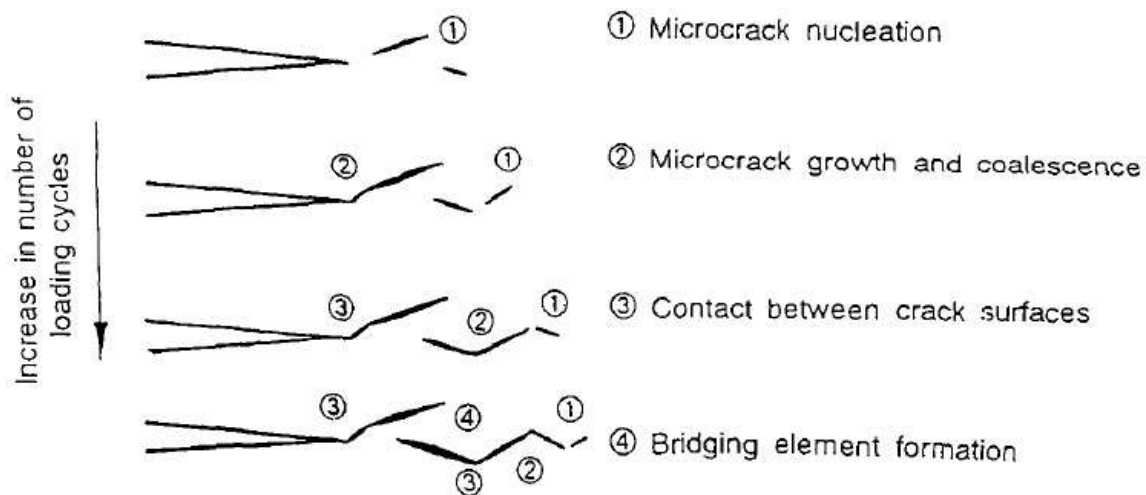


Figure 56: Schematic model of the fatigue crack growth process [104]

Microcracks nucleated near the crack tip and coalesced during cyclic loading. At the same time, new microcracks initiate ahead of the crack. During the repetition of this process, unbroken and bridging elements were formed in the crack wake, which induced a stress shielding effect. Contacts between crack surfaces due to crack path deflection (especially micro-tortuous crack path) induced crack closure. The study concluded that the lamellar microstructure exhibited high crack growth resistance compared with the duplex and equiaxed microstructures. However, the crack growth behavior of the lamellar microstructure materials was found to depend on the orientation of the lamellar lath to the crack plane [104]. When the crack tip encountered grains containing lamellar laths at an angle to the crack plane, a high resistance to the crack growth was offered. Though, when the crack tip encountered lamellar grains containing laths parallel to the crack plane, the crack propagated along the weak interfaces.



The fracture toughness at room temperature of the TAWBY alloys (Ti-45Al-8.5Nb-0.3W-0.3B-0.05Y) were studied [82]. Table 18 shows the value of fracture toughness for the lamellar and the duplex microstructures. The fracture toughness of the alloy with a fully lamellar microstructure was greater than that of the DP alloy.

	Microstructures	
	FL	DP
$K_{Ic}$ , MPa·m <sup>1/2</sup>	16	10

**Table 18:** Fracture toughness of TAWBY alloy at room temperature for fully lamellar (FL) and duplex (DP) microstructures [82]

The fracture toughness of the six alloys of table 14 was studied at room temperature [100, 105]. The values of toughness are displayed in table 19, on which the microstructural features were again detailed. A range in the fracture toughness values indicated *R*-curve behavior. The first value corresponds to the crack-initiation toughness,  $K_i$ . The second value corresponds to the steady-state toughness or maximum measured crack-growth resistance,  $K_{SS}$ .

Microstructure/Composition (At. Pct)	Equiaxed $\gamma$ Phase	Lamellar Colony Size, <i>D</i>	$\gamma$ Grain Size	Fracture Toughness (MPa $\sqrt{m}$ )
XD nearly lamellar / Ti-47.7Al-2.0Nb-0.8Mn + 1 vol pct TiB <sub>2</sub>	~30 pct	120 $\mu$ m	~23 $\mu$ m	12 to 16
MD fully lamellar/ Ti-47Al-2Nb-2Cr-0.2B	~4 pct	145 $\mu$ m	5 to 20 $\mu$ m	18 to 32
MD duplex/ Ti-47Al-2Nb-2Cr-0.2B	90 pct	—	17 $\mu$ m	—
P/M lamellar/ Ti-47Al-2Nb-2Cr	<5 pct	65 $\mu$ m	~1 $\mu$ m	18 to 22
G7 coarse lamellar/ Ti-47.3Al-2.3Nb-1.5Cr-0.4V	<5 pct	1 to 2 mm	10 to 40 $\mu$ m	18 to 39
G7 duplex/ Ti-47.3Al-2.3Nb-1.5Cr-0.4V	90 to 95 pct	—	15 to 40 $\mu$ m	11

**Table 19:** Fracture toughness at room temperature and microstructural features of some  $\gamma$ -TiAl alloys [100]

Regarding the fracture toughness of  $\gamma$ -TiAl alloys, coarse lamellar microstructures are generally superior to duplex and equiaxed microstructures. Figure 57 displays the  $K_R(\Delta a)$  resistance  $R$ -curves for the different materials of table 19. It characterizes the fracture toughness behavior in terms of monotonic crack-growth resistance ( $K_R$ ) as a function of crack extension ( $\Delta a$ ) using fatigue precracked compact-tension specimens. Clearly from table 19 and figure 54, the fracture toughness behavior of the lamellar materials was better. Furthermore, the coarser the grain size, the higher the crack growth resistance <sup>[100, 105]</sup>.

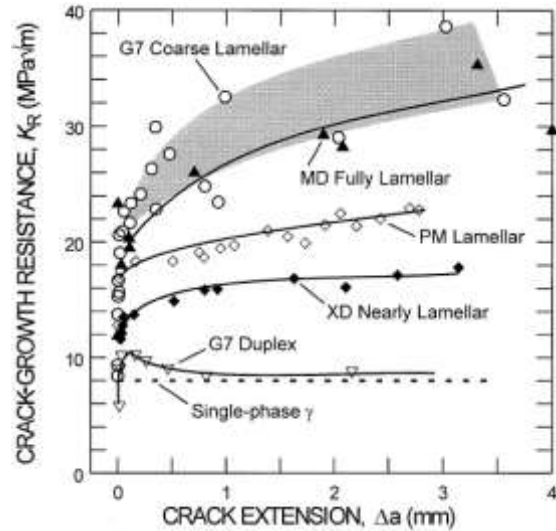


Figure 57: Monotonic fracture toughness behavior in the form of  $K_R(\Delta a)$  resistance curves <sup>[100]</sup>

The initiation toughness in lamellar structures is improved compared to that in duplex and single phase  $\gamma$  structures thanks to the presence of uncracked ligament bridging in the crack wake, which acts to shield the crack tip from the far-field loading. The presence of equiaxed  $\gamma$  grains is found to be detrimental for toughness and particularly for bridge formation. In general, the presence of the equiaxed  $\gamma$  phase lowers both the initiation and  $R$ -curve toughness. This can be clearly seen in figure 58, where the crack-initiation toughness ( $K_i$ ) and the maximum crack-growth toughness ( $K_{ss}$ ) display an inverse relationship with the volume fraction of equiaxed  $\gamma$  phase. The same observation has been previously reported for fracture toughness ( $K_{Ic}$ ) and  $R$ -curve crack initiation toughness. It is believed that the equiaxed phase degrades crack growth resistance by inhibiting the action of uncracked ligament bridging and crack closure (in the case of fatigue). Figure 59 represents the fatigue crack growth threshold as a function of the volume fraction of equiaxed  $\gamma$  phase. A deleterious correlation between fatigue crack growth resistance and the equiaxed  $\gamma$  phase is also observed.

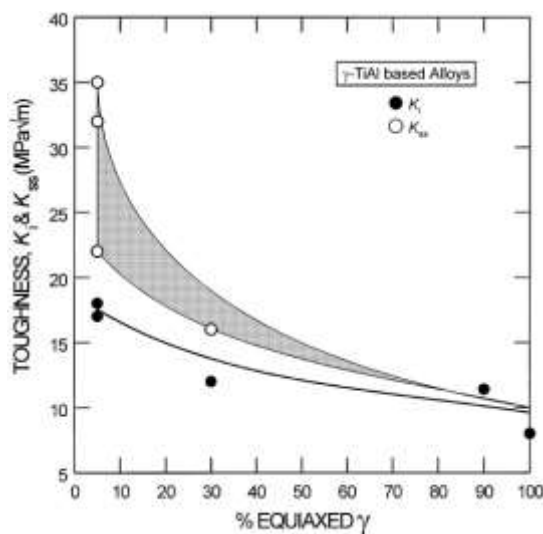


Figure 58: Relationships between toughness ( $K_i$  and  $K_{ss}$ ) and volume fraction of equiaxed  $\gamma$  phase <sup>[100]</sup>

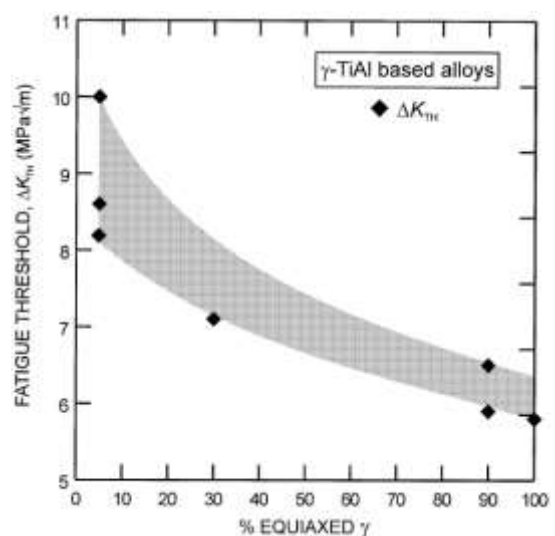
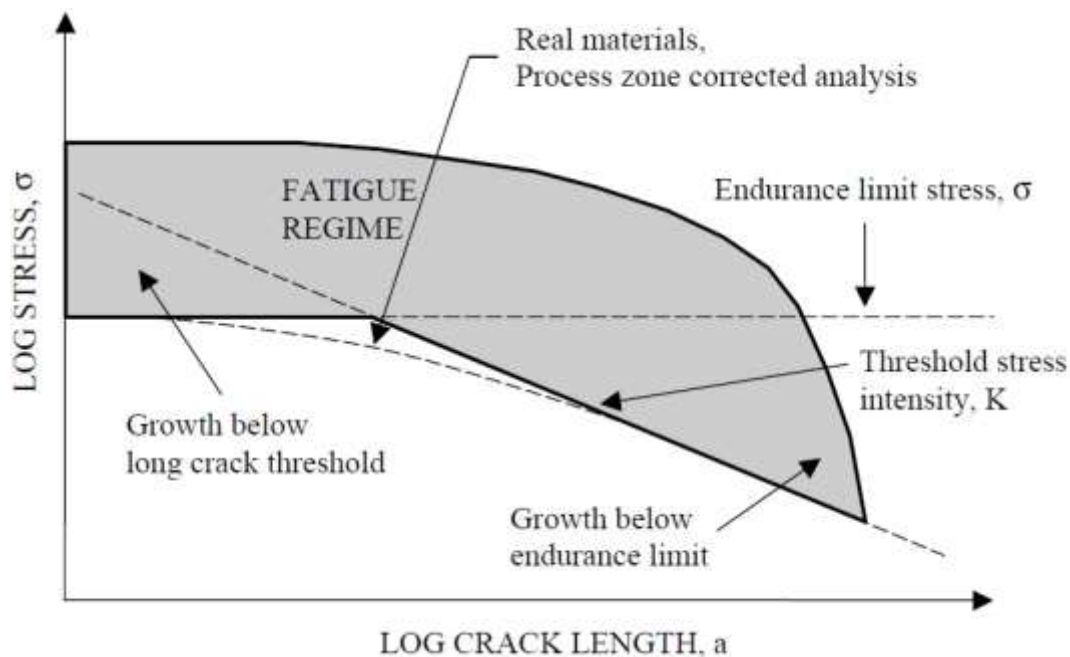


Figure 59: Fatigue crack growth threshold,  $\Delta K_{th}$  as a function of the volume fraction of equiaxed  $\gamma$  phase <sup>[100, 105]</sup>

The lamellar grains morphology also has an influence on toughness of  $\gamma$ -TiAl alloys. The smaller the grain size, the lower the toughness. However, the effect of grain size was rather limited. From figure 57 and table 19, the fracture toughness of the forged MD fully lamellar alloy was only slightly lower than that of the casted G7 coarse lamellar material. Despite a very different average lamellar grain size, the values of toughness were similar. On the other hand, the fracture toughness of the casted XD nearly lamellar alloy was significantly lower than that of the forged MD fully lamellar alloy that exhibited similar average lamellar grain size. Thus, the fracture resistance is assumed to be more dependent on the presence of the equiaxed  $\gamma$  phase rather than the lamellar colony size. Finally, for sufficiently small lamellar spacing ( $\lambda \leq \sim 1 \mu\text{m}$ ),  $K_i$  and  $K_{ss}$  are independent of the lamellar spacing. On the other hand, for  $\lambda \geq \sim 1 \mu\text{m}$ , both  $K_i$  and  $K_{ss}$  vary inversely with  $\lambda$ , in a manner similar to the Hall-Petch relation.

Defect sensitivity testing were carried out on wrought TNB (Ti-45Al-8Nb-0.2C) alloys to establish and validate a series of fatigue failure limit diagrams, commonly known as Kitigawa plots <sup>[106]</sup>. Figure 60 shows a schematic representation of Kitigawa plots that show fatigue strength as a function of defect or crack size.



**Figure 60:** Schematic representation of the Kitigawa diagram to model fatigue failures in pristine and damaged materials <sup>[106]</sup>

Notch sensitivity is normally influenced by microstructure or grain size and ductility of the material. The critical crack length for a material under static stress can be described by :

$$\sigma_f = \frac{K_{Ic}}{\sqrt{\pi a}}$$

Where  $\sigma_f$  is the fracture stress,  $K_{Ic}$  is the fracture toughness and  $a$  is the critical crack length <sup>[106]</sup>.

However, Voice et al. <sup>[106]</sup> showed that the effect of cracks is significantly underestimated in the case of fatigue of TNB alloys.

Figure 61 is a combination of the best fit lines through Kitagawa type data (fatigue strength vs defect size) for duplex and fully lamellar microstructures of TNB. As first consideration, the difference in fatigue strength between 20 and 700 °C was evident in duplex material but negligible in fully lamellar microstructure. The actual critical defect size under fatigue is about 40  $\mu\text{m}$  for the duplex microstructure and 15  $\mu\text{m}$  for the lamellar microstructure.

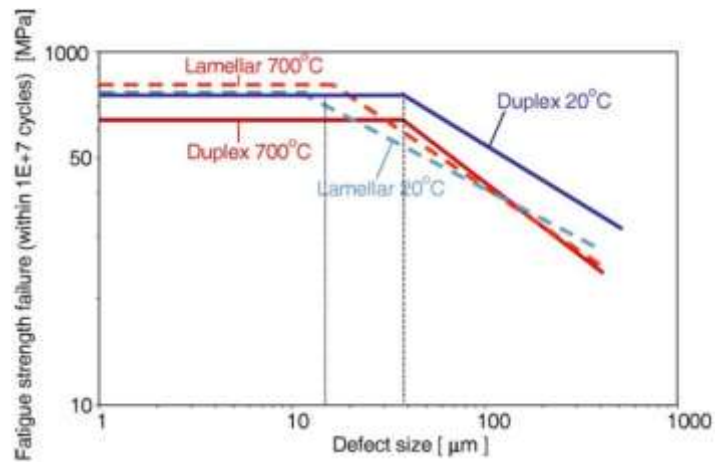


**Figure 61:** Summary of fatigue strength vs defect size of duplex and fully lamellar TNB microstructure <sup>[106]</sup>

#### d. Hardness

The effects of Niobium content and microstructure on hardness were investigated <sup>[102]</sup>. The materials used for hardness investigation were 20-30 g samples fabricated by means of an arc melting process and heat treated for homogenization at 1000 °C for 100 hours. Figure 62 shows the Vickers hardness values for a wide range of Ti-Al-Nb compositions. The hardness values for composition in the range of (45-50)Al and (0-10)Nb were circled. In this range of composition, the microstructure consisted on a  $\gamma$  and  $\alpha_2$  grains at 45Al and single  $\gamma$  grains at 50Al. The typical back scattered image of the Ti-45Al-5Nb material was inserted in figure 62.

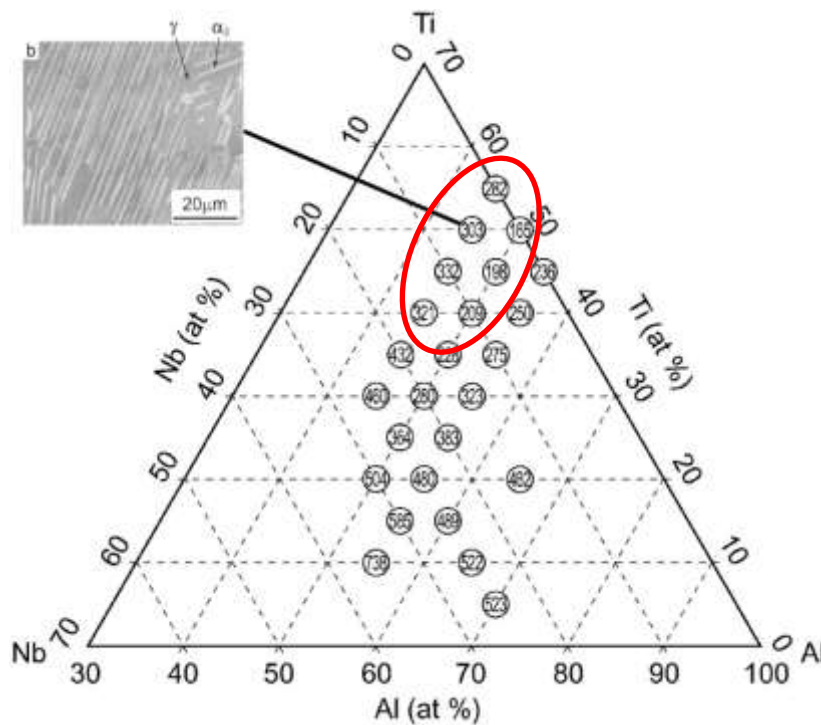


**Figure 62:** Vickers hardness of ternary Ti-Al-Nb alloys fabricated by arc melting process <sup>[102]</sup>

From figure 62, it was concluded that the hardness increased together with the Nb content. It was suggested that Niobium strengthens the  $\gamma$  phase by solution hardening. However, ductility decreased with Nb addition. Nb substitutes for Ti in  $\gamma$ -TiAl alloys, which involves lattice parameter  $c/a$  change increasing with the Nb content. The lattice distortion was believed to be responsible for the strengthening and embrittlement of the  $\gamma$  phase.

Kim et al. [107] also concluded that Nb strengthen the gamma phase, thus increasing the intrinsic strength. However, Nb addition significantly reduces the volume fraction of the  $\alpha_2$  phase which is about three times stronger than the  $\gamma$  phase.

Interestingly, data have been collected from measurements made on various  $\gamma$ -TiAl in order to find a relationship between hardness and yield strength [107]. A relationship was found between Rockwell C hardness (RcH), Vickers hardness (Hv) and tensile yield strength (YS). Figures 63 shows the relationship between RcH and Hv found for an alloy 03G (Ti-45Al-1Cr-6Nb-0.2W-0.2B-0.4C-0.2Si) forged and treated in different ways. Figure 64 on the other hand shows the relationship found between RcH and YS. By combination, YS and Hv were found related according to the following equation:

$$\text{Log (YS)} = 0.00239 (\text{Hv}) + 1.969 \quad [107]$$

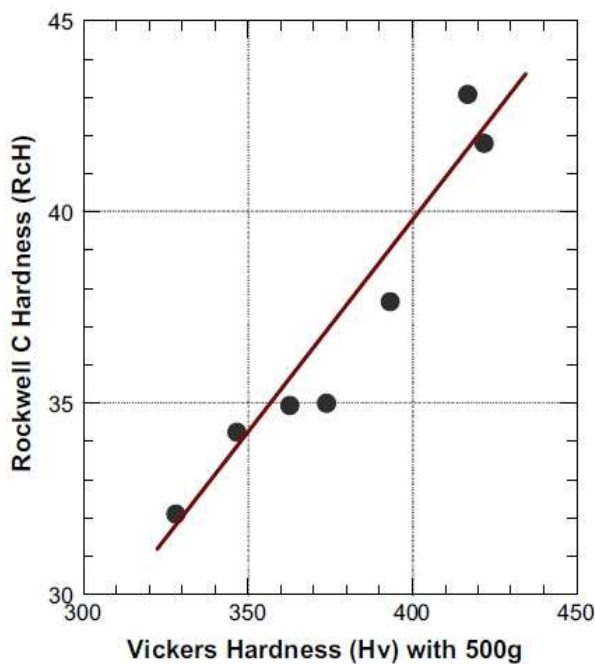


**Figure 63** : Vickers and Rockwell hardness values measured on bulk specimens of a gamma alloy in various annealing conditions showing a linear relationship [107]

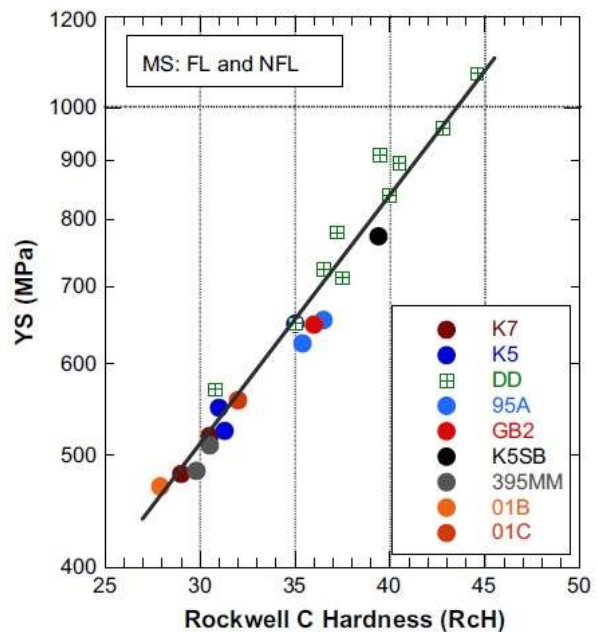


**Figure 64** : Relationship between Rockwell hardness values and yield strengths previously measured on bulk samples of various gamma alloys [107]

Thin sheets Ti-45Al-5Nb materials produced by pack rolling process were evaluated for microstructure variation and evolution taking place during aging and annealing treatments [107]. Figure 65 shows the Vickers hardness of the as-received and aged sheet materials at different temperatures for different time. The corresponding estimated yield strength values according to the previous equation were added on the Y-axis.

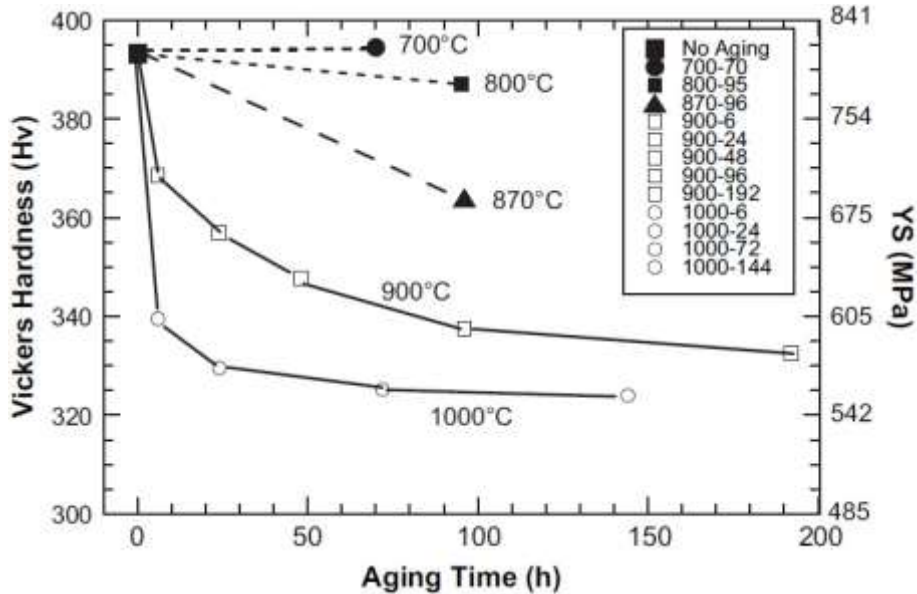


Figure 65: The effect of isothermal aging at different temperatures on Vickers hardness variation [107]

It was concluded from figure 65 that as the aging temperature increased, the strength level was lowered progressively faster with aging time and reached a quasi-steady-state value that apparently was specific to each aging temperature. The microstructure of the as-produced Gamma Met PX sheet materials was unstable above 840 °C, which was responsible of the strengthening. Annealing treatments in the range of 800-1000 °C therefore stabilized the microstructure.

Clemens et al. [108] made similar observations. The coarse fully lamellar microstructure of a PM Ti-46Al-9Nb alloy was refined by the massive transformation  $\alpha \rightarrow \gamma_M$ . The low  $c/a$  ratio and high hardness was attributed to high internal stresses and partially wrong site occupation of the atoms in the  $\gamma_M$  lattice. Annealing for 1 h above 800 °C led to a significant decrease in hardness due to annealing of defects and reduction of antiphase boundaries and internal stresses (Figure 66).

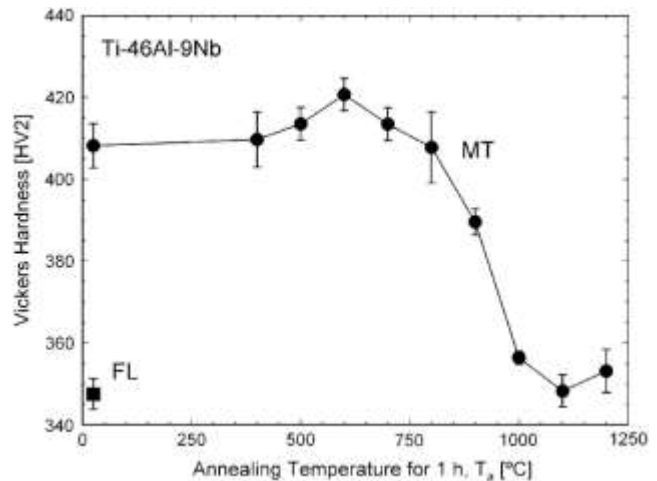
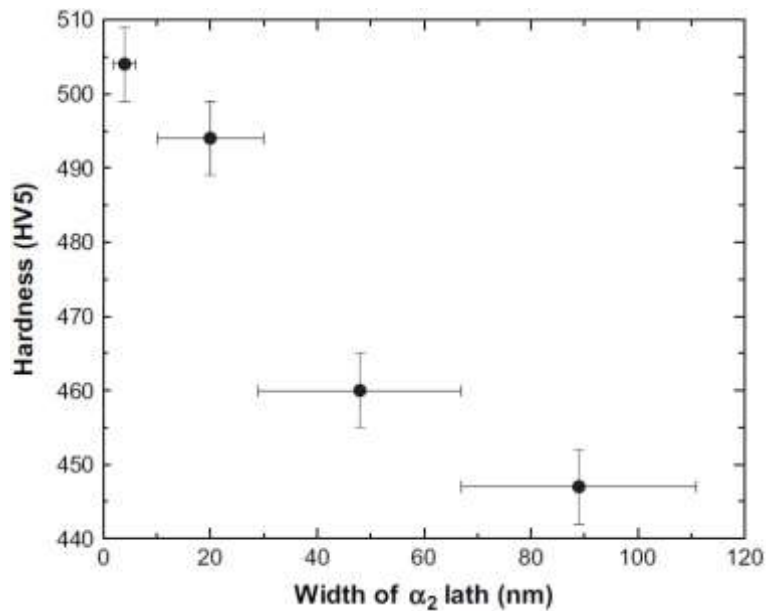


Figure 66: Vickers hardness (HV2) of massively transformed Ti-46Al-9Nb after 1 h annealing treatments. (■): Hardness of the starting fully lamellar microstructure [108]

These hardness and strength considerations highlighted the role of the processing route to fabricate the alloy and the conditions of possible heat treatments to set the microstructure.

Finally, the influence of the microstructural parameters of the lamellar structure on hardness was also studied <sup>[109]</sup>. A nanometer-scaled lamellar microstructure, with extremely fine  $\gamma$  laths, was developed in a PM Ti-45Al-7.5Nb alloy by means of a two-step heat treatment. It was found that the hardness was strongly dependent on the width of the constituting lamellae and their phase volume fractions. The studied samples had extremely fine  $\gamma$  laths (3.5-7.6 nm). Since dislocations could hardly glide or even be nucleated in the nano-scaled  $\gamma$  lamellae, the hardness of lamellar colonies only depended on  $\alpha_2$  laths. Hardness increased when the  $\alpha_2$  laths width decreased (figure 67). The dependency could be explained by the interaction between interfaces and the movement of dislocations.



**Figure 67:** Influence of  $\alpha_2$  laths width on hardness in a nanometer-scaled lamellar Ti-45Al-7.5Nb <sup>[109]</sup>

e. Oxidation

The poor oxidation resistance beyond 700 °C of TiAl-based materials is due to the fact they do not generally form long-lasting protective alumina scale, despite their high aluminum content. Niobium addition has been proved to enhance significantly the oxidation resistance [48, 59, 60, 70, 75, 99, 110]. Niobium, which solely occupies the Ti sublattice, enhance the formation of the protective oxide layer alumina. Early in 1992, Chen et. al. [111] showed the influence of Nb on the weight gain of TiAl alloys (figure 68).

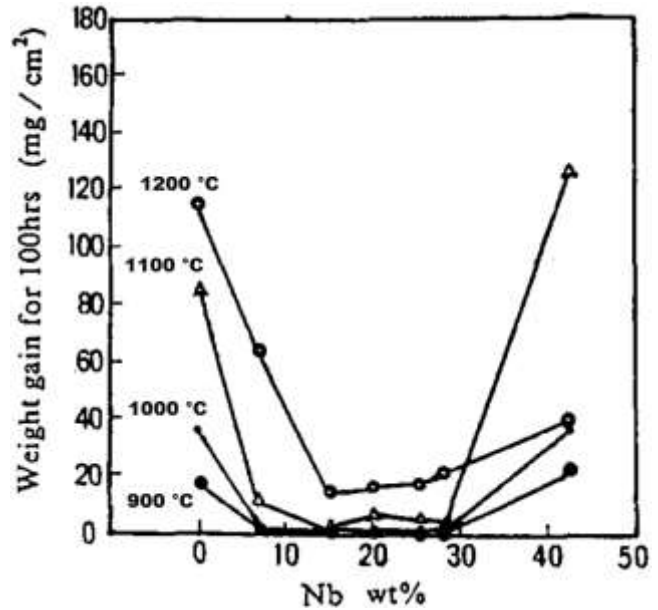


Figure 68: Effect of niobium content on the oxidation resistance of alloys (the Al content was constant: 36.5 wt.%) [111]

The influence of the alloy microstructure has been little studied. Nevertheless, Stroosnijder et al. [110] studied the isothermal and cyclic oxidation behavior at 800 °C of two  $\gamma$ -TiAl alloys. Ti-48Al-2Cr was obtained by vacuum melting and subsequent hot forging while Ti-48Al-2Cr-2Nb was obtained by HIPing of pre-alloyed gas atomized powder and subsequent hot forging. Different microstructures were obtained through heat treatments and the influence of microstructure on the oxidation behavior was highlighted.

Figure 69 shows the mass change of Ti-48Al-2Cr alloys with different microstructures during oxidation at 800 °C for 150 hours in air. Oxidation of the Ti-48Al-2Cr-2Nb alloy is also displayed to emphasize the beneficial effect of Nb addition. After an initial transient oxidation period, in which the oxidation kinetics are rather similar for both materials, the oxidation rate of Ti-48Al-2Cr increased significantly. The microstructure appeared to have a little effect. Only a slightly lower oxidation rate was measured in the case of the fully lamellar microstructure.

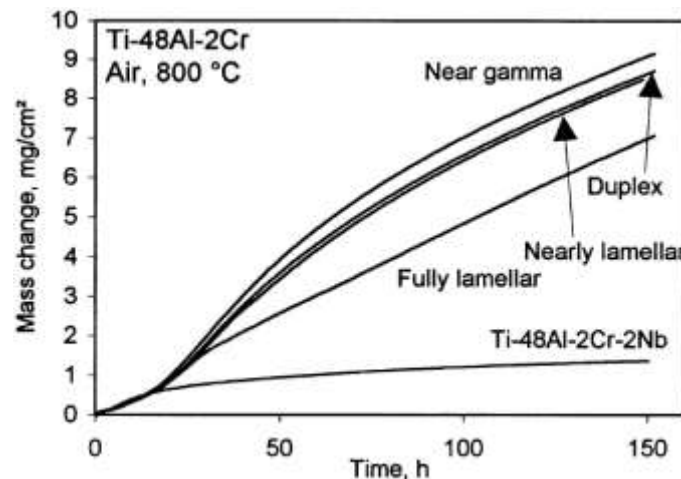
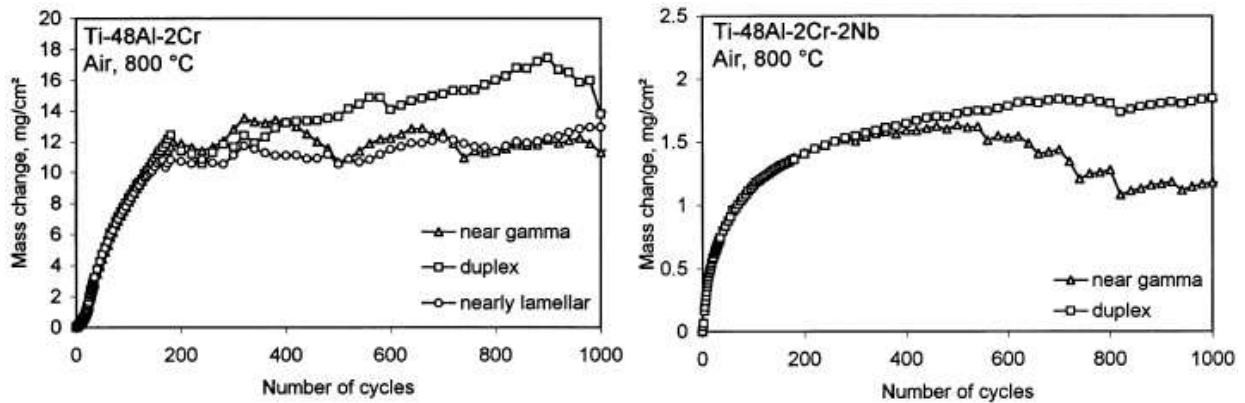


Figure 69: Mass change versus time for Ti-48Al-2Cr with different microstructures and near gamma Ti-48Al-2Cr-2Nb in air at 800 °C [110]



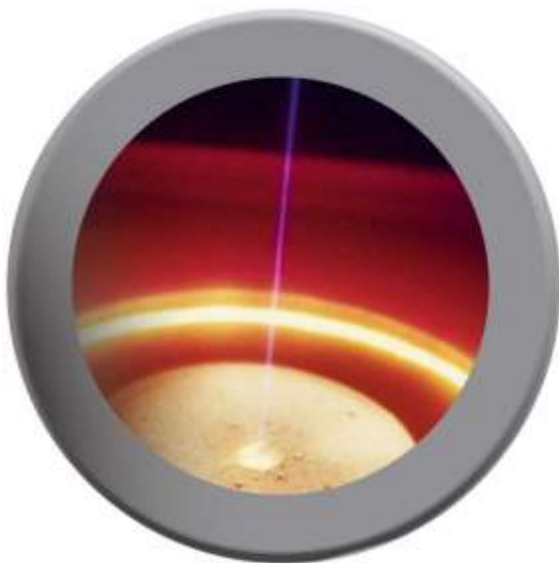
The effect of microstructure during cyclic oxidation between room temperature and 800 °C is shown figure 70. Each cycle consisted of a period of 1 h at 800°C and 12 min at ambient temperature. The specimens were inserted into and removed from the hot zone of the furnace within a few seconds to guarantee a rapid heating and cooling.



**Figure 70:** Mass change versus number of cycles for Ti-48Al-2Cr and Ti-48Al-2Cr-2Nb with different microstructures during cyclic oxidation in air between room temperature and 800 °C <sup>[110]</sup>

After a certain number of cycles, spallation of the oxide scale occurred. Again, when compared to Nb-free materials, Ti-48Al-2Cr-2Nb showed a better resistance to spallation. Spallation was observed only locally near sample edges over relatively large individual areas. The duplex and lamellar microstructures appeared slightly better regarding spallation than the equiaxed alloys. The study concluded that the investigated microstructures do not have an effect on the composition, structure and morphology of the corrosion scales as well as the growth rate.

**Part II**  
**The production of 3rd generation  $\gamma$ -TiAl alloys by  
Electron Beam Melting: fabrication,  
characterization and microstructure set-up**



Melting Pool, Arcam AB



$\gamma$ -TiAl  
Low Pressure Turbine  
Blade, Avio S.P.A

In this part, the development of 3<sup>rd</sup> generation  $\gamma$ -TiAl produced by the additive manufacturing process Electron Beam Melting is described. TiAl alloys are serious candidates to replace Ni-based superalloys in some structural parts of an aircraft gas turbine engine. At about half the density of superalloys and with similar specific properties, titanium aluminides are particularly attractive for low pressure turbine blades and vanes, and the last stages of the high pressure compressor. In the automotive industry, these light weight TiAl alloys showing good properties at high temperatures are particularly interesting to produce turbocharger turbines and vanes.

Always with the aim to increase the temperature capabilities and reduce the weight of critical components, TiAl alloys were intensively studied over the last 30 years [48, 50, 53-55, 58-60, 65-68, 70-74, 76, 77, 88, 110, 112-118]. Many research spotted the potential of these intermetallics and overcame the major drawbacks to applications. Attention was paid to increase the low ductility of these alloys and enhance the application possibilities to higher temperatures increasing creep and oxidation resistance. Also, the processing difficulties of such a material were dealt with.

Additive manufacturing, or building a part layer by layer, and in particular Electron Beam Melting emerged for about a decade as an outstanding manufacturing process [46, 47, 65, 66, 75, 84, 86, 119-125]. It offers many advantages for certain applications such as near net shape process which reduces material waste and post processing operations. It also allows the production of parts with a very complicated geometry.

## **I. The additive manufacturing process Electron Beam Melting (EBM)**

The idea of building parts layer by layer according to a computer assisted design (CAD) arose in the 1980's. It offered in particular the possibility to produce parts of almost any shape. For example, engineers could reconsider the designs to reduce weight or increase performances. It is particularly of interest in the aerospace and automotive industries. In addition, additive manufacturing processes often reduce time, cost and consequently the product development cycle. There are many different approaches to the production of parts through additive manufacturing [123].

The following figure 71 shows some of the most relevant and promising techniques.

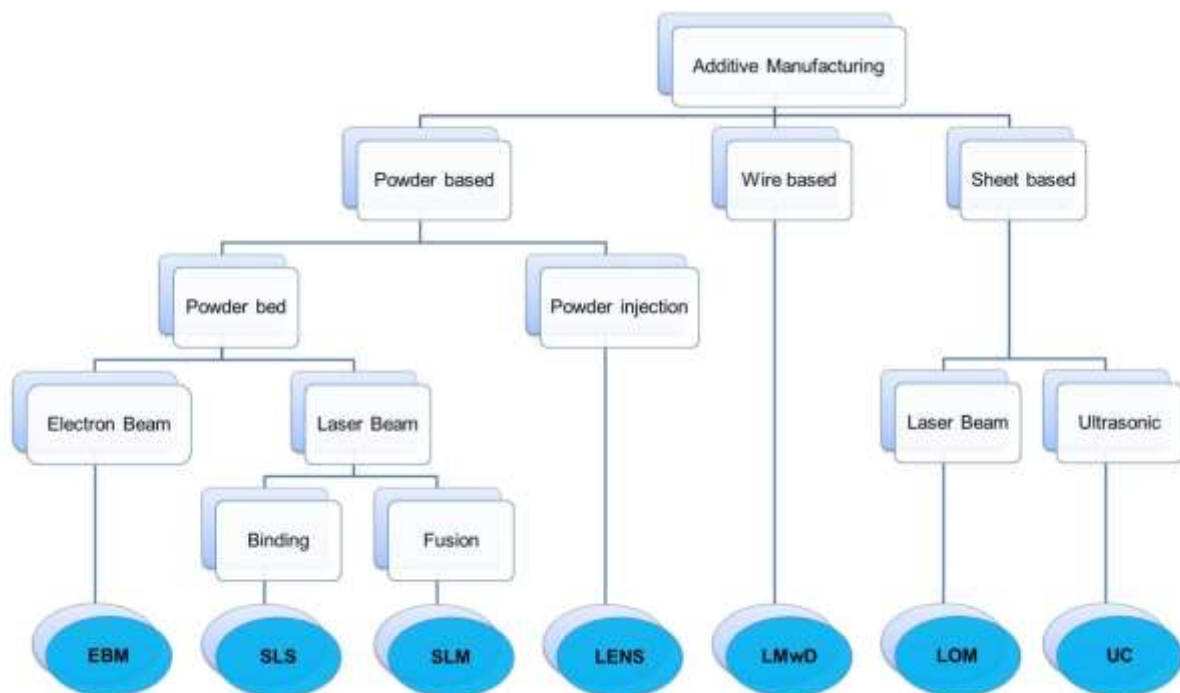


Figure 71: Additive Manufacturing processes

In figure 71, the different processes are classified according to the nature of the base material. The powder based techniques are very promising. The usually pre-alloyed powder can be either sprayed and melted by a gun or layer deposited and selectively melted according to CAD (figure 1). These techniques include notably Laminated Engineered Net Shaping (LENS), Selective Laser Sintering or Melting (SLS or SLM) and Electron Beam Melting (EBM).

Electron Beam Melting (EBM) has been developed by Arcam AB in Sweden and is commercially available since 2002. It was intended for building metal parts and in particular Ti-based alloys. It already proved to be a promising technique for the production of 2<sup>nd</sup> generation  $\gamma$ -TiAl alloys: Ti-(47–48)Al–2Cr–2Nb. Cormier et al. [47] were the first to describe some preliminary EBM fabrication of Ti–47Al–2Cr–2Nb followed by Murr et al. [84, 122] who showed the viability of the technique for the production of the same alloy. Biamino et al. [86] also published their results on Ti–48Al–2Cr–2Nb fabricated by EBM. The production of 2<sup>nd</sup> generation  $\gamma$ -TiAl alloys by Electron Beam Melting was the subject of the doctoral thesis of Andrea Penna realized between Politecnico di Torino (DISAT) and AvioProp, concluded in February 2013 [75].

Electron Beam Melting presents many advantages, listed below. Figure 72 shows the Arcam A2 machine, of which a schematic drawing and the data sheet are displayed figure 73 and table 20 respectively.

- Near-net-shape
- Complex design
- Good productivity
- Waste reduction
- Produce a fully dense material
- Vacuum melt process: low impurities
- Unique microstructure
- Low level of internal defects
- Freedom in chemical composition from pre-alloyed powder



Figure 72: Arcam A2 machine <sup>[119]</sup>

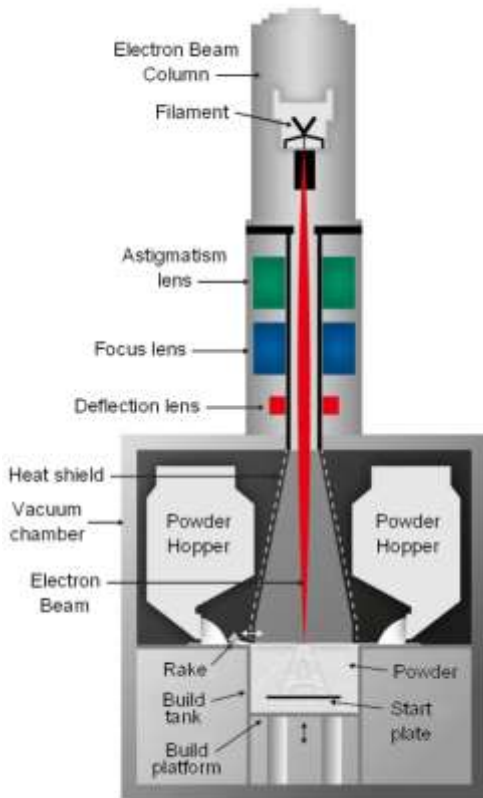


Figure 73: Schematic drawing of an Electron Beam Melting machine <sup>[120]</sup>

<b>Build tank volume (WxDxH)</b>	250x250x400 mm 350x350x250 mm
<b>Maximum build size (WxDxH)</b>	200x200x350 mm ∅300x200mm
<b>Model-to-Part accuracy long range (100 mm)</b>	± 0.20 mm
<b>Model-to-Part accuracy short range (10 mm)</b>	± 0.13 mm
<b>Surface finish (vertical/horizontal)</b>	Ra25/Ra35
<b>Typical powder size</b>	45 – 180 $\mu\text{m}$ (325 – 80 mesh)
<b>Beam power</b>	50-3500 W
<b>Beam spot size</b>	0.2 mm – 1.0 mm
<b>EB scan speed</b>	8000 $\text{m}\cdot\text{s}^{-1}$
<b>Layer thickness</b>	0.05 – 0.2 mm
<b>Build rate</b>	55/80 $\text{cm}^3\cdot\text{h}^{-1}$ (Ti6Al4V)
<b>N° of beam spots</b>	1 – 100
<b>Vacuum base pressure</b>	$\leq 10^{-2}$ Pa
<b>Size and weight (WxDxH)</b>	1850x900x2200 mm 1420 kg

Table 20: Technical data for the Arcam A2 machine <sup>[119]</sup>

A complete description along with videos of the process are available online on Arcam AB's website <sup>[120]</sup>. Basically, the principle is very similar to that of a scanning electron microscope <sup>[65, 66, 75, 86]</sup>. On top of the machine, a heated tungsten filament emits electrons which are collimated and accelerated to a kinetic energy of about 60 keV. The electron beam is controlled by magnetic coils. The first one is a magnetic lens which focuses the beam to the desired diameter, and the second one deflects the focused beam to the desired point on the building table. The electron beam gun itself is fixed; thus there are no moving mechanical parts involved in the beam deflection.

The beam current is controlled in the range 1–50mA and the beam diameter can be focused down to about 0.1mm. In order to increase the process productivity a new generation of multibeams apparatus have been recently developed thus allowing contemporary melting in different points of the chamber. In the chamber in the lower part of the machine, metal powder layers are formed by a raking mechanism. The powder is gravity fed from the hoppers and raked onto the building table. The typical layer thickness is in the range 0.05–0.2mm. Spherical or near-spherical powders with distributed particle sizes are more optimized for efficient flow, layer packing and melt uniformity.

The computer-controlled electron beam scans over the powder layer in a predefined pattern and consolidates the desired areas into solid and dense metal. The building platform is lowered, a new layer is created on top and the melting process is repeated. In this manner, the parts are built up layer-by-layer. The beam is initially scanning at high rate ( $\sim 10^4 \text{ mm.s}^{-1}$ ) and medium beam current ( $\sim 30 \text{ mA}$ , or up to 50 mA to reduce time) in multiple passes to preheat the powder up to 80 % of the actual melting temperature. For the actual melt, the beam scan rate and current are reduced ( $\sim 10^2 \text{ mm.s}^{-1}$  and 5 – 21 mA).

The whole process takes place under high vacuum. The typical pressure of residual gases in an Arcam EBM machine are  $\sim 10^{-2} \text{ Pa}$  in the vacuum chamber and  $10^{-4} \text{ Pa}$  in the electron gun. During the melting process, a small pressure of inert helium gas ( $10^{-2} \text{ Pa}$ ) is added to the vacuum chamber to avoid build-up of electrical charge in the powder, enhance heat conduction and component cooling. When all layers have been melted, the built parts are allowed to cool inside the process chamber filled up with helium gas to speed up the cooling.

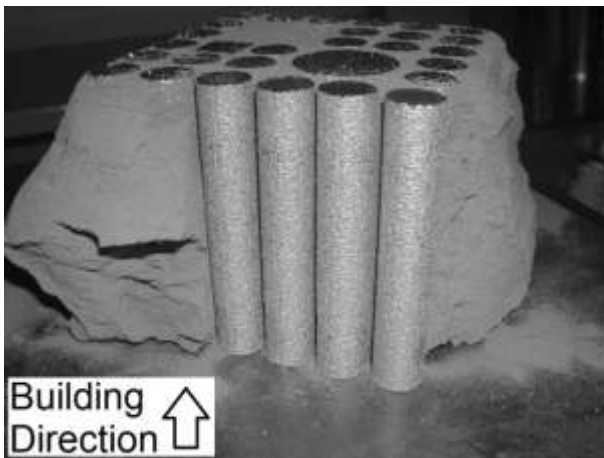


**Figure 74:** As-built specimens in the EBM chamber surrounded by un-sintered powder [65]

When the parts are taken out from the EBM machine, they are surrounded by a shell of softly agglomerated metal powder. Figure 74 shows an example of as-built specimens in the EBM chamber, where the un-sintered powder around the specimens can be seen. The specimens are then taken out of the powder bed and the powder can easily be disintegrated, sieved, and inserted again in the EBM machine to be reused in the next build. All powder that is not melted by the electron beam is recycled thanks to very low oxygen pick-up per build. Therefore, material waste is kept to minimum.

Avio prop, where the fabrication of 3<sup>rd</sup> generation TiAl alloys by EBM under investigation in this work was realized, owns both the A2 and A2X machines. The A2X machine is an alternative configuration that is more suitable for processing high temperature materials. In the following, the optimization of the process parameters are describe for the machine in the A2X configuration.

## II. Characterization of the base material: High Nb containing pre-alloyed powders

The base powder is an important factor to account in order to obtain a finished product of good quality. Following the successful production of 2<sup>nd</sup> generation  $\gamma$ -TiAl alloy by Electron Beam Melting [75, 86], the supplier was again ATI Metals Powder.

### 1. Chemical composition

The starting materials were gas atomized rapidly solidified  $\gamma$ -TiAl pre-alloyed powders. The target composition of the processed materials should have an aluminum content of 45-46 at.%, chromium content of 2 at.% and a high niobium content of 8 at.%. Due to the high temperature of the process and the vacuum environment, an evaporation of light weight elements was observed during the EBM [47, 65, 66, 75, 86]. This issue is detailed later when the actual fabrication of Ti-(45-46)Al-2Cr-8Nb by EBM is described (section III.2.A.a). However, it is worth noticing here that the aluminum loss is constant for identical processes, and for high niobium containing alloys was equal to 2 wt.%. The same behavior was noticed by Biamino et al. for EBM of Ti-48Al-2Cr-2Nb where a constant loss of 1 wt.% of Al was observed [75, 86].

Therefore, the chemical composition of the base powder might be adjusted to overcome the aluminum loss during the process. Two different powders have been used with a nominal composition of Ti-47Al-2Cr-8Nb and Ti-48Al-2Cr-8Nb (in at.%). The following table 21 and table 22 show the actual composition of the powder as-received. The composition was evaluated by Inductively Coupled Plasma (ICP) for aluminum, chromium and niobium, while oxygen was measured with a LECO instrument. Measures were realized by the certified organization Incotest. The at.% was calculated from wt.% and neglecting oxygen.

	Al	Cr	Nb	O	Ti
Powder as-received	Chemical composition in wt%				
	30.6	2.3	17.2	0.08	Bal.
	Chemical composition in at%				
	47.1	1.9	7.7		Bal.

**Table 21:** Actual chemical composition of Ti-47Al-2Cr-8Nb as-received powder measured by ICP and LECO instrument

	Al	Cr	Nb	O	Ti
Powder as-received	Chemical composition in wt%				
	31.3	2.2	17.2	0.04	Bal.
	Chemical composition in at%				
	48.0	1.7	7.7		Bal.

**Table 22:** Actual chemical composition of Ti-48Al-2Cr-8Nb as-received powder measured by ICP and LECO instrument

The actual compositions measured by ICP and LECO of the as-received powder were very similar the theoretical compositions. In addition, the impurities pick-up during the gas atomization process was very low ( $\leq 0.1$  wt.% for oxygen, which is a significant source of defects for TiAl alloys [48, 87, 126]).

## 2. Particle size distribution

A proper particle size distribution gives a higher packing density. Table 23 gives the particle size distributions of the Ti-(47-48)Al-2Cr-8Nb powders. The particle size distribution of the Ti-48Al-2Cr-2Nb powder used for the production of the 2<sup>nd</sup> generation  $\gamma$ -TiAl alloy by EBM is also displayed [75, 86]. Measurements were realized according to the ASTM standard B214-07. A minimum of three measurements were realized for each powder.

Diameter [ $\mu\text{m}$ ]	Particle size distribution (%)		
	Ti-48Al-2Cr-2Nb [75]	Ti-47Al-2Cr-8Nb	Ti-48Al-2Cr-8Nb
45	8	4.3	4.4
53	10.3	8.3	9
63	13.5	14.4	16.5
75	30.7	33	32.5
106	35	38.4	35.4
150	0.8	0.8	1.3

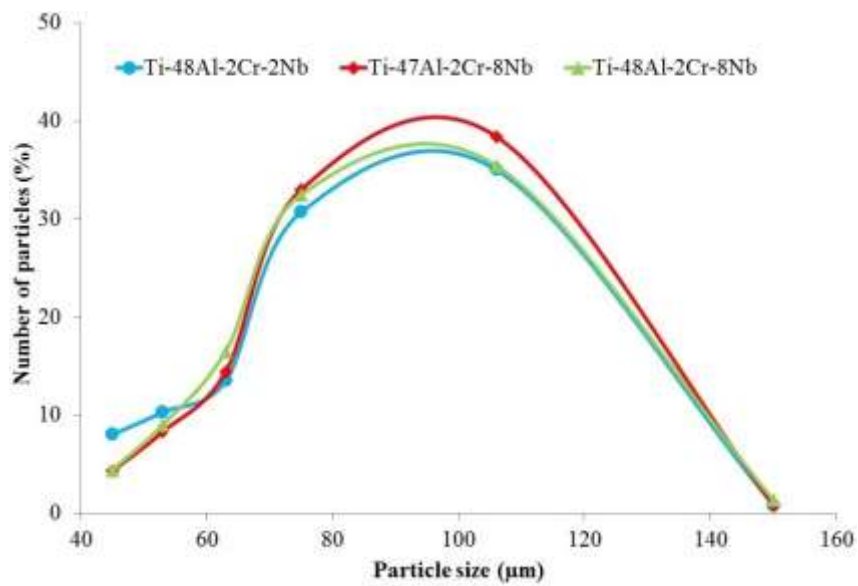


**Table 23:** Particle size distribution of Ti-48Al-2Cr-2Nb, Ti-47Al-2Cr-8Nb and Ti-48Al-2Cr-8Nb powders

The powders had a nominal particle size distribution between 45 and 150  $\mu\text{m}$  (-100/+325 mesh). One can note the rather wide range of mesh size of the base powders. Almost 40 % of the powder has an average diameter  $\geq 106 \mu\text{m}$ . It corresponds to a rather coarse grain size for powder metallurgy based process.

Both high Nb containing powders exhibit a particle size distribution very similar to that of Ti-48Al-2Cr-2Nb which led to the successful production of massive materials by EBM [75, 86]. The overall particle size of high Nb containing powders were slightly higher than that of Ti-48Al-2Cr-2Nb though. It reduced even more the restrictions on the base material.



### 3. Morphology

The aspect of Ti-(47-48)Al-2Cr-8Nb powders was observed by scanning electron microscopy (SEM). The SEM micrographs at magnifications x200 and x1000 are shown figure 75.

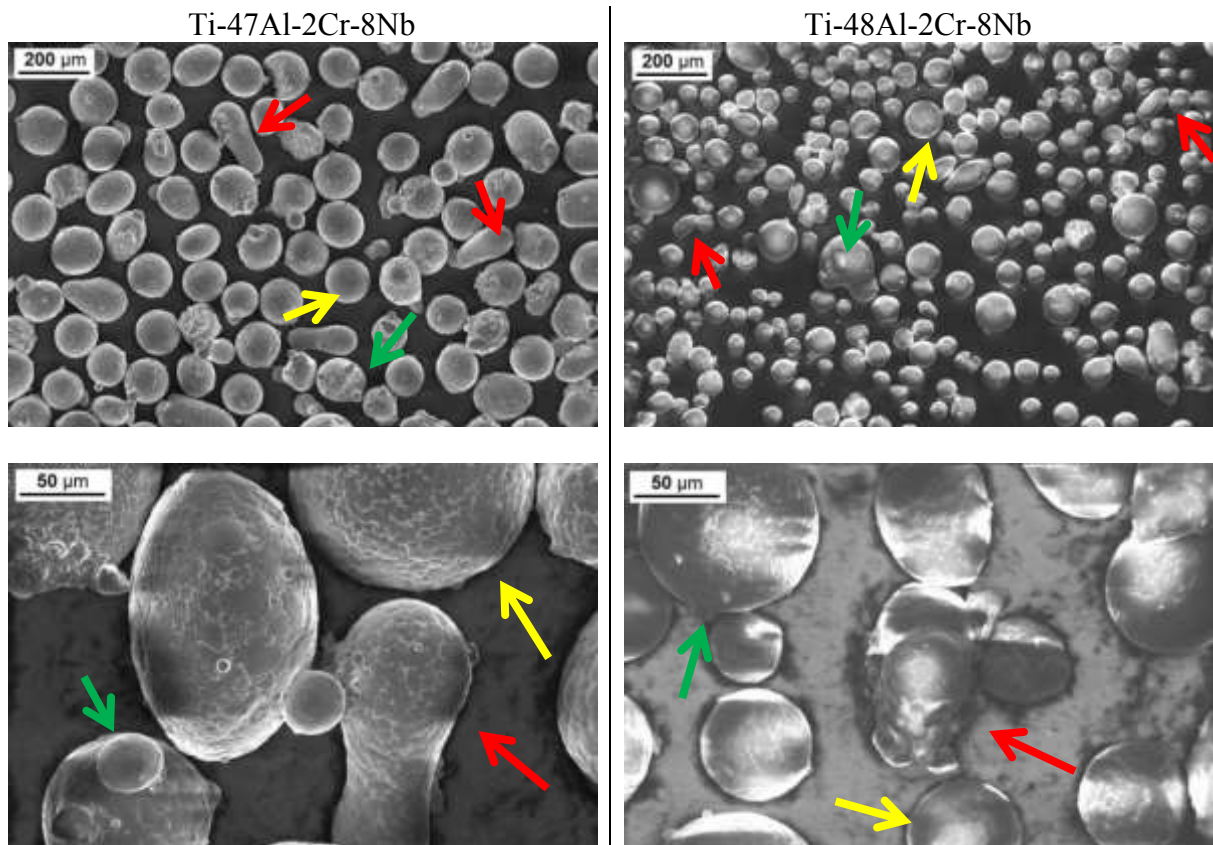


**Figure 75:** SEM micrographs of powders Ti-47Al-2Cr-8Nb and Ti-48Al-2Cr-8Nb as-received

The powders show some irregularities. A number of elongated particles or with an irregular shape could be seen (red arrows in figure 75). Also small particles agglomerated to bigger ones (green arrows in figure 75). However, most of the particles are spherical and regular (yellow arrows in figure 75) and the irregularities observed in the powders were not a problem for the EBM process. Ti-48Al-2Cr-2Nb powder presented a similar morphology with some non-spherical and agglomerated particles <sup>[75, 86]</sup>.

## 4. Flowability

The flowability of both high Nb containing powders have been measured according to ASTM B213-03. Table 24 shows the actual values of flowability measured in DISAT along with that of the Ti-48Al-2Cr-2Nb powder.

Powder as-received	Flowability (s)
Ti-48Al-2Cr-2Nb <sup>[75]</sup>	26 ± 1 s
Ti-47Al-2Cr-8Nb	29 ± 1 s
Ti-48Al-2Cr-8Nb	27 ± 1 s

**Table 24:** Flowability of Ti-48Al-2Cr-2Nb, Ti-47Al-2Cr-8Nb and Ti-48Al-2Cr-8Nb according to standard ASTM B213-03

The flowability of the Ti-(47-48)Al-2Cr-8Nb powders was similar to that of Ti-48Al-2Cr-2Nb used for the production of the 2<sup>nd</sup> generation  $\gamma$ -TiAl alloy by EBM <sup>[75]</sup>. The flowability is critical to insure a good layer deposition by the raking system.

## 5. Apparent density

The apparent density of Ti-(47-48)Al-2Cr-8Nb powders were measured according to ASTM B212-99. Table 25 shows the actual values of apparent density along with that of the Ti-48Al-2Cr-2Nb powder.

Powder as-received	Apparent density (g.cm <sup>-3</sup> )
Ti-48Al-2Cr-2Nb <sup>[75]</sup>	2.25 ± 0.15
Ti-47Al-2Cr-8Nb	2.31 ± 0.23
Ti-48Al-2Cr-8Nb	2.31 ± 0.21

**Table 25:** Apparent density of Ti-48Al-2Cr-2Nb, Ti-47Al-2Cr-8Nb and Ti-48Al-2Cr-8Nb according to standard ASTM B212-99

The apparent density of the high Nb containing powders was similar to that of Ti-48Al-2Cr-2Nb powder used for the production of the 2<sup>nd</sup> generation  $\gamma$ -TiAl alloy by EBM <sup>[75]</sup>.

Powder metallurgy processes such as SLM or EBM involve a controlled and accurate layer deposition, and a selective melting of the powder. Zhu et al. <sup>[127]</sup> reported the influence of powder apparent density on the actual density of the parts in direct laser sintering (DLS). It was concluded that the higher the powder apparent density, the higher the density in the part. The apparent density of the powder system is determined by the powder particles shape, size and distribution.

Zhu et al. <sup>[127]</sup> stated that generally packing of spheres leads to a higher density than other shapes, and added that the greater the surface roughness or the more irregular the particle shape, the lower the packing density. Ideally, the powder particles should be perfectly spherical with a low surface roughness. Also, a higher relative density can especially be achieved by mixing different sizes of powder. In the case of spherical powder particles, the idea is to fill up interstitial voids between big particles by smaller ones. The following figure 76 shows the principle.

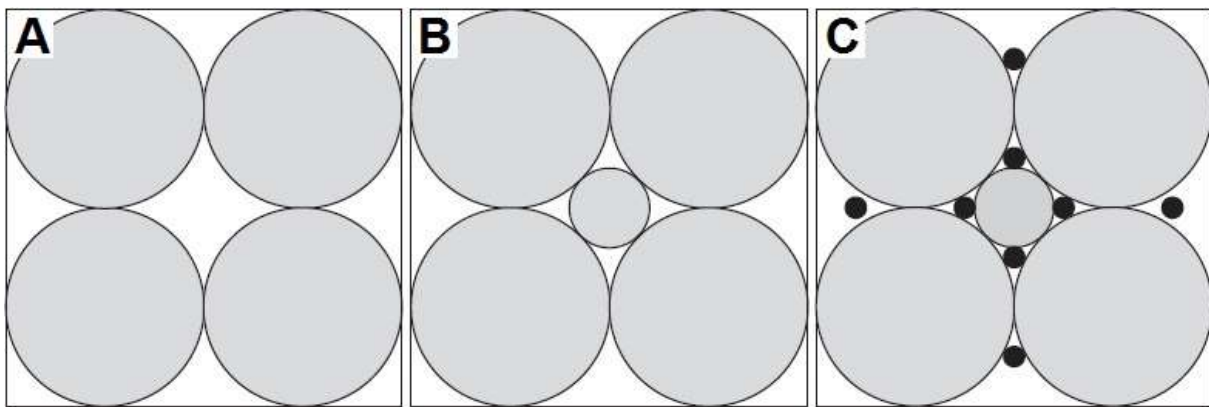


**Figure 76:** Schematic drawing of the effect of powder particles size on the apparent density: Monosized (A), Bimodal (B) and Trimodal (C) <sup>[127]</sup>

Both Ti-47Al-2Cr-8Nb and Ti-48Al-2Cr-8Nb powders were therefore found suitable for the production of dense parts by Electron Beam Melting.

### **III. Fabrication of Ti-(45-46)Al-2Cr-8Nb samples by EBM**

The successful production of the 2<sup>nd</sup> generation Ti-48Al-2Cr-2Nb alloy by EBM led to optimism <sup>[75, 86]</sup>, but 3<sup>rd</sup> generation  $\gamma$ -TiAl alloys contain a significantly higher amount of refractory elements (here 8 at.% of niobium). The feasibility of the production of 3<sup>rd</sup> generation  $\gamma$ -TiAl by electron beam melting was therefore initially investigated. An optimal set of parameters have to be found to produce a material that is dense, homogeneous and reliable. The optimization of EBM parameters was realized with Ti-47Al-2Cr-8Nb powder. The melting strategy used for the successful production of the 2<sup>nd</sup> generation Ti-48Al-2Cr-2Nb was the starting point. Cylindrical shape samples ( $\varnothing \approx 15$  mm and  $h \approx 150$  mm) were initially produced (see figure 78A).

Several sets of parameters have been tested in order to obtain a suitable material after EBM. As many as 20 parameters could be varied to lead to a valid building. The external roughness was checked by direct observation right after the fabrication of the samples, so were the open porosity, the design to part accuracy and the homogeneity inside the chamber.

A number of parameters of a typical EBM run control sheet are listed below:

- Layer thickness ( $\mu m$ )
- Average current ( $mA$ )
- Surface temperature ( $^{\circ}C$ )
- Number of Contours
- Contour order
- Wafer current ( $mA$ )
- Wafer speed ( $mm.s^{-1}$ )
- Wafer spot time ( $ms$ )
- Outer Contour number of spots
- Outer Contour spot time ( $ms$ )
- Inner Contour number of spots
- Inner Contour offset ( $mm$ )
- Inner Contour current ( $mA$ )
- Inner Contour spot time ( $ms$ )
- Hatch offset to Contour ( $mm$ )
- Hatch max current ( $mA$ )
- Hatch focus offset ( $mA$ )
- Hatch speed function
- Hatch line offset ( $mm$ )
- Hatch depth ( $mm$ )

Among all the process parameters, the above list is not exhaustive, some were particularly effective. First of all, the building path strategy was very important and was one of the critical parameters. Four different approaches were studied (figure 77).

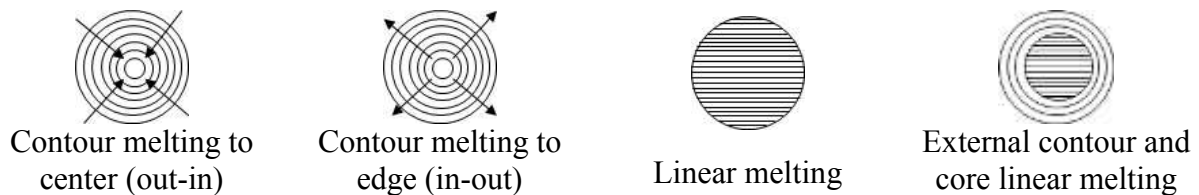


**Figure 77:** Building path strategies for the electron beam melting of 3<sup>rd</sup> generation  $\gamma$ -TiAl

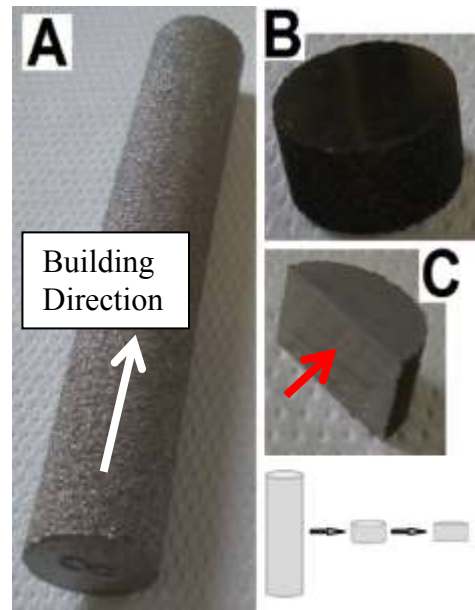
The average current beam was also crucial since it determined the actual powder melting temperature. Its value was typically varied from 20 to 30 mA. The layer deposition thickness was also critical. Obviously, the thicker the layer deposition the shorter the processing time. However, a layer thickness too high impeded a consistent melting. The layer thickness was varied from 200 down to 90  $\mu m$ . Finally, the scanning speed was another critical parameter.

The actual EBM conditions could not be detailed in this paper. The core of the present thesis consisted in the evaluation of residual defects of the as-EBM massive materials and the subsequent microstructure set up by heat treatment. In the following, the main steps of optimization of the EBM parameters are described. The optimization was divided into five major trials. Each trial or attempt was defined by a significant modification of one or more of the main parameters described earlier. Minor modifications of other parameters were also done. In fact, many tests with minor modifications of parameters were realized among the trials, based on the state of the as-built parts.

## 1. The measure of residual porosity to optimize the EBM process

The strategy to optimize the EBM parameters was the minimization of residual porosity, i.e. the porosity of the massive sample as-EBM. A residual porosity lower than 1 % is recommended but the scope was to produce a material as dense as possible.

Porosity was quantified according to the ASTM E2109-01 standard. Small samples of 10 mm height were cut from an as-built bar. These small specimens were subsequently cut along the cross section in order to observe the internal structure from the core to the edge of the cylindrical sample. The cuts were represented schematically in the right lower part of figure 78. The cross section allowed the analysis of the porosity along the building direction (the sample bars are built from bottom to top, white arrow in figure 78A). In figure 78C, the red arrow points the face observed for porosity analysis. In order to have a clean flat surface allowing the observation by optical microscopy, the specimens were ground with abrasive papers gradually from grit 600 to 4000. In addition, to ensure a scratch free surface, additional polishing with cloths and abrasive diamond pastes of 6 and 3  $\mu\text{m}$  was done. This allowed to obtain a highly reflective mirror-like surface, which thus appear uniformly white from optical microscopy. Samples were big enough to be polished without being cold mounted into epoxy resin although it was often preferred.

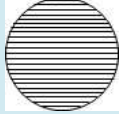


**Figure 78:** Photography of a bar as-built by EBM (A), a cylindrical sample of about 10 mm height (B) and a sample for microscopic observation and porosity investigation (C)

The diameter of the as-built bars were approximately 15 mm so that the surface area for porosity analysis was about  $15 \times 10 \text{ mm}^2$ . A total of 12 optical micrographs, equally distributed to cover the all surface, were systematically taken at magnification x50. The sample surface on a single image appeared completely white (reflecting the white light of the optical microscope) and pores were easily identified as black zones (the light was not reflected, since it was a “hole” on the surface). The image processing software Image Pro<sup>®</sup> Plus was used to quantify the porosity, simply counting the ratio of black on white thus giving the proportion of pores in the single image. For statistical purpose, the total residual porosity of a sample was obtained averaging the “local” porosity of each one of the 12 images. Finally, samples were taken in different locations of a single as-built bar, and from bars in different locations in the building chamber. It ensured a fair statistical measure of the porosity and homogeneity throughout the massive specimens. The optimization of the EBM process was published in Steel Research Int <sup>[65]</sup>.

### A. First trial

The first attempt was simply adapted from the successful production of 2<sup>nd</sup> generation  $\gamma$ -TiAl alloys by Biamino et al. [75, 86]. Minor modifications of the process parameters were done based on the macroscopic observation of the as-built parts by the operator. The following table details the actual building path strategy, the layer thickness and the principal component of the trial.

Comment on the 1 <sup>st</sup> Trial	Layer thickness	Building path strategy
Based on EBM production of Ti-48Al-2Cr-2Nb	180 $\mu\text{m}$	 Linear

The porosity was measured and was about  $2.68 \pm 1.05$  %. A representative optical micrograph is displayed figure 79. The actual porosity in figure 79 is 3.63 %.

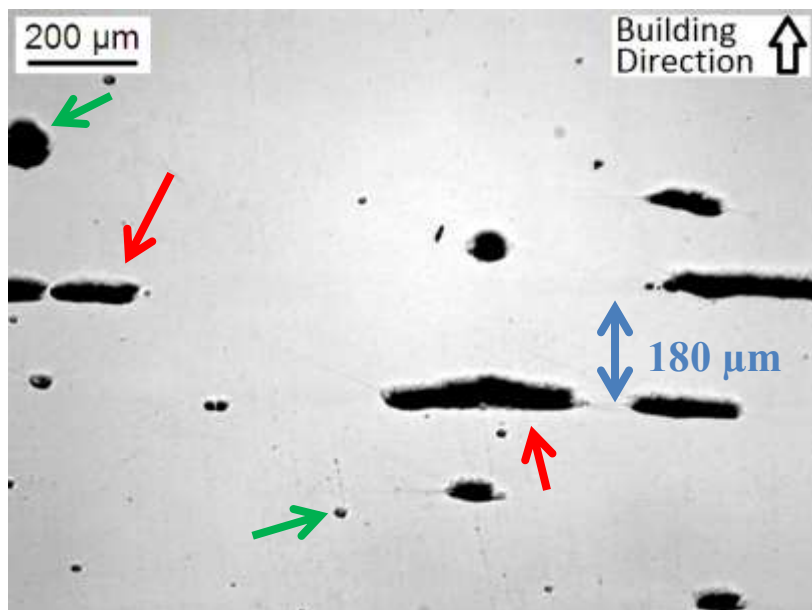


**Figure 79:** Optical micrograph showing the porosity of TiAl-2Cr-8Nb after the first EBM trial

Two types of pores could be identified. First big elongated pores were observed, highlighted by red arrows in figure 79. This porosity was a result of the EBM processing. On the one hand, a number of these pores had a size, or rather a length, greater than 200  $\mu\text{m}$ . Therefore, such pores could not result from the powder itself, since the maximum particle size was 180  $\mu\text{m}$ . On the other hand, these pores were almost always aligned along the layer deposition direction, and separated by about 180  $\mu\text{m}$  (figure 79) which was the actual layer thickness. Thus, this led to conclusion that these big elongated pores resulted from either a poor local melting of the powder or defects from the powder deposition by the raking system. These pores were found randomly over the whole volume of the as-built bar. A poor local melting would be expected more regularly which drives to lean towards a problem in the layer deposition.

Finally, the shape itself of these pores told it all. They were elongated along the layer deposition direction, most likely at layers interface, and seemed consistent to the underlying layer. It is believe that the powder was not uniformly deposited onto the previously melted layer.

The second type of pores were round shaped, pointed by green arrows in figure 79. This kind of pores resulted from residual porosity in the powder itself [48, 50, 65, 75, 84-86]. During the gas atomization process, argon was trapped and created argon bubbles imprisoned inside a number of particles. It explains the spherical shape. Furthermore no round shaped pores bigger than 180  $\mu\text{m}$ , the maximum particle size, was ever found. Figure 20 shows cavities inside a number of particles of Ti-48Al-2Cr-2Nb [75] highlighted by red arrows.

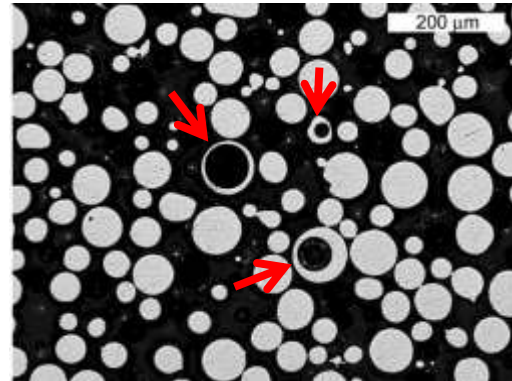


Figure 80: Micrograph showing cavities inside particles from argon bubbles trapped during the atomization process [75]

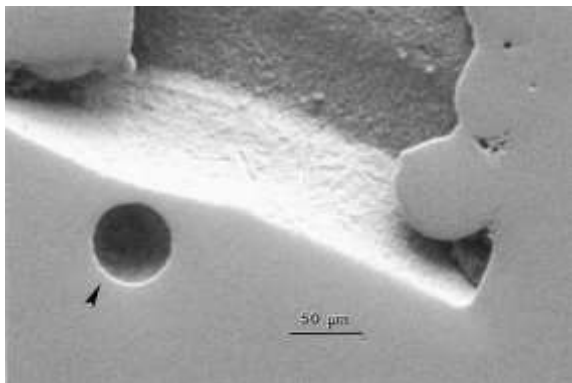



Figure 81: SEM micrograph showing residual porosity and a residual Ar bubble section at arrow [84]

Murr et al. [84] characterized 2<sup>nd</sup> generation  $\gamma$ -TiAl components fabricated by electron beam melting. The same kind of dual porosity was found. The round pore pointed by the arrow in figure 81 was attributed to argon gas content. On the other hand, the unconsolidated and unmetled regions were the result of non-optimized building conditions.

### B. Second trial

In the second trial, the scanning speed was decreased and the layer thickness was reduced compared to the previous tests. The modification of these parameters was believed to lead to a better melting and reduced or cancel process porosity. In this configuration, the other process parameters listed previously were slightly modified and a number of runs were needed.

Comment on the 2 <sup>nd</sup> Trial	Layer thickness	Building path strategy
Melting scanning speed reduced	150 $\mu\text{m}$	 Linear

The porosity was measured and was about  $1.1 \pm 0.5$  %. A representative optical micrograph is displayed figure 82. The actual porosity in figure 82 is 2.06 %.

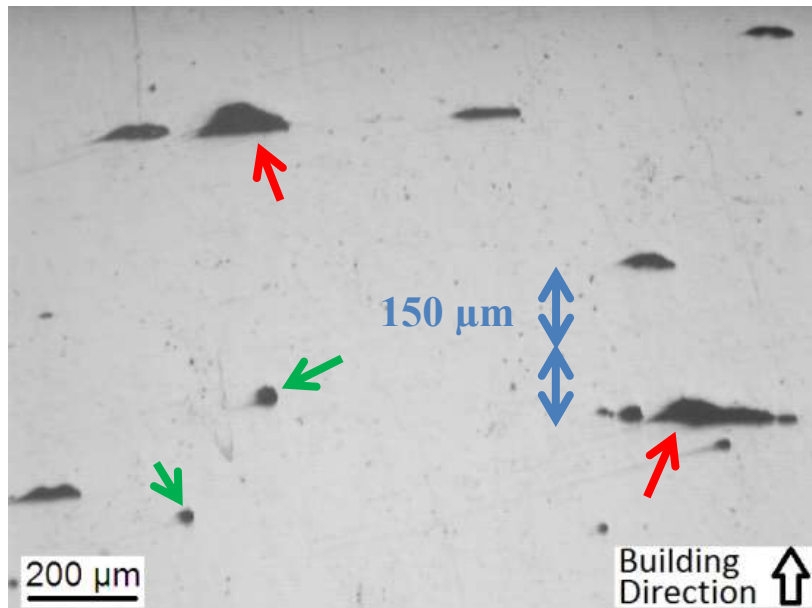



**Figure 82:** Optical micrograph showing the dual porosity of an as-built sample after the first optimization

The residual porosity was reduced in this second attempt, although higher than 1 %. It was still observed both powder and process porosity. The bigger defects had a size  $\geq 200$   $\mu\text{m}$ . Examples of porosity from powder defects are pointed by green arrows in figure 82. At layers interface, the elongated pores were still present with the same semicircular shape (red arrows in figure 82).

### C. Third trial

In the third attempt, the layer thickness was further reduced and minor modifications were made. Also, the building path strategy was changed to 4 circular contour melting and linear core melting. The reason for changing the strategy was to reduce external porosity and substantial roughness. Contour melting produced bars more regular and the macroscopic aspect was better. However, higher aluminum loss was found at the edge where the melting was circular. This point will be discussed in more details later (section II.2.A.b). The chemical composition and consequently the microstructure after heat treatment were very different between the core and the edge of the sample. However, the external part of the as-built material was anyway destined to be removed post processing to reduce the external roughness and insure material's homogeneity.

Comment on the 3 <sup>rd</sup> Trial	Layer thickness	Building path strategy
Building path strategy modified	120 $\mu\text{m}$	 4 circular contours and linear core
Layer thickness reduced		



The residual porosity in these conditions was very low:  $0.1 \pm 0.1$  %. A representative optical micrograph is displayed figure 83. The actual porosity in figure 83 is 0.03 %. Pores from the powder was the only source of porosity in the material. The densification was complete by the EBM process and this set of parameters were, regarding the residual porosity, optimal.

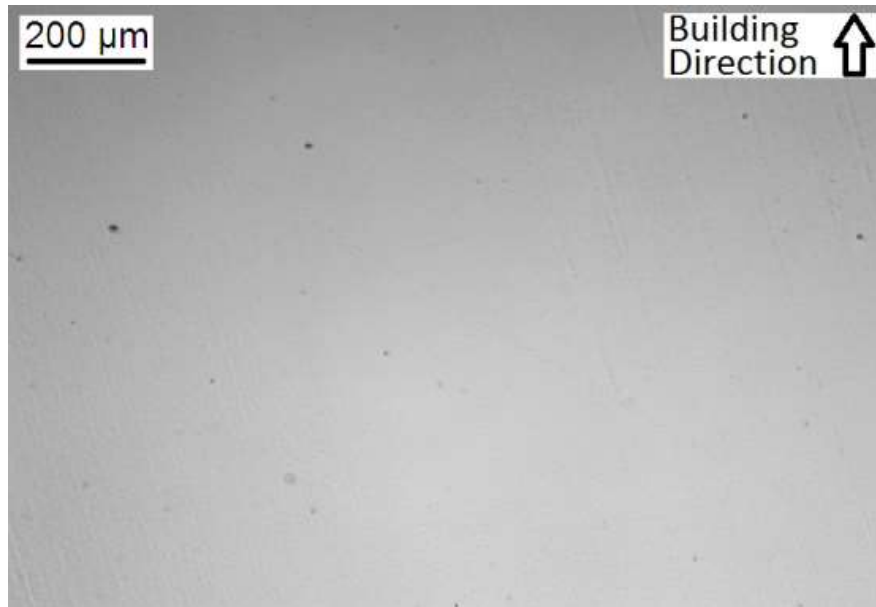


**Figure 83:** Optical micrograph showing only the porosity resulting from powder defects of an as-built sample after the 3<sup>rd</sup> trial


A number of pores were quite big. Figure 84 shows the bigger defects observed in the sample set. Such pores could be a source of cracks. However, the spherical shape limits substantially the effect compared to notch defects. In addition, defects smaller than 100 μm are considered acceptable for  $\gamma$ -TiAl, although the smaller the better<sup>[75]</sup>.

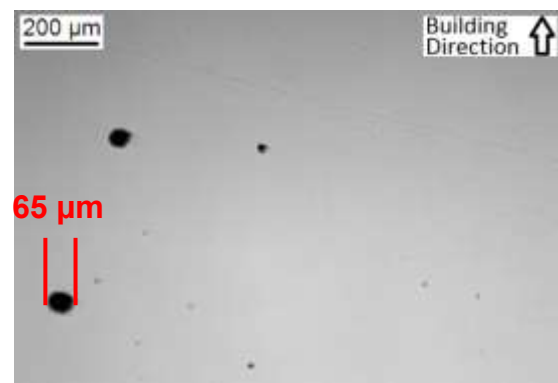


**Figure 84:** Optical micrograph showing the biggest pores in the as-built sample resulting from powder defects

#### D. Fourth trial

In the fourth attempt, the building path strategy was changed. As mentioned previously, the external contour presented a substantial difference in term of chemical composition with regards to the core of the sample. In this building, the contour melting was thus reduced to only one. It was expected a consistent material with a reduced external porosity and roughness and having very low residual porosity.

Comment on the 4 <sup>th</sup> Trial	Layer thickness	Building path strategy
Contour melting reduced	120 $\mu\text{m}$	 1 circular contour and linear core

The residual porosity in these conditions was very low again:  $0.08 \pm 0.09 \%$ . The micrograph figure 85 shows the biggest pores observed in the sample set. The actual porosity in figure 85 is 1 %. Again, porosity from the powder was the only source of cavities in the material. In figure 85 though, the biggest pore has a diameter about 130  $\mu\text{m}$  which is rather big. Given the particle size distribution of the powder, the probability of finding such pores is very low. Plus, from the EBM point of view, nothing can be done about that.

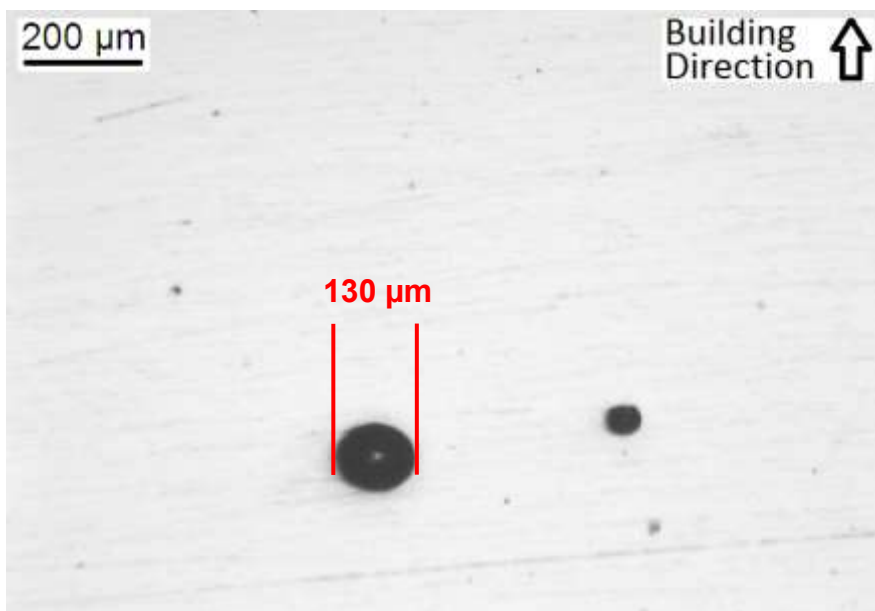



**Figure 85:** Optical micrograph showing the biggest pores resulting from powder defects of after the 4<sup>th</sup> trial

However, these conditions were not selected. With respect to the previous trial, the productivity was lower. Plus, Thermo Mechanical Analysis (TMA) exhibited what was concluded an inhomogeneous behavior in the microstructure. This question will be discussed later (section III.2.D.d). TMA was used in this study to determine the phase transition temperatures and to assess the homogeneity of the microstructure.

### **E. Fifth trial**

The set of EBM parameters were chosen from the optimization described previously and the fifth trial turned out optimal. The EBM fabrication of bar samples was realized from both starting powders Ti-47Al-2Cr-8Nb and Ti-48Al-2Cr-8Nb in the same conditions. The layer thickness was further decreased down to 90  $\mu\text{m}$  and the building path strategy comprised only 3 circular contour melting.

<b>Comment on the 5<sup>th</sup> Trial</b>	<b>Layer thickness</b>	<b>Building path strategy</b>
<b>Building path strategy modified</b>	90 $\mu\text{m}$	
<b>Layer thickness reduced</b>		
<b>Residual porosity after EBM <math>\leq 1</math> %</b>		

Basically, the residual porosity came from the powder porosity only, as defined previously. No sign of unmelted or unconsolidated zones was ever observed, which suggested the complete densification by EBM. Therefore, it can safely be concluded that no pore bigger than 150  $\mu\text{m}$  can be found in the sample. Furthermore, given the particle size distribution and the improbability of finding a pore almost as big as the particle itself, most of the residual porosity was smaller than 120  $\mu\text{m}$ .

The residual porosity in the as-built samples from the Ti-47Al-2Cr-8Nb powder by EBM in these conditions was very low:  $0.08 \pm 0.13$ . The starting powder Ti-48Al-2Cr-8Nb appeared more porous than the Ti-47Al-2Cr-8Nb powder. The average residual porosity after EBM of Ti-48Al-2Cr-8Nb powder was  $0.28 \pm 0.32$  %. Actually, samples presenting the highest porosity were found at the bottom of the selected bars, and one sample even exhibited  $0.99 \pm 0.5$  % residual porosity. It was unexpected and the actual reason could only be assessed. This could result from a higher powder porosity itself, but it did not explain why samples at the bottom of the as-built bars were more porous. This porosity could really be process porosity at the beginning of the process, but the same phenomenon was not observed with Ti-47Al-2Cr-8Nb powder. It is possible that at a certain point, the powder porosity was reduced by the EBM process itself during melting. Finally, the higher content of Al in Ti-48Al-2Cr-8Nb powder could be responsible. However, the aluminum evaporation that will be discussed in the next section was constant (2 wt.%) regardless the starting powder (section III.2.A.a).

In any case, the residual porosity measured in different points of different bars was below the acceptable value of 1 %, and except the particular situation described previously, porosity was well below this limit value. In addition, the biggest defect ever found had a diameter of 130  $\mu\text{m}$  (figure 85) which could be detrimental as a cracking source. Nevertheless, such pores are very rare and spherical (no notch effect).

The micrograph in figure 86 exhibits the typical porosity of as-built samples from the starting powder Ti-48Al-2Cr-8Nb taken at least a centimeter away from the bottom of the bar. The actual porosity in figure 86 is 0.13 %. On the other hand, figure 87 shows the higher porosity of a sample from the same powder at the bottom of a bar. The micrograph was selected to highlight the high porosity and not all samples looked that bad. The actual porosity in figure 87 is 0.86 %



**Figure 86:** Micrograph showing the typical porosity in as-built sample from powder Ti-48Al-2Cr-8Nb

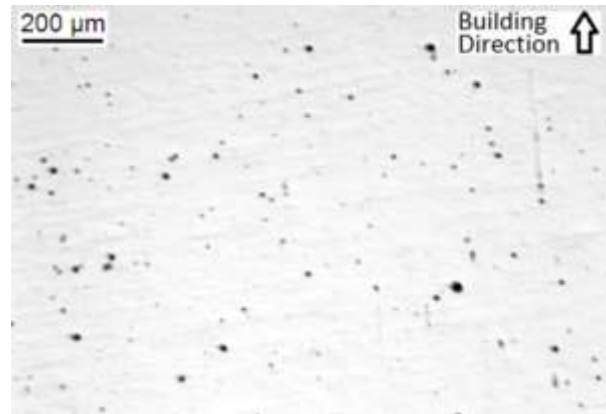


**Figure 87:** Micrograph showing the high porosity at the bottom of bars in as-built sample from powder Ti-48Al-2Cr-8Nb

From the porosity point of view, the EBM process was very valuable leading to massive samples with very low residual porosity  $\leq 1$  %, maximum defects size of 130 μm anyway very rare, and consistent geometry very close to the original design.

## 2. Characterization of the massive samples

In order to validate the process, the chemical composition was analyzed in different points of a single as-built bar (green arrows in figure 88), in different bars from the same building (red arrows in figure 88) and from different building sessions <sup>[65]</sup>.

The chemical composition was evaluated by Inductively Coupled Plasma (ICP) for aluminum, chromium and niobium, while oxygen was measured with a LECO instrument. For Al, Cr and Nb, 5g samples ( $10 \times 10 \times 14$  mm<sup>3</sup>) were taken from the core of the as-built bars. For oxygen instead, 2-3g samples ( $9 \times 9 \times 9$  mm<sup>3</sup>) were prepared. The measures were performed by IncoTest.

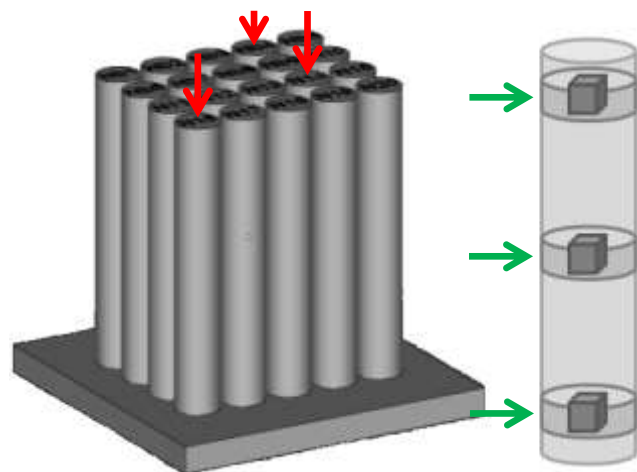


**Figure 88:** Schematic representation of as-built bars and samples for chemical analysis

The actual composition of the as-built materials by EBM is described later (section III.2.A). The results were very homogeneous and the difference in composition from one sample to another was below the experimental error given for the analysis:  $\pm 0.3$  wt.% for aluminum,  $\pm 0.1$  wt.% for chromium,  $\pm 0.15$  wt.% for niobium and  $\pm 0.01$  wt.% for oxygen. This suggested an acceptable homogeneity regarding the chemical composition.

In addition, thermo mechanical analysis (TMA) were realized on samples selected in the same way, in different points of different bars (figure 88). TMA measurements were primarily used for determining the phase transition temperatures [68]. This point will be discussed later (section III.2.D). However, such analysis could give interesting information on chemical composition and microstructure evolution. TMA basically measured the micro displacement during constant heating between room temperature and 1400 °C. As described in more details later, TMA allowed to determine the temperature at which microstructural changes occur during phase transition. Since in particular the  $\alpha$ -Transus temperature depend on the chemical composition, homogeneity in the composition could be assessed comparing the TMA curves of different test samples.

4x4x9 mm<sup>3</sup> samples were prepared from the core of as-built bars and TMA measurements were realized in argon flow from room temperature to 1400 °C (heating rate: 10 °C.min<sup>-1</sup>). The results, although slightly different, confirmed that as-built materials were homogeneous all along the bars and no substantial difference was observe regarding the position of the bars in the building chamber. However, substantial difference was observe when compared the result for sample taken from the core of the bars (linear core melting) and the edge (circular contour melting) (figure 107). Anyway, the external part of the as-built sample is meant to be removed and therefore should not be considered.

It could thus be concluded the feasibility of the fabrication of 3<sup>rd</sup> generation  $\gamma$ -TiAl alloys by electron beam melting:

- The residual porosity was below the maximum tolerance of 1 %.
- The EBM parameters were optimized to completely densify the bars.
- The residual porosity came only from powder porosity as a result of the gas atomization process.
- The chemical composition and TMA results were similar everywhere but in the external contour.

## A. Chemical composition

### a. Core of the samples

The target composition of the massive materials fabricated by EBM was: Ti-(45-46)Al-2Cr-8Nb. As suggested before (section II.1), in order to overcome evaporation of lightweight elements during the EBM process <sup>[47, 65, 66, 75, 86]</sup>, the chemical composition of the powders were tailored. Two pre-alloyed powders were used as base materials: Ti-47Al-2Cr-8Nb and Ti-48Al-2Cr-8Nb powders.

The following table 26 displays the actual chemical composition of the powders, and the subsequent massive materials after EBM. The results in table 26 are given both in wt.% and at.%. The aluminum, chromium and niobium contents were determined by ICP while the oxygen content was determined by a LECO instrument.

		Al	Cr	Nb	O	Ti
<b>Starting powder</b>		Chemical composition in wt.%				
<b>Ti-47Al-2Cr-8Nb</b>	Powder as-received	30.6	2.3	17.2	0.08	Bal.
	Material as-EBM	28.7	2.2	17.4	0.11	Bal.
<b>Ti-48Al-2Cr-8Nb</b>	Powder as received	31.3	2.2	17.2	0.04	Bal.
	Material as-EBM	29.3	2.2	17.3	0.07	Bal.
		Chemical composition in at.%				
<b>Ti-47Al-2Cr-8Nb</b>	Powder as-received	47.1	1.9	7.7		Bal.
	Material as-EBM	44.8	1.8	7.9		Bal.
<b>Ti-48Al-2Cr-8Nb</b>	Powder as received	48.0	1.7	7.7		Bal.
	Material as-EBM	45.6	1.8	7.8		Bal.

**Table 26: Chemical composition of the powder as-received (Ti-47Al-2Cr-8Nb and Ti-48Al-2Cr-8Nb) and the corresponding materials as-EBM**

First of all, oxygen impurities are found to dramatically reduce the room temperature ductility of  $\gamma$ -TiAl based alloys <sup>[48, 87, 126]</sup>. During the EBM process, the oxygen pickup is very low thanks to the vacuum environment (from 0.08 wt.% in the powder to 0.11 wt.% in the massive sample starting from Ti-47Al-2Cr-8Nb powder, and from 0.04 wt.% in the powder to 0.07 wt.% in the massive sample starting from Ti-48Al-2Cr-8Nb powder).

However, this high vacuum process leads to the evaporation of lightweight elements such as aluminum. For example, Cormier et al. <sup>[47]</sup> experienced in 2007 a loss of about 6.1 wt% of aluminum after the EBM process of their Ti-47Al-2Cr-2Nb powder based material. This drastic loss reduced the aluminum content from 46.20 at.% in the powder to 38.83 at.% in the final part. The loss was reduced to about 1 wt.% after EBM of the Ti-48Al-2Cr-2Nb material by Biamino et al <sup>[75, 86]</sup>. In the case of the 3<sup>rd</sup> generation alloys under study, a difference of 2 wt.% of aluminum is observed between the powder and the as-EBM material, as seen table 26.

It was nevertheless a rather limited loss and more importantly it was repeatable when keeping the same process parameters. Indeed, with the same EBM parameters, both Ti-47Al-2Cr-8Nb and Ti-48Al-2Cr-8Nb powder based alloys exhibited a 2 wt.% loss of Al, thus allowing to control the final composition of the massive sample from the composition of the base powder. Therefore, after the EBM process, the massive material fabricated from the Ti-47Al-2Cr-8Nb powder had the following composition: Ti-45Al-2Cr-8Nb. On the other hand, the massive material fabricated from the Ti-48Al-2Cr-8Nb powder had the following composition: Ti-46Al-2Cr-8Nb.

*b. Core-edge composition difference*

The difference between the chemical composition at the core of the samples (linear core melting) and in the edge (circular contour melting) has been mentioned previously (section III.1.C). The actual chemical composition could not be assessed by ICP since it was not possible to easily extract as much as 5g of material from the thin edge of the sample. However atomic absorption, which required much less material, was used to determinate the aluminum content in both positions. Atomic absorption is an analytical technique that measures the concentrations of elements. The technique makes use of the wavelengths of light specifically absorbed by an element, here aluminum. They correspond to the energies needed to promote electrons from one energy level to another. Basically, the amount of light absorbed is proportional to the number of aluminum atoms. A calibration curve was constructed by running several samples of known Al concentration under the same conditions as the unknown.

About 300 mg of material was taken at the core of an as-built sample, and in the edge (figure 21). It was then dissolve in a 5 ml acid solution composed by 3HF+1HNO<sub>3</sub> (in part per volume) and subsequently brought to 500 mL with distilled water. The measures were all doubled, and a set of 3 samples from each region was used for statistical purpose. These test were realized by the author in Politecnico while ICP was done by the professional testing expert IncoTest. Nevertheless, the results obtained were qualitatively trustworthy and a systematic correlation with results from ICP was done for verification.

Figure 89 shows the end side of an as-built bar. It can be seen the two different building path strategies. This study was realized on massive Ti-45Al-2Cr-8Nb built by EBM according to the 3<sup>rd</sup> trial described in the previous section III.1.C. Atomic absorption measurements were also done on Ti-48Al-2Cr-2Nb and compared to ICP results (table 27).

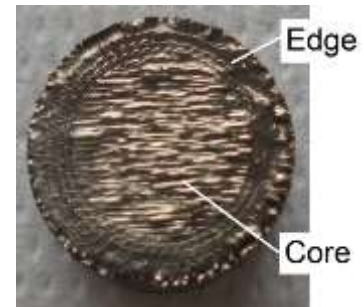


**Figure 89:** View of the bottom surface of an as-built bar (3<sup>rd</sup> Trial) where the circular contour and linear core melting can be identified

Sample	Aluminum content (at.%)		
	AA (Politecnico)		ICP (IncoTest)
	1 <sup>st</sup> run	2 <sup>nd</sup> run	
Ti-48Al-2Cr-2Nb	49.2	48.1	47.3
Ti-45Al-2Cr-8Nb (Core)	46.5	45.2	44.8
Ti-45Al-2Cr-8Nb (Edge)	45.4	44.2	-

**Table 27:** Measurements of the aluminum content of different materials and positions by atomic absorption

The aluminum contents given by the atomic absorption measurements (AA in table 27) were substantially different than those given by ICP. In addition, from one run to the other, the values differed by more than 1 at.%. This could result from the effect of other elements present in the solution (Ti, Nb, Cr, etc.). Also, for the first run, the calibration curve was doubtful. The machine had not been used for long time and did not work as new for a number of reasons. Therefore, atomic absorption measurements could not be trusted and only the values given by ICP realized by the professional organization IncoTest were considered as a quantitative measure of the chemical composition.

However, qualitatively, the results confirm a lower amount of Al in the edge of the sample. For both run, the aluminum content measured by AA in the edge was 1 at.% lower than in the core of the specimens. Although it could not be concluded that the actual Al content in the edge was 1 at.% lower than in the core, which would bring the Al content to 43.8 at.%, the actual value was probably in that neighborhood. Other clues such as TMA measurements and microstructure analysis after heat treatment will confirm later that aluminum depletion in the edge (Section III.2.D.d).

### B. Phase analysis by X-ray diffraction

In the range of composition considered, ~ (45-46) at.% of Al, TiAl alloys are mainly composed by the phases  $\gamma$ -TiAl and  $\alpha/\alpha_2$ -Ti<sub>3</sub>Al. However the addition of Nb has a significant effect on the phase transformations of TiAl alloys. In 1999, Chen et al. [112] studied high-Nb containing TiAl-based alloys and in particular reassessed the binary phase diagram for alloys containing Nb. Figure 90 shows in solid lines the partial phase diagram for Ti-Al containing 8 at.% of niobium according to Chen et al. [112]. For comparison, the binary Ti-Al phase diagram was presented as dotted lines. The red lines highlight the 45Al and 46Al compositions. According to the opposite revisited phase diagram, the addition of niobium leads both alloys to form the  $\beta$ -phase during solidification. Therefore such phase was also expected in Ti-45Al-2Cr-8Nb and Ti-46Al-2Cr-8Nb.

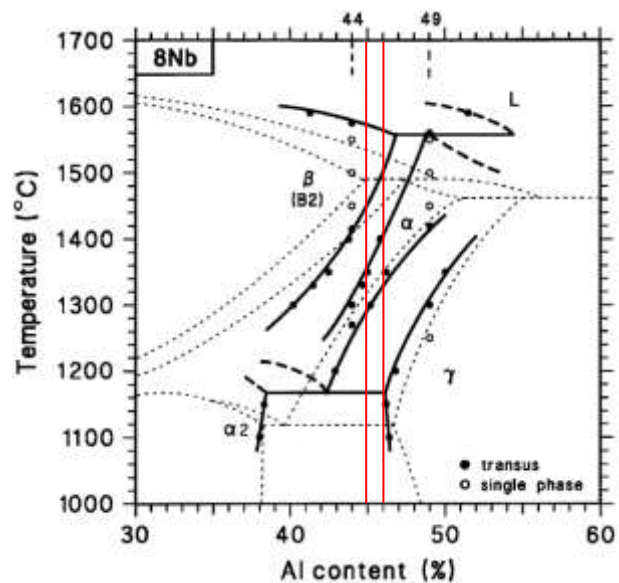
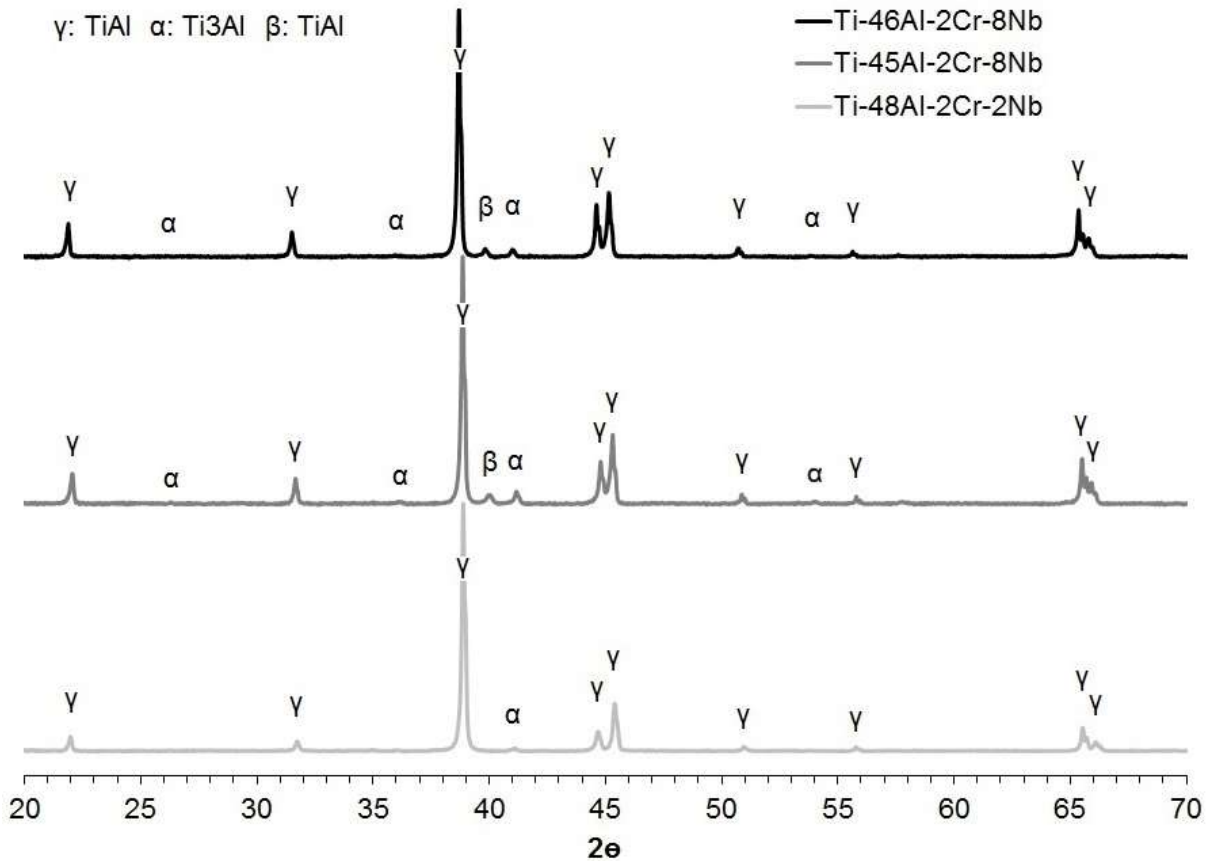


Figure 90: The quasi phase diagram showing the effect of -8Nb addition on the phase relationship of  $\gamma$ -TiAl alloys (solid lines). The binary Ti-Al phase diagram is drawn in dotted lines for reference [112]



X-ray diffraction analysis (Philips PW1710  $\text{Cu}_{K\alpha}$  radiation) were performed on as-EBM samples of Ti-45Al-2Cr-8Nb, Ti-46Al-2Cr-8Nb and Ti-48Al-2Cr-2Nb alloys. The measures were done on the same surface of that for porosity analysis (figure 78C). The X-ray diffraction patterns are displayed figure 91.



**Figure 91:** X-ray diffraction patterns of Ti-48Al-2Cr-2Nb (light grey), Ti-45Al-2Cr-8Nb (dark grey) and Ti-46Al-2Cr-8Nb (black) alloys as-EBM

The  $\gamma$  phase was the undeniable dominant phase for all three alloys. A low amount of  $\alpha$  phase was also present in all samples. The X-ray diffraction patterns of the high Nb containing alloys were very similar (figure 91). They both exhibited 3 phases:  $\gamma$ -TiAl,  $\alpha$ -Ti<sub>3</sub>Al and  $\beta$ -TiAl. Furthermore, it appeared from the curves in figure 91 that Ti-45Al-2Cr-8Nb had a slightly higher amount of  $\alpha$  than Ti-46Al-2Cr-8Nb. This is explain by the different content of Al. The lower the Al content, the higher the amount of  $\alpha/\alpha_2$  (figure 90). Ti-48Al-2Cr-2Nb with the highest Al content exhibited the lower amount of  $\alpha$  phase. Finally, both high Nb containing alloys contained a low amount of  $\beta$  phase while Ti-48Al-2Cr-2Nb did not. This is the result of higher content of Nb, a  $\beta$ -stabilizer, which extend the  $\beta$  phase field (figure 90)<sup>[48, 59, 128-135]</sup>. The  $\beta$ -phase was also clearly observed by microscopy (section III.2.C).

### C. Microstructure analysis of the materials as-EBM

The microstructure of the as-built Ti-45Al-2Cr-8Nb and Ti-46Al-2Cr-8Nb alloys was observed by means of optical and electron microscopy. The metallographic preparation was similar to that for the measure of porosity (section III.1). 10 mm height samples were cut from as-built bars and cut in half to observe the cross section along the building direction (figure 78C). If necessary, small samples were mounted in epoxy resin before polishing. The surface was ground with abrasive paper from grit 600 to 4000. Then, fine polishing with cloths and abrasive diamond pastes of 6 and 3  $\mu\text{m}$  was done. Chemical etching was used in order to reveal the microstructure. The commonly used Kroll's reagent (91 mL  $\text{H}_2\text{O}$ , 6 mL  $\text{HNO}_3$ , 3 mL HF) was chosen. After polishing, specimens were immersed in the etchant for about 15 seconds, immediately rinsed with distilled water and cleaned in ethanol for 30 min in an ultrasonic bath to remove polishing and etching contaminants.

The following figures 92 and 93 show the typical microstructure as-EBM of Ti-45Al-2Cr-8Nb and Ti-46Al-2Cr-8Nb alloys respectively observed by optical microscopy at the core of the specimens. For comparison, optical micrographs of Ti-48Al-2Cr-2Nb are also displayed figure 94.

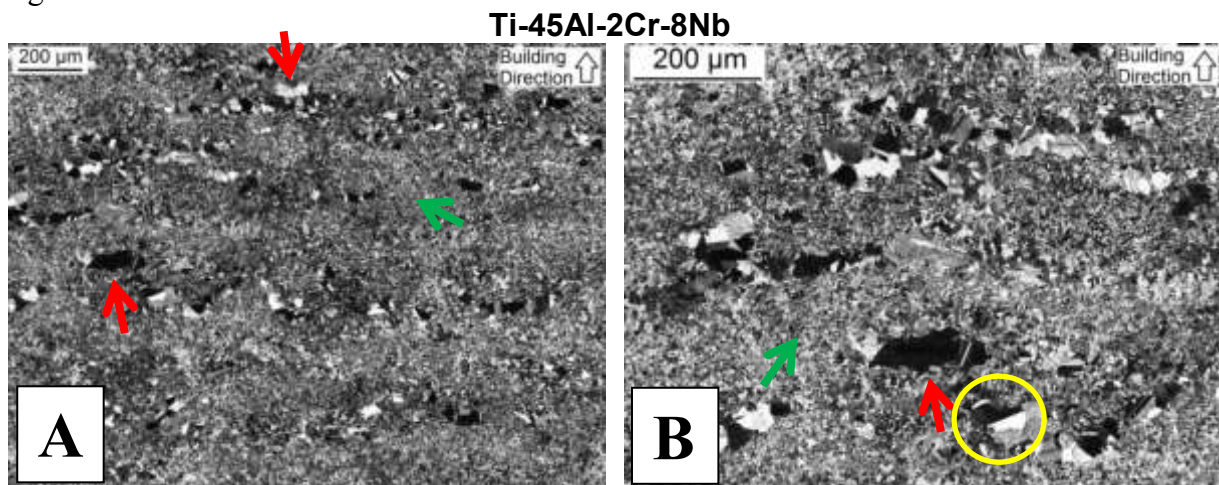


Figure 92: Optical micrograph of Ti-45Al-2Cr-8Nb showing the microstructure at magnification x50 (A) and x100 (B)

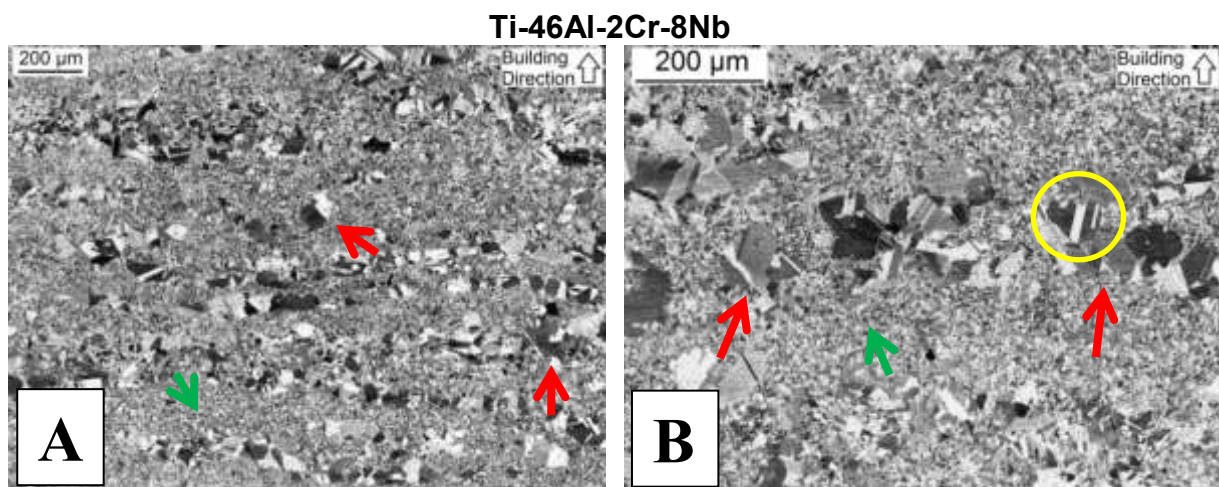


Figure 93: Optical micrograph of Ti-46Al-2Cr-8Nb showing the microstructure at magnification x50 (A) and x100 (B)

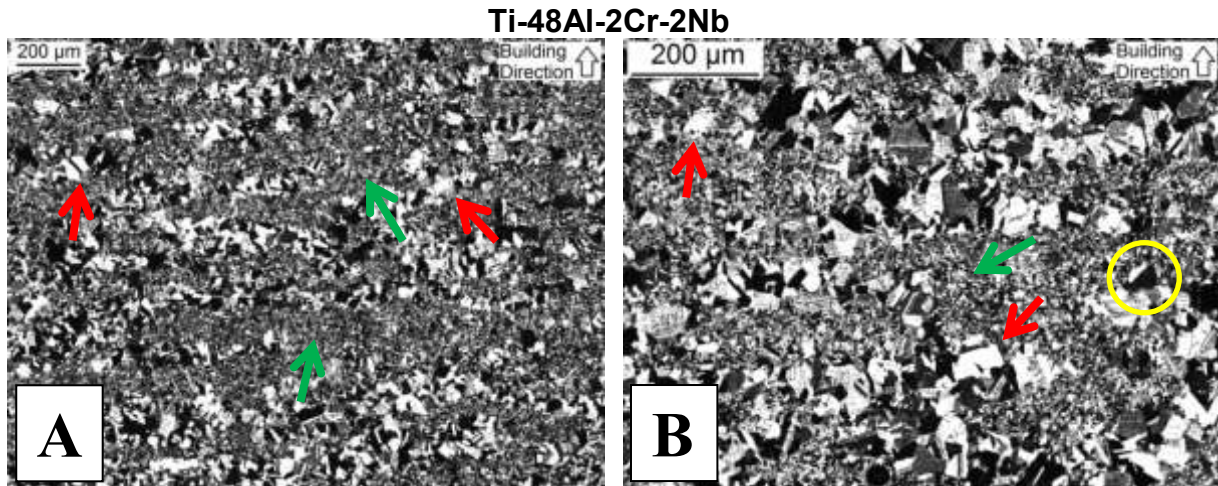


Figure 94: Optical micrograph of Ti-48Al-2Cr-2Nb showing the microstructure at magnification x50 (A) and x100 (B)

The fine equiaxed microstructures in evidence figures 92, 93 and 94 were typical of the EBM processing of  $\gamma$ -TiAl alloys, which involves rapid solidification. It consisted of a mixture of very fine equiaxed  $\gamma$ -TiAl and  $\alpha$ -Ti<sub>3</sub>Al grains (pointed by green arrows in figures 92, 93 and 94) along with bigger grains of the same nature (pointed by red arrows in figures 92, 93 and 94). The overall microstructure was very fine for all three materials. It could be noted the higher amount of bigger grains in the case of Ti-48Al-2Cr-2Nb. It is believed that the higher building temperature for the fabrication of high-Nb containing alloys involved a more rapid solidification responsible for the finer microstructure. It could also result from a better optimized EBM process. Finally, the bigger grains could simply come from bigger initial powder particles size. However, the particle size distributions of all three starting powders were very similar (table 23).

In most cases, the bigger grains were clustered along the layer deposition direction, which is more evident in figures 92A and 93A. Therefore, it was suggested that some consolidated areas, more likely the top surface of an as-built layer, went through overheating during the melting of the subsequent layer. This would lead to partial recrystallization and grain growth in the underlying massive material during melting of a layer <sup>[75]</sup>. But this was only a suggestion and no concrete proof could induce any conclusion.

The as-EBM microstructure presented a lot of twinning. Examples of such grains are highlighted by yellow circles in figures 92B, 93B and 94B. Twin boundaries have a lower interface energy or grain boundary energy. They are either created during solidification or by a deformation process. It was thus possible that the high number of twins resulted from the cutting and mechanical polishing of the samples for observation. However, the rapid solidification involved by the EBM process was most likely the cause.

Movements of dislocations in the crystals create coherent boundaries which grow (figure 95, from (a) to (e)). If that growth is impeded by the growth of adjacent grains for example, the coherence is threaten (figure 95 (f))<sup>[136-138]</sup>.

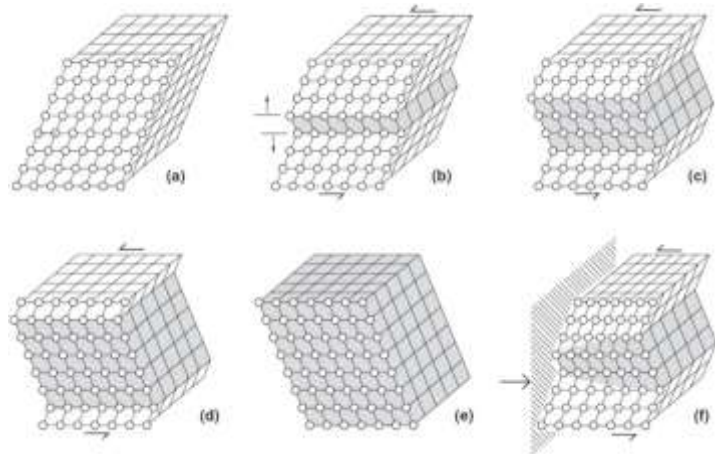


**Figure 95: Progressive germination of a calcite crystal, in grey the germinated part ((a)-(e)). Germination of a crystal of which one side is strongly impeded to grow (f)**<sup>[136]</sup>

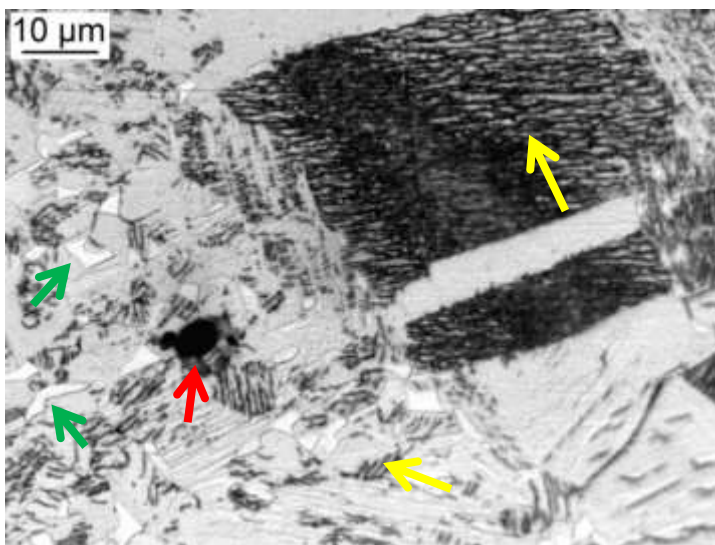


**Figure 96: High magnification micrograph of a selected zone of as-EBM Ti-46Al-2Cr-8Nb**

Figure 96 is a selected optical micrograph at high magnification ( $\times 1000$ ) of Ti-46Al-2Cr-8Nb. It can be seen on left side very fine equiaxed grains while on the right side bigger grains are observed. The  $\beta$  phase that has been identified in the X-ray diffraction patterns of the high-Nb containing alloys (figure 91) is pointed by green arrows in figure 96. It appeared as a bright shiny white phase at grain boundaries. Pointed by a red arrow, a small spherical pore is highlighted. Finally, inside the grains could be observed irregular black lines (pointed by yellow arrows in figure 96). These could result from both the mechanical polishing and chemical etching.

Titanium aluminides are typically chemically etched with Kroll's reagent. A lot of optical and SEM micrographs have been reported at high magnification and did not exhibit such features inside the grains (yellow arrows in figure 96). It is therefore unlikely that the chemical etching alone with Kroll's reagent was responsible for that. However, it was reported that etching with Kroll's solution resulted in somewhat blurred images, in particular the equiaxed  $\gamma$ -grains did not appear with sharp edges<sup>[139]</sup>.

These features were further observed at higher magnification by means of scanning electron microscopy (SEM). The following figures show SEM micrographs of Ti-45Al-2Cr-8Nb at magnification x5000 (figure 97) and Ti-46Al-2Cr-8Nb at magnification x20000 (figure 98).

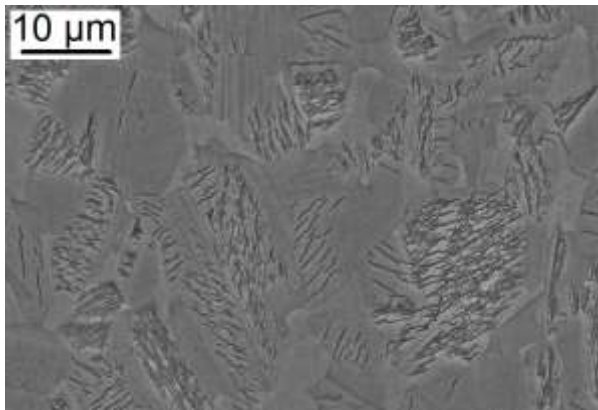


**Figure 97:** SEM micrograph of Ti-45Al-2Cr-8Nb at magnification x5000

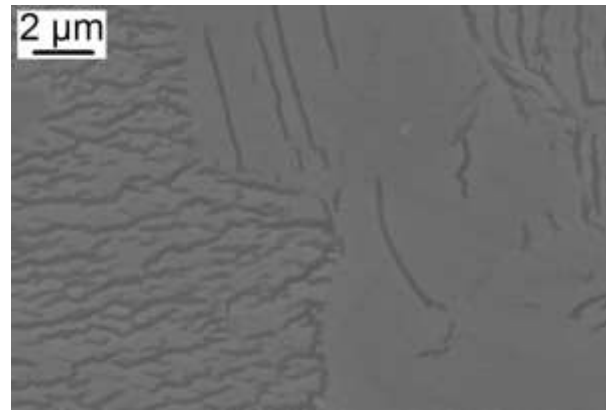


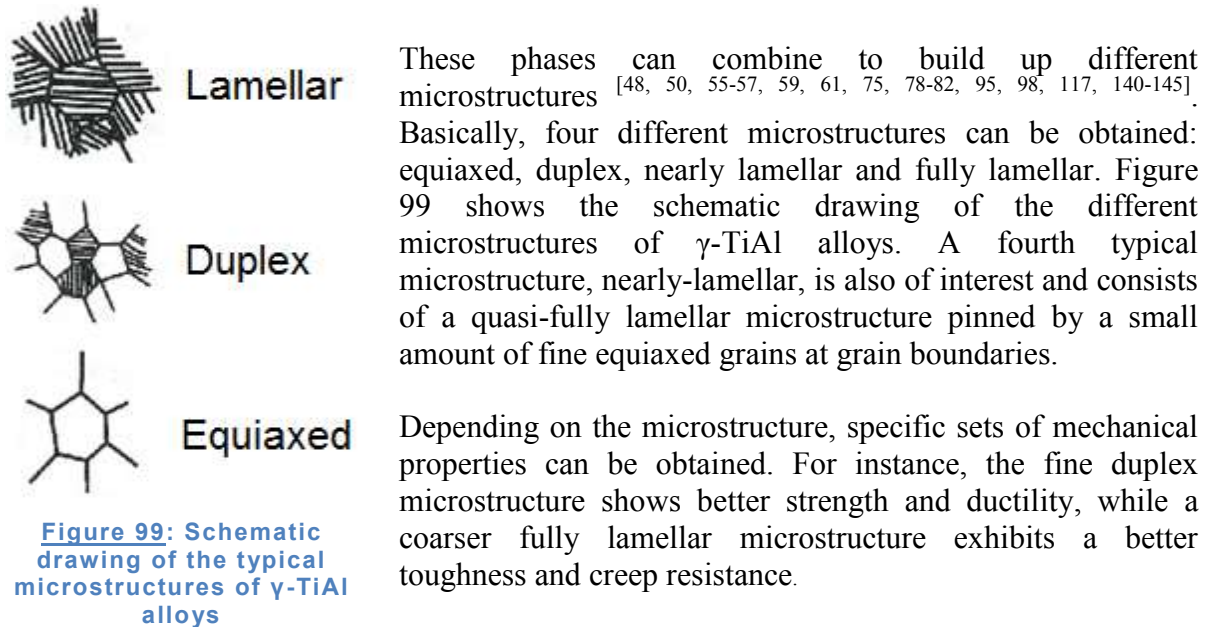
**Figure 98:** SEM micrograph of Ti-46Al-2Cr-8Nb at magnification x20000

The “defects” pointed by yellow arrows in figure 96 are clearly observed in figures 97 and 98. They actually looked like small cracks, were not observed in all the grains and did not clearly show preferential orientation. However, inside a single grain, the orientation was similar. It has been reported that metallographic preparation could distort the true microstructure of TiAl alloys <sup>[139]</sup>. In particular, the preparation steps of cutting, grinding and mechanical polishing could induce surface cracking.

Therefore, it was concluded that these microcrack-like features inside the grains were artifacts caused by mechanical polishing and subsequent chemical etching. Electrolytic polishing is usually used to avoid this problem. Nevertheless, high magnification micrographs of high quality were not necessary in this study. The microstructures were quantified at magnification x100. The simple metallographic preparation described earlier was thus satisfactory in this work, despite those features. Actually, it was found useful to differentiate the grains at lower magnification since they were not well defined by the chemical etching.

#### D. Phase transitions analysis by TMA

The mechanical properties of  $\gamma$ -TiAl alloys are very sensitive to microstructure. From the previous sections, the microstructure as-EBM was a mixture of fine equiaxed  $\gamma$ -TiAl and  $\alpha$ -Ti<sub>3</sub>Al grains, along with a little amount of  $\beta$ -phase.



The different microstructures can be obtained by careful heat treatment at given temperatures in relation with the alpha transus temperature  $T_\alpha$  of the alloy (i.e. the transition between the  $\alpha$  mono-phase region and the  $(\alpha + \gamma)$  biphasic region, see the phase diagram figure 90) [48, 50, 75]. The phase transition temperatures depend on the chemical composition of the alloy and it is thus of great interest to assess easily the alpha transus temperature  $T_\alpha$  for a given composition since the phase diagram might not be available. In addition to the evident scientific interest, it is also industrially convenient to be able to quickly set up the proper thermal treatment.

The traditional way to assess equilibrium phase diagrams for complex alloys, determined by annealing heat treatments followed by metallographic examination of the microstructure, can be heavy and expensive in alloy screening and development [48, 50, 112, 146-149]. Differential scanning calorimetry (DSC) [48, 78, 108, 148, 150, 151] and differential thermal analysis (DTA) [152] usually are the preferred techniques to identify transformations by measuring the heat evolution. Also, Thermo-Calc CALPHAD method showed good agreement with experimental data [148, 153-155] as well as high energy X-ray diffraction [156].

Thermo Mechanical Analysis (TMA) was proposed as an alternative method to determine the transition temperatures and in particular  $T_\alpha$ . TMA is generally used to measure the glass transition in polymers based on changes in thermal expansion. It was suggested that the microstructural rearrangement that occurs during phase transitions might be observed by TMA. In particular, the change in lattice parameter during the transformation between L1<sub>0</sub> and D0<sub>19</sub> at  $T_\alpha$ . This study was published in Scripta Materialia [68].

a. Comparison between TMA and DSC

Thermo mechanical analysis (Setsys Evolution, Setaram) were performed on  $4 \times 4 \times 10 \text{ mm}^3$  specimens in  $20 \text{ ml.min}^{-1}$  argon flow to prevent oxidation. Specimens were heated from room temperature to  $1400 \text{ }^\circ\text{C}$  with different heating rates in the range  $5\text{-}50 \text{ }^\circ\text{C.min}^{-1}$ , hence giving as results dynamic transitions. All measurements were realized along the height of the sample, i.e. the longest direction which was the building direction. Figure 100 shows a typical sample for TMA measurement installed in the machine.

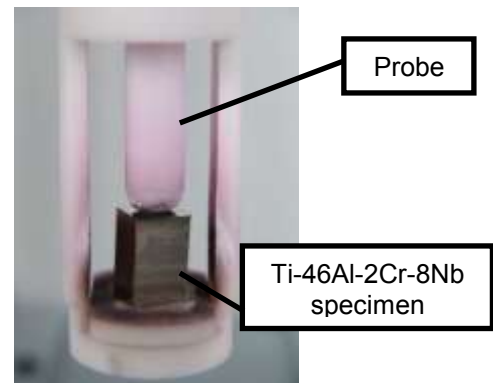


Figure 100:  $4 \times 4 \times 10 \text{ mm}^3$  specimen for TMA analysis

On the other hand, DSC (TGA-DSC 92, Setaram) were performed on  $1.5 \times 1.5 \times 3 \text{ mm}^3$  specimens in  $20 \text{ ml.min}^{-1}$  argon flow. Specimens were heated from room temperature to  $1400 \text{ }^\circ\text{C}$  with a heating rates of  $5 \text{ }^\circ\text{C.min}^{-1}$ . TMA and DSC were used to identify the phase transition temperatures of 2<sup>nd</sup> and 3<sup>rd</sup> generation  $\gamma$ -TiAl produced by electron beam melting (EBM) under investigation in this study.

Figure 101 shows in continuous line the displacement curve measured by TMA of Ti-47Al-2Cr-2Nb as a function of temperature during heating at  $5 \text{ }^\circ\text{C.min}^{-1}$  from room temperature to  $1400 \text{ }^\circ\text{C}$ . Normally, the displacement increases almost linearly when temperature increases as a result of thermal expansion. However, at temperatures close to the transitions anticipated from the phase diagram in figure 90, rather sudden changes were observed and are pointed out by circles in figure 101. This behavior became even more evident when plotting the derivative curve of the displacement (in dotted line in figure 101): two distinct peaks are observed. Such peaks in the derivative curve represent the sudden change of microstructural parameters during phase transitions.

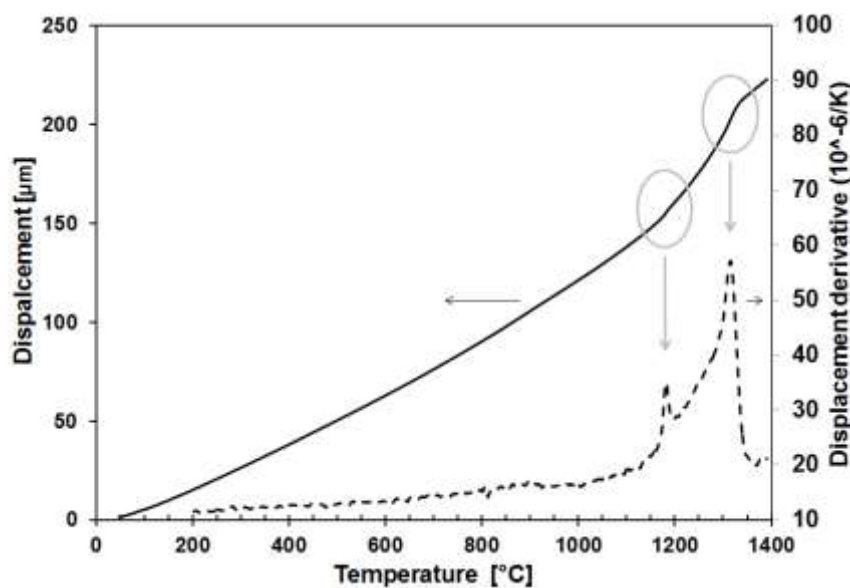
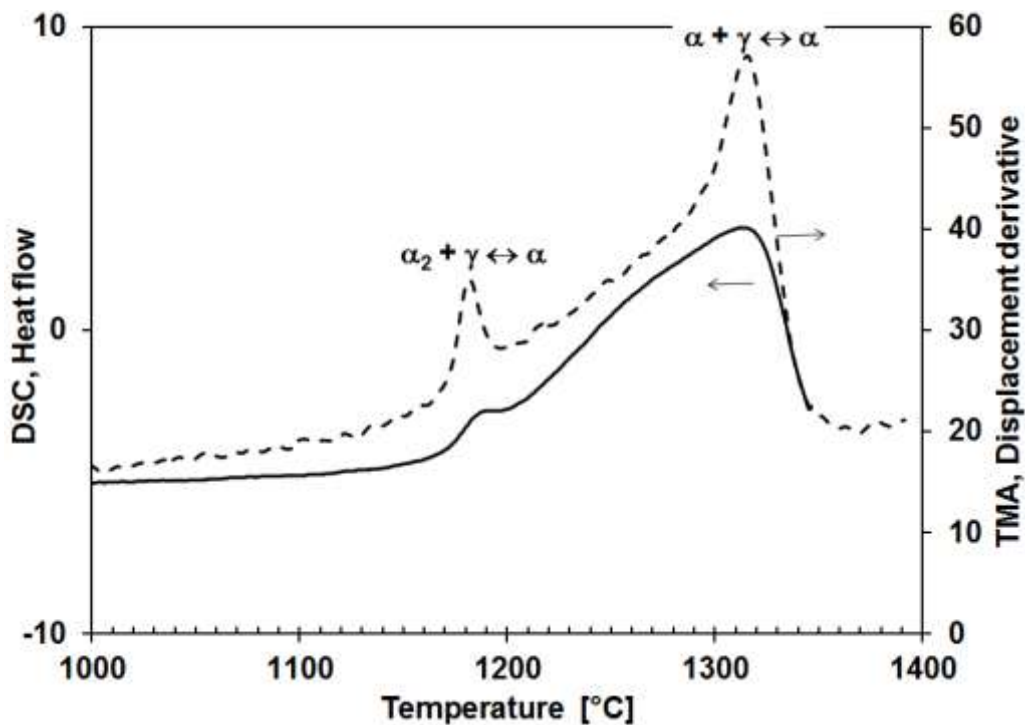


Figure 101: TMA measurement of Ti-47Al-2Cr-2Nb: displacement (continuous line) and derivative of the displacement (dotted line) as functions of temperature [68]

In order to confirm and analyze the accuracy of the measurements by TMA, results were compared to DSC measurements which in literature is a well-established technique for  $\gamma$ -TiAl phase transitions evaluation. Figure 102 shows the derivative curve of the displacement as a function of temperature obtained by TMA (dotted line) along with the DSC curve (continuous line) of Ti-47Al-2Cr-2Nb. Both measurements in figure 102 were realized in argon atmosphere with the same heating rate of  $5\text{ }^{\circ}\text{C}\cdot\text{min}^{-1}$ . One can appreciate the similarity between the two curves. Rather evident peaks are observed and the temperatures at which the variations are identified for both techniques correspond very well. A similar comparison between TMA and DSC was carried out to assess the glass transition temperature of latex films showing good results <sup>[157]</sup>.



**Figure 102:** Comparison between DSC curve (continuous line) and the derivative of the displacement measured by TMA (dashed line) for Ti-47Al-2Cr-2Nb in argon atmosphere and  $5\text{ }^{\circ}\text{C}\cdot\text{min}^{-1}$  heating rate <sup>[68]</sup>

According to the literature <sup>[48, 75, 78, 148, 150, 151]</sup>, the first peak corresponds to the eutectoid transformation  $(\alpha_2 + \gamma) \leftrightarrow \alpha$  and is identified in figure 102 at a temperature  $T_{\text{eu}} = 1180\text{ }^{\circ}\text{C}$ . The second peak corresponds to the transformation  $(\alpha + \gamma) \leftrightarrow \alpha$  at the alpha transus temperature  $T_{\alpha} = 1315\text{ }^{\circ}\text{C}$  in figure 102. The position of the two peaks were identified graphically at the abscissa of the maximums of the displacement derivative versus temperatures plots. From figure 102, some conclusions could be drawn. First of all, the results showed that TMA actually allows the identification of phase transition temperatures. Just like DSC, only transition temperatures can be determined by TMA and additional measures such as X-ray Diffraction (XRD) or Energy Dispersive Spectroscopy (EDS) are needed to identify the actual phase composition. Furthermore, the derivative curves exhibit well defined peaks that enable to accurately determine the transition temperatures while identifying the precise position of the peaks is more difficult by the analysis of the DSC results. Finally, TMA allows more freedom with regards to the specimen geometry than DSC. In particular, TMA allows to test bigger specimens than DSC which are more representative of real components.



b. Effect of alloying elements to validate the model

In order to validate the model, in terms of TMA accuracy for  $\gamma$ -TiAl phase transformations evaluation, TMA tests were realized on materials with different chemical compositions since alloying elements are known to modify the phase transition temperatures. The effect of alloying elements on phase transitions of  $\gamma$ -TiAl alloys has been widely studied. For example, Huang et al. [158] showed that Cr addition decreases both the  $\alpha$  transus temperature  $T_\alpha$  and the eutectoid temperature  $T_{eu}$ . Niobium on the other hand was found to increase the eutectoid temperature  $T_{eu}$  but have little influence on the  $\alpha$ -transus temperature [48, 78, 112, 148, 150]. Thereby, TMA measurements were performed on three different TiAl alloys with slightly different compositions and produced by EBM under equivalent conditions.

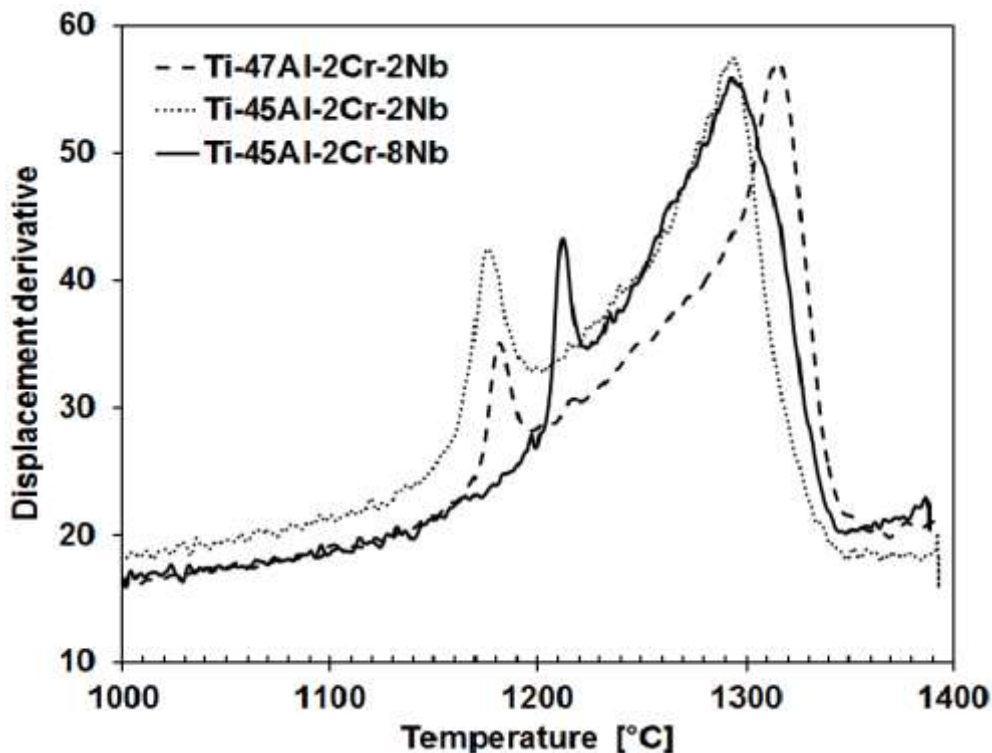


Figure 103: Comparison of the derivative of the displacement measured by TMA between Ti-47Al-2Cr-2Nb (dashed line), Ti-45Al-2Cr-2Nb (dotted line) and Ti-45Al-2Cr-8Nb (solid line) [68]

Figure 103 shows the derivative curve of the displacement of Ti-47Al-2Cr-2Nb (fine dotted line), Ti-45Al-2Cr-2Nb (dotted line) and Ti-45Al-2Cr-8Nb (continuous line). Both materials with the same 45 at.% Al content exhibit almost the same  $\alpha$ -transus temperature  $T_\alpha \sim 1295^\circ\text{C}$  while  $T_{eu}$  increases with the increase of Nb from  $1175^\circ\text{C}$  to  $1215^\circ\text{C}$ . On the other hand, both materials with the same 2 at.% Nb content show that varying the Al content leads to different  $T_\alpha$  whereas  $T_{eu}$  remains the same ( $1175$ - $1180^\circ\text{C}$ , as can be seen figure 103). In particular, higher  $T_\alpha$  was found when the aluminum content increases (from  $1295^\circ\text{C}$  for 45 at.% Al to  $1315^\circ\text{C}$  for 47 at.% Al). This is consistent with the trend of the alpha transus line in the Ti-Al phase diagram figure 90.

c. Dynamic to static results

The transition temperatures determined by either DSC, DTA or TMA are measured dynamically and vary substantially with different heating rate. However, by extrapolation and linear regression, as it was realized for DSC analysis [148, 151] or DTA [152], it is possible to correlate dynamic and static conditions according to the following equation:

$$T_{\dot{R}_{eu,\alpha}} = k \cdot \dot{R} + T_{0_{eu,\alpha}} \quad (1)$$

Where  $T_{\dot{R}_{eu,\alpha}}$  is the transition temperature for a given heating rate  $\dot{R}$ ,  $k$  a coefficient and  $T_{0_{eu,\alpha}}$  is the transition temperature for a theoretical heating rate of 0 °C.min<sup>-1</sup> or static transition temperature.

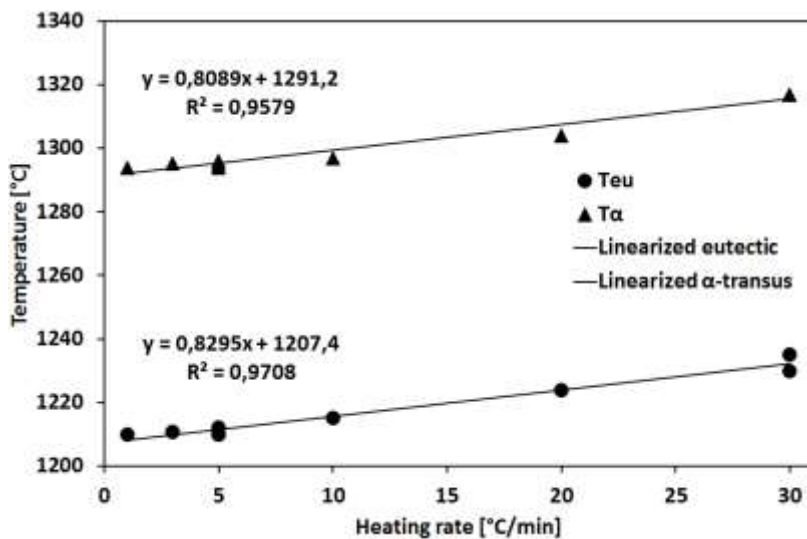


Figure 104: Linear regression from dynamic transition temperatures  $T_{\dot{R}_{eu,\alpha}}$  measured at different heating rate  $\dot{R}$  of Ti-46Al-2Cr-8Nb [68]

TMA were realized on Ti-45Al-2Cr-8Nb with the different heating rates 1, 3, 5, 10, 20, 30 °C.min<sup>-1</sup> and the values of  $T_{eu}$  and  $T_{\alpha}$  were identified. The results are plotted figure 104. By linear regression, the eutectoid temperature  $T_{eu}$  and the  $\alpha$ -transus temperature  $T_{\alpha}$  could be approach by equation (1). It was found for Ti-45Al-2Cr-8Nb the following values:

- $T_{0_{eu}} = 1207$  °C
- $T_{0_{\alpha}} = 1291$  °C

TMA was thus found reliable to assess the phase transition temperatures of  $\gamma$ -TiAl alloys. When compared to other well established techniques (such as DSC or DTA), TMA exhibits sharper well-defined peaks to identify the phase transition temperatures. This method is obviously quicker than annealing heat treatments and metallographic observations. When one changes the composition of the  $\gamma$ -TiAl alloy, a rather quick and reliable method to identify the transition temperature variations is a powerful tool.

d. TMA of the EBM optimization trials

Thermo mechanical analysis were systematically performed on as-EBM samples after each trial described earlier. TMA helped selecting the optimal parameters for the EBM. Small rectangular samples were therefore prepared from the core of an as-built bar (figure 100). It was found that the shape and dimensions of the samples influenced the results. For example, the higher the sample height the higher the peaks. For that reason, only the abscissas of the peaks tip were considered and the vertical axis was not relevant in this study.

Figure 105 shows the displacement derivatives as a function of temperature measured by TMA of Ti-45Al-2Cr-8Nb alloys after the different EBM trials describe earlier. All measures were performed on rectangular 4 x 4 x 10 mm<sup>3</sup> specimens in argon flow to avoid oxidation from room temperature to 1400 °C with a constant heating rate of 5 °C.min<sup>-1</sup>. Since the ordinates were not taken into account, the curves were translated along the y-axis for better reading.

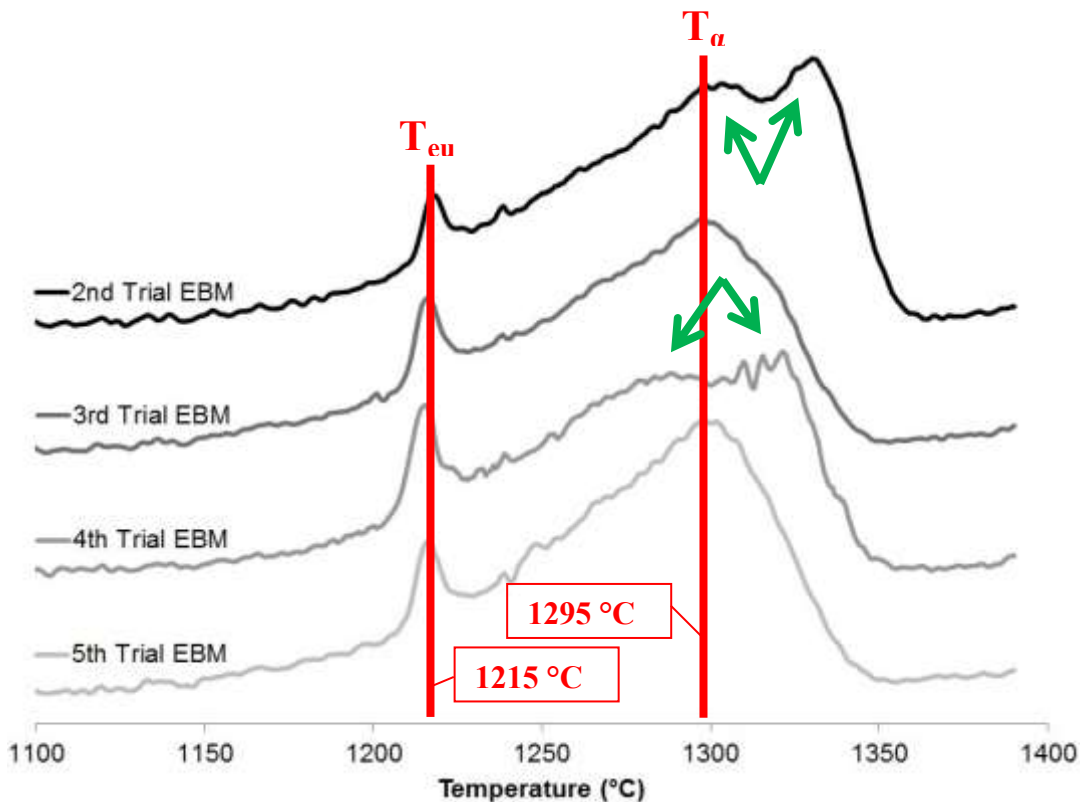


**Figure 105:** Displacement derivative vs. temperature measured by TMA of Ti-45Al-2Cr-8Nb after each trial of the EBM process optimization. From top to down: 2<sup>nd</sup> trial (black line), 3<sup>rd</sup> trial (dark grey line), 4<sup>th</sup> trial (grey line) and 5<sup>th</sup> Trial (light grey)

Figure 105 highlights the influence of the EBM processing on microstructure and homogeneity in the as-built material. All four materials exhibited a first peak at a temperature of ~ 1215 °C, which corresponds to the eutectoid temperature  $T_{eu}$  of Ti-45Al-2Cr-8Nb (figure 103). In figure 90, the eutectoid temperature for such 8Nb containing alloys appears lower but the phase diagram in figure 90 does not take into account the effect of Cr addition. The heating rate of 5 °C.min<sup>-1</sup> also had an influence (figure 104). Despite different EBM process, the Nb and Cr ratio barely vary and it was thus expected to find the same eutectoid temperature.

The  $\alpha$ -transus temperature  $T_\alpha$  of Ti-45Al-2Cr-8Nb alloys presented some differences according to the EBM trial. For the 3<sup>rd</sup> trial considered viable and consequently the 5<sup>th</sup> trial EBM processing, a well-defined single peak was observed (figure 105). It corresponded to an  $\alpha$ -transus temperature of  $T_\alpha \sim 1295$  °C. On the other hand, the 2<sup>nd</sup> and 4<sup>th</sup> trial exhibited a double-peak highlighted by green arrows in figure 105. This behavior was not completely understand. It is believe that it resulted either from the residual porosity or a significant inhomogeneity in the microstructure. Either way, it was concluded from the TMA measurements that these EBM processing were inadequate.

Figure 106 shows the derivative displacement as a function of temperature obtained by TMA of Ti-45Al-2Cr-8Nb and Ti-46Al-2Cr-8Nb. Again, the curves in figure 36 were translated along the y-axis for better reading.

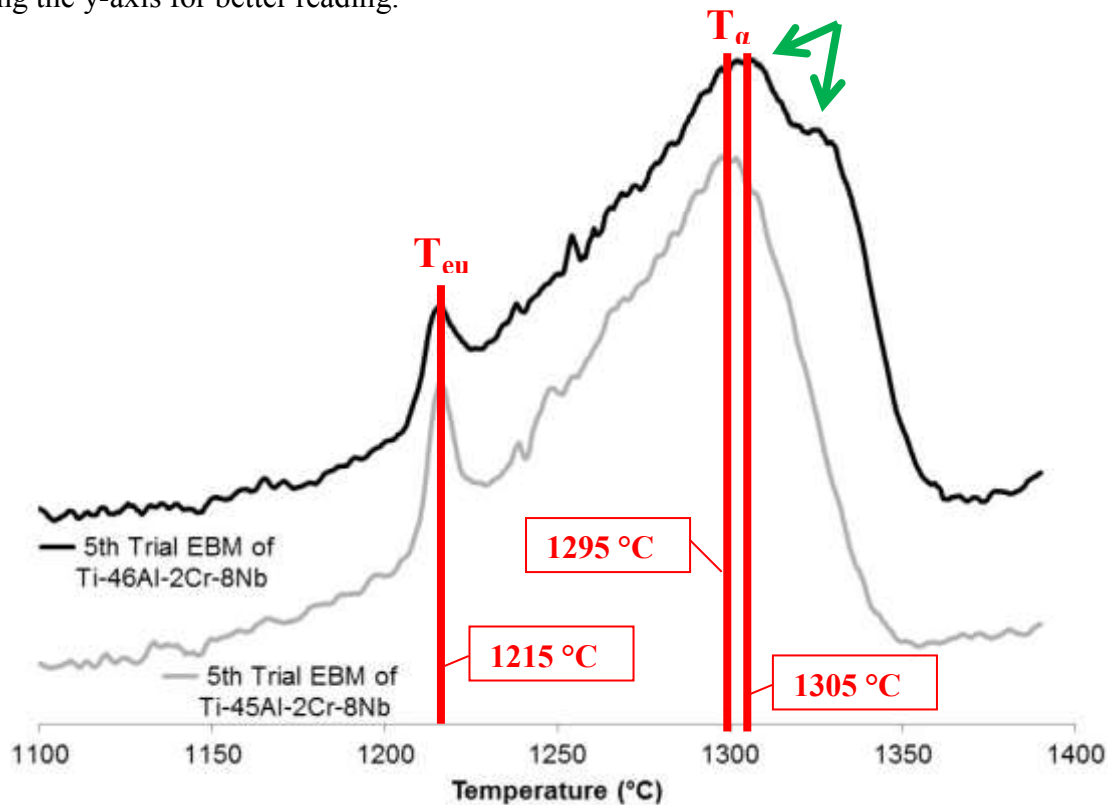


**Figure 106:** Displacement derivative vs. temperature measured by TMA of Ti-45Al-2Cr-8Nb (light grey line) and Ti-46Al-2Cr-8Nb (black line) fabricated by EBM according to the selected conditions

First of all, the eutectoid temperature were identical for both alloys at  $T_{eu} = 1215$  °C. This was expected since the Nb and Cr contents were equal. Furthermore, it confirmed the reliability of the measure. On the other hand, the  $\alpha$ -transus temperatures were slightly different. This was consistent since Ti-46Al-2Cr-8Nb has a slightly higher amount of Al than Ti-45Al-2Cr-8Nb. As suggested before, higher amount of aluminum led to higher  $\alpha$ -transus temperature (figure 90). In figure 103,  $T_\alpha$  increased from 1295 °C for 45 at.% Al to 1315 °C for 47 at.% Al. Here,  $T_\alpha \sim 1295$  °C for Ti-45Al-2Cr-8Nb while  $T_\alpha \sim 1305$  °C for Ti-46Al-2Cr-8Nb. However, the TMA curve of Ti-46Al-2Cr-8Nb alloy exhibited a kind of double peak as could be observed in figure 105, although less pronounced (green arrows in figure 106). This suggested that the EBM parameters could be further optimized for the fabrication of Ti-46Al-2Cr-8Nb which contains higher amount of aluminum. Though the TMA of Ti-46Al-2Cr-8Nb was not perfectly clear, it was acceptable and the EBM conditions were judged satisfactory.

In figure 107, the difference between the core and the edge of the samples was highlighted by TMA. As it was previously evidenced by atomic absorption (section III.2.a.2), the contour (external circular melting) of the as-built samples exhibited a lower amount of aluminum. TMA was used to confirm that observation. Smaller  $2 \times 2 \times 5 \text{ mm}^3$  samples were prepared from the contour or edge, which was too thin to get bigger samples (figure 89). Bigger  $4 \times 4 \times 10 \text{ mm}^3$  specimens were taken from the core instead. TMA were performed in the same conditions, with a heating rate of  $5 \text{ }^\circ\text{C}\cdot\text{min}^{-1}$ .

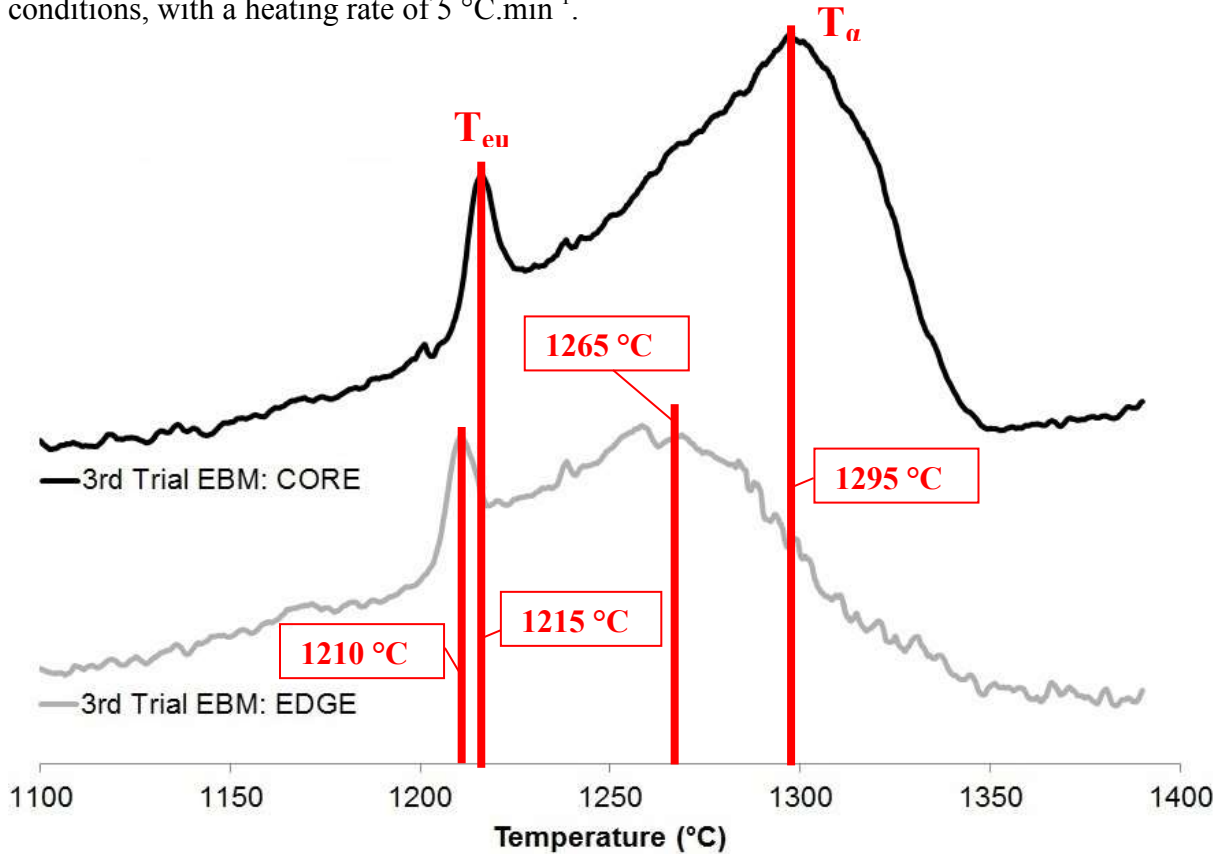


Figure 107: Displacement derivative vs. temperature measured by TMA in the core (black line) and the edge (light grey line) of Ti-45Al-2Cr-8Nb fabricated by EBM according to the selected conditions

The eutectoid temperatures identified from the derivative of the displacement measured by TMA in the edge and the core of Ti-45Al-2Cr-8Nb were slightly different. In the edge  $T_{eu} \sim 1210 \text{ }^\circ\text{C}$  while in the core  $T_{eu} \sim 1215 \text{ }^\circ\text{C}$ . The aluminum content has no effect on the eutectoid temperature (figure 103) but the evaporation of aluminum in the edge was so high that the chemical composition ratio was modified. Secondly, the  $\alpha$ -transus temperatures identified from TMA in the core and the edge of the as-built specimen were very different. In the core  $T_{\alpha} \sim 1295 \text{ }^\circ\text{C}$  while in the edge  $T_{\alpha} \sim 1265 \text{ }^\circ\text{C}$ . This suggested, according to the trend of the  $\alpha$ -transus temperature in figure 90, that the edge contained a lot less aluminum.

## **IV. Microstructure set-up by post processing heat treatment**

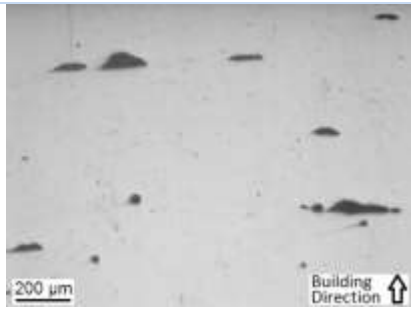
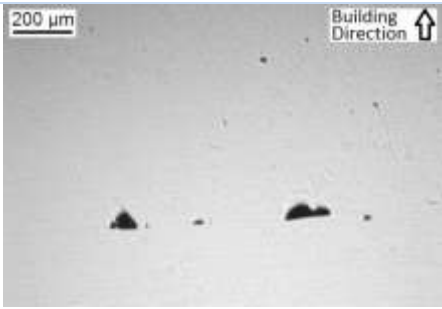




### **1. Hot Isostatic Pressing (HIP)**

Hot Isostatic Pressing (HIP) is a treatment that combines high temperature and pressure in order to improve material properties. Materials are held for a certain time at high temperature and subjected at the same time to high pressure applied by an inert gas. For example, cast materials for critical applications are often HIPed to eliminate or reduce the internal porosity to improve mechanical properties. In powder metallurgy, HIP emerged as an outstanding manufacturing process to consolidate fully dense components from powders. It allowed in particular to produce near-net-shape parts. For the production near-net-shaped  $\gamma$ -TiAl components for structural applications, Hot Isostatic Pressing is performed either to reduce porosity of cast parts or direct fabrication from powders <sup>[48, 59, 75, 159]</sup>.

In this study, HIP was used or rather studied after the EBM processing for two purposes. It was primarily used to further reduce the residual porosity, source of defects, although already very low as described previously (section III.1). Secondly, it was used as a homogenization treatment at high temperature in the lower part of the ( $\alpha + \gamma$ ) phase field that led to recrystallization. The conditions of HIPing were 1260 °C under an argon pressure of 170 MPa for 4 hours.

#### *A. Reduction of residual porosity by Hot Isostatic Pressing*

As described previously in section III.1, the EBM process could not produce fully dense materials. Residual porosity, resulting from the process itself and/or the initial powders porosity, was always observed. Therefore, bars as-built by EBM were subjected to HIP with the scope to reduce to the minimum the residual porosity. The following table 28 displays representative micrographs of the average residual porosity of materials as-EBM and as-HIP. The measure of porosity was inserted.

Ti-45Al-2Cr-8Nb		
	As-EBM	As-HIP
<b>EBM 2<sup>nd</sup> Trial</b>	 <p style="text-align: center;">Average porosity : <math>1.1 \pm 0.5</math> %.</p>	 <p style="text-align: center;">Average porosity : <math>0.14 \pm 0.24</math> %.</p>
<b>EBM 5<sup>th</sup> Trial</b>	 <p style="text-align: center;">Average porosity : <math>0.08 \pm 0.13</math> %.</p>	 <p style="text-align: center;">Average porosity : <math>0.14 \pm 0.13</math> %.</p>
Ti-46Al-2Cr-8Nb		
	As-EBM	As-HIP
<b>EBM 5<sup>th</sup> Trial</b>	 <p style="text-align: center;">Average porosity : <math>0.28 \pm 0.32</math> %.</p>	 <p style="text-align: center;">Average porosity : <math>0.06 \pm 0.08</math> %.</p>

**Table 28:** Residual porosity as measured in samples after EBM and after subsequent HIP for Ti-45Al-2Cr-8Nb and Ti-46Al-2Cr-8Nb.

For the 2<sup>nd</sup> EBM Trial that exhibited a residual porosity  $\geq 1\%$ , subsequent hot isostatic pressing drastically reduced the porosity down to an average of  $0.14 \pm 0.24$  %. However, some elongated pores attributed to the process could still be observed and displayed in the figure in table 28. It suggested that HIP in these conditions was not sufficient to completely eliminate the process residual porosity, which led to the subsequent process optimizations described earlier in section III.1.

In the case of the selected EBM conditions (5<sup>th</sup> Trial EBM) used to fabricate both Ti-45Al-2Cr-8Nb and Ti-46Al-2Cr-8Nb alloys, the effect of HIP was not obvious (table 28). The porosity measured as-EBM and as-HIP were similar and the differences resulted from the statistical point of view. Both as-EBM and as-HIP materials showed very low residual porosity  $\ll 1\%$ .

Considering residual porosity, it was found that hot isostatic pressing effectively reduced the porosity resulting from the EBM process. On the other hand, for an optimized EBM process that did not induce residual porosity from unconsolidated and unmelted regions, HIP was not found significantly beneficial. It was therefore concluded that Hot Isostatic Pressing to reduce the residual porosity of the as-EBM  $\gamma$ -TiAl alloys under investigation was not necessary.

### *B. Recrystallization by Hot Isostatic Pressing*

Since HIP was performed at 1260 °C, which is in the ( $\alpha + \gamma$ ) phase field (figure 90), it was expected that the effect of temperature led to a certain recrystallization of the microstructure. The as-EBM microstructure described earlier exhibited an equiaxed microstructure composed by very fine and bigger  $\gamma$  and  $\alpha$  grains (figures 92 and 93). The following tables show representative optical micrographs of the microstructure of Ti-45Al-2Cr-8Nb (table 29) and Ti-46Al-2Cr-8Nb (table 30) after EBM (as-EBM) and after subsequent HIP (as-HIP).

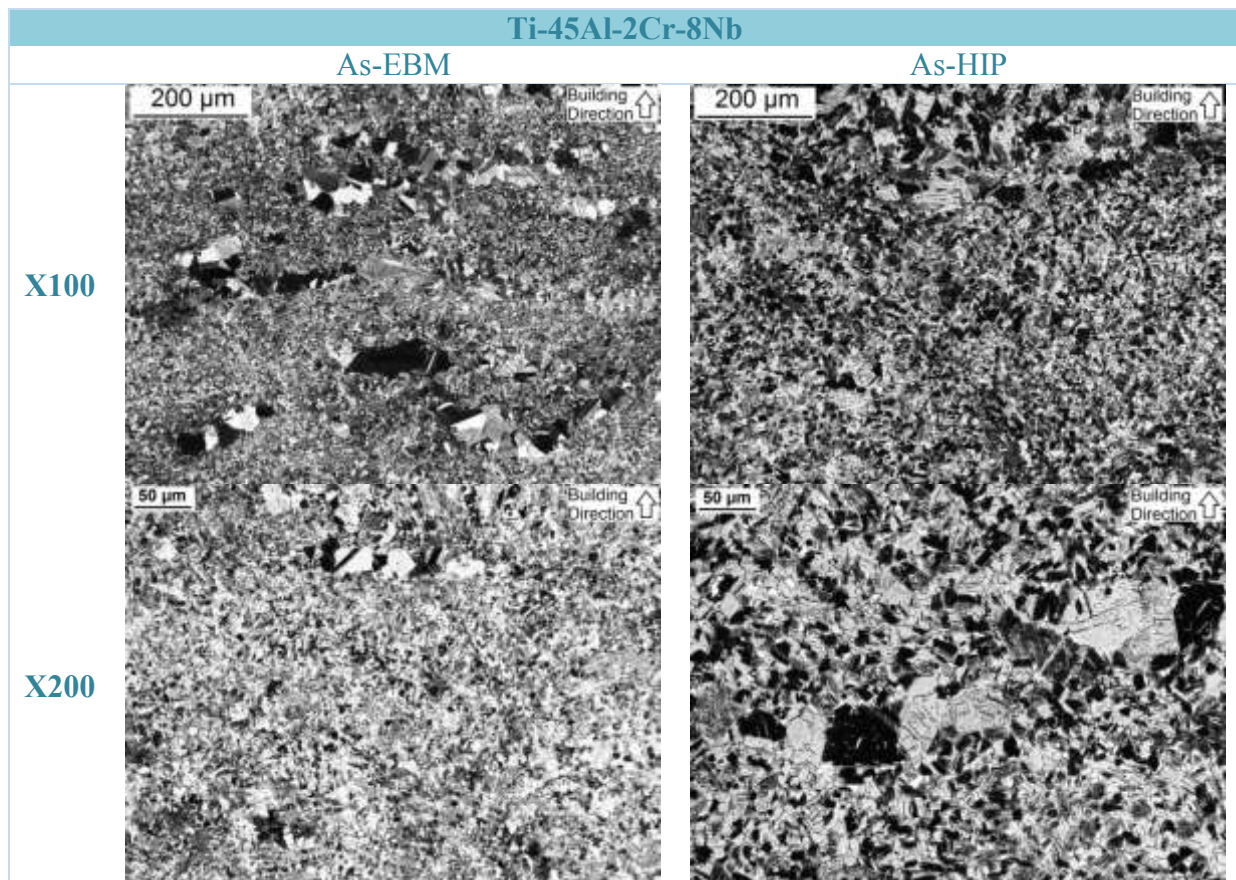


**Table 29:** Optical micrograph at magnifications x100 and x200 of Ti-45Al-2Cr-8Nb alloys after EBM and after subsequent HIP



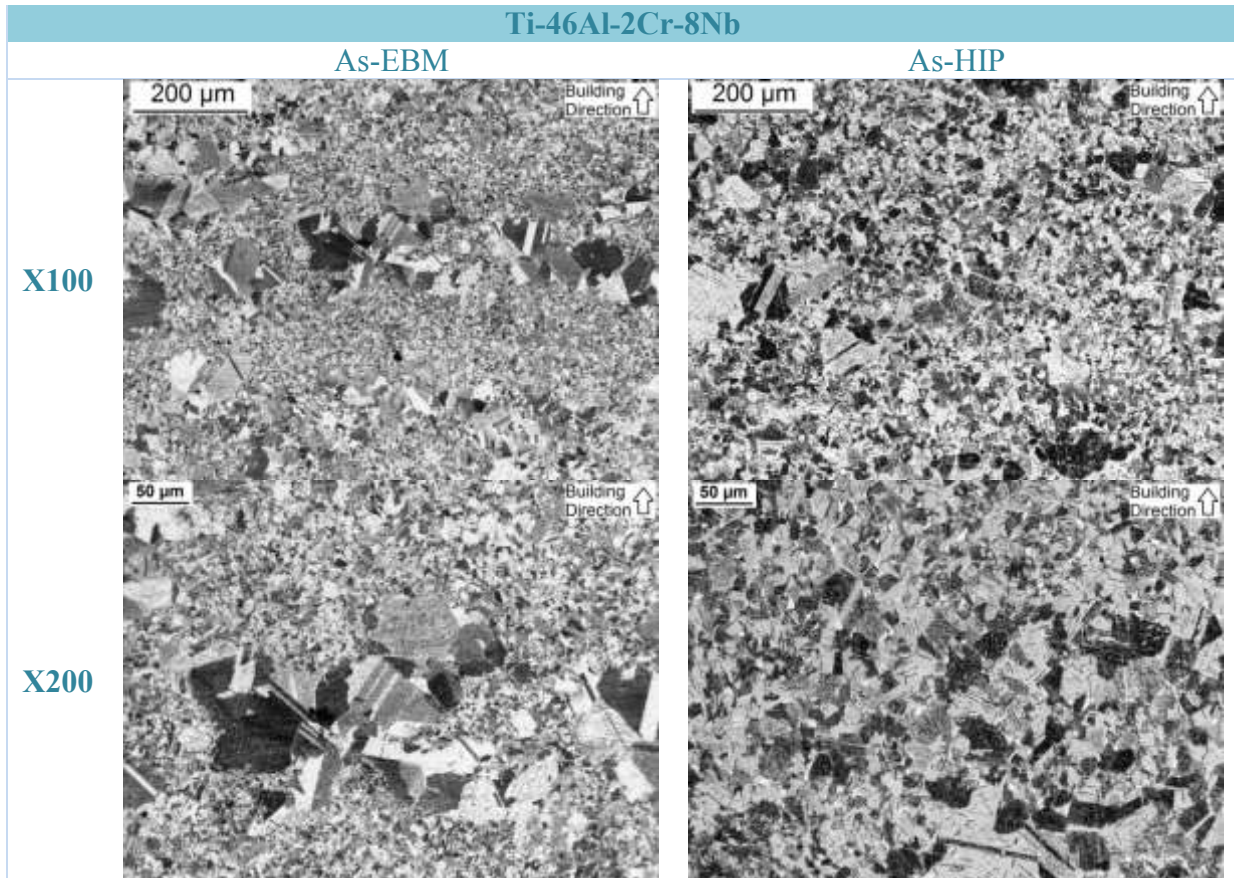


**Table 30:** Optical micrograph at magnifications x100 and x200 of Ti-46Al-2Cr-8Nb alloys after EBM and after subsequent HIP

As it was anticipated considering the high temperature of the HIP treatment, a slight but significant recrystallization could be observed. In particular, growth of the very fine grains was noticed while the maximum grain size remained similar to that of as-EBM materials. This led to an as-HIP microstructure interestingly more homogeneous than as-EBM.

This recrystallization was associated to the temperature only and the role of pressure on that matter was unclear. Samples as-EBM of Ti-45Al-2Cr-8Nb were treated in argon for 4 hours at 1260 °C, that were the same conditions of the HIP treatment without pressure, defined as Simul-HIP or SHIP. The SHIP treatment and all the following heat treatments were realized in a GERO high temperature laboratory furnace type LHTW (figure 108). The schematic drawing of the Simul-HIP treatment is shown figure 109. The x50 magnification micrographs of both materials after HIP and SHIP are displayed in figure 110 and 111 respectively. The micrographs are the reconstruction of x50 images taken edge to edge of the samples and stitched together. The microstructure was symmetrical with respect to the center of the cylindrical samples. Figure 110 and 111 thus represent the microstructures along the layer deposition direction from edge to core.



**Figure 108:** GERO furnace for heat treatment of  $\gamma$ -TiAl alloys

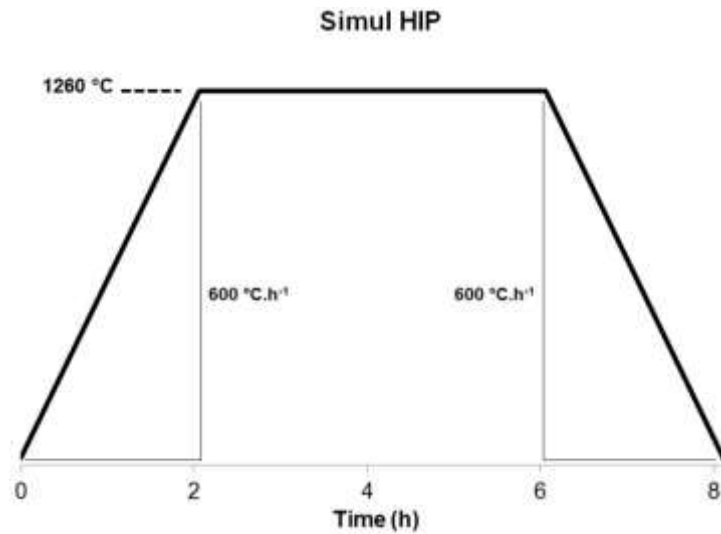


Figure 109: Schematic drawing of the Simul-HIP treatment

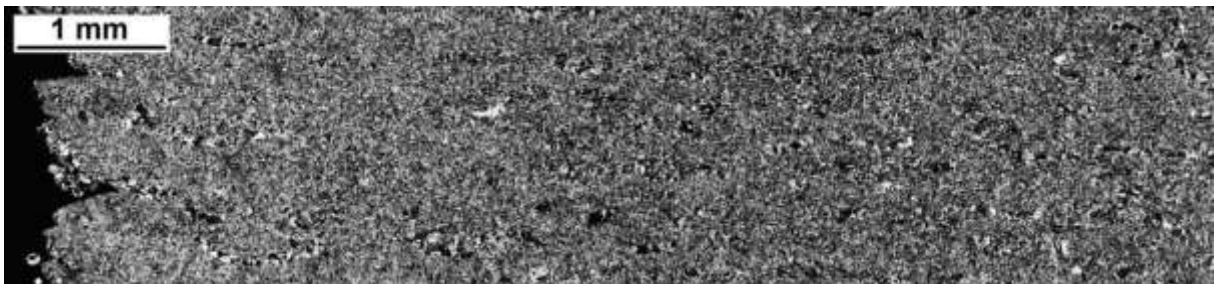


Figure 110: Optical micrograph at magnification x50 of Ti-45Al-2Cr-8Nb after HIP (1260 °C, 170 MPa, 4h, Argon)

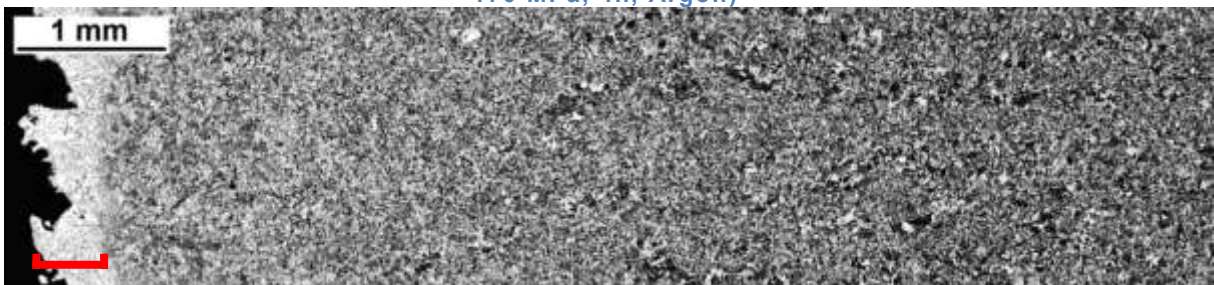


Figure 111: Optical micrograph at magnification x50 of Ti-45Al-2Cr-8Nb after SHIP (1260 °C, 4h, Argon)

The fine equiaxed microstructures of HIP and SHIP of Ti-45Al-2Cr-8Nb alloys were very similar (figure 110 and 111) which suggested that the pressure had little influence on microstructure. The materials were treated in different furnaces (HIP furnace and GERO furnace) by different organization (Avio's supplier for HIP and DISAT for SHIP). Yet the microstructures were very alike, confirming the dominant role of temperature.

Vickers microhardness measurements were done on both HIP and SHIP Ti-45Al-2Cr-8Nb alloys. A set of 10 imprints were realized on each materials. The average Vickers microhardness values were reported in the following table 31.

Alloy Ti-45Al-2Cr-8Nb	Microhardness (Hv)
HIP	322 ± 19
SHIP	326 ± 12

**Table 31:** Vickers microhardness of Ti-45Al-2Cr-8Nb after HIP and SHIP treatment

The microhardness of HIP and SHIP Ti-45Al-2Cr-8Nb materials were very similar. It suggested that both HIP and SHIP microstructure were equivalent. HIP advantageously recrystallized the as-EBM microstructure more homogeneously. However, the same result could be obtained more economically through conventional heat treatment in argon (to avoid severe oxidation at high temperature) in the same conditions (4 hours at 1260 °C).

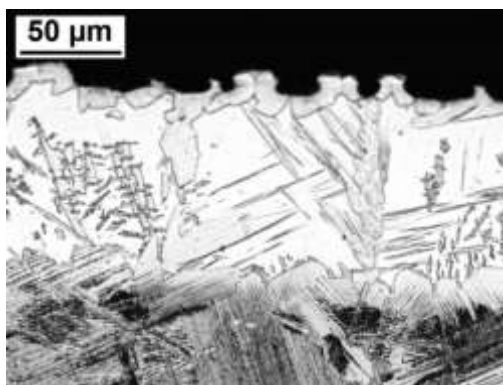


**Figure 112:** Top surface of a Ti-46Al-2Cr-8Nb sample HIPed and subsequently heat treated at 1315 °C for 2h in vacuum in GERO furnace.

The main difference observed for SHIP with respect to HIPed materials was a white zone at the very edge of the sample, highlighted in figure 111 by a red bracket. This defect was identified for all samples treated in DISMIC in the GERO furnace. It was thus concluded that it resulted from the heat treatment. It was in particular also observed on the top surface of every small cylindrical samples (figure 78B). The opposite figure 112 shows this defect on the top surface of a HIPed Ti-46Al-2Cr-8Nb sample after subsequent treatment at 1315 °C.

The reason was not clear and different cause have been assessed. It was suggested that the pressureless Ar environment in the GERO furnace could be responsible. Else, materials from the furnace chamber (tungsten, molybdenum, alumina) could diffuse on the sample's surface during the treatment. In any case, these defect zones which composition was not studied were limited and would anyway be removed chemically after heat treatments at the same time of the Al-depleted contour.

## 2. Heat treatments around $T_\alpha$ to set the microstructure

The heat treatments were done in the electric GERO furnace (figure 108). All treatments were realized under high vacuum ( $10^{-4}$  mbar) to avoid oxidation. Figure 113 shows four cylindrical  $\gamma$ -TiAl samples installed in the chamber. Heat treatments were usually performed one sample at a time, positioned in the center of the chamber to increase homogeneity of the temperature. A schematic drawing of the heat treatment is displayed figure 114.

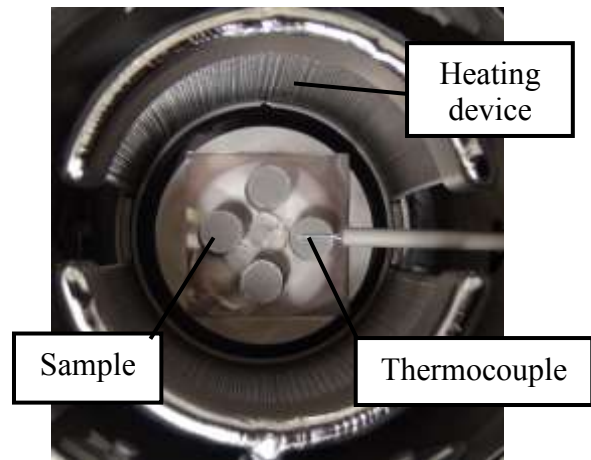


**Figure 113:** 4 TiAl samples in the furnace chamber of the GERO furnace for heat treatments

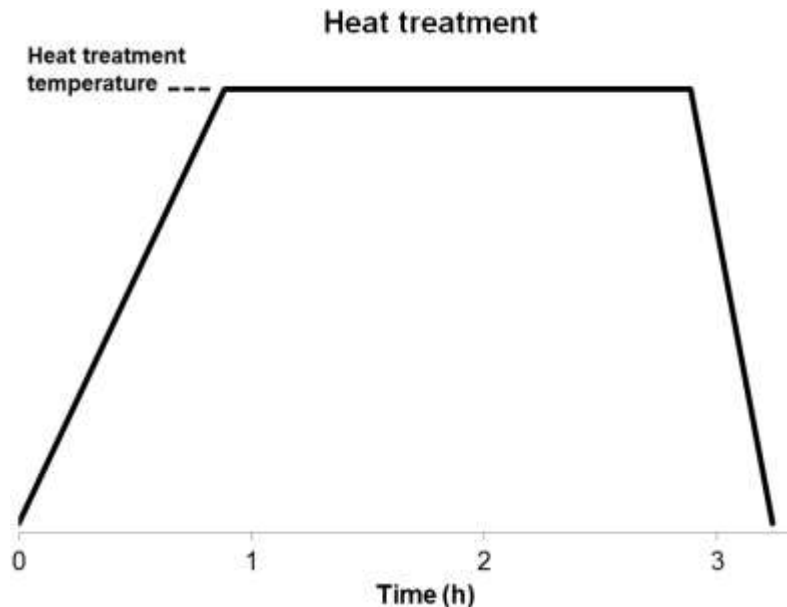


**Figure 114:** Schematic drawing of the heat treatment performed in GERO furnace under high vacuum ( $10^{-4}$  mbar)

10 mm height cylindrical samples (figure 78B) were heat treated in the GERO furnace. Samples were hold at the selected heat treatment temperature for 2 hours. Finally, the samples were furnace cooled down to room temperature.

### A. Set-up of Ti-45Al-2Cr-8Nb's microstructure

Samples of the Ti-45Al-2Cr-8Nb alloy were cut out of as-built EBM bars. The base microstructure, weather as-EBM or as-HIP, consisted of a mixture of fine equiaxed  $\alpha$  and  $\gamma$  grains. Heat treatment in the vicinity of the  $\alpha$ -transus temperature  $T_\alpha$  would produce a duplex microstructure composed by fine equiaxed grains and coarser lamellar grains. The higher the heat treatment temperature the higher the amount of lamellar grains, up to a fully lamellar microstructure.  $T_\alpha$  was identified by TMA at 1295 °C for Ti-45Al-2Cr-8Nb (figure 106). Heat treatments were therefore performed on as-EBM samples, which had not been Simul-HIPed, every 5 °C from 1285 °C to 1310 °C.

Figure 115 shows the microstructure of the samples after treatment. The micrographs are the reconstruction of x50 images taken edge to edge of the samples and stitched together, thus representing by symmetry the microstructure over the whole section. The phase diagram in figure 115 was taken from the partial phase diagram for Ti-Al containing 8 at.% of niobium according to Chen et al (figure 90) <sup>[112]</sup>.

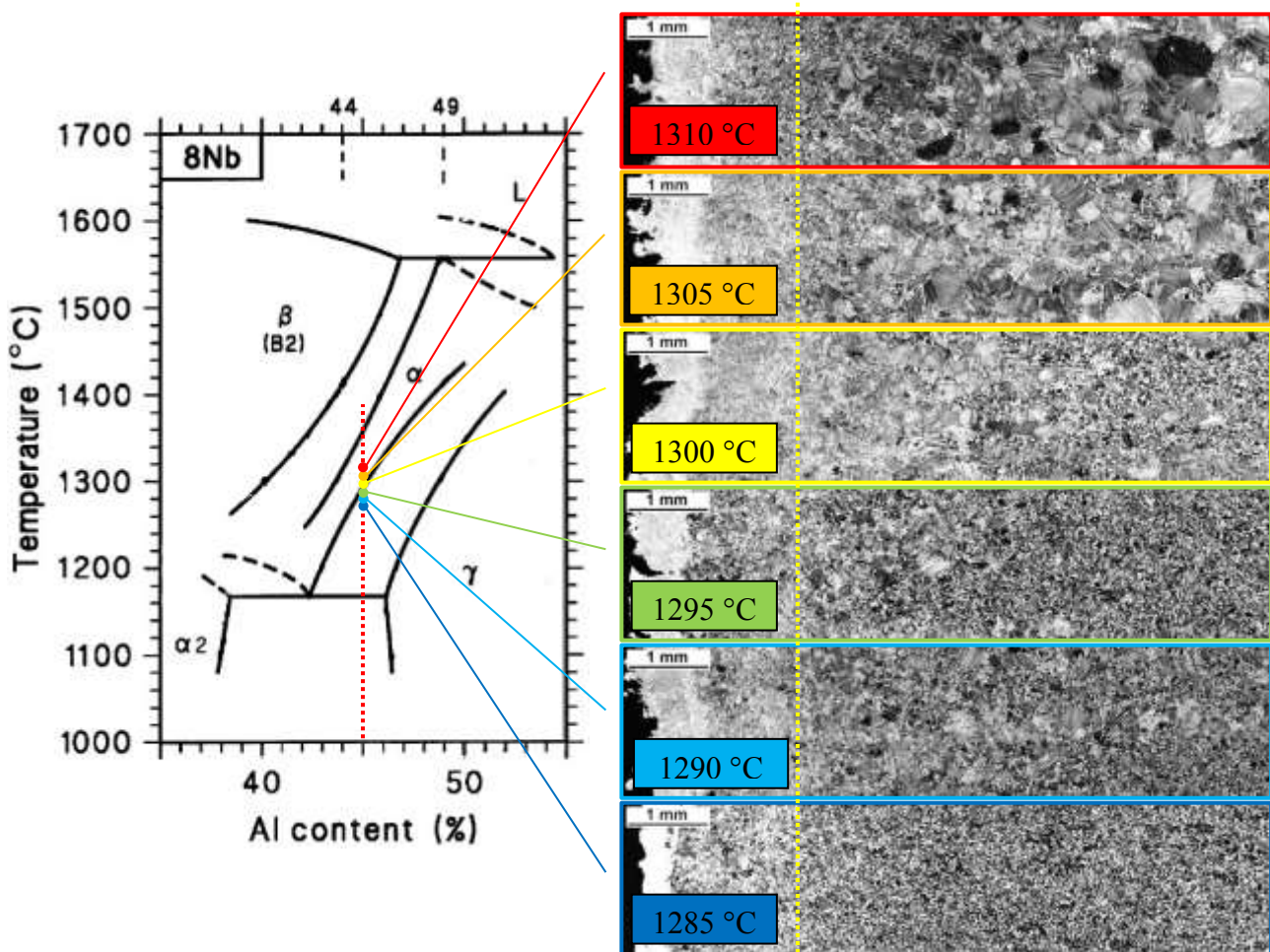


**Figure 115:** Optical micrographs representing the microstructure along the layer deposition direction of as-EBM Ti-45Al-2Cr-8Nb alloys treated at different temperatures in the vicinity of  $T_{\alpha} = 1295 \text{ }^{\circ}\text{C}$

In figure 115, it is obviously observed the evolution of microstructure in correspondence to the heat treatment temperature. As first consideration, the external 2mm Al-depleted contour should not be taken into account. The yellow dotted line in figure 115 illustrates the virtual border. As expected, the microstructure was significantly different in the external contour and the core of the sample.

At 1285 °C, the microstructure was very similar to that of the SHIP samples (figure 111). The first lamellar grains could be observed after heat treatment at 1290 °C. After treatment at 1295 °C, slightly under 50 % lamellar grains were counted, in a lesser amount at the very core of the sample. At 1300 °C, over 50 % of lamellar grains were more homogeneously distributed among fine equiaxed  $\alpha$  and  $\gamma$  grains. However, at such lamellar ratio a substantial inhomogeneity of the microstructure throughout the sample was observed. The lamellar grains ratio and average lamellar grain size increased when the temperature increased to 1305 °C. Also, the microstructure was homogeneous and lamellar grains were uniformly distributed. After treatment at 1310 °C for 2 hours the microstructure was nearly lamellar, consisting in 90 % of coarse lamellar grains pinned mostly at grain boundaries by fine equiaxed grains. Over 1315 °C, the microstructure was fully lamellar composed by coarse (300-500  $\mu\text{m}$ ) lamellar  $\gamma/\alpha$  colonies.

The fine equiaxed as-EBM microstructure could be modified by simple heat treatments at a temperature around  $T_{\alpha}$  (figure 115). The microstructure could thus be set-up from the as-EBM fine equiaxed to duplex with any lamellar grain ratio, up to coarse fully lamellar. The mechanical properties of  $\gamma$ -TiAl alloys are very sensitive to microstructure. Therefore, the ability to set any microstructure by simple post-processing heat treatment is of great interest.

The Vickers hardness were measured for the different microstructures in figure 115. A set of 10 measurements were realized on Ti-46Al-2Cr-8Nb and the average value was calculated. The following table 32 displays the values of Vickers hardness measured on samples treated at different temperature, exhibiting as-HIP microstructure and duplex microstructure with 35 and 80 % of lamellar grain quantified according to ASTM E562-01.

Microstructure	Hardness (Hv)
HIP	272 $\pm$ 3
lamellar ratio: 35 %	343 $\pm$ 17
lamellar ratio: 80 %	291 $\pm$ 4

**Table 32:** Vickers hardness measurements and corresponding yield strength according to Kim et al. of Ti-46Al-2Cr-8Nb alloys with different microstructure

The standard deviation of the hardness measurements in table 32, significantly high for a lamellar ratio of only 35 %, resulted from the inhomogeneity of the microstructure previously mentioned.

Samples as-EBM and as-HIP of Ti-45Al-2Cr-8Nb were treated together and the microstructures of both materials were analyzed. Figure 116 shows the microstructures of as-EBM and as-HIP specimens after heat treatment at different temperatures. In general terms, the microstructures of samples that had been subjected to HIP were obtained with treatments at temperatures 5 °C lower with respect to as-EBM materials.

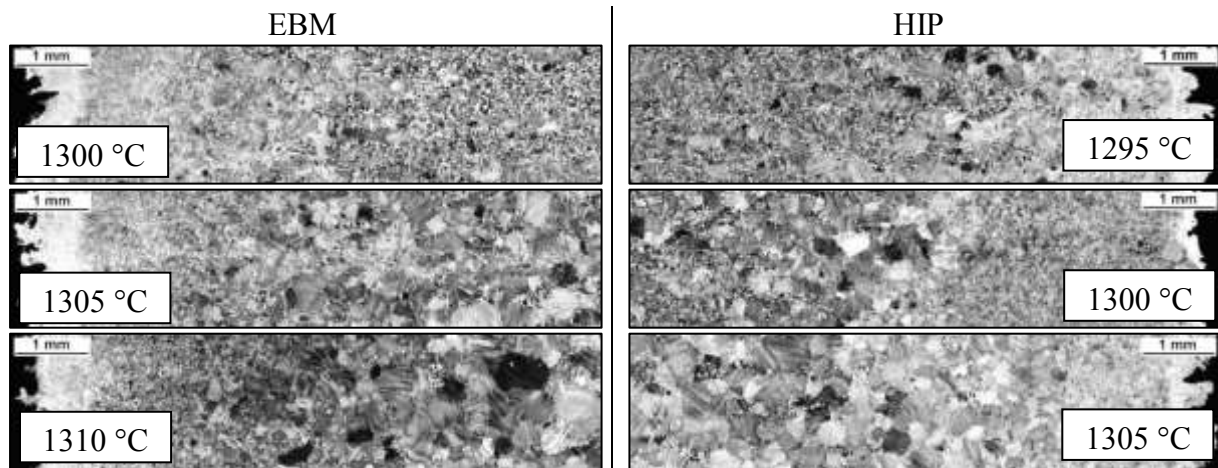


**Figure 116:** Duplex microstructures of Ti-45Al-2Cr-8Nb obtained by heat treatment at 1300, 1305 and 1310 °C for EBM materials and 1295, 1300, 1305 °C for EBM + HIP materials.

The microstructure of EBM materials obtained after heat treatment at 1300 °C was very similar to that of materials that had been subjected to subsequent HIP after processing and treated at 1295 °C. The lamellar ratio of EBM specimens treated at 1300 °C was slightly over 50 %, while lamellar ratio of HIP specimens treated at 1295 °C was about 65 %. At temperatures 5 and 10 °C higher, the correlations were even closer. The lamellar ratio of EBM and HIP specimens treated at 1305 and 1300 °C were 72 % and 73 % respectively. Likewise, the lamellar ratio of EBM and HIP specimens treated at 1300 and 1305 °C were 87 % and 90 % respectively (figure 116).

The reason of such a behavior was not clear. Initially, it was believed that the recrystallization induced by HIP was responsible (tables 29 and 30). However, as-EBM samples had been Simul-HIP (figure 109) and subsequently heat treated in the same conditions (figure 116). Even though the original microstructures of Simul-HIP specimens were similar to that of HIP specimens, the microstructures after heat treatment of Simul-HIP samples were similar to that of heat treated as-EBM specimens (left side in figure 116). It was therefore assumed that the pressure during HIP could have an effect.

However, the control of the actual temperature in the GERO furnace was critical and regular calibrations were needed. To control the actual temperature in the GERO furnace, pure copper and iron were heated around their melting temperature (1083 °C for Cu and 1536 °C for Fe). The difference between the actual temperature in the furnace and the setpoint temperature could thus be determined. The HIP specimens have been heat treated significantly later than the EBM specimens and no calibration was done in between. It was therefore most likely that the actual heat treatment temperatures were slightly different even though the setpoint temperatures were equal. At that point of the study, a 5 °C difference was hardly identified.

### B. Set-up of Ti-46Al-2Cr-8Nb's microstructure

The 3<sup>rd</sup> generation  $\gamma$ -TiAl alloy under investigation containing higher content of aluminum was also treated for microstructural set-up. Samples as-EBM and as-HIP of Ti-46Al-2Cr-8Nb were treated together and the microstructures of both materials were analyzed. Figure 117 shows the microstructures of as-EBM and as-HIP specimens after heat treatment at different temperatures.

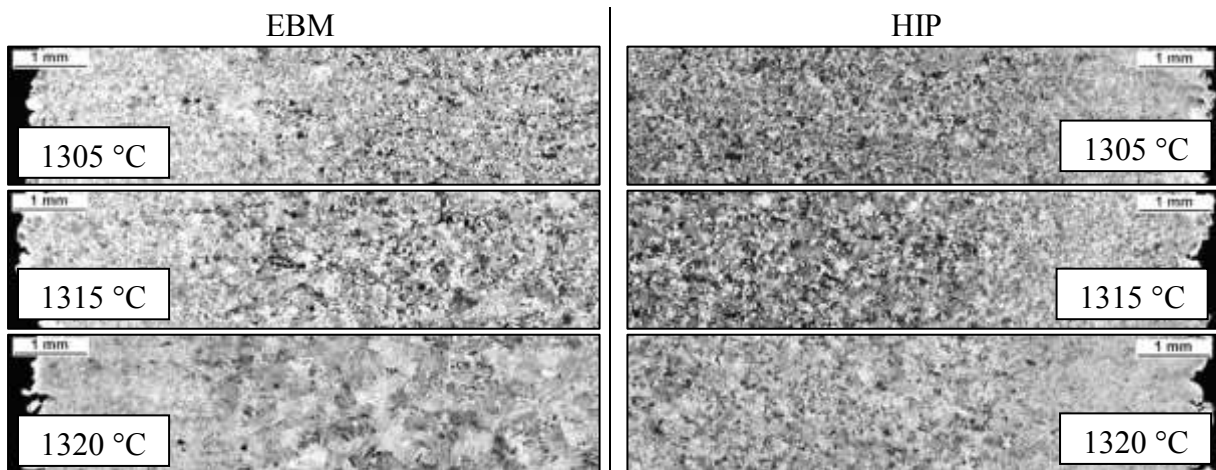


**Figure 117: Duplex microstructures of Ti-46Al-2Cr-8Nb obtained by heat treatments at 1305, 1315 and 1320 °C for EBM and EBM + HIP materials.**

The  $\alpha$ -transus temperature of Ti-46Al-2Cr-8Nb identified by TMA was  $T_{\alpha} = 1305$  °C (figure 116), which is 10 °C higher than that of Ti-45Al-2Cr-8Nb. It was therefore expected that heat treatment of Ti-46Al-2Cr-8Nb at temperatures 10 °C higher with respect to Ti-45Al-2Cr-8Nb would set similar microstructures. As first consideration, the difference of microstructure between EBM and EBM + HIP samples treated at the same temperature was less obvious in figure 117. This time, EBM and EBM + HIP samples have been treated at the same time. It thus suggested that the difference observed figure 116 likely resulted from the calibration as suggested. Measures over a bigger area of the samples showed the microstructure had a lamellar ratio only about 5 % higher for HIPed specimens although the average lamellar grain size was smaller.

In the case of Ti-46Al-2Cr-8Nb, the set-up of the desired microstructure was achieved as well. As it was anticipated from TMA analysis, heat treatments at temperatures 10 °C higher with respect to Ti-45Al-2Cr-8Nb led to similar microstructures. Lamellar grains ratio of about 75 % was achieved by heat treatment at 1315 °C for 2 hours. Lamellar grains ratio of about 90 % was achieved by heat treatment at 1320 °C for 2 hours.



### *C. Details of the 80 % lamellar microstructure*

The heat treatment was selected with regards to the materials properties, strongly dependent on the microstructure for a given composition. Therefore, the best compromise should be found to obtain satisfying properties at all temperatures. With regards to creep resistance, a high amount of coarse lamellar grains is sought. The presence of a low amount of fine equiaxed grains is also desirable to increase ductility at low temperatures. Considerations on fracture toughness of  $\gamma$ -TiAl alloys recommend a lamellar grains ratio higher than 70 %. Regarding the tensile properties, a duplex microstructure with rather fine lamellar grains is suitable.

With these considerations, Ti-(45-46)Al-2Cr-8Nb alloys were treated to obtain a duplex microstructure composed by 80 % to 90 % of lamellar grains pinned by fine equiaxed grains preferably at grain boundaries. Ti-45Al-2Cr-8Nb and Ti-46Al-2Cr-8Nb alloys in as-EBM conditions were therefore heat treated at 1305 °C and 1320 °C respectively. The heat treatment temperature for Ti-45Al-2Cr-8Nb was 1305 °C rather than 1310 °C which exhibited lamellar grains significantly bigger (figure 116).

Figure 118 shows the microstructure of Ti-45Al-2Cr-8Nb treated at 1305 °C in the GERO furnace according to the heat treatment described figure 114. The microstructure in the edge and the core of the sample are highlighted at magnification x100 (figure 118B and 118C) and x200 (figure 118D and 118E).

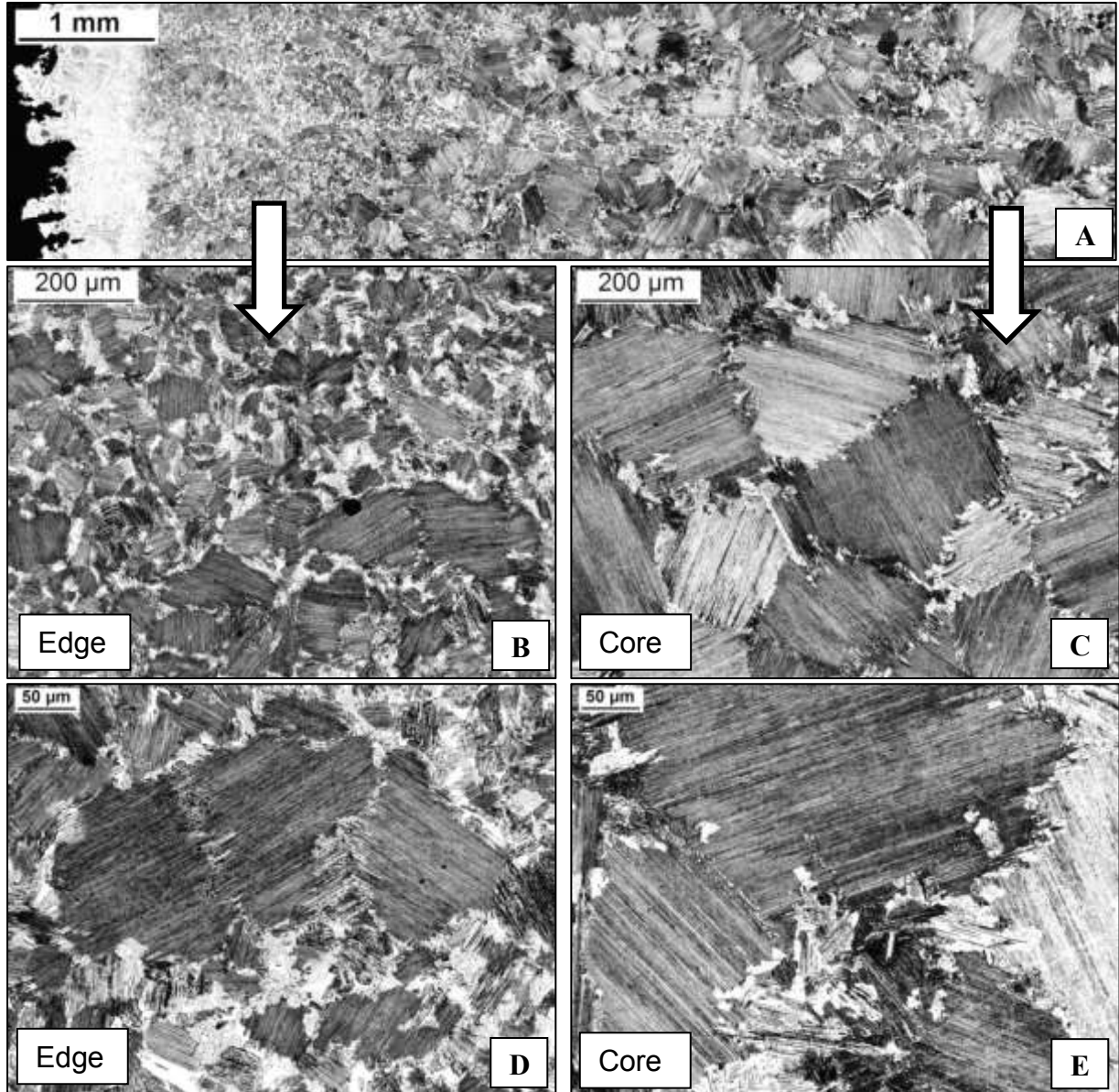


**Figure 118:** Optical micrographs showing the microstructure of as-EBM Ti-45Al-2Cr-8Nb material heat treated at 1305 °C for 2 hours in vacuum. A is the composition of images taken at magnification x50 stitched together, B and C were taken at magnification x100 respectively in the edge and the core of the specimen, D and E were taken at magnification x200 respectively in the edge and the core of the specimen

The microstructure in the core of Ti-45Al-2Cr-8Nb after heat treatment at 1305 °C was homogeneous. It was composed by 80 % of lamellar grain with a size comprised between 100 and 300  $\mu\text{m}$ . At lamellar grain boundaries, fine equiaxed grains smaller than 50  $\mu\text{m}$  were observed.

Figure 119 shows the microstructure of Ti-46Al-2Cr-8Nb treated at 1320 °C in the GERO furnace according to the heat treatment described figure 114. The microstructure in the edge and the core of the sample are highlighted at magnification x100 (figure 119B and 119C) and x200 (figure 119D and 119E).

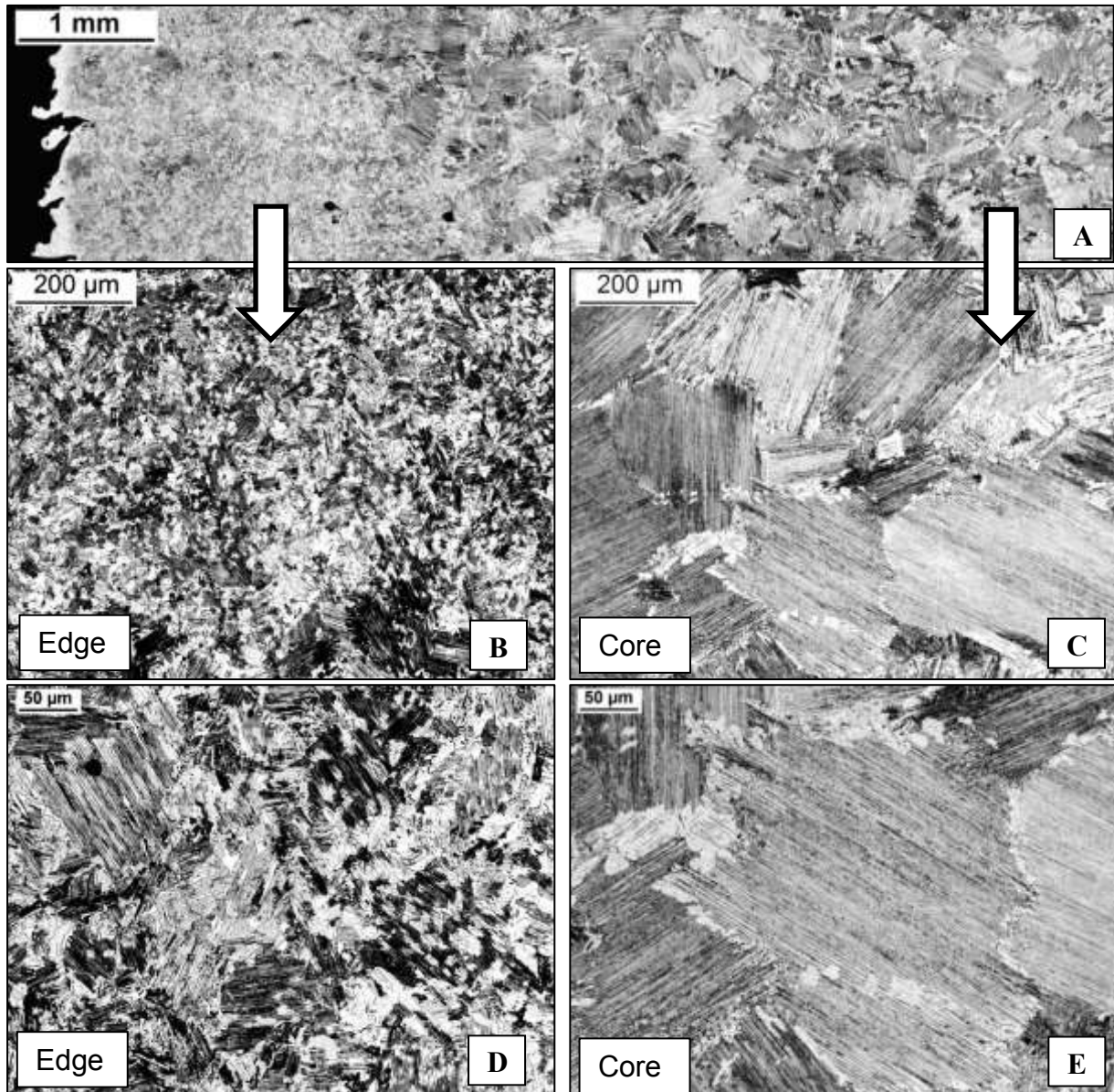


**Figure 119:** Optical micrographs showing the microstructure of as-EBM Ti-46Al-2Cr-8Nb material heat treated at 1320 °C for 2 hours in vacuum. A is the composition of images taken at magnification x50 stitched together, B and C were taken at magnification x100 respectively in the edge and the core of the specimen, D and E were taken at magnification x200 respectively in the edge and the core of the specimen

The microstructure in the core of Ti-46Al-2Cr-8Nb after heat treatment at 1320 °C was very similar to that of Ti-45Al-2Cr-8Nb after heat treatment at 1305 °C (figure 118), composed by 80 % of lamellar grain with a size comprised between 100 and 300 μm and pinned by fine equiaxed grains smaller than 50 μm.

The external contour, about 2 mm wide, contained an Al content significantly lower than the core. This was most likely due to higher evaporation of aluminum during the EBM process. This consideration was confirmed on the one hand by TMA which exhibited  $T_{\alpha}(\text{edge}) < T_{\alpha}(\text{core})$  (figure 107), suggesting a lower amount of aluminum (figure 90). On the other hand, atomic absorption analysis of materials from the core and the edge of as-built specimens also confirmed an Al depletion in the edge (table 27).

The optical micrographs exhibited a microstructures which further confirmed a lower amount of aluminum in the edge. From the revised phase diagram displayed in figure 90, both 45Al and 46Al alloys pass through the  $\beta$ -phase field upon solidification. In figure 90, the less the Al content the more the amount of  $\beta$ -phase. This soft phase is of particular interest for wrought alloys because it allowed hot working. However, this phase is detrimental for creep resistance. In the case of EBM materials, the  $\beta$ -phase is rather to avoid since this near-net-shape process does not need post-processing shaping [48, 59, 128-135].

Figures 120 and 121 show the microstructure at high magnification (x500) in the edge and in the core of Ti-45Al-2Cr-8Nb and Ti-46Al-2Cr-8Nb respectively.

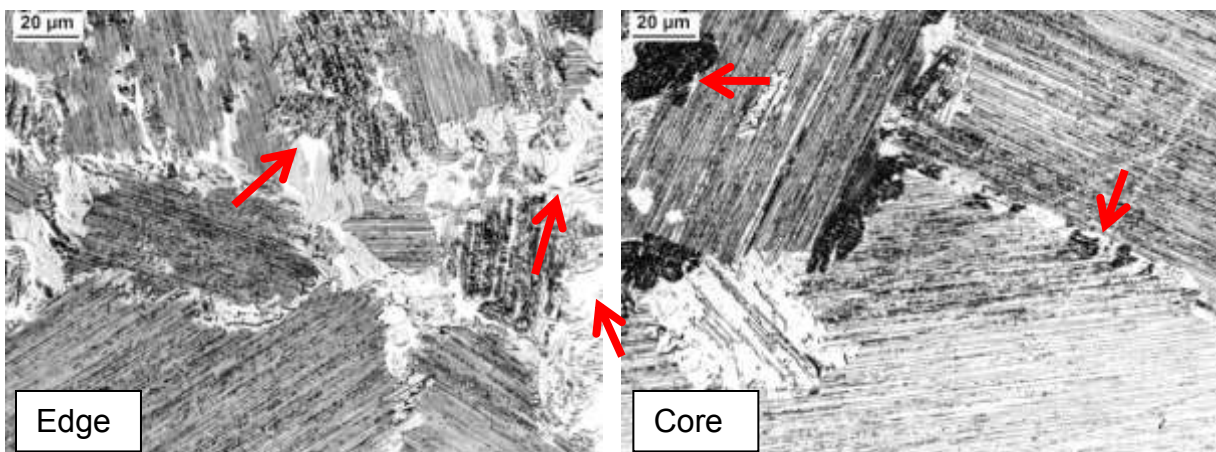


**Figure 120:** High magnification (x500) optical micrographs taken in the edge and the core of as-EBM Ti-45Al-2Cr-8Nb heat treated at 1305 °C

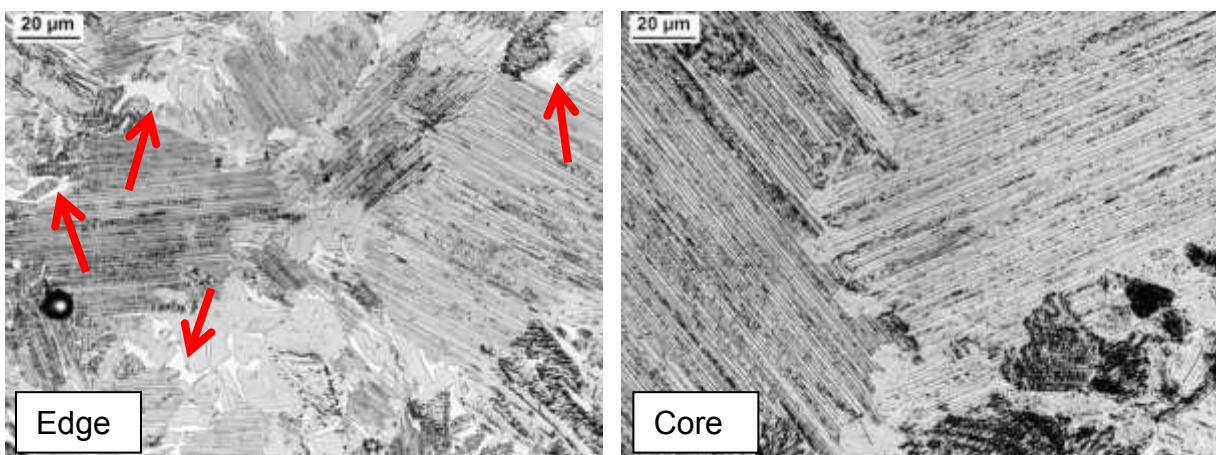


**Figure 121:** High magnification (x500) optical micrographs taken in the edge and the core of as-EBM Ti-46Al-2Cr-8Nb heat treated at 1320 °C

In figures 120 and 121, a rather high amount of  $\beta$ -phase can be observed. Such phase, which appears bright white with no preferential shape, was highlighted by red arrows. The edge of the samples contained definitely more amount of  $\beta$ -phase than the core. The same observation could be made at lower magnification figures 118 and 119. In the core, a few amount of  $\beta$ -phase could be observed randomly distributed mostly at grain boundaries. In any case, the higher amount of  $\beta$ -phase in the edge of the sample confirmed the lower amount of aluminum in the edge.

As can be seen figure 118 for Ti-45Al-2Cr-8Nb and figure 119 for Ti-46Al-2Cr-8Nb, the microstructure in the edge of sample treated at 1305 °C and 1320 °C respectively was composed by fine lamellar grains, very fine equiaxed grains and  $\beta$ -phase at the grain boundaries. Not only the aluminum content was lower in the edge due to higher evaporation during the EBM process, the effects of temperature and cooling rate were different between the edge and the core.

## **V. Oxidation behavior of 2<sup>nd</sup> and 3<sup>rd</sup> generation $\gamma$ -TiAl alloys**

$\gamma$ -TiAl based alloys have received much attention in the past 20 years as alternative light-weight materials for high temperature structural applications, with particular interest for aeroengines and turbochargers rotating parts [48, 50, 53-56, 59, 65-68, 70-74, 76, 77, 88, 110, 112-118, 160]. Such applications require specific material properties such as high temperature strength, fatigue strength, fracture toughness, room-temperature ductility. Moreover, temperature in the aeroengine turbines and the last stages of the high pressure compressor exceeds 700 °C and can be as high as 1000 °C in turbochargers for gasoline engines. Thus, oxidation resistance at high temperature is a critical property of  $\gamma$ -TiAl based alloys.

Much research have focused on enhancing the oxidation resistance of TiAl based alloys by means of material's selection and processing. The poor oxidation resistance of  $\gamma$ -TiAl is attributed to the deficiency of external alumina scales and undesired rapid growth of rutile [48, 56, 67, 76, 88, 110, 111, 114, 116, 161]. While microstructure has little influence on the oxidation behavior of  $\gamma$ -TiAl, alloying elements addition is found promising in order to increase significantly the oxidation resistance and keep a good balance of mechanical properties [48, 50, 53, 56, 70, 76, 110, 111, 114, 160, 162]. This led to the development of third generation  $\gamma$ -TiAl, highly alloyed with refractory elements for high temperature applications. Nb, Ta, Mo, W, Si, B, Zr, Cl when added in a proper range are substantially beneficial with regards to  $\gamma$ -TiAl oxidation resistance.

It has been widely accepted the beneficial effect of Nb [48, 50, 54-56, 67, 70, 72, 75-77, 86, 88, 102, 110, 111, 113, 114, 160, 162]. In addition to an enhanced creep resistance,  $\gamma$ -TiAl alloyed with Nb exhibit a significant increase in oxidation resistance. Having a higher value of valence than Ti, Nb is believed to reduce the oxygen vacancy concentration thus slowing down rutile growth. The Nb content should be over 2 at.% to show some benefits and kept under 20 at.% to prevent the formation of Nb<sub>2</sub>O<sub>5</sub> detrimental for oxidation resistance.

The alloys under investigation in this study had a nominal composition of Ti-45Al-2Cr-8Nb and Ti-46Al-2Cr-8Nb. The higher content of Nb with respect to 2<sup>nd</sup> generation  $\gamma$ -TiAl alloys suggests increased oxidation resistance of the studied 3<sup>rd</sup> generation alloys, regardless the fabrication method. Therefore, the oxidation behavior of the studied alloys Ti-45Al-2Cr-8Nb and Ti-46Al-2Cr-8Nb produced by Electron Beam Melting were investigated. The oxidation tests were systematically carried on the 2<sup>nd</sup> generation Ti-48Al-2Cr-2Nb alloy as well, produced by EBM too. This study was published in the EuroPM 2013 Proceedings<sup>[67]</sup>.

## 1. Thermogravimetric analysis in air up to 1000 °C

Small 5x5x5 mm<sup>3</sup> cubic samples of Ti-45Al-2Cr-8Nb, Ti-46Al-2Cr-8Nb and Ti-47Al-2Cr-2Nb were precisely cut from the core of as-EBM bars for thermogravimetric analysis (Mettler Toledo AG – TGA/STDA851e). Particular care was taken so that samples from both alloys were identical in order to avoid shape influence on the oxidation performance, in particular due to different surface-core ratios. The specimens were continuously heated in a 50 mL.min<sup>-1</sup> air flow from 25 to 750 °C with a heating rate of 10 °C.min<sup>-1</sup>. From 750 °C to 1000 °C, the heating rate was reduced to 0.5 °C.min<sup>-1</sup> in order to reduce dynamic effects. Figure 122 shows the results of the thermogravimetric analysis. The graph plots the mass gain in percentage as a function of temperature and highlights the 750 - 1000 °C portion in which the heating rate was reduced to 0.05°C.min<sup>-1</sup>.

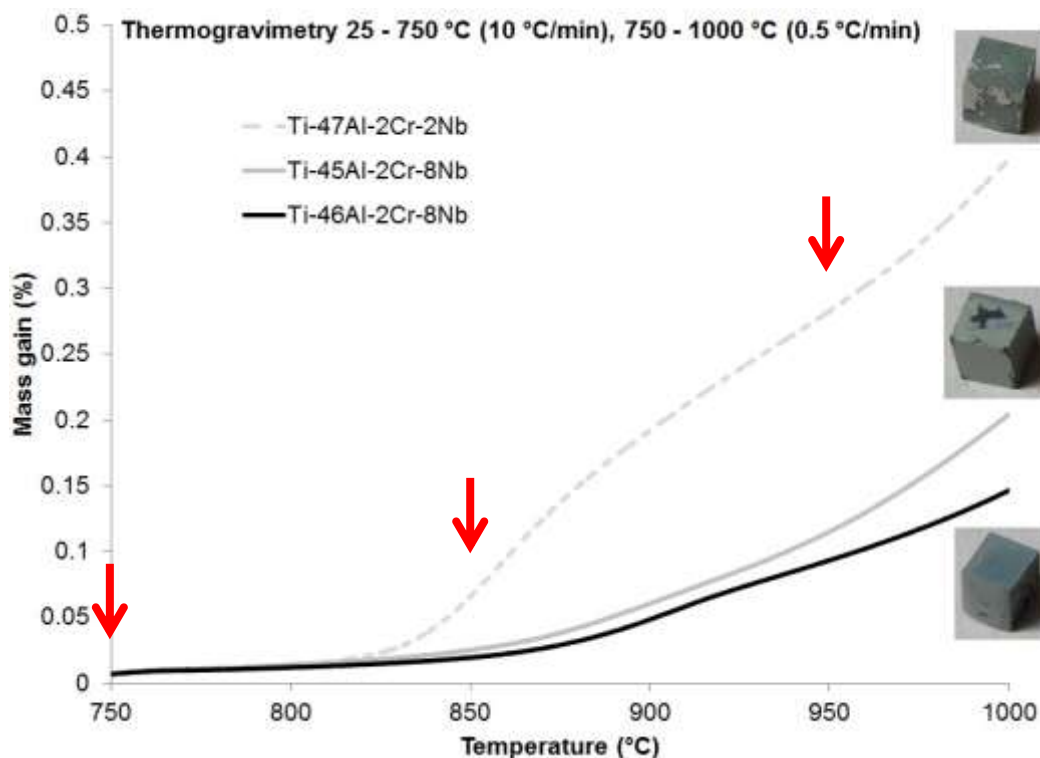


**Figure 122:** Mass gain versus temperature of Ti-45Al-2Cr-8Nb, Ti-46Al-2Cr-8Nb and Ti-47Al-2Cr-2Nb during heating in air from 25 to 750 °C at 10 °C.min<sup>-1</sup> and from 750 to 1000 °C at 0.05 °C.min<sup>-1</sup>. The figure highlights the 750 - 1000 °C portion of the graph

In figure 122, it is clearly observed a significant increase in the oxidation rate of Ti-47Al-2Cr-2Nb around 830 °C, which is not evidenced for Ti-45Al-2Cr-8Nb and Ti-46Al-2Cr-8Nb. Except from this noticeable difference, the oxidation behavior of the  $\gamma$ -TiAl alloys were very similar. It suggested that at a certain critical temperature the lowly alloyed Ti-47Al-2Cr-2Nb was subjected to accelerated oxidation, which the high content of Nb of Ti-(45-46)Al-2Cr-8Nb seemed to suppress or rather postpone. From figure 122, the oxidation rate of all three materials were similar at the end of the experiment although the increase of the oxidation rate appeared smoother in the case of high Nb containing Ti-(45-46)Al-2Cr-8Nb alloys. At the end of the experiment, Ti-47Al-2Cr-2Nb exhibited a mass gain of about 0.39 % with respect to the initial weight of the sample. On the other hand, a mass gain of about 0.20 % was observed for Ti-45Al-2Cr-8Nb and 0.15 % for Ti-46Al-2Cr-8Nb.

Regarding the 3<sup>rd</sup> generation alloys containing high content of Nb, the oxidation behavior during constant heating were very similar. When temperature raised over 850 °C, the mass gain of Ti-46Al-2Cr-8Nb was slightly lower than that of Ti-45Al-2Cr-8Nb. This was anticipated since the higher amount of Al in Ti-46Al-2Cr-8Nb is beneficial for oxidation resistance, promoting the formation of alumina Al<sub>2</sub>O<sub>3</sub> over rutile TiO<sub>2</sub>.

Pictures of the samples after the test were integrated in figure 122 in correspondence to the proper curve. The Ti-48Al-2Cr-2Nb specimen presented major spallation of the surface. Almost the entire external layer was removed. In the case of Ti-(45-46)Al-2Cr-8Nb alloys, the spallation was much lower. The color of the external layers gave a hint about the nature of the oxides. The green yellowish was typical of rutile while clearer area suggested alumina. The more the sample was oxidized the more its aspect was rutile-like (figure 122).

From the thermogravimetric analysis represented figure 122, three critical temperatures were identified: 750 °C, 850 °C and 950 °C indicated by red arrows. At 750 °C, all three materials showed almost no sign of mass gain due to oxidation. At 850 °C on the other hand, Ti-47Al-2Cr-2Nb only exhibited a critical increase of the oxidation rate. Finally at 950 °C, the oxidation of the three materials were similar, slightly lower for the high Nb containing alloys.

## 2. Thermogravimetric analysis in air during isothermal oxidation at 750, 850 and 950 °C for 10 hours.

Thermogravimetric analysis (TGA) were realized on Ti-47Al-2Cr-2Nb, Ti-45Al-2Cr-8Nb and Ti-46Al-2Cr-8Nb alloys during isothermal oxidation for 10 hours at the critical temperatures identified in the previous section. Small 5x5x5 mm<sup>3</sup> cubic samples were precisely cut from the core of as-EBM bars and heated at 10 °C.min<sup>-1</sup> up to a temperature of 750, 850 and 950 °C. The samples were then kept at these temperatures for 10 hours and the mass gain over time was recorded. Figures 123, 124 and 125 show the result of the TGA during isothermal oxidation at 750, 850 and 950 °C respectively. Images of the samples at the end of the tests were inserted in figures 53, 54 and 55 to detail the aspect of the external layer, and the potential occurrence of spallation.

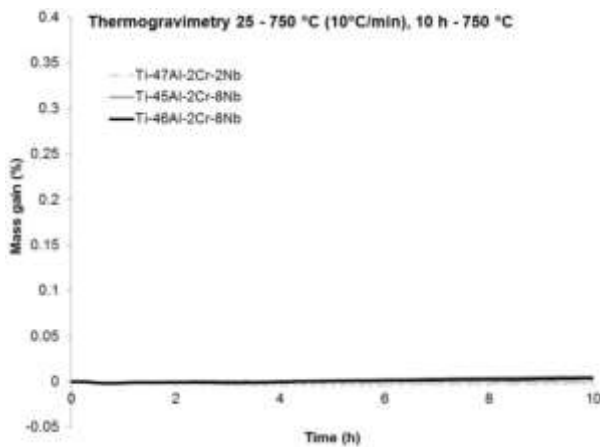


Figure 123: Mass gain versus time of Ti-47Al-2Cr-2Nb, Ti-45Al-2Cr-8Nb and Ti-46Al-2Cr-8Nb alloys during isothermal oxidation in air at 750 °C for 10 hours

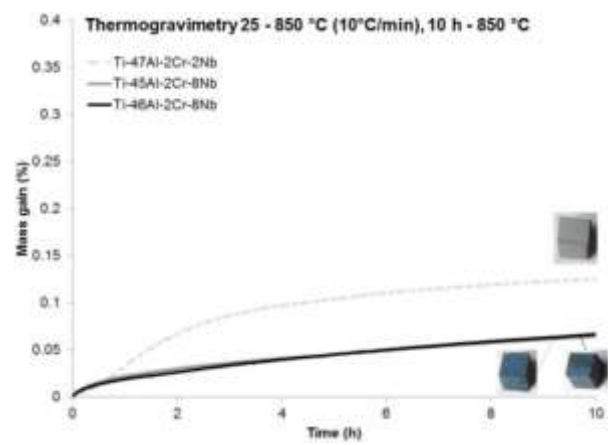


Figure 124: Mass gain versus time of Ti-47Al-2Cr-2Nb, Ti-45Al-2Cr-8Nb and Ti-46Al-2Cr-8Nb alloys during isothermal oxidation in air at 850 °C for 10 hours

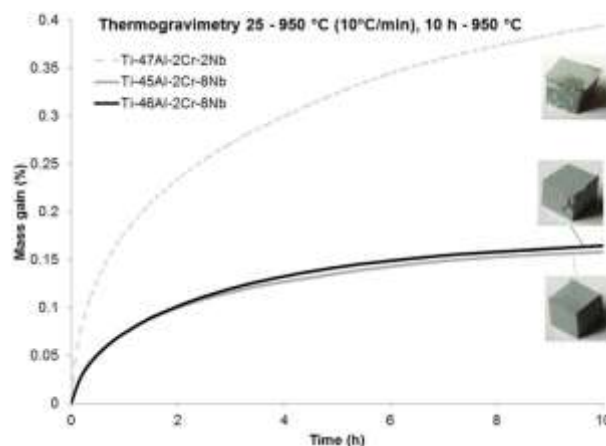


Figure 125: Mass gain versus time of Ti-47Al-2Cr-2Nb, Ti-45Al-2Cr-8Nb and Ti-46Al-2Cr-8Nb alloys during isothermal oxidation in air at 950 °C for 10 hours



In figure 123, all three samples were kept at 750 °C for 10 hours under a continuous air flow of 50 mL.min<sup>-1</sup>. After the experiment, the specimens didn't show any sign of oxidation. No significant mass gain was recorded by TGA over the 10 hours at 750 °C. It was therefore concluded that no relevant oxidation takes place in air after short time at 750 °C for Ti-(45-47)Al-2Cr-(2-8)Nb alloys.

Figure 124 shows the mass gain over time of samples hold at 850 °C for 10 hours in air. This temperature was identified in figure 55 as critical for the lowly alloyed Ti-47Al-2Cr-2Nb. The mass gain versus time curves in figure 56 highlight the higher oxidation resistance of Ti-(45-46)Al-2Cr-8Nb alloys. After 10 hours at 850 °C, the mass gain was about 0.06 % for Ti-(45-46)Al-2Cr-8Nb alloys while it was 0.12 % for Ti-47Al-2Cr-2Nb. Also, the external layer of Ti-47Al-2Cr-2Nb was brighter than that of Ti-(45-46)Al-2Cr-8Nb alloys. No spallation was observed but the nature of the oxides was clearly different between 2Nb and 8Nb containing alloys.

Figure 125 shows the mass gain over time of samples hold at 950 °C for 10 hours in air. The oxidation was clearly higher compared to isothermal oxidation at 850 °C for all materials. Again, Ti-47Al-2Cr-2Nb appeared much more oxidized than Ti-(45-46)Al-2Cr-8Nb alloys. After 10 hours at 950 °C in air, the mass gain of Ti-47Al-2Cr-2Nb was slightly under 0.4 %. Ti-(45-46)Al-2Cr-8Nb alloys on the other hand exhibited a mass gain of about 0.16 %. Only little spallation was observed for Ti-(45-46)Al-2Cr-8Nb alloys while the most part of the external layer appeared consistent. On the contrary, the spallation was significant in the case of Ti-47Al-2Cr-2Nb (figure 125).

The beneficial effect of higher amount of Nb was obvious in figure 124 and 125. The Ti-(45-46)Al-2Cr-8Nb alloys exhibited very similar behavior, suggesting that the effect of Nb on oxidation resistance in such range of composition takes over compared to the Al content. Actually, despite a higher amount of Al, the mass gain of Ti-47Al-2Cr-2Nb was at least twice that of Ti-(45-46)Al-2Cr-8Nb alloys after oxidation at 850 °C and 950 °C for 10 hours in air. The same behavior was observed during heating (figure 122) where the mass gain of Ti-(45-46)Al-2Cr-8Nb alloys were half that of Ti-47Al-2Cr-2Nb. Therefore, it was concluded from TGA that increasing the amount of niobium from 2 to 8 at.% led to increase the oxidation resistance by two for short time exposure at high temperature ( $\leq 1000$  °C).

### 3. Isothermal oxidation in air at 850 °C up to 100 hours.

The application temperature of conventional  $\gamma$ -TiAl is limited due to a significant oxidation above 700 °C [48, 58, 63, 70-77]. The development of 2<sup>nd</sup> generation  $\gamma$ -TiAl alloys containing a small amount of refractory elements allowed to slightly higher the application temperature [48, 75]. From figure 122 and 123, Ti-47Al-2Cr-2Nb showed no sign of oxidation up to 750 °C. It was found in the previous section that for short time exposure, the oxidation resistance of Ti-(45-46)Al-2Cr-8Nb alloys was twice that of Ti-47Al-2Cr-2Nb (figure 122, 124 and 125). Therefore, the oxidation behavior of the Ti-47Al-2Cr-2Nb and Ti-45Al-2Cr-8Nb were compared during long-term isothermal oxidation at 850 °C, which is over 100 °C higher than the application temperature recommended for conventional  $\gamma$ -TiAl alloys.

A set of bigger 10x10x10 mm<sup>3</sup> cubic samples from Ti-47Al-2Cr-2Nb and Ti-45Al-2Cr-8Nb alloy were cut from the core of as-EBM bars, polished down to 4000 grit (~ 6 $\mu$ m abrasive paper) and the surface area of each one of the specimen was calculated. These specimens were put together in a furnace in static air at 850 °C for 7, 30, 50 and 100 hours. After the given time, the Ti-47Al-2Cr-2Nb and Ti-45Al-2Cr-8Nb samples were simultaneously taken out of the furnace and cooled down in ambient air. At this stage, the specimens experienced cooling from 850 °C to room temperature in air which in some case caused spallation of the oxide scale (circled points in figure 126). Once at room temperature, the specimens were weighted with a 0.1 mg precision balance. The mass gain per surface area was plotted in figure 126. The macroscopic aspect of the oxidized samples is also shown in figure 126. When spallation occurred, the spall were weighted as much as possible (specimens were hold in a ceramic crucible).

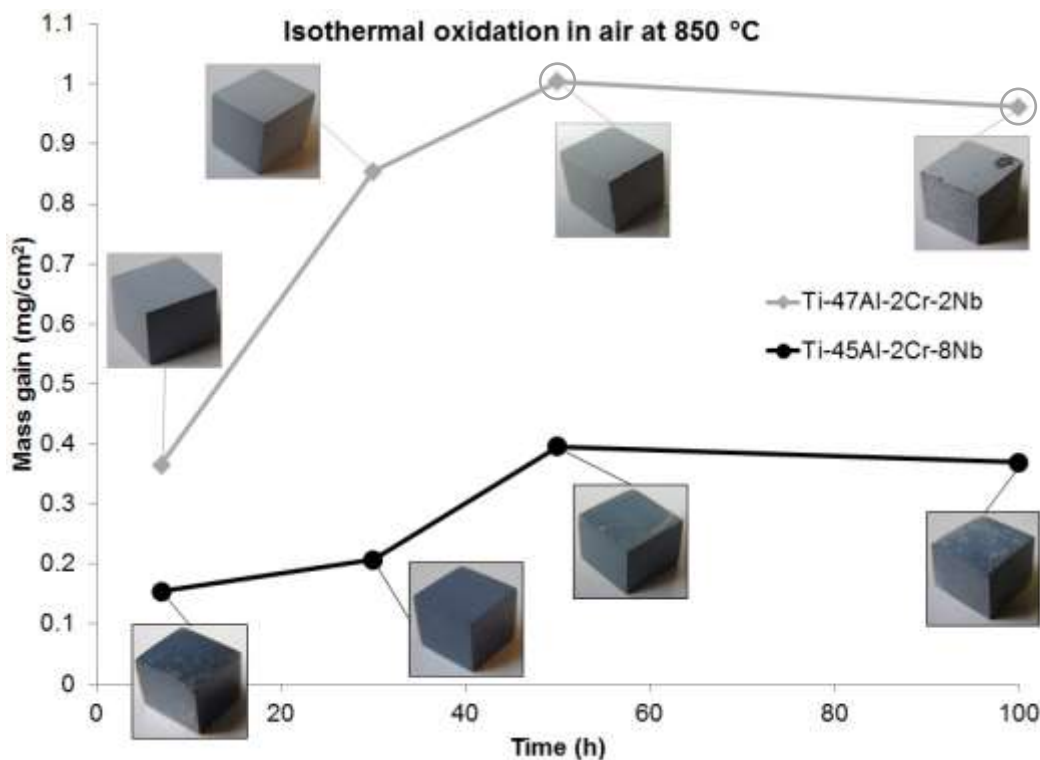


**Figure 126:** Mass gain by surface area of Ti-47Al-2Cr-2Nb and Ti-45Al-2Cr-8Nb after oxidation in air at 850 °C for 7, 30, 50 and 100 hours. Circled points indicate that spallation occurred [67]

It is clear from figure 126 that the oxidation resistance of Ti-45Al-2Cr-8Nb was significantly higher than that of Ti-47Al-2Cr-2Nb. The mass gain by surface area of the high Nb containing alloy was lower than half that of the lowly alloyed  $\gamma$ -TiAl. Moreover, the macroscopic aspect of the external oxides was different from an alloy to another which suggests differences of the grown oxide. On the one hand, the oxide grown on Ti-47Al-2Cr-2Nb exhibited a light grey color and was uniformly distributed over the whole surface. Already after 7 h of oxidation, the base alloy was completely covered. After 50 h of oxidation, the first signs of spallation were observed at the corners of the cubic sample and spallation was substantial after 100 hours. In addition, the surface of the sample exhibited some area clearly more damaged.

On the other hand, oxidized Ti-45Al-2Cr-8Nb exhibited a dark grey color. After 30 hours of oxidation, the specimen still displayed mirror-like reflections which suggests a very thin oxide layer. Else, all oxidized Ti-45Al-2Cr-8Nb specimens showed a non-uniform external oxide scale with lighter low-Nb-like zone. After 100 hours of oxidation, no sign of spallation was observed.

Moreover, the oxidation rate appears different during the first 50 hours of oxidation. While the mass gain per surface area of Ti-47Al-2Cr-2Nb increases quickly, the mass gain of Ti-45Al-2Cr-8Nb has a much slower rise. Though further tests should be done at intermediate temperature, it suggests that Nb addition reduces the oxidation rate of TiAl alloys, as it was observed in figures 122, 124 and 125.

X-ray diffraction analysis were carried on the surface of as-EBM samples before any treatment and of each specimen after oxidation in static air at 850 °C for 7, 30, 50 and 100 h for both Ti-47Al-2Cr-2Nb (figure 127A) and Ti-45Al-2Cr-8Nb (figure 127B). The actual composition of the oxide scales could thus be determined.

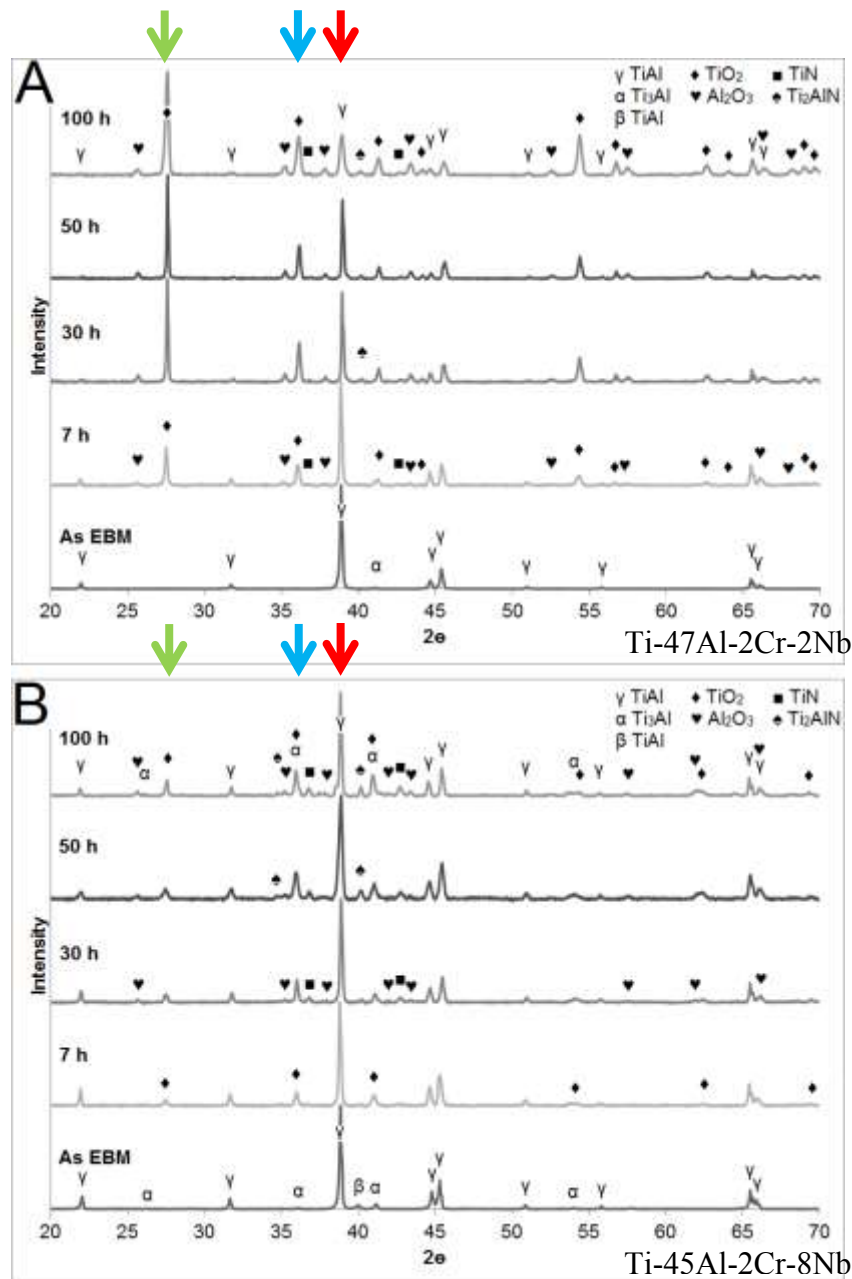


**Figure 127:** X-ray diffraction patterns of the surface of Ti-47Al-2Cr-2Nb (A) and Ti-45Al-2Cr-8Nb (B) as-EBM and after 7, 30, 50 and 100 hours of oxidation in static air at 850 °C [67]

The X-ray diffraction patterns of the base alloys, identified “As EBM” in figure 127A and 127B show that TiAl phase ( $\gamma$ ) was the dominant phase for both alloys. The main peak of TiAl phase ( $\gamma$ ) is highlighted by a red arrow in figures 127A and 127B. Only a slightly higher amount of  $Ti_3Al$  phase ( $\alpha$ ) was detected for Ti-45Al-2Cr-8Nb. The  $\alpha$ -phase can be detrimental for oxidation resistance because it intrinsically contains more Ti [88], however the effect of Nb takes over in this proportion. The X-ray diffraction patterns of as-EBM materials were analyzed previously (figure 91).

After only 7 hours of oxidation in static air at 850 °C, remarkable differences were observed. Ti-47Al-2Cr-2Nb appeared more oxidized than high Nb containing Ti-45Al-2Cr-8Nb. TiAl ( $\gamma$ ) from the base material remained the principal phase evidenced for both alloys which suggests a rather thin oxidation layer. However, while only a little amount of rutile TiO<sub>2</sub> ( $\blacklozenge$ ) was detected on Ti-45Al-2Cr-8Nb, the low-Nb containing alloy Ti-47Al-2Cr-2Nb already exhibited peaks of oxides with a much higher intensity. It was identified two different oxides: rutile TiO<sub>2</sub> and corundum Al<sub>2</sub>O<sub>3</sub> ( $\heartsuit$ ); and the titanium nitride: osbornite TiN ( $\blacksquare$ ). The main peak of rutile TiO<sub>2</sub> ( $\blacklozenge$ ) is highlighted by a green arrow in figures 57A and 57B, while the main peak of corundum Al<sub>2</sub>O<sub>3</sub> ( $\heartsuit$ ) is highlighted by a blue arrow.

After 30 hours, the XRD pattern of Ti-45Al-2Cr-8Nb was similar to that after 7 h. The dominant phase remained undoubtedly TiAl ( $\gamma$ ) (red arrow figure 127B), the growth of TiO<sub>2</sub> was very low, and corundum Al<sub>2</sub>O<sub>3</sub> and TiN were barely found. In contrast, Ti-47Al-2Cr-2Nb experienced a critical growth of TiO<sub>2</sub>, which became the main phase identified (green arrow figure 127A). An overall growth of oxides and nitride was observed. Furthermore, another phase was evidenced: the aluminum titanium nitride Ti<sub>2</sub>AlN ( $\clubsuit$ ). After 50 hours, the amount of oxide and nitride compounds increased slightly for both materials. Ti<sub>2</sub>AlN was identified also on Ti-45Al-2Cr-8Nb, which still exhibited TiAl ( $\gamma$ ) from the base material as the obvious dominant phase.

Finally, after 100 hours of oxidation in air at 850 °C, the XRD patterns of the samples surface highlighted a different behavior between Ti-45Al-2Cr-8Nb and Ti-47Al-2Cr-2Nb. Even though both materials presented the same phases on their surface: TiO<sub>2</sub> ( $\blacklozenge$ ), Al<sub>2</sub>O<sub>3</sub> ( $\heartsuit$ ), TiN ( $\blacksquare$ ) and Ti<sub>2</sub>AlN ( $\clubsuit$ ); and peaks of the underlying materials were observed: TiAl ( $\gamma$ ), Ti<sub>3</sub>Al ( $\alpha$ ) and  $\beta$ -TiAl ( $\beta$ ); the alloy with a lower content of Nb Ti-47Al-2Cr-2Nb appeared much more oxidized than Ti-45Al-2Cr-8Nb where the base material phase TiAl ( $\gamma$ ) remained the major phase identified from the XRD patterns. In fact, addition of Nb does not change the fundamental oxidation mechanism, but rather slows down the growth of rutile TiO<sub>2</sub> and promotes the formation of alumina Al<sub>2</sub>O<sub>3</sub>, thus reducing the overall kinetics of oxidation <sup>[50, 110, 113, 162]</sup>.

In the literature, different oxides have been identified <sup>[56, 70-73, 76, 88, 110, 111, 114, 115, 162]</sup>. First of all, the oxide scale grown on  $\gamma$ -TiAl alloys is always described as an inner Al<sub>2</sub>O<sub>3</sub> + TiO<sub>2</sub> mixed oxides and an outer non-protective TiO<sub>2</sub>. Also, the nitrogen effect is often mentioned and the presence of nitrides such as TiN and Ti<sub>2</sub>AlN is detected at the oxide/substrate interface. Other oxides, mainly titanium oxides, are sometimes cited such as TiO and Ti<sub>2</sub>O<sub>3</sub> but they eventually transform to more stable TiO<sub>2</sub> <sup>[72, 76]</sup>.

The difference in morphology of the outer oxide scales were studied by mean of Scanning Electron Microscopy (SEM). In addition, EDS analysis were performed to identify phases and elements distribution. Figure 128 shows the SEM micrographs of two selected zones on the top surface of Ti-47Al-2Cr-2Nb (figure 128A) and Ti-45Al-2Cr-8Nb (figure 128B) oxidized in air for 100 hours.

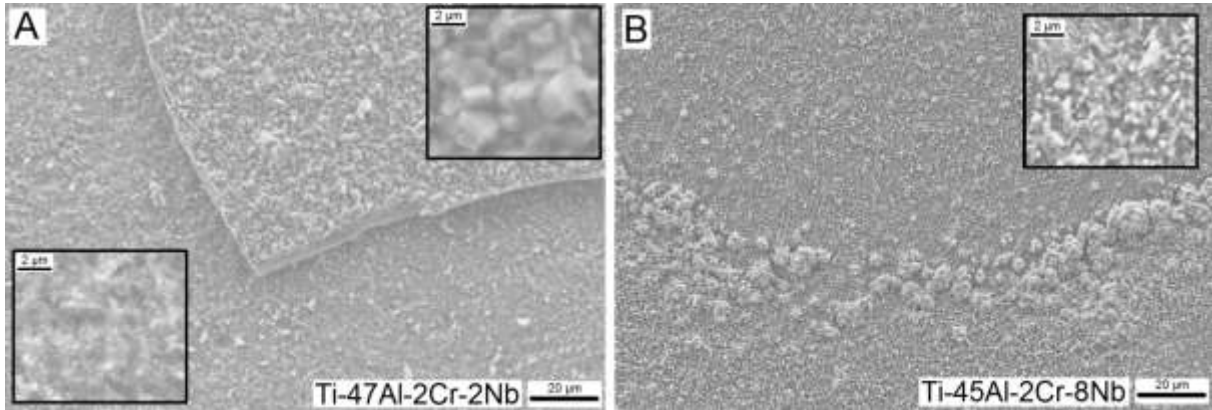


**Figure 128:** SEM micrographs of the top surface of oxidized samples for 100 hours at 850 °C showing: (A) spalled and underlying oxides layers on Ti-47Al-2Cr-2Nb and (B) inhomogeneous consistent oxides layer on Ti-45Al-2Cr-8Nb [67]

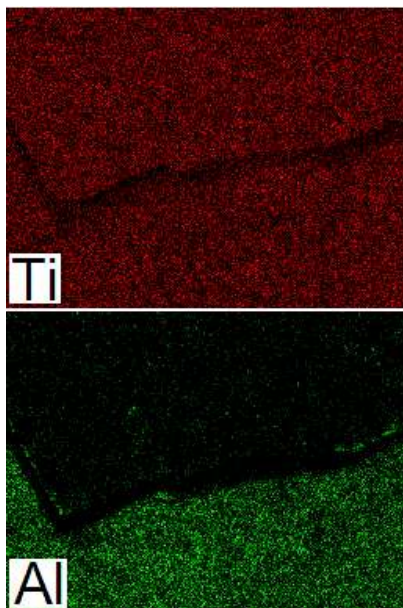


**Figure 129:** Element map from EDS analysis showing the titanium and aluminum distribution in a spalled area of the surface of Ti-47Al-2Cr-2Nb sample after 100 °C of oxidation in air at 850 °C

In figure 128A, it can be seen a spalled area of the outer layer of Ti-47Al-2Cr-2Nb. It is clear that the morphology was different on the underlying layer which is higher magnified in the bottom-left hand insert in figure 128A, from the outer layer that had partially spalled which is higher magnified in the top-right hand insert on figure 128A. On the one hand, the outer layer was composed by rather big cuboidal crystals, rich in Ti and O, typical of  $\text{TiO}_2$  [115, 163-165]. EDS revealed that Aluminum was barely detected, under 0.7 at.%. On the other hand, the underlying layer exhibited a much smaller structure with a mixture of small whisker-like and bigger cuboidal crystals, typical of  $\text{Al}_2\text{O}_3$  and  $\text{TiO}_2$  respectively [115, 163-165]. The elements distribution revealed that the underlying layer contained 14 at.% of Al. The opposite figure 129 shows the Ti and Al distribution of the selected area figure 128A. It is clearly seen in figure 129 the much lower amount of Al in outer scale suggesting that spallation was caused by  $\text{TiO}_2$ . Furthermore, the Nb content was found higher in the underlying layer rich in Al.

Figure 128B shows the top surface of Ti-45Al-2Cr-8Nb. As mentioned earlier, even though no sign of spallation was observed, the external oxide layer appeared non-uniform and exhibited some lighter areas (figure 126). Figure 128B shows such inhomogeneity. First of all, the overall morphology is much alike the underlying layer in figure 128A rather than the outer one. It could be seen a mixture of small whisker-like and cuboidal crystals, higher magnified in the top-right hand insert in figure 128B. However, some bigger cuboidal crystals richer in Ti could be observed in the lower part of the micrograph. EDS on the full region in figure 128B suggested a content of 19 at.% of Al.

#### 4. Isothermal oxidation in air at 950 °C up to 50 hours

Given the enhanced oxidation resistance of Ti-45Al-2Cr-8Nb compared to Ti-47Al-2Cr-2Nb, it was studied the oxidation behavior of Ti-45Al-2Cr-8Nb at 950 °C up to 50 hours in air. The mass gain per surface area of Ti-45Al-2Cr-8Nb oxidized for 7, 30 and 50 hours was compared to the mass gain per surface area of Ti-45Al-2Cr-8Nb and Ti-47Al-2Cr-2Nb oxidized at 850 °C for the same time. The results are shown in figure 130. Images of the aspect of the samples after the tests were inserted in figure 130. Again, when spallation occurred, the spall were weighted as much as possible (specimens were hold in a ceramic crucible). The points circled in figure 130 indicate that spallation occurred.

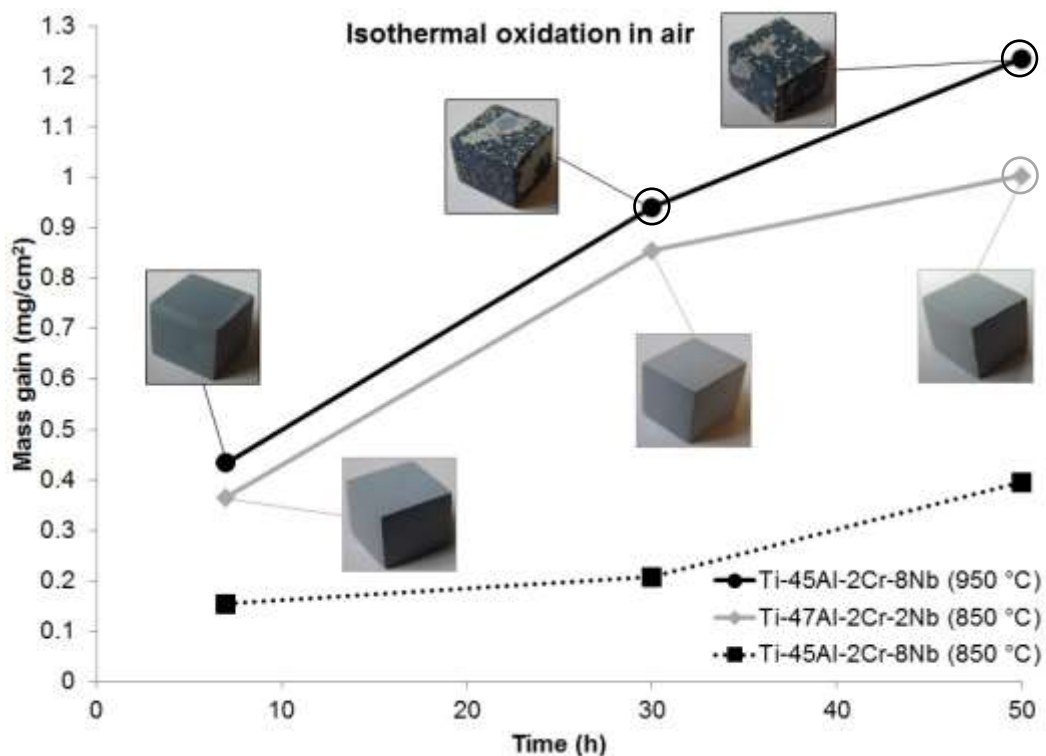


**Figure 130:** Mass gain by surface area of Ti-47Al-2Cr-2Nb and Ti-45Al-2Cr-8Nb after oxidation in air for 7, 30 and 50 hours at 850 °C and 950 °C respectively

After 7 hours at 950 °C, Ti-45Al-2Cr-8Nb already exhibited a uniform oxide layer on its surface which was not the case at 850 °C (figure 126). The external surface had a lighter grey color at the edges of the sample, similar to the surface of Ti-47Al-2Cr-2Nb after 7h at 850 °C (figure 130). The mass gain per surface area was similar to that of Ti-47Al-2Cr-2Nb oxidized at 850 °C.

Over the first 30 hours of oxidation in air, the mass gain of Ti-45Al-2Cr-8Nb oxidized at 950 °C was very similar to that of Ti-47Al-2Cr-2Cr oxidized at 850 °C. However, after only 30 hours of oxidation in air at 950 °C, Ti-45Al-2Cr-8Nb exhibited significant spallation which made doubtful the measure of the final weight. It was not clear in what extend the air quenching from 950 °C (100 °C higher than for Ti-47Al-2Cr-2Cr) triggered spallation compared to the oxidation itself.

The same consideration can be made after 50 hours. Almost the entire external layer of Ti-45Al-2Cr-8Nb was spalled while Ti-47Al-2Cr-2Cr only showed the first signs of spallation at the edge and corner of the sample.



## VI. Mechanical properties

### 1. Tensile properties

The tensile properties of the Ti-46Al-2Cr-8Nb alloy were studied and compared to Ti-48Al-2Cr-2Nb produced by EBM. The microstructure of Ti-46Al-2Cr-8Nb was duplex with about 80 % of lamellar grains with a size comprised between 100 and 300  $\mu\text{m}$  and 20 % of fine equiaxed grains smaller than 50  $\mu\text{m}$  at lamellar grain boundaries (figure 119). On the other hand, Ti-48Al-2Cr-2Nb had a duplex microstructure with only 60 % lamellar grains. The average grain size was similar. The results of tensile tests at different temperatures in air in the same conditions for both Ti-46Al-2Cr-8Nb and Ti-48Al-2Cr-2Nb alloys are displayed figures 131, 132 and 133. In figures 131 and 132, the strength values were divided by the materials' density. The density of both alloys was measured by Archimedes' principle. Ti-46Al-2Cr-8Nb exhibited a density of  $4.23 \text{ g.cm}^{-3}$  and Ti-48Al-2Cr-2Nb exhibited a density of  $3.99 \text{ g.cm}^{-3}$ .

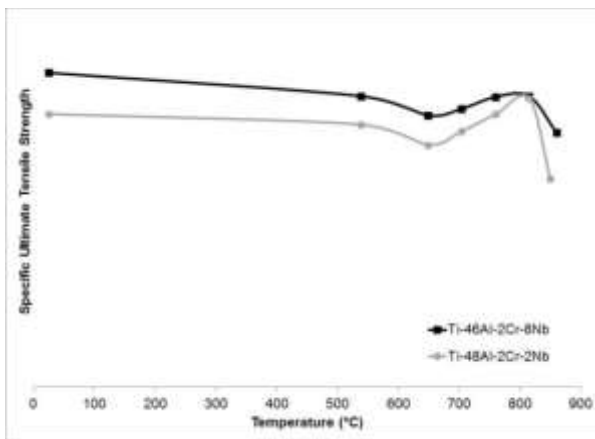


**Figure 131:** Specific Ultimate Tensile Strength (UTS) as a function of temperature of Ti-46Al-2Cr-8Nb (black) and Ti-48Al-2Cr-2Nb (grey)

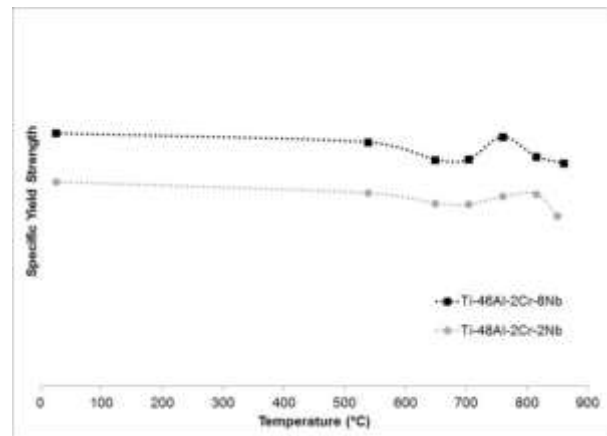


**Figure 132:** Specific Yield Strength (YS) as a function of temperature of Ti-46Al-2Cr-8Nb (black) and Ti-48Al-2Cr-2Nb (grey)

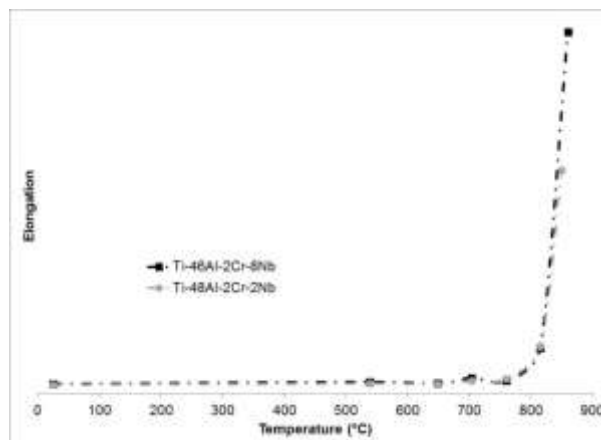


**Figure 133:** Elongation as a function of temperature of Ti-46Al-2Cr-8Nb (black) and Ti-48Al-2Cr-2Nb (grey)

In figure 133, the total elongation was minimum at room temperature. The minimum value of 1 % was reached and ductility increased significantly over 815 °C for both alloys. Compared to superalloys, the ductility of TiAl alloys was much lower but sufficient for applications as low pressure turbine blades and vanes and turbocharger turbines.

From figures 131 and 132, the high Nb containing Ti-46Al-2Cr-8Nb alloy exhibited both specific ultimate tensile strength and specific yield strength 20 MPa higher than that of Ti-48Al-2Cr-2Nb. The strength values of both TiAl alloys was rather consistent up to 815 °C. Over 850 °C, a significant reduction of UTS was observed.

The specific strength levels obtained for Ti-46Al-2Cr-8Nb alloy fabricated by EBM were similar to that of superalloys Inconel 738 and Udimet 710 with a density of  $8.11 \text{ g.cm}^{-3}$  and  $8.08 \text{ g.cm}^{-3}$  respectively [11, 28, 166]. The specific strengths of Ti-46Al-2Cr-8Nb, Inconel 738 and Udimet 710 superalloys were plot figures 134 and 135. The tensile stress experienced by the rotating parts of gas turbines derive from centrifugal force caused by the high rotation speed. At about half the density of superalloys, Ti-46Al-2Cr-8Nb therefore suggests a significant weight reduction of the blades themselves and consequently the turbine discs.

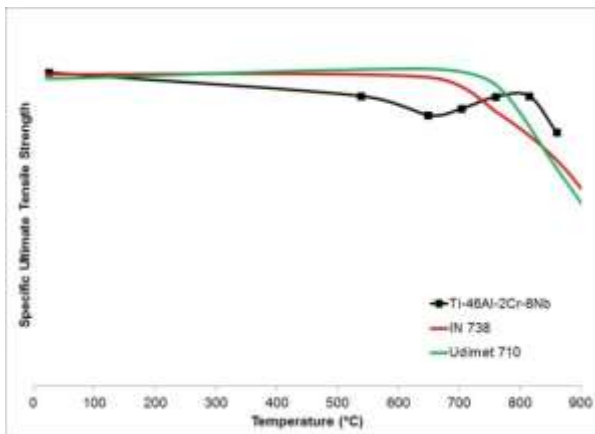


**Figure 134:** Specific Ultimate Tensile Strength (UTS) as a function of temperature of Ti-46Al-2Cr-8Nb (black) and superalloys Inconel 718 (red) and Udimet 710 (green)

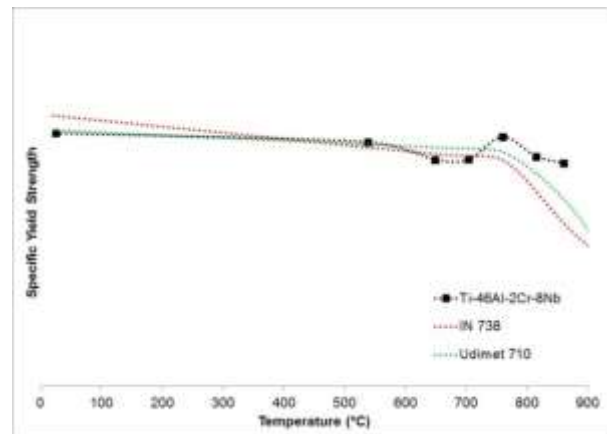


**Figure 135:** Specific Yield Strength (YS) as a function of temperature of Ti-46Al-2Cr-8Nb (black) and superalloys Inconel 718 (red) and Udimet 710 (green)

## 2. Creep resistance

The creep resistance of Ti-46Al-2Cr-8Nb was studied under different conditions. The creep tests were conducted at 760, 815 °C. All samples were treated in the same way as for tensile tests. Figure 136 shows the stress to rupture versus the time to rupture for both alloys.

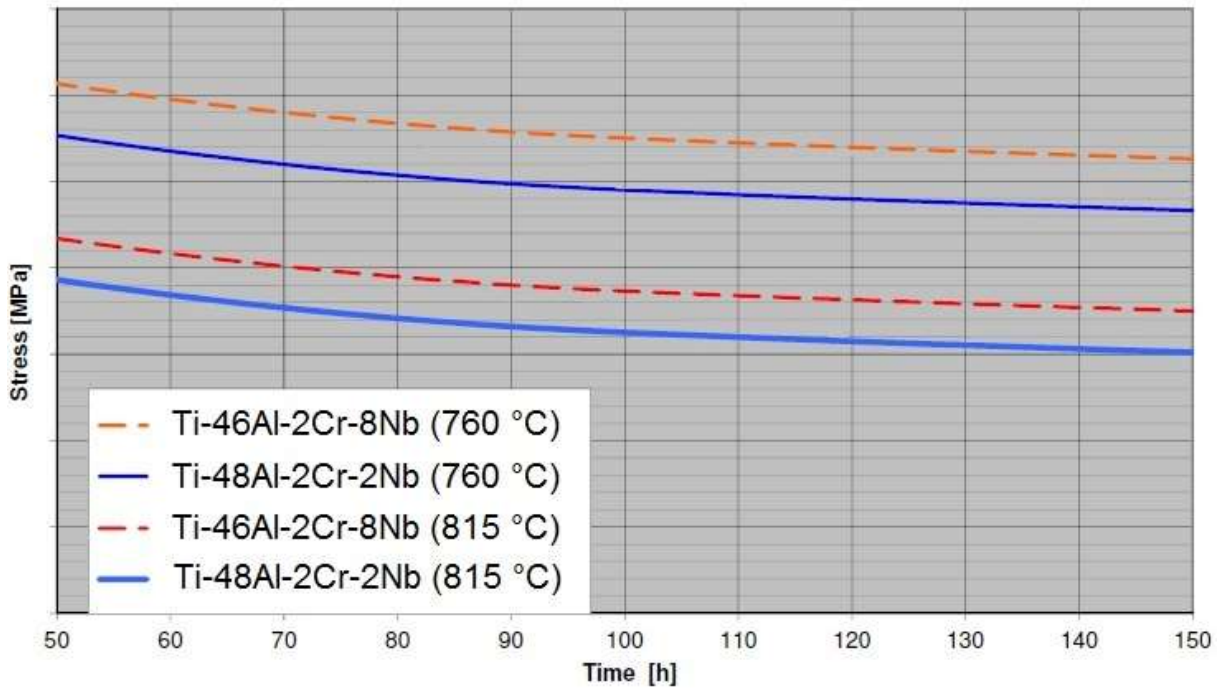


**Figure 136:** Stress to rupture as a function of time of Ti-46Al-2Cr-8Nb (red) and Ti-48Al-2Cr-2Nb (blue) at 760 °C, 815 °C

From figure 136, the creep resistance of Ti-46Al-2Cr-8Nb was higher than that of Ti-48Al-2Cr-2Nb at 760 °C and 815 °C. It could therefore be concluded that the high Nb containing alloy exhibited better creep resistance. This was in accordance with the beneficial effect of Nb addition regarding high temperature properties of  $\gamma$ -TiAl alloys.

## Conclusion

Nickel-based superalloys are currently preferred for high temperature structural parts in gas turbine aeroengines. In order to increase efficiency, reduce weight, fuel consumption and harmful emissions, new class of materials are being studied.

Ceramic-based composites offer strength and lightness despite their fragility, and retain their properties up to very high temperatures. Ceramics thus have a great potential as structural materials of the combustion chamber and high pressure turbine.

TiAl-based intermetallics have been extensively studied for the past 30 years. At about half the density of Ni-based superalloys, they exhibit similar specific properties up to about 800 °C. Since the main load of rotating parts derive from centrifugal force caused by high speed rotation, the lighter the part the lower the stress. Therefore, TiAl alloys emerged as outstanding candidates to replace Ni-based alloys used for rotating components of the low pressure turbine and the last stages of the high pressure compressor. The low pressure turbine of the latest GEnx (General Electric) and LEAP (CFM) engines adopted the GE's Ti-48Al-2Cr-2Nb alloy produced by casting routes. The emergence of powder-based additive manufacturing process consented to tailor the chemical composition and microstructure of  $\gamma$ -TiAl alloys towards definite set of properties. Addition of chromium and niobium together with a fine duplex microstructure with a substantial amount of lamellar grains significantly increase ductility, integrity and high temperature properties.

Electron Beam Melting, proposed by Arcam AB since 2005, was found of particular interest for the production of 2<sup>nd</sup> generation Ti-48Al-2Cr-2Nb alloys. 3<sup>rd</sup> generation  $\gamma$ -TiAl alloys with higher amount of refractory elements extend the application of such materials to higher temperatures. In the present work, Ti-(45-46)Al-2Cr-8Nb alloys were produced by EBM. The process parameters were optimized to produce homogeneous materials with very low residual porosity inferior to 1 %, only resulting from the gas atomized powder porosity. A slight and constant evaporation of light-weight aluminum was observed due to the high temperature vacuum environment during the process. Analysis have shown that the chemical composition was very homogeneous except in the external contour melting were higher Al evaporation was experienced. However, the external contour is anyway to remove by post processing. The microstructure of the as-produced material was equiaxed composed by fine and very fine  $\gamma$  and  $\alpha$  grains ( $\leq 50 \mu\text{m}$ ), with a low amount of  $\beta$  phase.

Hot Isostatic Pressing in the ( $\alpha + \gamma$ ) phase field, or pressure-less Simul-HIP treatment, led to recrystallization and homogenization of the microstructure. The fully equiaxed microstructure of the as-produced materials could then be transformed to any duplex and fully lamellar microstructures by heat treatment in vacuum around the  $\alpha$ -Transus temperature  $T_\alpha$ . Thermo Mechanical Analysis was proposed as an innovative method to identify the phase transition temperatures of Ti-(45-46)Al-2Cr-8Nb alloys and in particular the  $\alpha$ -Transus temperature. A fine homogeneous nearly lamellar microstructure composed by about 80 % lamellar grains pinned at grain boundaries by fine equiaxed grains was therefore produced.

The primary mechanical tests on tensile and creep resistance suggested higher level of properties of Ti-46Al-2Cr-8Nb when compared to Ti-48Al-2Cr-2Nb produced by EBM. Oxidation analysis highlighted the beneficial effect of high Nb addition. The oxidation resistance in air of Ti-46Al-2Cr-8Nb when compared to Ti-48Al-2Cr-2Nb was clearly higher. The formation of detrimental rutile TiO<sub>2</sub> was impeded which reduced oxidation kinetics and spallation. With regard to oxidation resistance, the application temperature of Ti-46Al-2Cr-8Nb was 60 to 100 °C higher than that of Ti-48Al-2Cr-2Nb.

Furthermore, the specific strength levels of Ti-46Al-2Cr-8Nb alloy were similar to that of Ni-based superalloys Inconel 718 and Udimet 710 used for LPT blades.

## Table of Figures

FIGURE 1: TIMELINE OF THE JOM TOP 10 GREATEST MOMENTS IN MATERIALS SCIENCE AND ENGINEERING HISTORY .....	6
FIGURE 2: EXAMPLES OF APPLICATIONS WHERE MATERIALS SCIENCE ADVANCES ARE A KEY FACTOR: AERONAUTICS, AUTOMOBILE, MARINE, CIVIL, SPACE, INFORMATICS, ENERGY.....	7
FIGURE 3: FORCES APPLIED TO AN AIRCRAFT IN FLIGHT .....	9
FIGURE 4: SCHEMATIC REPRESENTATION OF ROCKET PROPULSION .....	10
FIGURE 5: EXAMPLE OF ROCKET PROPULSION. ARIANE LAUNCH ON 26 <sup>TH</sup> NOVEMBER 2010 (LEFT) AND A MISSILE (RIGHT). .....	10
FIGURE 6: T-S DIAGRAM OF THE BRAYTON CYCLE <sup>[15]</sup> .....	11
FIGURE 7: SCHEMATIC DRAWING OF THE GAS GENERATOR, CORE OF ANY GAS TURBINE ENGINE <sup>[7]</sup> .....	11
FIGURE 8: SCHEMATIC DRAWINGS OF THE DIFFERENT GAS TURBINE ENGINES. TURBOJET (LEFT), TURBOPROP (CENTER) AND TURBOFAN (RIGHT).....	12
FIGURE 9: EFFICIENCY CHARACTERISTICS OF TYPICAL AIRCRAFT ENGINES <sup>[7]</sup> .....	13
FIGURE 10: SPECIFIC THRUST CHARACTERISTICS OF TYPICAL AIRCRAFT ENGINES <sup>[7]</sup> .....	14
FIGURE 11: THRUST SPECIFIC FUEL CONSUMPTION CHARACTERISTICS OF TYPICAL AIRCRAFT ENGINES <sup>[7]</sup> .....	14
FIGURE 12: SCHEMATIC CUTAWAY REPRESENTATION OF CFM56-7B DEVELOPED BY CFM INTERNATIONAL.....	15
FIGURE 13: SCHEMATIC TECHNOLOGICAL DRAWING OF THE CFM56-7B ENGINE DISPLAYING THE DIFFERENT COMPONENTS <sup>[23]</sup> .....	16
FIGURE 14: TEMPERATURE AND PRESSURE PROFILES OF AIR IN A GAS TURBINE <sup>[25]</sup> .....	16
FIGURE 15: EXPLODED VIEW OF THE FAN MAJOR MODULE OF THE CFM56-7 ENGINES <sup>[26]</sup> .....	17
FIGURE 16: EXPLODED VIEW OF THE CORE MAJOR MODULE OF THE CFM56-7 ENGINES <sup>[26]</sup> .....	17
FIGURE 17: EXPLODED VIEW OF THE LPT MAJOR MODULE OF THE CFM56-7 ENGINES <sup>[26]</sup> .....	18
FIGURE 18: MATERIAL COMPOSITION IN TURBOFAN ENGINES BY TOTAL WEIGHT.....	19
FIGURE 19: CONVENTIONALLY CAST, DIRECTIONALLY SOLIDIFIED (DS) AND SINGLE CRYSTAL (SC) BLADE TECHNOLOGIES .....	22
FIGURE 20: SPECIFIC STRENGTH COMPARISON OF CERAMICS AND METALS <sup>[3]</sup> .....	23
FIGURE 21: COMPARISON OF MONOLITHIC CERAMICS AND CERAMIC COMPOSITES STRESS VS. STRAIN BEHAVIOR <sup>[3]</sup> .....	23
FIGURE 22: SEM IMAGES SHOWING THE MICROSTRUCTURE OF A CROSS SECTION PERPENDICULAR TO THE SOLIDIFICATION DIRECTION OF THE AL <sub>2</sub> O <sub>3</sub> /GAP SYSTEM MGC MATERIAL (A), AND THE CONFIGURATION OF SINGLE CRYSTAL GAP (B) <sup>[39]</sup> .....	28
FIGURE 23: TYPICAL STRESS-DISPLACEMENT CURVES IN THREE-POINT FLEXURAL TEST AT 1873K OF MGC MATERIALS. (A) AL <sub>2</sub> O <sub>3</sub> /GAP SYSTEM MGC MATERIALS, (B) AL <sub>2</sub> O <sub>3</sub> /YAG SYSTEM MGC MATERIALS, (C) AL <sub>2</sub> O <sub>3</sub> /GAP SINTERED COMPOSITE <sup>[39]</sup> .....	28
FIGURE 24: RELATIONSHIP BETWEEN FATIGUE CRACK GROWTH RATE DA/DN AND MAXIMUM STRESS INTENSITY FACTOR K <sub>MAX</sub> <sup>[40]</sup> ....	29
FIGURE 25: TEMPERATURE DEPENDENCE OF THE BENDING OF MONOLITHIC SiALON (SQUARES) AND SiTiCO <sub>(F)</sub> /SiALON COMPOSITE (EMPTY CIRCLES) AND THE INTERLAMELLAR SHEAR STRENGTH OF THE COMPOSITE (FULL CIRCLES) <sup>[42]</sup> .....	31
FIGURE 26: FRACTURE TOUGHNESS AND LOAD-DEFLECTION CURVES OF MONOLITHIC SiALON AND SiTiCO(F)/SiALON COMPOSITE MEASURED BY SENB METHOD <sup>[42]</sup> .....	32
FIGURE 27: 10 % SHORT FIBER REINFORCED B-SiALON COMPOSITES HOT PRESSED AT 1650 °C <sup>[43]</sup> .....	33
FIGURE 28: MICRO-HARDNESS (A) AND FRACTURE TOUGHNESS (B) OF B-SiALON COMPOSITES AS A CONSEQUENCE OF SHORT FIBERS RATE <sup>[43]</sup> .....	33
FIGURE 29: THERMAL EXPANSION DATA FOR MoSi <sub>2</sub> BASE MATERIALS AND SiC REINFORCING PHASE <sup>[45]</sup> .....	34
FIGURE 30: SECOND STAGE CREEP RATE VERSUS SPECIFIC STRESS AT 1200 °C FOR MoSi <sub>2</sub> -50Si <sub>3</sub> N <sub>4</sub> COMPARED WITH OTHER MATERIALS <sup>[45]</sup> .....	35
FIGURE 31: TEMPERATURE DEPENDANCE OF FRACTURE TOUGHNESS OF MoSi <sub>2</sub> -Si <sub>3</sub> N <sub>4</sub> BASE MATERIALS <sup>[45]</sup> .....	35
FIGURE 32: LOAD-TIME CURVES FROM CHEVRON NOTCHED 4 POINT BEND SPECIMENS OF SCS-6/MoSi <sub>2</sub> -Si <sub>3</sub> N <sub>4</sub> AND MoSi <sub>2</sub> -Si <sub>3</sub> N <sub>4</sub> TESTED AT ROOM TEMPERATURE <sup>[45]</sup> .....	36
FIGURE 33: ROOM TEMPERATURE TENSILE STRESS-STRAIN CURVES FOR 6-PLY SCS-6/MoSi <sub>2</sub> -Si <sub>3</sub> N <sub>4</sub> HYBRID COMPOSITES <sup>[45]</sup> .....	36
FIGURE 34: TEMPERATURE DEPENDENCE OF ULTIMATE TENSILE STRENGTH OF 6PLY SCS-6/MoSi <sub>2</sub> -50Si <sub>3</sub> N <sub>4</sub> HYBRID COMPOSITES COMPARED WITH OTHER MATERIALS <sup>[45]</sup> .....	37
FIGURE 35: OXIDATION BEHAVIOR OF MoSi <sub>2</sub> -BASE MATERIALS CYCLICALLY OXIDIZED AT 500 °C IN AIR <sup>[45]</sup> .....	37
FIGURE 36: SPECIFIC WEIGHT GAIN VERSUS NUMBER OF CYCLES PLOT FOR MoSi <sub>2</sub> -50Si <sub>3</sub> N <sub>4</sub> MONOLITHIC AND SCS-6/ MoSi <sub>2</sub> -50Si <sub>3</sub> N <sub>4</sub> HYBRID COMPOSITE CYCLICALLY OXIDIZED AT 1250 °C IN AIR <sup>[45]</sup> .....	37
FIGURE 37: TEMPERATURE DEPENDENCE OF SPECIFIC STRENGTH OF VARIOUS GROUPS OF ALLOYS <sup>[69]</sup> .....	39

FIGURE 38: SPECIFIC PROPERTIES THAT MAKE TiAl-BASED ALLOYS OF INTEREST WHEN COMPARED TO ALLOY STEEL, Ti ALLOYS AND Ni-BASED SUPERALLOYS <sup>[57]</sup> .....	39
FIGURE 39: DEPENDENCE OF MECHANICAL PROPERTIES SUCH AS FRACTURE TOUGHNESS, STRENGTH, ELONGATION, IMPACT RESISTANCE (IR), CREEP RESISTANCE (CR), AND GRAIN SIZE ON THE MICROSTRUCTURE TYPE (NEAR GAMMA, DUPLEX, FULLY LAMELLAR) <sup>[50]</sup> .....	40
FIGURE 40: INFLUENCE OF THE AL CONTENT ON STRENGTH AND DUCTILITY IN THE CASE OF Ti-xAl-2Cr-2Nb ALLOYS <sup>[87]</sup> .....	41
FIGURE 41: SECTION OF THE TiAl PHASE DIAGRAM SHOWING THE EFFECT OF ALLOYING ELEMENTS ON PHASE BOUNDARIES <sup>[57]</sup> .....	43
FIGURE 42: TENSILE DUCTILITY AT ROOM TEMPERATURE AS A FUNCTION OF Cr CONTENT IN Ti-48Al-xCr ALLOYS .....	46
FIGURE 43: : THE TOTAL STRAIN TO FRACTURE VALUES ARE PLOTTED AGAINST GRAIN SIZE FOR BOTH DUPLEX AND LAMELLAR TiAl ALLOYS (Ti-(46-48)Al-3(Cr,Mn,V)-(2-3)Nb-(0-1)(W,Hf,Mo)) <sup>[80]</sup> .....	47
FIGURE 44: STRESS-STRAIN CURVE OF A TENSILE TEST CONDUCTED AT RT ON ANNEALED (1000°C/3H) SHEET MATERIAL <sup>[85]</sup> .....	47
FIGURE 45 : TENSILE FLOW BEHAVIOR OF Ti-46Al-9Nb SHEET MATERIAL WHICH SHOWS A NG STRUCTURE : TRUE STRESS VS. STRAIN CURVES FOR A CONSTANT STRAIN RATE <sup>[101]</sup> .....	49
FIGURE 46: TENSILE STRENGTH (CIRCLES) AND YIELD STRENGTH (TRIANGLES) AS A FUNCTION OF TEMPERATURE, OBTAINED FROM PRIMARY ANNEALED Ti-46Al-9Nb SHEETS WITH NG MICROSTRUCTURE IN THE ROLLING DIRECTION (OPEN SYMBOLS) AND TRANSVERSE TO THE ROLLING DIRECTION (CLOSED SYMBOLS) <sup>[85]</sup> .....	49
FIGURE 47: TENSILE STRENGTHS OF ISOTHERMALLY FORGED Ti-50Al-7.5Nb SHOWING A NEAR-GAMMA (NG) MICROSTRUCTURE AT VARIOUS TEMPERATURE <sup>[102]</sup> .....	50
FIGURE 48: TENSILE FLOW CURVES FOR TiAl ALLOYS IN TWO TYPICAL MICROSTRUCTURAL FORMS WITH VARIOUS GRAIN SIZE <sup>[80]</sup> .....	50
FIGURE 49: RELATIONSHIPS BETWEEN YIELD STRESS, GRAIN SIZE (D) AND LAMELLAR SPACING ( $\lambda$ ) IN FL MATERIALS <sup>[80]</sup> .....	50
FIGURE 50 : A COMPARISON OF THE CREEP CURVES OF THE THREE TYPICAL MICROSTRUCTURES IN $\gamma$ -BASED ALLOYS <sup>[97]</sup> .....	51
FIGURE 51 : CREEP PROPERTY OF TNB (Ti-46Al-9Nb) SHEETS WITH NG MICROSTRUCTURE IN ROLLING DIRECTION <sup>[79]</sup> .....	52
FIGURE 52 : CREEP BEHAVIOR OF TNB (Ti-46Al-9Nb) SHEET MATERIALS WITH A FINE-FL MICROSTRUCTURE. THE MEAN LAMELLAR SPACING IS 110 nm $\pm$ 27 FOR (1) AND 170 nm $\pm$ 43 FOR (2) <sup>[79]</sup> .....	52
FIGURE 53 : CREEP BEHAVIOR OF FULLY LAMELLAR Ti-46Al-9Nb SHEET MATERIAL WITH DIFFERENT LAMELLAR SPACING: FL110 (1,3); FL170 (2,4); FL470 (5) IN NANOMETER <sup>[79]</sup> .....	52
FIGURE 54 : SECTION OF THE LONG-TERM CREEP EXPERIMENT BEHAVIOR OF Ti-46Al-9Nb SHEET MATERIAL WITH DIFFERENT LAMELLAR SPACING AT 800°C AFTER SECOND STRESS CHANGE (125–150 MPa) <sup>[79]</sup> .....	52
FIGURE 55: BACK-SCATTERED ELECTRON MICROGRAPH OF THE MICROSTRUCTURE OF Ti-45Al-10Nb PRIOR TO CREEP TEST <sup>[103]</sup> .....	53
FIGURE 56: SCHEMATIC MODEL OF THE FATIGUE CRACK GROWTH PROCESS <sup>[104]</sup> .....	54
FIGURE 57: MONOTONIC FRACTURE TOUGHNESS BEHAVIOR IN THE FORM OF $K_R(\Delta a)$ RESISTANCE CURVES <sup>[100]</sup> .....	56
FIGURE 58: RELATIONSHIPS BETWEEN TOUGHNESS ( $K_I$ AND $K_{SS}$ ) AND VOLUME FRACTION OF EQUIAXED $\gamma$ PHASE <sup>[100]</sup> .....	56
FIGURE 59: FATIGUE CRACK GROWTH THRESHOLD, $\Delta K_{TH}$ AS A FUNCTION OF THE VOLUME FRACTION OF EQUIAXED $\gamma$ PHASE <sup>[100, 105]</sup> .....	56
FIGURE 60: SCHEMATIC REPRESENTATION OF THE KITAGAWA DIAGRAM TO MODEL FATIGUE FAILURES IN PRISTINE AND DAMAGED MATERIALS <sup>[106]</sup> .....	57
FIGURE 61: SUMMARY OF FATIGUE STRENGTH VS DEFECT SIZE OF DUPLEX AND FULLY LAMELLAR TNB MICROSTRUCTURE <sup>[106]</sup> .....	58
FIGURE 62: VICKERS HARDNESS OF TERNARY Ti-Al-Nb ALLOYS FABRICATED BY ARC MELTING PROCESS <sup>[102]</sup> .....	58
FIGURE 63 : VICKERS AND ROCKWELL HARDNESS VALUES MEASURED ON BULK SPECIMENS OF A GAMMA ALLOY IN VARIOUS ANNEALING CONDITIONS SHOWING A LINEAR RELATIONSHIP <sup>[107]</sup> .....	59
FIGURE 64 : RELATIONSHIP BETWEEN ROCKWELL HARDNESS VALUES AND YIELD STRENGTHS PREVIOUSLY MEASURED ON BULK SAMPLES OF VARIOUS GAMMA ALLOYS <sup>[107]</sup> .....	59
FIGURE 65: THE EFFECT OF ISOTHERMAL AGING AT DIFFERENT TEMPERATURES ON VICKERS HARDNESS VARIATION <sup>[107]</sup> .....	60
FIGURE 66: VICKERS HARDNESS (HV2) OF MASSIVELY TRANSFORMED Ti-46Al-9Nb AFTER 1 h ANNEALING TREATMENTS. (■): HARDNESS OF THE STARTING FULLY LAMELLAR MICROSTRUCTURE <sup>[108]</sup> .....	60
FIGURE 67: INFLUENCE OF A2 LATHS WIDTH ON HARDNESS IN A NANOMETER-SCALED LAMELLAR Ti-45Al-7.5Nb <sup>[109]</sup> .....	61
FIGURE 68: EFFECT OF NIOBIUM CONTENT ON THE OXIDATION RESISTANCE OF ALLOYS (THE AL CONTENT WAS CONSTANT: 36.5 WT.%) <sup>[111]</sup> .....	62
FIGURE 69: MASS CHANGE VERSUS TIME FOR Ti-48Al-2Cr WITH DIFFERENT MICROSTRUCTURES AND NEAR GAMMA Ti-48Al-2Cr-2Nb IN AIR AT 800°C <sup>[110]</sup> .....	62
FIGURE 70: MASS CHANGE VERSUS NUMBER OF CYCLES FOR Ti-48Al-2Cr AND Ti-48Al-2Cr-2Nb WITH DIFFERENT MICROSTRUCTURES DURING CYCLIC OXIDATION IN AIR BETWEEN ROOM TEMPERATURE AND 800°C <sup>[110]</sup> .....	63
FIGURE 71: ADDITIVE MANUFACTURING PROCESSES .....	66
FIGURE 72: ARCAM A2 MACHINE <sup>[119]</sup> .....	67
FIGURE 73: SCHEMATIC DRAWING OF AN ELECTRON BEAM MELTING MACHINE <sup>[120]</sup> .....	67
FIGURE 74: AS-BUILT SPECIMENS IN THE EBM CHAMBER SURROUNDED BY UN-SINTERED POWDER <sup>[65]</sup> .....	68
FIGURE 75: SEM MICROGRAPHS OF POWDERS Ti-47Al-2Cr-8Nb AND Ti-48Al-2Cr-8Nb AS-RECEIVED .....	71

FIGURE 76: SCHEMATIC DRAWING OF THE EFFECT OF POWDER PARTICLES SIZE ON THE APPARENT DENSITY: MONOSIZED (A), BIMODAL (B) AND TRIMODAL (C) <sup>[127]</sup> .....	73
FIGURE 77: BUILDING PATH STRATEGIES FOR THE ELECTRON BEAM MELTING OF 3 <sup>RD</sup> GENERATION $\gamma$ -TiAl .....	74
FIGURE 78: PHOTOGRAPHY OF A BAR AS-BUILT BY EBM (A), A CYLINDRICAL SAMPLE OF ABOUT 10 MM HEIGHT (B) AND A SAMPLE FOR MICROSCOPIC OBSERVATION AND POROSITY INVESTIGATION (C) .....	75
FIGURE 79: OPTICAL MICROGRAPH SHOWING THE POROSITY OF TiAl-2Cr-8Nb AFTER THE FIRST EBM TRIAL .....	76
FIGURE 80: MICROGRAPH SHOWING CAVITIES INSIDE PARTICLES FROM ARGON BUBBLES TRAPPED DURING THE ATOMIZATION PROCESS <sup>[75]</sup> .....	77
FIGURE 81: SEM MICROGRAPH SHOWING RESIDUAL POROSITY AND A RESIDUAL AR BUBBLE SECTION AT ARROW <sup>[84]</sup> .....	77
FIGURE 82: OPTICAL MICROGRAPH SHOWING THE DUAL POROSITY OF AN AS-BUILT SAMPLE AFTER THE FIRST OPTIMIZATION.....	78
FIGURE 83: OPTICAL MICROGRAPH SHOWING ONLY THE POROSITY RESULTING FROM POWDER DEFECTS OF AN AS-BUILT SAMPLE AFTER THE 3 <sup>RD</sup> TRIAL .....	79
FIGURE 84: OPTICAL MICROGRAPH SHOWING THE BIGGEST PORES IN THE AS-BUILT SAMPLE RESULTING FROM POWDER DEFECTS.....	79
FIGURE 85: OPTICAL MICROGRAPH SHOWING THE BIGGEST PORES RESULTING FROM POWDER DEFECTS OF AFTER THE 4 <sup>TH</sup> TRIAL .....	80
FIGURE 86: MICROGRAPH SHOWING THE TYPICAL POROSITY IN AS-BUILT SAMPLE FROM POWDER Ti-48Al-2Cr-8Nb .....	82
FIGURE 87: MICROGRAPH SHOWING THE HIGH POROSITY AT THE BOTTOM OF BARS IN AS-BUILT SAMPLE FROM POWDER Ti-48Al-2Cr-8Nb .....	82
FIGURE 88: SCHEMATIC REPRESENTATION OF AS-BUILT BARS AND SAMPLES FOR CHEMICAL ANALYSIS .....	82
FIGURE 89: VIEW OF THE BOTTOM SURFACE OF AN AS-BUILT BAR (3 <sup>RD</sup> TRIAL) WHERE THE CIRCULAR CONTOUR AND LINEAR CORE MELTING CAN BE IDENTIFIED .....	85
FIGURE 90: THE QUASI PHASE DIAGRAM SHOWING THE EFFECT OF -8Nb ADDITION ON THE PHASE RELATIONSHIP OF $\gamma$ -TiAl ALLOYS (SOLID LINES). THE BINARY Ti-AL PHASE DIAGRAM IS DRAWN IN DOTTED LINES FOR REFERENCE <sup>[112]</sup> .....	86
FIGURE 91: X-RAY DIFFRACTION PATTERNS OF Ti-48Al-2Cr-2Nb (LIGHT GREY), Ti-45Al-2Cr-8Nb (DARK GREY) AND Ti-46Al-2Cr-8Nb (BLACK) ALLOYS AS-EBM.....	87
FIGURE 92: OPTICAL MICROGRAPH OF Ti-45Al-2Cr-8Nb SHOWING THE MICROSTRUCTURE AT MAGNIFICATION x50 (A) AND x100 (B).....	88
FIGURE 93: OPTICAL MICROGRAPH OF Ti-46Al-2Cr-8Nb SHOWING THE MICROSTRUCTURE AT MAGNIFICATION x50 (A) AND x100 (B).....	88
FIGURE 94: OPTICAL MICROGRAPH OF Ti-48Al-2Cr-2Nb SHOWING THE MICROSTRUCTURE AT MAGNIFICATION x50 (A) AND x100 (B).....	89
FIGURE 95: PROGRESSIVE GERMINATION OF A CALCITE CRYSTAL, IN GREY THE GERMINATED PART ((A)-(E)). GERMINATION OF A CRYSTAL OF WHICH ONE SIDE IS STRONGLY IMPEDED TO GROW (F) <sup>[136]</sup> .....	90
FIGURE 96: HIGH MAGNIFICATION MICROGRAPH OF A SELECTED ZONE OF AS-EBM Ti-46Al-2Cr-8Nb .....	90
FIGURE 97: SEM MICROGRAPH OF Ti-45Al-2Cr-8Nb AT MAGNIFICATION x5000 .....	91
FIGURE 98: SEM MICROGRAPH OF Ti-46Al-2Cr-8Nb AT MAGNIFICATION x20000 .....	91
FIGURE 99: SCHEMATIC DRAWING OF THE TYPICAL MICROSTRUCTURES OF $\gamma$ -TiAl ALLOYS .....	92
FIGURE 100: 4x4x10 MM <sup>3</sup> SPECIMEN FOR TMA ANALYSIS .....	93
FIGURE 101: TMA MEASUREMENT OF Ti-47Al-2Cr-2Nb: DISPLACEMENT (CONTINUOUS LINE) AND DERIVATIVE OF THE DISPLACEMENT (DOTTED LINE) AS FUNCTIONS OF TEMPERATURE <sup>[68]</sup> .....	93
FIGURE 102: COMPARISON BETWEEN DSC CURVE (CONTINUOUS LINE) AND THE DERIVATIVE OF THE DISPLACEMENT MEASURED BY TMA (DASHED LINE) FOR Ti-47Al-2Cr-2Nb IN ARGON ATMOSPHERE AND 5 °C.MIN <sup>-1</sup> HEATING RATE <sup>[68]</sup> .....	94
FIGURE 103: COMPARISON OF THE DERIVATIVE OF THE DISPLACEMENT MEASURED BY TMA BETWEEN Ti-47Al-2Cr-2Nb (DASHED LINE), Ti-45Al-2Cr-2Nb (DOTTED LINE) AND Ti-45Al-2Cr-8Nb (SOLID LINE) <sup>[68]</sup> .....	95
FIGURE 104: LINEAR REGRESSION FROM DYNAMIC TRANSITION TEMPERATURES $TR_{eu}, \alpha$ MEASURED AT DIFFERENT HEATING RATE $R$ OF Ti-46Al-2Cr-8Nb <sup>[68]</sup> .....	96
FIGURE 105: DISPLACEMENT DERIVATIVE VS. TEMPERATURE MEASURED BY TMA OF Ti-45Al-2Cr-8Nb AFTER EACH TRIAL OF THE EBM PROCESS OPTIMIZATION. FROM TOP TO DOWN: 2 <sup>ND</sup> TRIAL (BLACK LINE), 3 <sup>RD</sup> TRIAL (DARK GREY LINE), 4 <sup>TH</sup> TRIAL (GREY LINE) AND 5 <sup>TH</sup> TRIAL (LIGHT GREY) .....	97
FIGURE 106: DISPLACEMENT DERIVATIVE VS. TEMPERATURE MEASURED BY TMA OF Ti-45Al-2Cr-8Nb (LIGHT GREY LINE) AND Ti-46Al-2Cr-8Nb (BLACK LINE) FABRICATED BY EBM ACCORDING TO THE SELECTED CONDITIONS .....	98
FIGURE 107: DISPLACEMENT DERIVATIVE VS. TEMPERATURE MEASURED BY TMA IN THE CORE (BLACK LINE) AND THE EDGE (LIGHT GREY LINE) OF Ti-45Al-2Cr-8Nb FABRICATED BY EBM ACCORDING TO THE SELECTED CONDITIONS .....	99
FIGURE 108: GERO FURNACE FOR HEAT TREATMENT OF $\gamma$ -TiAl ALLOYS.....	103
FIGURE 109: SCHEMATIC DRAWING OF THE SIMUL-HIP TREATMENT .....	104
FIGURE 110: OPTICAL MICROGRAPH AT MAGNIFICATION x50 OF Ti-45Al-2Cr-8Nb AFTER HIP (1260 °C, 170 MPa, 4h, ARGON) .....	104
FIGURE 111: OPTICAL MICROGRAPH AT MAGNIFICATION x50 OF Ti-45Al-2Cr-8Nb AFTER SHIP (1260 °C, 4h, ARGON) .....	104



FIGURE 112: TOP SURFACE OF A Ti-46Al-2Cr-8Nb SAMPLE HIPED AND SUBSEQUENTLY HEAT TREATED AT 1315 °C FOR 2H IN VACUUM IN GERO FURNACE.....	105
FIGURE 113: 4 TiAl SAMPLES IN THE FURNACE CHAMBER OF THE GERO FURNACE FOR HEAT TREATMENTS .....	106
FIGURE 114: SCHEMATIC DRAWING OF THE HEAT TREATMENT PERFORMED IN GERO FURNACE UNDER HIGH VACUUM ( $10^{-4}$ MBAR) .....	106
FIGURE 115: OPTICAL MICROGRAPHS REPRESENTING THE MICROSTRUCTURE ALONG THE LAYER DEPOSITION DIRECTION OF AS-EBM Ti-45Al-2Cr-8Nb ALLOYS TREATED AT DIFFERENT TEMPERATURES IN THE VICINITY OF $T_A = 1295$ °C .....	107
FIGURE 116: DUPLEX MICROSTRUCTURES OF Ti-45Al-2Cr-8Nb OBTAINED BY HEAT TREATMENT AT 1300, 1305 AND 1310 °C FOR EBM MATERIALS AND 1295, 1300, 1305 °C FOR EBM + HIP MATERIALS.....	109
FIGURE 117: DUPLEX MICROSTRUCTURES OF Ti-46Al-2Cr-8Nb OBTAINED BY HEAT TREATMENTS AT 1305, 1315 AND 1320 °C FOR EBM AND EBM + HIP MATERIALS.....	110
FIGURE 118: OPTICAL MICROGRAPHS SHOWING THE MICROSTRUCTURE OF AS-EBM Ti-45Al-2Cr-8Nb MATERIAL HEAT TREATED AT 1305 °C FOR 2 HOURS IN VACUUM. A IS THE COMPOSITION OF IMAGES TAKEN AT MAGNIFICATION X50 STITCHED TOGETHER, B AND C WERE TAKEN AT MAGNIFICATION X100 RESPECTIVELY IN THE EDGE AND THE CORE OF THE SPECIMEN, D AND E WERE TAKEN AT MAGNIFICATION X200 RESPECTIVELY IN THE EDGE AND THE CORE OF THE SPECIMEN .....	112
FIGURE 119: OPTICAL MICROGRAPHS SHOWING THE MICROSTRUCTURE OF AS-EBM Ti-46Al-2Cr-8Nb MATERIAL HEAT TREATED AT 1320 °C FOR 2 HOURS IN VACUUM. A IS THE COMPOSITION OF IMAGES TAKEN AT MAGNIFICATION X50 STITCHED TOGETHER, B AND C WERE TAKEN AT MAGNIFICATION X100 RESPECTIVELY IN THE EDGE AND THE CORE OF THE SPECIMEN, D AND E WERE TAKEN AT MAGNIFICATION X200 RESPECTIVELY IN THE EDGE AND THE CORE OF THE SPECIMEN .....	113
FIGURE 120: HIGH MAGNIFICATION (X500) OPTICAL MICROGRAPHS TAKEN IN THE EDGE AND THE CORE OF AS-EBM Ti-45Al-2Cr-8Nb HEAT TREATED AT 1305 °C .....	114
FIGURE 121: HIGH MAGNIFICATION (X500) OPTICAL MICROGRAPHS TAKEN IN THE EDGE AND THE CORE OF AS-EBM Ti-46Al-2Cr-8Nb HEAT TREATED AT 1320 °C .....	114
FIGURE 122: MASS GAIN VERSUS TEMPERATURE OF Ti-45Al-2Cr-8Nb, Ti-46Al-2Cr-8Nb AND Ti-47Al-2Cr-2Nb DURING HEATING IN AIR FROM 25 TO 750 °C AT $10$ °C.MIN <sup>-1</sup> AND FROM 750 TO 1000 °C AT $0.05$ °C.MIN <sup>-1</sup> . THE FIGURE HIGHLIGHTS THE 750 - 1000 °C PORTION OF THE GRAPH .....	116
FIGURE 123: MASS GAIN VERSUS TIME OF Ti-47Al-2Cr-2Nb, Ti-45Al-2Cr-8Nb AND Ti-46Al-2Cr-8Nb ALLOYS DURING ISOTHERMAL OXIDATION IN AIR AT 750 °C FOR 10 HOURS .....	118
FIGURE 124: MASS GAIN VERSUS TIME OF Ti-47Al-2Cr-2Nb, Ti-45Al-2Cr-8Nb AND Ti-46Al-2Cr-8Nb ALLOYS DURING ISOTHERMAL OXIDATION IN AIR AT 850 °C FOR 10 HOURS .....	118
FIGURE 125: MASS GAIN VERSUS TIME OF Ti-47Al-2Cr-2Nb, Ti-45Al-2Cr-8Nb AND Ti-46Al-2Cr-8Nb ALLOYS DURING ISOTHERMAL OXIDATION IN AIR AT 950 °C FOR 10 HOURS .....	118
FIGURE 126: MASS GAIN BY SURFACE AREA OF Ti-47Al-2Cr-2Nb AND Ti-45Al-2Cr-8Nb AFTER OXIDATION IN AIR AT 850 °C FOR 7, 30, 50 AND 100 HOURS. CIRCLED POINTS INDICATE THAT SPALLATION OCCURRED <sup>[67]</sup> .....	120
FIGURE 127: X-RAY DIFFRACTION PATTERNS OF THE SURFACE OF Ti-47Al-2Cr-2Nb (A) AND Ti-45Al-2Cr-8Nb (B) AS-EBM AND AFTER 7, 30, 50 AND 100 HOURS OF OXIDATION IN STATIC AIR AT 850 °C <sup>[67]</sup> .....	122
FIGURE 128: SEM MICROGRAPHS OF THE TOP SURFACE OF OXIDIZED SAMPLES FOR 100 HOURS AT 850 °C SHOWING: (A) SPALLED AND UNDERLYING OXIDES LAYERS ON Ti-47Al-2Cr-2Nb AND (B) INHOMOGENEOUS CONSISTENT OXIDES LAYER ON Ti-45Al-2Cr-8Nb <sup>[67]</sup> .....	124
FIGURE 129: ELEMENT MAP FROM EDS ANALYSIS SHOWING THE TITANIUM AND ALUMINUM DISTRIBUTION IN A SPALLED AREA OF THE SURFACE OF Ti-47Al-2Cr-2Nb SAMPLE AFTER 100 °C OF OXIDATION IN AIR AT 850 °C.....	124
FIGURE 130: MASS GAIN BY SURFACE AREA OF Ti-47Al-2Cr-2Nb AND Ti-45Al-2Cr-8Nb AFTER OXIDATION IN AIR FOR 7, 30 AND 50 HOURS AT 850 °C AND 950 °C RESPECTIVELY .....	125
FIGURE 131: SPECIFIC ULTIMATE TENSILE STRENGTH (UTS) AS A FUNCTION OF TEMPERATURE OF Ti-46Al-2Cr-8Nb (BLACK) AND Ti-48Al-2Cr-2Nb (GREY) .....	127
FIGURE 132: SPECIFIC YIELD STRENGTH (YS) AS A FUNCTION OF TEMPERATURE OF Ti-46Al-2Cr-8Nb (BLACK) AND Ti-48Al-2Cr-2Nb (GREY) .....	127
FIGURE 133: ELONGATION AS A FUNCTION OF TEMPERATURE OF Ti-46Al-2Cr-8Nb (BLACK) AND Ti-48Al-2Cr-2Nb (GREY) ....	127
FIGURE 134: SPECIFIC ULTIMATE TENSILE STRENGTH (UTS) AS A FUNCTION OF TEMPERATURE OF Ti-46Al-2Cr-8Nb (BLACK) AND SUPERALLOYS INCONEL 718 (RED) AND UDIMET 710 (GREEN).....	128
FIGURE 135: SPECIFIC YIELD STRENGTH (YS) AS A FUNCTION OF TEMPERATURE OF Ti-46Al-2Cr-8Nb (BLACK) AND SUPERALLOYS INCONEL 718 (RED) AND UDIMET 710 (GREEN) .....	128
FIGURE 136: STRESS TO RUPTURE AS A FUNCTION OF TIME OF Ti-46Al-2Cr-8Nb (RED) AND Ti-48Al-2Cr-2Nb (BLUE) AT 760 °C, 815 °C .....	129

TABLE 1: TITANIUM ALLOYS USED FOR COMPRESSOR PARTS IN AIRCRAFT ENGINES <sup>[28]</sup> .....	19
TABLE 2: SHEETS SUPERALLOYS FOR COMBUSTOR PARTS IN AEROENGINE GAS TURBINE ENGINES <sup>[28]</sup> .....	20
TABLE 3: INGOT METALLURGY (A286 AND 718) AND PM SUPERALLOYS FOR TURBINE DISCS IN AEROENGINE GAS TURBINE ENGINES <sup>[28]</sup> .....	21
TABLE 4: NOMINAL CONSTITUENT AND ROOM TEMPERATURE THERMOSTRUCTURAL PROPERTIES FOR SOME ADVANCED CMC SYSTEMS OF CURRENT INTEREST FOR HOT SECTION ENGINE COMPONENTS <sup>[36]</sup> .....	25
TABLE 5: 500-HOUR RUPTURE STRENGTH IN X-DIRECTION AND UPPER USE TEMPERATURES FOR THE CMC IN TABLE 4 <sup>[36]</sup> .....	26
TABLE 6: DENSITY AND MECHANICAL PROPERTIES OF SAMPLES SINTERED BY VARIOUS SINTERING TECHNIQUES AT DIFFERENT TEMPERATURES <sup>[41]</sup> .....	30
TABLE 7: BULK DENSITY, OPEN POROSITY AND RELATIVE DENSITY OF MONOLITHIC SiALON AND SiTiCO FIBRE/SiALON COMPOSITE <sup>[42]</sup> .....	31
TABLE 8: MECHANICAL PROPERTIES IMPROVEMENT ON Si <sub>3</sub> N <sub>4</sub> BY MoSi <sub>2</sub> ADDITION <sup>[34]</sup> .....	34
TABLE 9: TOUGHNESS IMPROVEMENT ON Si <sub>3</sub> N <sub>4</sub> BY MoSi <sub>2</sub> ADDITION <sup>[34]</sup> .....	34
TABLE 10: TiAl STATE-OF-THE-ART ALLOYS <sup>[50]</sup> .....	42
TABLE 11: EFFECT OF ALLOYING ELEMENT ADDITION TO $\gamma$ -TiAl ALLOYS .....	44
TABLE 12: GENERAL PROPERTIES OF 1ST AND 2ND GENERATION $\gamma$ -TiAl ALLOYS .....	45
TABLE 13: TENSILE STRENGTH OF TAWBY (Ti-45Al-8.5Nb-0.3W-0.3B-0.05Y) ALLOYS AT ROOM TEMPERATURE COMPARED TO OTHER FULLY LAMELLAR HIGH Nb CONTAINING TiAl ALLOYS <sup>[82]</sup> .....	46
TABLE 14: MICROSTRUCTURAL FEATURES AND TENSILE PROPERTIES AT ROOM TEMPERATURE OF SOME $\gamma$ -TiAl ALLOYS <sup>[100]</sup> .....	48
TABLE 15: TENSILE STRENGTH OF TAWBY (Ti-45Al-8.5Nb-0.3W-0.3B-0.05Y) ALLOYS AT HIGH TEMPERATURES COMPARED TO OTHER $\gamma$ -TiAl ALLOYS <sup>[82]</sup> .....	48
TABLE 16: MECHANICAL PROPERTIES OF Ti-46Al-9Nb SHEET MATERIAL AS OBTAINED FROM TENSILE TESTS <sup>[101]</sup> .....	49
TABLE 17: COMPARISON OF THE MINIMUM CREEP RATES OF TiAl-BASE ALLOYS AT 760°C <sup>[103]</sup> .....	53
TABLE 18: FRACTURE TOUGHNESS OF TAWBY ALLOY AT ROOM TEMPERATURE FOR FULLY LAMELLAR (FL) AND DUPLEX (DP) MICROSTRUCTURES <sup>[82]</sup> .....	55
TABLE 19: FRACTURE TOUGHNESS AT ROOM TEMPERATURE AND MICROSTRUCTURAL FEATURES OF SOME $\gamma$ -TiAl ALLOYS <sup>[100]</sup> .....	55
TABLE 20: TECHNICAL DATA FOR THE ARCAM A2 MACHINE <sup>[119]</sup> .....	67
TABLE 21: ACTUAL CHEMICAL COMPOSITION OF Ti-47Al-2Cr-8Nb AS-RECEIVED POWDER MEASURED BY ICP AND LECO INSTRUMENT .....	69
TABLE 22: ACTUAL CHEMICAL COMPOSITION OF Ti-48Al-2Cr-8Nb AS-RECEIVED POWDER MEASURED BY ICP AND LECO INSTRUMENT .....	69
TABLE 23: PARTICLE SIZE DISTRIBUTION OF Ti-48Al-2Cr-2Nb, Ti-47Al-2Cr-8Nb AND Ti-48Al-2Cr-8Nb POWDERS .....	70
TABLE 24: FLOWABILITY OF Ti-48Al-2Cr-2Nb, Ti-47Al-2Cr-8Nb AND Ti-48Al-2Cr-8Nb ACCORDING TO STANDARD ASTM B213-03 .....	72
TABLE 25: APPARENT DENSITY OF Ti-48Al-2Cr-2Nb, Ti-47Al-2Cr-8Nb AND Ti-48Al-2Cr-8Nb ACCORDING TO STANDARD ASTM B212-99 .....	72
TABLE 26: CHEMICAL COMPOSITION OF THE POWDER AS-RECEIVED (Ti-47Al-2Cr-8Nb AND Ti-48Al-2Cr-8Nb) AND THE CORRESPONDING MATERIALS AS-EBM .....	84
TABLE 27: MEASUREMENTS OF THE ALUMINUM CONTENT OF DIFFERENT MATERIALS AND POSITIONS BY ATOMIC ABSORPTION .....	85
TABLE 28: RESIDUAL POROSITY AS MEASURED IN SAMPLES AFTER EBM AND AFTER SUBSEQUENT HIP FOR Ti-45Al-2Cr-8Nb AND Ti-46Al-2Cr-8Nb. ....	101
TABLE 29: OPTICAL MICROGRAPH AT MAGNIFICATIONS X100 AND X200 OF Ti-45Al-2Cr-8Nb ALLOYS AFTER EBM AND AFTER SUBSEQUENT HIP .....	102
TABLE 30: OPTICAL MICROGRAPH AT MAGNIFICATIONS X100 AND X200 OF Ti-46Al-2Cr-8Nb ALLOYS AFTER EBM AND AFTER SUBSEQUENT HIP .....	103
TABLE 31: VICKERS MICROHARDNESS OF Ti-45Al-2Cr-8Nb AFTER HIP AND SHIP TREATMENT .....	105
TABLE 32: VICKERS HARDNESS MEASUREMENTS AND CORRESPONDING YIELD STRENGTH ACCORDING TO KIM ET AL. OF Ti-46Al-2Cr-8Nb ALLOYS WITH DIFFERENT MICROSTRUCTURE .....	108

## Bibliography

1. TMS, *Greatest Moments in Materials Science and Engineering*. (2007). Available from: <http://www.materialmoments.org/top100.html>.
2. JOM, *The Member Journal of TMS - About JOM*. (2012). Available from: <http://www.tms.org/pubs/journals/JOM/aboutJOM.aspx>.
3. J.P. Angus. *Aero engine ceramics - the vision, the reality and the progress*, in Institution of Mechanical Engineers, Part G: Journal of Aerospace Engineering. (1993). pp. 83-96.
4. J.E. Allen, F.W. Armstrong and R.M. Denning. *Evolution of aviation and propulsion systems: the next fifty years*, in Institution of Mechanical Engineers, Part G: Journal of Aerospace Engineering. (1995), ISBN: 0954-4100. pp. 15-33.
5. A.D. Kumar, S. Sathyanarayanan, S.D. Gupta and M.N. Rao, *Gas Turbine Materials - Current status and its development prospects*.
6. R.A. Braeunig, *Basics of Space Flight - Rocket Propulsion*. (2012). Available from: <http://www.braeunig.us/space/propuls.htm>.
7. J.D. Mattingly, *Elements of Gas Turbine Propulsion* (2005), ISBN: 0-07-060628-5. pages. 754.
8. J.D. Mattingly and H. von Ohain, *Introduction to Air Breathing Engines*, in *Elements of Propulsion: Gas Turbines and Rockets* (2006), ISBN: 1563477793.
9. T.A. Çetinkaya, *Gas Turbines And Jet Propulsion*. (2013). Available from: <http://www.me.metu.edu.tr/courses/me423/index.html>.
10. M. Bellis, *Different Types of Jet Engines*. Available from: [http://inventors.about.com/od/jstartinventions/ss/jet\\_engine.htm](http://inventors.about.com/od/jstartinventions/ss/jet_engine.htm).
11. E. Campo and V. Lupinc, *High temperature structural materials for gas turbines*. Metallurgical Science and Technology, 11 (1): 1993. pp. 31-47.
12. N-Prize, *Turbofan*. (2011). Available from: <http://lcas.otaski.org/index.php/Category:Turbofan>.
13. B. Udden, *Thermal kinematics - Gas Turbine For the Best Performance*. Available from: <http://miblawofthermal.blogspot.it/2011/08/gas-turbine-for-best-performance.html>.
14. T. Giampaolo, *Gas Turbine Handbook - Principles and Practice* (2009). The Fairmont Press, ISBN: 0-88173-613-9.
15. NASA, *Turbine Engine Thermodynamic Cycle - Brayton Cycle*. (2008). Available from: <http://www.grc.nasa.gov/WWW/k-12/airplane/brayton.html>.
16. Z.S. Spakovszky, E.M. Greitzer and I.A. Waitz, *Thermodynamics and Propulsion*. Available from: <http://web.mit.edu/16.unified/www/FALL/thermodynamics/notes/notes.html>.
17. Wikipédia, *Turbofan*. (2013). Available from: <http://en.wikipedia.org/wiki/Turbofan>.
18. J.B. Husband, *Developing an Efficient FEM Structural Simulation of a Fan Blade Off test in a Turbofan jet engine* (2007). University of Saskatchewan.
19. P.P. Walsh and P. Fletcher, *Gas Turbine Performance* (2004). Blackwell Science Ltd, ISBN: 0-632-06434-X.
20. Rolls-Royce, *Journey through a jet engine*. (2013). Available from: [http://www.rolls-royce.com/interactive\\_games/journey03/index.html](http://www.rolls-royce.com/interactive_games/journey03/index.html).

21. C. International, *The CFM56 Turbofan Engine Product Line*. Available from: <http://www.cfmaeroengines.com/engines>.
22. G. Aviation, *Aviation History*. Available from: <http://www.geaviation.com/company/aviation-history.html>.
23. T.B. Company, *CFM56-7 Engine Ground Handling Document*. (2011).
24. Wikipédia, *CFM International - CFM56*. (2013). Available from: [http://fr.wikipedia.org/wiki/CFM\\_International\\_CFM56](http://fr.wikipedia.org/wiki/CFM_International_CFM56).
25. D.R. Greatrix, *Gas Turbine Engines: Fundamentals*, in *Powered Flight* (2012). Springer, ISBN: 978-1-4471-2484-9. pp. 147-231.
26. Snecma, *CFM 56-7 Tooling Catalogue*. (2007). Available from: <http://www.snecma.com/catalogues/tooling/engines/CFM56-7/CFM56-7.htm>.
27. P.F. Products, *Products*. Available from: <http://www.pccforgedproducts.com/products/>.
28. N.R. Muktinutalapati, *Materials for Gas Turbines - An Overview*, in *Advances in Gas Turbine Technology* (2011). InTech, ISBN: 978-953-307-611-9. pp. 293-314.
29. G.F. Vander Voort, *Materials Characterization & Testing: Microstructure of Titanium & Its Alloys*. Available from: <http://vacaero.com/information-resources/metallography-with-george-vander-voort/870-materials-characterization-a-testing-microstructure-of-titanium-and-its-alloys.html>.
30. M. Whittaker, *Titanium in the Gas Turbine Engine*, in *Advances in Gas Turbine Technology* (2011). InTech, ISBN: 978-953-307-611-9. pp. 316-336.
31. P.W. Schilke, *Advanced Gas Turbine materials and coatings*. GE Energy, 2004. pp. 1-30.
32. Rolls-Royce, *High temperature materials*. Available from: [http://www.rolls-royce.com/about/technology/material\\_tech/high\\_temperature\\_materials.jsp](http://www.rolls-royce.com/about/technology/material_tech/high_temperature_materials.jsp).
33. D.W. Richerson. *Historical Review of Addressing the Challenges of Use of Ceramic Components in Gas Turbine Engines*, in ASME Turbo Expo 2006: Power for Land, Sea and Air. (2006), Barcelon, Spain, ISBN: 0-7918-4237-1. pp. 241-254.
34. J.-Y. Guedou. *Materials evolution in hot parts of aero-turbo-engines*, in ICAS2010. (2010).
35. H. Ohnabea, S. Masakia, M. Onozukaa, K. Miyaharab and T. Sasab, *Potential application of ceramic matrix composites to aero-engine components*. Composites, Part A (30): 1999. pp. 489-496.
36. J.A. DiCarlo and M. van Roode. *Ceramic composite development for gas turbine engine hot section components*, in ASME Turbo Expo 2006: Power of Land, Sea and Air. (2006), Barcelona, Spain, ISBN: 0-7918-4237-1. pp. 221-231.
37. M. Parlier, R. Valle, L. Perrière, S. Lartigue-Korinek and L. Mazerolles, *Potential of Directionally Solidified Eutectic Ceramics for High Temperature Applications*. Journal Aerospace Lab, High Temperature Materials (3): 2011.
38. Y. Zheng, T. Zhou, G. Ye and X. Zhang. *Microstructure and mechanical properties of eutectic composite ceramic Al<sub>2</sub>O<sub>3</sub>-ZrO<sub>2</sub> by explosion synthesis*, in The 18th International Conference on Composite Materials. (2011), ICC Jeju, Korea.
39. Y. Waku, *A New Ceramic Eutectic Composite with High Strength at 1873 K*. Advanced Materials, 10 (8): 1998. pp. 615-617.
40. K. Hirano, *Application of eutectic composites to gas turbine system and fundamental fracture properties up to 1700 °C*. Journal of the European Ceramic Society, 25 2005. pp. 1191-1199.
41. O. Esera and S. Kurama, *A comparison of sintering techniques using different particle sized Beta-SiAlON powders*. Journal of the European Ceramic Society, 32 2012. DOI: 10.1016/j.jeurceramsoc.2011.08.026. pp. 1343-1347.

42. T. Inoue and K. Ueno, *Mechanical Properties and Fracture Behaviour of SiTiCO Fibre/SiAlON Composite*. Ceramics International, 24 **1996**. pp. 565-569.
43. A. Demir, *Effect of Nicalon SiC fibre heat treatment on short fibre reinforced Beta-SiAlON ceramics*. Journal of the European Ceramic Society, 32 **2012**. pp. 1405-1411.
44. A. Demir and D.P. Thompson, *High performance SiC-fibre reinforced Beta-Sialon CMCs prepared from Heat-treated Nicalon fibres*. Journal of the European Ceramic Society, 21 **2001**. pp. 639-647.
45. M.G. Hebsur, *Development and characterization of SiC(f) MoSi<sub>2</sub>-Si<sub>3</sub>N<sub>4</sub>(p) hybrid composites*. Materials Science and Engineering, A261 **1999**. pp. 24-37.
46. S.F. Franzén and J. Karlsson, *Gamma Titanium Aluminide Manufactured by Electron Beam Melting (2010)*. Chalmers University of Technology,. p. 89.
47. D. Cormier, O. Harrysson, T. Mahale and H. West, *Freeform Fabrication of Titanium Aluminide via Electron Beam Melting Using Prealloyed and Blended Powders*. Research Letters in Materials Science, **2007**. DOI: 10.1155/2007/34737. pp. 1-4.
48. F. Appel, J.D.H. Paul and M. Oehring, *Gamma Titanium Aluminide alloys: Science and Technology (2011)*. Wiley VCH, ISBN: 978-3-527-31525-3. pages. 762.
49. M.T. Jovanović, B. Dimčić, I. Bobić, S. Zec and V. Maksimović, *Microstructure and mechanical properties of precision cast TiAl turbocharger wheel*. Journal of Materials Processing Technology, 167 (1): **2005**. DOI: 10.1016/j.jmatprotec.2005.03.019. pp. 14-21.
50. K. Kothari, R. Radhakrishnan and N.M. Wereley, *Advances in gamma titanium aluminides and their manufacturing techniques*. Progress in Aerospace Sciences, 55 **2012**. DOI: 10.1016/j.paerosci.2012.04.001. pp. 1-16.
51. T. Noda, *Application of cast gamma TiAl for automobiles*. Intermetallics, 6 **1998**. pp. 709-713.
52. B.A. Pint, J.A. Haynes and B.L. Armstrong, *Performance of advanced turbocharger alloys and coatings at 850-950°C in air with water vapor*. Surface and Coatings Technology, 215 **2013**. DOI: 10.1016/j.surfcoat.2012.08.099. pp. 90-95.
53. T. Tetsui, *Gamma Ti aluminides for non-aerospace applications*. Solid State and Materials Science, 4 **1999**. pp. 243-248.
54. T. Tetsui, *TiAl intermetallic compound-based alloy (2001)*. Mitsubishi Heavy Industries Ltd. p. 7.
55. T. Tetsui, *Development of a TiAl turbocharger for passenger vehicles*. Materials Science and Engineering, A329-331 **2002**. pp. 582-588.
56. T. Tetsui and S. Ono, *Endurance and composition and microstructure effects on endurance of TiAl used in turbochargers*. Intermetallics, 7 **1999**. pp. 687-697.
57. X. Wu, *Review of alloy and process development of TiAl alloys*. Intermetallics, 14 (10-11): **2006**. DOI: 10.1016/j.intermet.2005.10.019. pp. 1114-1122.
58. H.-E. Zschau, M. Schütze, H. Baumann and K. Bethge, *The time behaviour of surface applied fluorine inducing the formation of an alumina scale on gamma-TiAl during oxidation at 900°C in air*. Intermetallics, 14 (10-11): **2006**. DOI: 10.1016/j.intermet.2006.01.063. pp. 1136-1142.
59. M. Thomas and M.-P. Bracos, *Processing and characterization of TiAl based alloys - towards an industrial scale*. Journal Aerospace Lab, (3): **2011**. pp. 1-11.
60. Z.C. Liu, J.P. Lin, Y.L. Wang, Z. Lin, G.L. Chen and K.M. Chang, *High temperature deformation behaviour of As-cast Ti-46Al-8.5Nb-0.2W alloy*. Materials Letters, 58 (6): **2004**. DOI: 10.1016/j.matlet.2003.07.049. pp. 948-952.
61. P.A. Bartolotta and D.L. Krause. *Titanium aluminide applications in the high speed civil transport*, in Gamma Titanium Aluminides. (1999), San Diego, California. The Minerals, Metals & Materials Society. pp. 12.

62. TITAL, *Gamma Tial Would Be the Ideal Choice for Turbines*. (2009). Available from: [http://www.aerospace-technology.com/contractors/sub\\_contract/tital/press9.html](http://www.aerospace-technology.com/contractors/sub_contract/tital/press9.html).
63. S.B. Abu Sulik, K. Takeshita, H. Kitagawa, T. Tetsui and K. Hasezaki, *Preparation and high temperature oxidation behavior of refractory disilicide coatings for  $\gamma$ -TiAl intermetallic compounds*. Intermetallics, 15 (8): 2007. DOI: 10.1016/j.intermet.2007.01.004. pp. 1084-1090.
64. W.J. Zhang, B.V. Reddy and S.C. Deevi, *Physical properties of TiAl-base alloys*. Scripta Materialia, 45 2001. pp. 645-651.
65. M. Terner, S. Biamino, P. Epicoco, A. Penna, O. Hedin, S. Sabbadini, . . . and C. Badini, *Electron Beam Melting of High Niobium Containing TiAl Alloy: Feasibility Investigation*. steel research international, 83 (10): 2012. DOI: 10.1002/srin.201100282. pp. 943-949.
66. M. Terner, S. Biamino, A. Penna, O. Hedin, S. Sabbadini, P. Fino, . . . and C. Badini. *Material properties of TiAl alloy with high Nb content produced by the additive manufacturing technology of Electron Beam Melting*, in Euro PM 2012. (2012), Montpellier, France. European Powder Metallurgy Association, ISBN: 978-1-899072-25-5. pp. 163 - 167.
67. M. Terner, S. Biamino, S. Sabbadini, F. Pelissero, P. Fino, M. Pavese and C. Badini. *Oxidation behavior of Ti-47Al-2Cr-2Nb and Ti-45Al-2Cr-8Nb produced by Electron Beam Melting*, in Proceedings Euro PM 2013 (2013), Basel, Switzerland. European Powder Metallurgy Association, ISBN: 978-1-899072-42-2. pp. 55 - 60.
68. M. Terner, S. Biamino, D. Ugues, S. Sabbadini, P. Fino, M. Pavese and C. Badini, *Phase transitions assessment on  $\gamma$ -TiAl by Thermo Mechanical Analysis*. Intermetallics, 37 2013. DOI: 10.1016/j.intermet.2013.01.019. pp. 7-10.
69. J. Lapin. *TiAl-Based Alloys - Present Status and Future Perspectives*, in METAL 2009. (2009), Hradec nad Moravicí.
70. V.A.C. Haanappel, H. Clemens and M.F. Stroosnijder, *The high temperature oxidation behaviour of high and low alloyed TiAl-based intermetallics*. Intermetallics, 10 2002. pp. 293-305.
71. W. Lu, C. Chen, Y. Xi, F. Wang and L. He, *The oxidation behavior of Ti-46.5Al-5Nb at 900°C*. Intermetallics, 15 (8): 2007. DOI: 10.1016/j.intermet.2006.09.010. pp. 989-998.
72. M. Mitoraj, E. Godlewska, O. Heintz, N. Geoffroy, S. Fontana and S. Chevalier, *Scale composition and oxidation mechanism of the Ti-46Al-8Nb alloy in air at 700 and 800 °C*. Intermetallics, 19 (1): 2011. DOI: 10.1016/j.intermet.2010.09.006. pp. 39-47.
73. M. Mitoraj and E.M. Godlewska, *Oxidation of Ti-46Al-8Ta in air at 700 °C and 800 °C under thermal cycling conditions*. Intermetallics, 34 2013. DOI: 10.1016/j.intermet.2012.10.014. pp. 112-121.
74. S. Nishikiori, *Ti-Al-(Mo,V,Si,Fe) alloys and method of their manufacture* (2000). p. 18.
75. A. Penna, *Gamma-TiAl Fabricated by EBM as Innovative Material for Aerospace Applications with Low Environmental Impact* (2013). Politecnico di Torino. p. 333.
76. M. Schutze and M. Hald, *Improvement of the oxidation resistance of TiAl alloys by using the chlorine effect*. Materials Science and Engineering, A239-240 1997. pp. 847-858.
77. T. Tetsui, *TiAl intermetallic compound-based alloys and method for preparing same* (2000). Mitsubishi Jukogyo Kabushiki Kaisha. p. 13.
78. F. Appel, M. Oehring and R. Wagner, *Novel design concepts for gamma-base titanium aluminide alloys*. Intermetallics, 8 2000. pp. 1283-1312.

79. S. Bystrzanowski, A. Bartels, H. Clemens, R. Gerling, F.P. Schimansky, G. Dehm and H. Kestler, *Creep behaviour and related high temperature microstructural stability of Ti-46Al-9Nb sheet material*. Intermetallics, 13 (5): **2005**. DOI: 10.1016/j.intermet.2004.09.001. pp. 515-524.
80. Y.-W. Kim, *Strength and ductility in TiAl alloys*. Intermetallics, 6 **1998**. pp. 623-628.
81. M. Yamaguchi, H. Zhu, M. Suzuki, K. Maruyama and F. Appel, *Importance of microstructural stability in creep resistance of lamellar TiAl alloys*. Materials Science and Engineering: A, 483-484 **2008**. DOI: 10.1016/j.msea.2006.09.147. pp. 517-520.
82. Y.Q. Yan, L. Zhou, W.S. Wang and Y.N. Zhang, *8.5Nb-TiAl alloy with fine grains*. Journal of Alloys and Compounds, 361 (1-2): **2003**. DOI: 10.1016/s0925-8388(03)00427-4. pp. 241-246.
83. J. Lasalle and S. Das, *Castable gamma titanium-aluminide alloy containing niobium, chromium and silicon (1996)*.
84. L.E. Murr, S.M. Gaytan, A. Ceylan, E. Martinez, J.L. Martinez, D.H. Hernandez, . . . and S. Collins, *Characterization of titanium aluminide alloy components fabricated by additive manufacturing using electron beam melting*. Acta Materialia, 58 (5): **2010**. DOI: 10.1016/j.actamat.2009.11.032. pp. 1887-1894.
85. R. Gerling, A. Bartels, H. Clemens, H. Kestler and F.-P. Schimansky, *Structural characterization and tensile properties of a high niobium containing gamma TiAl sheet obtained by powder metallurgical processing*. Intermetallics, 12 (3): **2004**. DOI: 10.1016/j.intermet.2003.10.005. pp. 275-280.
86. S. Biamino, A. Penna, U. Ackelid, S. Sabbadini, O. Tassa, P. Fino, . . . and C. Badini, *Electron beam melting of Ti-48Al-2Cr-2Nb alloy: Microstructure and mechanical properties investigation*. Intermetallics, 19 (6): **2011**. DOI: 10.1016/j.intermet.2010.11.017. pp. 776-781.
87. A. Lasalmonie, *Intermetallics: Why is it so difficult to introduce them in gas turbine engines?* Intermetallics, 14 (10-11): **2006**. DOI: 10.1016/j.intermet.2006.01.064. pp. 1123-1129.
88. S. Taniguchi and T. Shibita, *Influence of additional elements on the oxidation behaviour of TiAl*. Intermetallics, 4 **1996**. pp. 85-93.
89. K.J. Harrison, *Turbofan manufacturers continue 'green' efforts*. (2010). Available from: <http://www.ainonline.com/aviation-news/aviation-international-news/2010-08-27/turbofan-manufacturers-continue-green-efforts>.
90. E.A. Loria, *Quo vadis gamma titanium aluminide*. Intermetallics, 9 (12): **2001**. DOI: 10.1016/s0966-9795(01)00064-4. pp. 997-1001.
91. Wikipédia, *General Electric - GENx*. (2013). Available from: [http://en.wikipedia.org/wiki/General\\_Electric\\_GENx](http://en.wikipedia.org/wiki/General_Electric_GENx).
92. I. CFM, *LEAP brochure (2013)*.
93. H. Kawaura, K. Nishino and T. Saito, *TiAl based alloys with excellent oxidation resistance and method for producing the same (2002)*. p. 15.
94. H. Kawaura, H. Kawahara, K. Nishino and T. Saito, *New surface treatment using shot blast for improving oxidation resistance of TiAl-base alloys*. Materials Science and Engineering, A329-331 **2002**. pp. 589-595.
95. D. Hu, A.J. Huang, D. Novovic and X. Wu, *The effect of boron and alpha grain size on the massive transformation in Ti-46Al-8Nb-xB alloys*. Intermetallics, 14 (7): **2006**. DOI: 10.1016/j.intermet.2005.12.003. pp. 818-825.
96. G. Sauthoff, *Intermetallics (1995)*. VCH Verlagsgesellschaft.
97. S.C. Huang and J.C. Chesnutt, *Gamma TiAl and its alloys (1995)*. John Wiley & Sons Ltd.

98. J.N. Wang, J. Yang and Y. Wang, *Grain refinement of a Ti-47Al-8Nb-2Cr alloy through heat treatments*. Scripta Materialia, 52 (4): **2005**. DOI: 10.1016/j.scriptamat.2004.10.004. pp. 329-334.
99. H.G. Jung, D.J. Jung and K.Y. Kim, *Effect of Cr addition on the properties of aluminide coating layers formed on TiAl alloys*. Surface and Coatings Technology, 154 **2002**. pp. 75-81.
100. J.P. Campbell, K.T. Venkateswara Rao and R.O. Ritchie, *The Effect of Microstructure on Fracture Toughness and Fatigue Crack Growth Behavior in gamma-Titanium Aluminide Based Intermetallics*. Metallurgical and Materials Transactions A, 30A **1999**. pp. 563-577.
101. S. Bystrzanowski, A. Bartels, H. Clemens and R. Gerling, *Characteristics of the tensile flow behavior of Ti-46Al-9Nb sheet material – Analysis of thermally activated processes of plastic deformation*. Intermetallics, 16 (5): **2008**. DOI: 10.1016/j.intermet.2008.02.008. pp. 717-726.
102. T. Tetsui, *Effect of high Nb addition on the mechanical properties and high-temperature deformability of gamma TiAl alloys*. Intermetallics, 10 **2002**. pp. 239-245.
103. W.J. Zhang, G.L. Chen, F. Appel, T.G. Nieh and S.C. Deevi, *A preliminary study on the creep behavior of Ti-45Al-10Nb alloy*. Materials Science and Engineering, A315 **2001**. pp. 250-253.
104. R. Gnanamoorthy, Y. Mutoh and Y. Mizuhara, *Fatigue crack growth behavior of equiaxed, duplex and lamellar microstructure gamma-base TiAl*. Intermetallics, 4 **1996**. pp. 525-532.
105. J.P. Campbell, K.T. Venkateswara Rao and R.O. Ritchie, *On the role of microstructure in fatigue-crack growth of gamma-based TiAl*. Materials Science and Engineering, A239-240 **1997**. pp. 722-728.
106. W.E. Voice, M. Henderson, E.F.J. Shelton and X. Wu, *Gamma titanium aluminide, TNB*. Intermetallics, 13 (9): **2005**. DOI: 10.1016/j.intermet.2004.12.021. pp. 959-964.
107. Y.W. Kim, A. Rosenberger and D.M. Dimiduk, *Microstructural changes and estimated strengthening contributions in a gamma alloy Ti-45Al-5Nb pack-rolled sheet*. Intermetallics, 17 (12): **2009**. DOI: 10.1016/j.intermet.2009.05.018. pp. 1017-1027.
108. H. Clemens, A. Bartels, S. Bystrzanowski, H. Chladil, H. Leitner, G. Dehm, . . . and F.P. Schimansky, *Grain refinement in  $\gamma$ -TiAl-based alloys by solid state phase transformations*. Intermetallics, 14 (12): **2006**. DOI: 10.1016/j.intermet.2005.11.015. pp. 1380-1385.
109. L. Cha, C. Scheu, H. Clemens, H.F. Chladil, G. Dehm, R. Gerling and A. Bartels, *Nanometer-scaled lamellar microstructures in Ti-45Al-7.5Nb-(0; 0.5)C alloys and their influence on hardness*. Intermetallics, 16 (7): **2008**. DOI: 10.1016/j.intermet.2008.03.009. pp. 868-875.
110. M.F. Stroosnijder, V.A.C. Haanappel and H. Clemens, *Oxidation behaviour of TiAl-based intermetallics - influence of heat treatment*. Materials Science and Engineering, A239-240 **1997**. pp. 842-846.
111. G. Chen, Z. Sun and X. Zhou, *Oxidation and mechanical behavior of intermetallic alloys in the Ti-Nb-Al ternary system*. Materials Science and Engineering, A153 **1992**. pp. 597-601.
112. G.L. Chen, W.J. Zhang, Z.C. Liu and S.J. Li. *Microstructure and Properties of High-Nb containing TiAl-base alloys*, in Gamma Titanium Aluminide. (1999). The Minerals, Metals & Materials Society. pp. 371-380.



113. G.L. Chen, L.L. Zhao, J.P. Lin and X.J. Xu. *Recent Progress in high temperature TiAl Alloys*, in The Minerals, Metals & Materials Society. (2011). John Wiley & Sons, ISBN: 9781118029466. pp. 547-555.
114. V.A.C. Haanappel, J.D. Sunderkotter and M.F. Stroosnijder, *The isothermal and cyclic high temperature oxidation behaviour of Ti-48Al-2Mn-2Nb compared with Ti-48Al-2Cr-2Nb and Ti-48Al-2Cr*. Intermetallics, 7 1999. pp. 529-541.
115. A. Zeller, F. Dettenwanger and M. Schutze, *Influence of water vapour on the oxidation behaviour of titanium aluminides*. Intermetallics, 10 2002. pp. 59-72.
116. Y.C. Zhu, X.Y. Li, K. Fujita, N. Iwamoto, Y. Matsunaga, K. Nakagawa and S. Taniguchi, *The improvement of the oxidation resistance of TiAl alloys by fluorine plasma-based ion implantation*. Surface and Coatings Technology, 158-159 2002. pp. 503-507.
117. H. Saage, A.J. Huang, D. Hu, M.H. Loretto and X. Wu, *Microstructures and tensile properties of massively transformed and aged Ti46Al8Nb and Ti46Al8Ta alloys*. Intermetallics, 17 (1-2): 2009. DOI: 10.1016/j.intermet.2008.09.006. pp. 32-38.
118. T.K. Heckel and H.J. Christ, *Thermomechanical Fatigue of the TiAl Intermetallic Alloy TNB-V2*. Experimental Mechanics, 50 (6): 2009. DOI: 10.1007/s11340-009-9264-3. pp. 717-724.
119. ArcamAB, *Arcam A2: Setting the standard for Additive Manufacturing*.
120. ArcamAB, *EBM® Electron Beam Melting*. Available from: <http://www.arcam.com/technology/electron-beam-melting/>.
121. D.D. Challenge, *Arcam A2 Electron Beam Melting technology at work*. (2010). Available from: <http://blog.sculpteo.com/2011/04/27/arcam-a2-electron-beam-melting-technology-at-work/>.
122. L.E. Murr, S.M. Gaytan, D.A. Ramirez, E. Martinez, J. Hernandez, K.N. Amato, . . . and R.B. Wicker, *Metal Fabrication by Additive Manufacturing Using Laser and Electron Beam Melting Technologies*. Journal of Materials Science & Technology, 28 (1): 2012. DOI: 10.1016/s1005-0302(12)60016-4. pp. 1-14.
123. K.V. Wong and A. Hernandez, *A Review of Additive Manufacturing*. ISRN Mechanical Engineering, 2012. DOI: 10.5402/2012/208760. pp. 10.
124. B. Vayre, F. Vignata and F. Villeneuve. *Identification on Some Design Key Parameters for Additive Manufacturing: Application on Electron Beam Melting*, in Forty Sixth CIRP Conference on Manufacturing Systems. (2013). Elsevier B. V. pp. 264–269.
125. E.O. Olakanmi, *Direct Selective Laser Sintering of Aluminum alloy powders* (2008). University of Leeds. p. 415.
126. M. Lamirand, J.-L. Bonnentien, G. Ferriere, S. Guerin and J.-P. Chevalier, *Relative effects of chromium and niobium on microstructure and mechanical properties as a function of oxygen content in TiAl alloys*. Scripta Materialia, 56 2007. pp. 325-328.
127. H.H. Zhu, J.Y.H. Fuh and L. Lu, *The influence of powder apparent density on the density in direct laser-sintered metallic parts*. International Journal of Machine Tools & Manufacture, 47 2007. pp. 294–298.
128. F.-S. Sun, C.-X. Cao, S.-E. Kim, Y.-T. Lee and M.-G. Yan, *Alloying mechanism of Beta stabilizers in a TiAl alloy*. Metallurgical and Materials Transactions A, 32A 2001. pp. 1573-1589.
129. H. Clemens, H.F. Chladil, W. Wallgram, G.A. Zickler, R. Gerling, K.D. Liss, . . . and W. Smarsly, *In and ex situ investigations of the  $\beta$ -phase in a Nb and Mo containing  $\gamma$ -TiAl based alloy*. Intermetallics, 16 (6): 2008. DOI: 10.1016/j.intermet.2008.03.008. pp. 827-833.

130. S. Taniguchi, M. Yoshihara and K. Fujita, *Oxidation Resistance of TiAl Improved by Ion Implantation of Beta-former Elements*. Materials Transactions, 45 (5): **2004**. pp. 1693-1699.
131. D. Hu and R.R. Botten, *Phase transformations in some TiAl-based alloys*. Intermetallics, 10 **2002**. pp. 701-715.
132. T. Novoselova, S. Malinov, W. Sha and A. Zhecheva, *High-temperature synchrotron X-ray diffraction study of phases in a gamma TiAl alloy*. Materials Science and Engineering: A, 371 (1-2): **2004**. DOI: 10.1016/j.msea.2003.12.015. pp. 103-112.
133. J. Lapin and Z. Gabalcová, *Solidification behaviour of TiAl-based alloys studied by directional solidification technique*. Intermetallics, 19 (6): **2011**. DOI: 10.1016/j.intermet.2010.11.021. pp. 797-804.
134. C. Guoqing, Z. Binggang, L. Wei and F. Jicai, *Crack formation and control upon the electron beam welding of TiAl-based alloys*. Intermetallics, 19 (12): **2011**. DOI: 10.1016/j.intermet.2011.07.017. pp. 1857-1863.
135. G.L. Chen, X.J. Xu, Z.K. Teng, Y.L. Wang and J.P. Lin, *Microsegregation in high Nb containing TiAl alloy ingots beyond laboratory scale*. Intermetallics, 15 (5-6): **2007**. DOI: 10.1016/j.intermet.2006.10.003. pp. 625-631.
136. P. Conti, *Microstrutture, tessiture e meccanismi deformativi* (2003). Dipartimento di Scienze della Terra, Università di Siena.
137. F.O. Encyclopedia, *Definition of Twinning*. (2002). Available from: <http://encyclopedia2.thefreedictionary.com/Twinning>.
138. J.J. Xiong and R.A. Shenoi, *Fatigue and Fracture Reliability Engineering* (2011). Springer, ISBN: 978-0-85729-217-9.
139. V. Retina, J. Ahlstriim and B. Karlsson, *Sample preparation and microstructural characterization of the Gamma Titanium Aluminide Ti-48Al-2W-0.5Si*. Materials Characterization, 38 **1997**. pp. 287-300.
140. W.J. Zhang, L. Francesconi, E. Evangelista and G.L. Chen, *Characterization of widmanstätten laths and interlocking boundaries in fully-lamellar TiAl-base alloy*. Scripta Materialia, 37 (5): **1997**. pp. 627-633.
141. P. Wang, G.B. Viswanathan and V.K. Vasudevan, *Observation of a Massive Transformation from alpha to gamma in quenched Ti-48Al alloys*. Metallurgical Transactions A, 23A **1992**. pp. 690-697.
142. T. Novoselova, S. Malinov and W. Sha, *Experimental study of the effects of heat treatment on microstructure and grain size of a gamma TiAl alloy*. Intermetallics, 11 (5): **2003**. DOI: 10.1016/s0966-9795(03)00028-1. pp. 491-499.
143. A. Huang, D. Hu, X. Wu and M.H. Loretto, *The influence of interrupted cooling on the massive transformation in Ti46Al8Nb*. Intermetallics, 15 (9): **2007**. DOI: 10.1016/j.intermet.2007.02.002. pp. 1147-1155.
144. A. Huang, D. Hu, M.H. Loretto and X. Wu, *The formation of grain boundary gamma during cooling of Ti46Al8Nb*. Intermetallics, 17 (5): **2009**. DOI: 10.1016/j.intermet.2008.09.012. pp. 285-290.
145. S.R. Dey, A. Hazotte, E. Bouzy and S. Naka, *Development of Widmanstätten laths in a near- $\gamma$  TiAl alloy*. Acta Materialia, 53 (14): **2005**. DOI: 10.1016/j.actamat.2005.04.007. pp. 3783-3794.
146. H. Okamoto, *Phase diagram Al-Ti*. Journal of Phase Equilibria 14 (1): **1993**. pp. 120.
147. H. Okamoto, *Phase diagram Al-Ti*. Journal of Phase Equilibria, 21 (3): **2000**. pp. 311.
148. H.F. Chladil, H. Clemens, H. Leitner, A. Bartels, R. Gerling, F.P. Schimansky and S. Kremmer, *Phase transformations in high niobium and carbon containing  $\gamma$ -TiAl based alloys*. Intermetallics, 14 (10-11): **2006**. DOI: 10.1016/j.intermet.2005.11.016. pp. 1194-1198.

149. J.C. Schuster and M. Palm, *Reassessment of the binary Aluminum-Titanium phase diagram*. Journal of Phase Equilibria and Diffusion, 27 (3): **2006**. DOI: 10.1361/154770306X109809. pp. 255-277.
150. F. Appel, M. Oehring, J.D.H. Paul, C. Klinkenberg and T. Carneiro, *Physical aspects of hot-working gamma-based titanium aluminides*. Intermetallics, 12 (7-9): **2004**. DOI: 10.1016/j.intermet.2004.02.042. pp. 791-802.
151. S. Malinov, T. Novoselova and W. Sha, *Experimental and modelling studies of the thermodynamics and kinetics of phase and structural transformations in a gamma TiAl-based alloy*. Materials Science and Engineering: A, 386 (1-2): **2004**. DOI: 10.1016/j.msea.2004.07.052. pp. 344-353.
152. P.A. McQuay, *Thermal analysis of phase transformations in a gamma-TiAl alloy*. Materials Science and Engineering, A185 **1994**. pp. 55-63.
153. N. Saunders. *Phase Equilibria in Multi-component Gamma-TiAl based alloys*, in Gamma Titanium Aluminides. (**1999**). The Minerals, Metals & Materials Society. pp. 183-188.
154. G. Shao and P. Tsakiroopoulos. *Interplay of Thermodynamics and Transformation Kinetics on Microstructural Development in TiAl-based Alloys*, in Gamma Titanium Aluminides. (**1999**). The Minerals, Metals & Materials Society. pp. 189-194.
155. M. Beschliesser, H. Clemens, H. Kestler and F. Jeglitsch, *Phase stability of a gamma-TiAl based alloy upon annealing: comparison between experiment and thermodynamic calculations*. Scripta Materialia, 49 **2003**. pp. 279-284.
156. L.A. Yeoh, K.-D. Liss, A. Bartels, H. Chladil, M. Avdeev, H. Clemens, . . . and T. Buslaps, *In situ high-energy X-ray diffraction study and quantitative phase analysis in the  $\alpha+\gamma$  phase field of titanium aluminides*. Scripta Materialia, 57 (12): **2007**. DOI: 10.1016/j.scriptamat.2007.08.021. pp. 1145-1148.
157. K. Backfolk, R. Holmes, P. Ihalainen, P. Sirvio, N. Triantafillopoulos and J. Peltonen, *Determination of the glass transition temperature of latex films: Comparison of various methods*. Polymer Testing, 26 **2007**. pp. 1031-1040.
158. S.C. Huang, E.L. Hall and D.S. Shih, *Microstructure and Ductility of TiAl alloys modified by Cr additions*. ISIJ International, 31 (10): **1991**. pp. 1100-1105.
159. MPIF, *Isostatic Pressing*. Available from: <http://www.mpif.org/DesignCenter/isostatic.asp?linkid=108>.
160. T. Tetsui and Y. Miura, *Heat-resistant Cast TiAl Alloy for Passenger Vehicle turbochargers*. Mitsubishi Heavy Industries, Technical Review, 39 (1): **2002**. pp. 1-5.
161. A. Donchev, B. Gleeson and M. Schütze, *Thermodynamic considerations of the beneficial effect of halogens on the oxidation resistance of TiAl-based alloys*. Intermetallics, 11 (5): **2003**. DOI: 10.1016/s0966-9795(03)00003-7. pp. 387-398.
162. Y. Shen, X. Ding and F. Wang, *High temperature oxidation behavior of Ti-Al-Nb ternary alloys*. Journal of Materials Science, 39 **2004**. pp. 6583- 6589.
163. S.-B. Li, L.-F. Cheng and L.-T. Zhang, *The morphology of oxides and oxidation behavior of Ti<sub>3</sub>SiC<sub>2</sub>-based composite at high-temperature*. Composites Science and Technology, 63 (6): **2003**. DOI: 10.1016/s0266-3538(02)00285-3. pp. 813-819.
164. W.S. Yang, Z.Y. Xiu, X. Wang, Y.M. Liu, G.Q. Chen and G.H. Wu, *Microstructure evolution and oxidation behaviour of Tif/TiAl<sub>3</sub> composites*. Materials & Design, 32 (1): **2011**. DOI: 10.1016/j.matdes.2010.06.009. pp. 207-216.
165. S.-B. Li, L.-F. Cheng and L.-T. Zhang, *Oxidation behavior of Ti<sub>3</sub>SiC<sub>2</sub> at high temperature in air*. Materials Science and Engineering, A341 **2003**. pp. 112-120.
166. I. Limited, *High Temperature High Strength Nickel Base Alloys*, (**1995**). Nickel Development Institute. pp. 76.